# Chemical interaction between ocean and atmosphere

Dissertation
zur Erlangung des Grades
"Doktor der Naturwissenschaften"

am Fachbereich Physik, Mathematik und Informatik
der Johannes Gutenberg-Universität
in Mainz

Bastian Kern
geb. in Lahnstein

Mainz, den 06.11.2013

D77 – Mainzer Dissertation

1. Berichterstatter:
2. Berichterstatter:

Tag der mündlichen Prüfung: 11. März 2014

# Abstract

The exchange of chemical constituents between ocean and atmosphere provides potentially important feedback mechanisms in the climate system. The aim of this study is to develop and evaluate a chemically coupled global atmosphere-ocean model.

For this, an atmosphere-ocean general circulation model with atmospheric chemistry has been expanded to include oceanic biogeochemistry and the process of air-sea gas exchange. The calculation of seawater concentrations in the oceanic biogeochemistry submodel has been expanded from DMS, $CO_2$, and $N_2O$ to include also CO and isoprene ($C_5H_8$). Further new implementations comprise the possibilities to consider the nutrient import by rivers into the ocean, and the dust deposition as a source of silicic acid ($Si(OH)_4$) from silica ($SiO_2$) in addition to iron (Fe). Moreover, the climatological dust deposition can now be replaced by a simulated one from the atmospheric model.

To evaluate the novel model system, a set of simulations under year-2000 conditions focusing on the major chemical interactions between ocean and atmosphere have been performed. With additional sensitivity studies the impact of a modified nutrient import from interactive dust deposition and from additional nutrient import by rivers has been assessed. To prepare the model system for studies on climatological time-scales, cloud parameterisation related parameters have been optimised for a suited model resolution.

The simulations show robust and consistent responses of the model system to forcings in terms of interactive oceanic biogeochemistry. Deficiencies in the representation of oceanic net primary production (NPP) have been identified, depending strongly on the coupling frequency providing solar irradiance at the ocean's surface. An approximately linear relationship between air-sea gas fluxes and surface water concentrations for the interactively simulated reactive species (DMS, $C_5H_8$, and CO) has been found. Additional nutrient import to the ocean by rivers shows only weak, insignificant impacts on the atmospheric composition, mostly due to the coarse resolution and the not well represented shelf areas. The modified dust deposition shows only a minor effect, although the interactively simulated amount of dust deposited into the ocean is twice as large as the previously used climatology. This weak impact of enhanced Fe and $SiO_2$ deposition is due to the limitation of phytoplankton growth by nitrate in aqueous phase ($NO_3^-$) in the main dust deposition regions.

In summary, the chemically coupled model system is well prepared for applications in chemistry-climate research.

# Zusammenfassung

Der Austausch chemischer Stoffe zwischen Ozean und Atmosphäre stellt einen möglichen wichtigen Rückkopplungsmechanismus im Klimasystem dar. Ziel dieser Studie ist die Entwicklung und Evaluierung eines chemisch gekoppelten globalen Atmosphäre-Ozean-Modells.

Dazu wurde ein Atmosphäre-Ozean-Zirkulationsmodell mit atmosphärischer Chemie um wichtige Prozesse der ozeanischen Biogeochemie und um den Gasaustausch zwischen Ozean und Atmosphäre erweitert. Zusätzlich zu Meerwasserkonzentrationen von DMS, $CO_2$ und $N_2O$ berechnet das ozeanische Biogeochemiemodell nun auch die von CO und Isopren ($C_5H_8$). Weitere Neuerungen umfassen die Möglichkeiten Nährstoffeintrag aus Flüssen in den Ozean und Staubdeposition als Quelle von Kieselsäure ($Si(OH)_4$) aus Siliziumdioxid ($SiO_2$), neben Eisen (Fe), zu berücksichtigen. Des Weiteren kann die klimatologische Staubdeposition durch die interaktiv berechnete des Atmosphärenmodells ersetzt werden.

Die Evaluierung des neuen Modellsystems erfolgte durch Simulationen unter gleichbleibenden Bedingungen für das Jahr 2000 und einer Analyse der wichtigsten chemischen Wechselwirkungen. Die Einflüsse modifizierter Nährstoffeinträge durch interaktive Staubdeposition und zustätzlicher Nährstoffeinträge aus Flüssen wurden anhand weiterer Sensitivitätsstudien abgeschätzt. Zur Vorbereitung des Modellsystems für Studien auf klimatologischen Zeitskalen wurden Parameter der Wolkenparametrisierung für eine entsprechende Modellauflösung optimiert.

Das Verhalten des Modells mit interaktiver Biogeochemie ist stabil und die Ergebnisse sind konsistent. Defizite wurden bei der ozeanischen Primärproduktion identifiziert. Diese ist von der Kopplungsfrequenz abhängig, die die solare Strahlungsdichte am Ozeanoberrand beeinflusst. Es besteht eine nahezu lineare Abhängigkeit zwischen Ozean-Atmosphäre-Gasflüssen und ozeanischen Oberflächenkonzentrationen der interaktiv simulierten reaktiven Komponenten (DMS, $C_5H_8$ und CO). Zusätzlicher Nährstoffeintrag aus Flüssen bedingt geringe, nicht signifikante Einflüsse auf die atmosphärische Zusammensetzung, begründet in der groben Modellauflösung und der eingeschränkten Darstellung des Kontinentalschelfs. Die modifizierte Staubdeposition zeigt nur geringen Einfluss, obwohl der interaktive Staubeintrag in den Ozean doppelt so groß ist wie der zuvor benutzte klimatologische. Dieser schwache Einfluss erhöhter Einträge von Fe und $SiO_2$ wird durch die Limitierung des Phytoplanktonwachstums durch Nitrat ($NO_3^-$) in den Hauptdepositionsgebieten erklärt.

Insgesamt ist das neue, chemisch gekoppelte Modellsystem für zukünftige Studien zur Klima-Chemie Wechselwirkung einsatzbereit.

We can only see a short distance ahead, but we can see plenty there that needs to be done.

*Turing (1950)*

# Contents

# Chapter 1

# Introduction

The ocean plays a prominent role in the Earth's climate system. More than 70 % of the Earth's surface is covered by seawater. As Earth's main water reservoir, the ocean influences the hydrological cycle and atmospheric radiative transfer, accounting for 85 % of the atmospheric water vapour (Bigg et al., 2003), which is the major natural greenhouse gas (GHG). Providing an estimated water volume of $1.3324 \times 10^9\,\mathrm{km}^3$ (Charette and Smith, 2010) the ocean conducts a "thermal lag on the climate" (Bigg et al., 2003) via its thermal inertia, because of the specific heat capacity of water. The heat exchange between ocean and atmosphere strongly depends on the time scale. The mixed layer of the ocean plays a role on shorter time scales up to decades, whereas on time scales of hundreds to thousands of years the deep ocean, which provides a larger effective heat capacity than the mixed layer, is also important (Bigg et al., 2003).

The ocean's surface area of $361.84 \times 10^6\,\mathrm{km}^2$ (Charette and Smith, 2010) provides a large interface to the atmosphere. At this interface a variety of interactions between ocean and atmosphere take place, influencing the dynamics and chemistry in each of the two domains. Fig. 1.1 shows a schematic overview of the atmosphere-ocean system and the interactions between the domains. Atmosphere-ocean interactions can be divided into physical and chemical processes.

Physical interactions are exchange of heat, momentum, and water mass. Heat exchange occurs by sensible heat flux, due to conduction, and latent heat flux via evaporation of water, both determined by the ocean's surface temperature. Momentum exchange at the atmosphere-ocean interface depends on the wind stress applied to the ocean surface and on the ocean surface roughness. Water mass is exchanged between atmosphere and ocean by evaporation and precipitation,

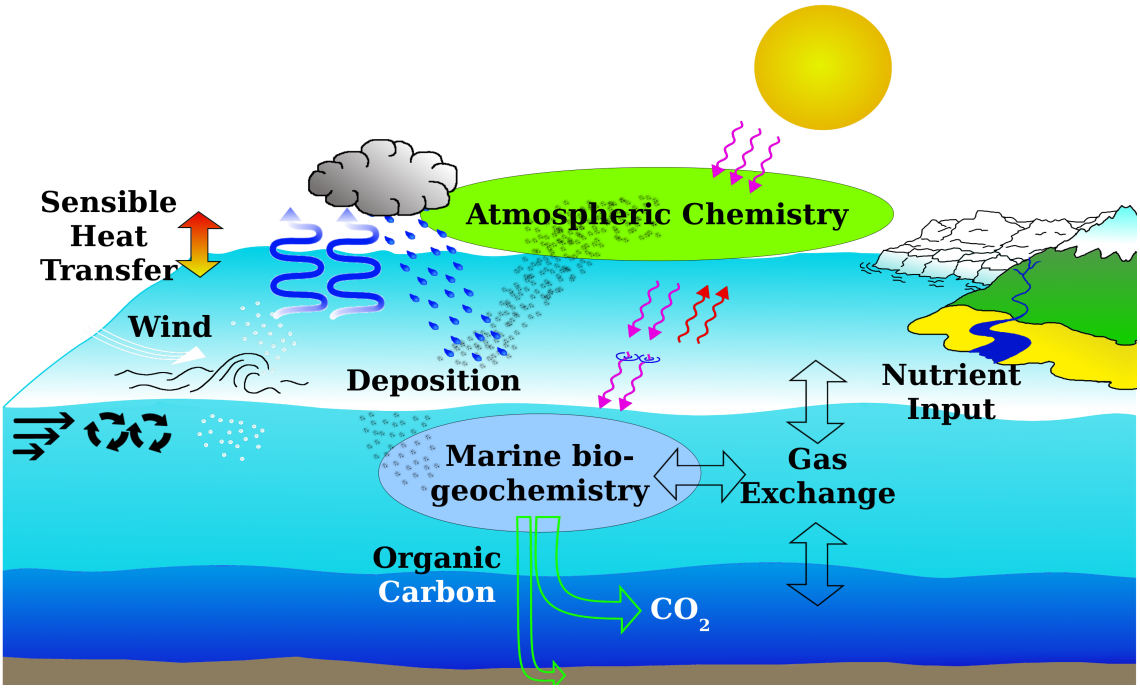


**Figure 1.1:** Interactions in the atmosphere ocean system. Interactions at the air-sea interface can be divided into physical and chemical processes. Physical interactions are momentum exchange by wind stress (white arrow)—generating waves, bubbles and sea spray (white circles), shear, and eddies (black arrows)—, heat transfer (red-yellow arrow), and exchange of water by riverine and glacial freshwater input, precipitation, and evaporation (blue arrows). Chemical interactions are oceanic import by dry and wet deposition and sedimentation in the atmosphere (gray dots), natural and anthropogenic riverine input, and air-sea gas exchange (black open arrows). Chemical compounds imported to the ocean act as nutrients (gray dots) on marine biological production. Incoming solar radiation (violet arrows) is altered by the atmospheric chemical composition, partly reflected (red arrows) and absorbed by seawater. A fraction of solar irradiance—the photosynthetically available radiation (PAR)—is available to marine biological production via photosynthesis. Dead phytoplankton is exported (open green arrows) to the deep ocean (dark blue) in form of particulate organic carbon (POC) and buried in the sediments (brown), parts are re-mineralised in deeper ocean layers. Based on SOLAS (2004).

determining the atmospheric hydrological cycle and influencing Earth's radiation budget. Physical interactions directly impact the dynamics of the domains, but also influence chemical and biogeochemical processes by changes in circulation and temperature. Evaporation and freshwater input from the atmosphere by precipitation and by river discharge act on the oceanic circulation, on seawater density, and on seawater temperature.

The chemical interaction between the atmosphere and the ocean is determined by the exchange of chemically, biologically, and radiatively reactive compounds between the two domains. This exchange alters the concentrations of chemical compounds in the atmosphere and in the ocean, and in this way acts on atmospheric chemistry and oceanic biogeochemistry, which both eventually impact the dynamics of the particular domain. Chemical compounds enter the ocean via air-sea gas exchange, wet and dry deposition, and input from rivers. Air-sea gas exchange depends on the oceanic and atmospheric concentration of the specific gas, its solubility, seawater temperature, ocean salinity, and the physical state of the ocean surface. The physical state of the ocean surface is determined by wind stress, sea spray, and bubbles of atmospheric gas composition in the upper ocean layer (Wanninkhof et al., 2009). Air-sea gas exchange is also altered by atmospheric boundary layer stability and the presence of surfactants on the water surface, which tend to suppress gas fluxes between the two domains (Wanninkhof, 1992).

In the ocean, biological production impacts chemical concentration and composition. Biological production depends on the availability of nutrients, light, and on temperature. The nutrient availability in the open ocean surface water is determined by wet and dry deposition of atmospheric constituents, import from rivers, and advection. An important nutrient is iron, which acts as micronutrient on phytoplankton and influences plankton growth and bloom (Mills et al., 2004; Moore et al., 2009). The main source of iron to open ocean waters is mineral dust, transported from deserts and deposited to the ocean. Mineral dust can be transported over long distances from its emission regions before being deposited onto Earth's surface. For instance, dust plumes originating from dust outbreaks in the Saharan desert can reach the Amazon forest (Martin et al., 2010). During the transport, dust is subject to chemical modifications, which alter iron solubility (Shi et al., 2011). It has been estimated that dust deposition is the main input mechanism of iron to high nutrient low chlorophyll (HNLC) areas in the ocean (Martin et al., 1991; Jickells et al., 2005; Boyd et al., 2007). Hence dust deposition influences phytoplankton and therefore indirectly impacts oceanic concentrations of chemical compounds.

Changes in surface seawater concentrations directly influences the air-sea gas exchange by changing the ocean-to-atmosphere difference in concentrations, and eventually alter the atmospheric composition and chemistry, and hence impact radiative forcing (Jickells et al., 2005). In coastal areas, rivers transport additional chemical compounds into the ocean, where they partly act as nutrients on oceanic biogeochemistry (Meybeck, 1982, 1998; Cotrim da Cunha et al., 2007). The natural

origin of these compounds is chemical erosion of soils and rocks, but there are also anthropogenic sources like sewage and fertilisers used in agriculture (Martin and Meybeck, 1979; GESAMP, 1987; Seitzinger et al., 2005). The composition and concentrations reaching the ocean are further influenced by damming (Seitzinger et al., 2010).

Chemical changes in the ocean and atmosphere impact the dynamics of the two domains. In the ocean, changes in biogeochemistry affect the biological pump (Longhurst, 1991; Lam et al., 2011), which redistributes chemicals in the vertical, and light absorption in upper water layers (Wetzel et al., 2006). In the atmosphere, the chemical composition has a direct impact on the atmospheric radiative transfer and radiation balance. Some of the chemical compounds form aerosol particles, partly acting as cloud condensation nuclei (CCN), and in this way have a direct or indirect effect on radiation (Denman et al., 2007). Changes in the dynamics, on the other side, alter the spatial variation of chemical concentrations and therefore feed back on the chemical state of the atmosphere.

The sun is the main driver of the Earth's weather and climate system. Weather and climate depend on the quantity and distribution of incoming solar radiation (Trenberth et al., 2009). The global energy flow in the Earth system, broken down into its components, is shown in Fig 1.2. In addition to the ocean's direct energy flows via sensible and latent heat flux, the air-sea gas exchange impacts Earth's energy budget via changes in atmospheric concentrations of radiative important gases (greenhouse gases (GHGs)) and their precursors.

The ocean acts as sink or source of atmospheric gases, corresponding to the relative under- or over-saturation of surface seawater at a certain location with respect to the atmospheric concentration of the specific gas. The local oceanic concentration of chemical compounds is determined by transport via advection and mixing, fluxes at the air-sea interface and from the sediments, and internal sources and sinks by chemical and biological processes (Sarmiento and Gruber, 2006). Inorganic chemicals are removed from seawater by photosynthesis and chemosynthesis, which are driven by light and chemical reactions as energy source, respectively (Sarmiento and Gruber, 2006). These processes mainly happen in the upper 100 m of the ocean, where sufficient light for photosynthesis is available. This layer is called the euphotic zone. Below the euphotic zone biological processes act as source of inorganic chemicals via remineralisation (cf. Fig. 1.1). The photosynthetically available radiation (PAR) at Earth's—and hence the ocean's—surface depends on the amount of radiation (irradiance) reaching this level. Surface irradiance depends on the

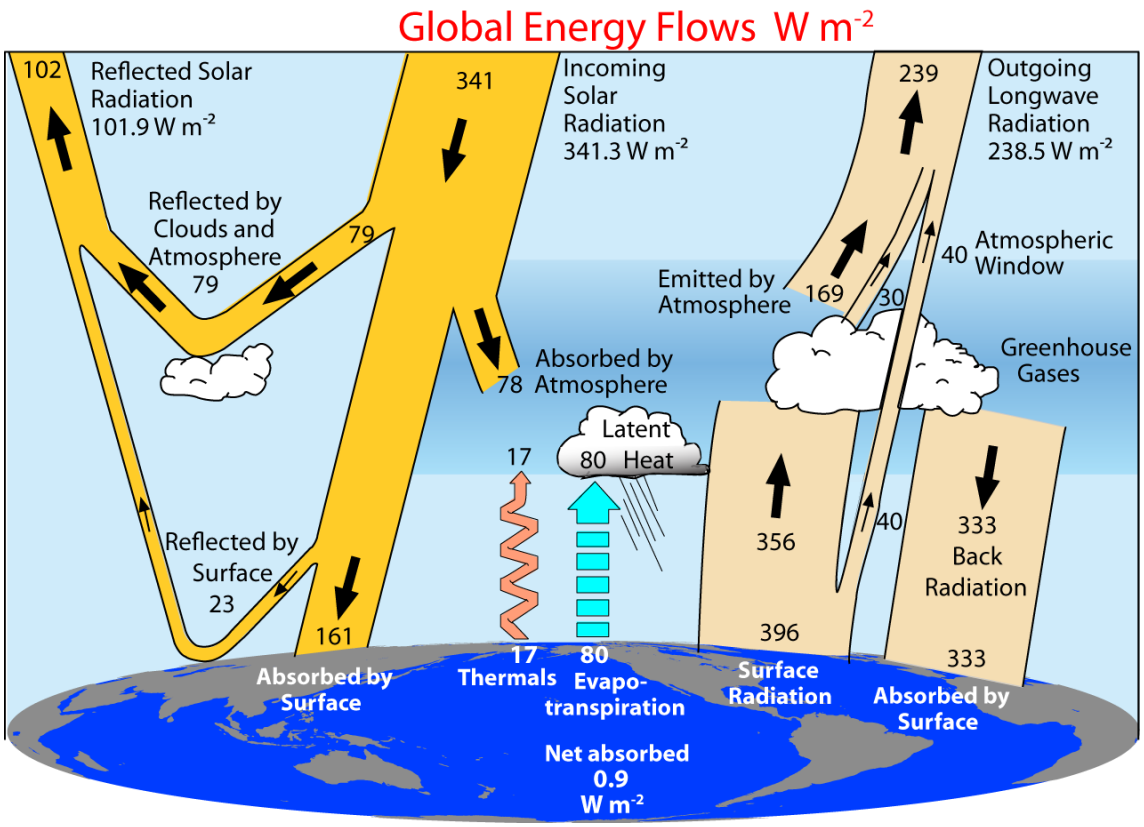


**Figure 1.2:** Earth's global annual mean energy budget for March 2000 to May 2004. Energy fluxes are given in W m$^{-2}$. The broadness of each schematic energy flow is proportional to its importance. From Trenberth et al. (2009).

atmospheric radiative transfer, which is influenced by the atmospheric chemical composition, clouds, and aerosols. Air-sea gas fluxes have an impact on atmospheric gas concentration and composition, and thus on atmospheric radiative transfer. Therefore, via the control of the oceanic chemical concentration by photosynthesis, air-sea gas exchange provides a feedback mechanism between oceanic biogeochemistry and atmospheric chemistry.

Some of the various feedback mechanisms in the atmosphere-ocean system have been studied, but are not well quantified. Feedback mechanisms impact each other, which makes it difficult to separate and quantify impacts of individual processes. To study the complex system of feedbacks and to assess the impact of individual processes, numerical models are used. In this study, an oceanic biogeochemistry model and an atmospheric chemistry climate model (CCM) are coupled. The process of air-sea gas exchange is included in the model system, to represent chemical feedback mechanisms between the ocean and the atmosphere. The aim is to quantify the

impact of oceanic biogeochemistry and its variability on atmospheric composition and atmospheric chemical reactions. The CCM is extended with the necessary processes, to provide a model system for the analysis of the dynamically and chemically coupled ocean-atmosphere system, to gain a deeper understanding of feedback mechanisms and to provide the possibility to assess the impact of individual processes in the Earth's climate system.

## 1.1 Motivation

The atmospheric composition determines the radiative transfer in the atmosphere (see also Fig. 1.2). This does not only impact surface temperatures but also PAR, which both impact biological production in the ocean's euphotic zone. Uptake and emission of radiative active compounds and chemically reactive gases into and from the ocean depends on surface oceanic concentrations. Oceanic surface concentrations are determined by biogeochemical processes in the ocean. Air-sea gas fluxes, in turn, impact the atmospheric concentrations of the corresponding gas, providing a feedback mechanism between atmospheric and oceanic tracer concentrations. Some of the oceanic emissions are precursor gases for formation of secondary organic aerosol (SOA) particles, which impact the climate system via a direct effect on atmospheric radiation and also via an indirect effect by forming CCN (e.g. Carslaw et al., 2010). Although the impact of ocean-atmosphere exchange on atmospheric particle formation is considered to be important for radiative processes in the atmosphere, this study is a first step towards coupling oceanic biogeochemistry and detailed tropospheric chemistry in a model system, and thus focuses on impacts of ocean-atmosphere interactions on atmospheric gas-phase chemistry only.

In this way a strong coupling exists between climate and biogeochemical cycling of the Earth's major elements (Sarmiento and Gruber, 2006). The strength of theses feedbacks and interactions between different feedbacks is not yet well quantified. One goal of this study is to estimate the impact of oceanic emissions of chemically reactive gases on the atmospheric chemical composition, to provide one step for analysing feedback mechanisms between oceanic biogeochemistry and atmospheric chemistry. The resulting numerical model system provides a tool for future projects on quantifying the impact of individual feedback mechanisms on the climate system.

Interactive changes in atmospheric concentrations of dimethyl sulphide ($(CH_3)_2S$, DMS), isoprene ($C_5H_8$), carbon monoxide (CO), and methanol ($CH_3OH$) from their oceanic emissions are analysed here, focusing on the impact on tropospheric chemistry

on time scales of years. Oceanic fluxes of carbon dioxide ($CO_2$) and nitrous oxide ($N_2O$) are also considered in the simulations, but their atmospheric concentrations are prescribed. On longer time scales, these longer lived species are important in radiative transfer and stratospheric chemistry. The sources of these species and their role in atmospheric chemistry, in atmospheric chemical composition, and in atmospheric radiative transfer will be briefly discussed in the remainder of this section. Because the present model system lacks an interactive vegetation model, the carbon cycle is not further investigated in this study.

### 1.1.1 Carbon dioxide ($CO_2$)

Carbon dioxide ($CO_2$) is known to be an important trace gas in connection with climate change. It absorbs radiation in the infrared wavelengths and impacts stratospheric ozone ($O_3$) concentrations. The radiative impact of $CO_2$ in the present atmosphere is seconded only by the radiative impact of water vapour ($H_2O$; Seinfeld and Pandis, 1998).

With the beginning of the Industrial Revolution in the mid to late 18th century, fossil fuel and cement production became the main carbon dioxide sources. They account "for more than 75 % of the increase in atmospheric $CO_2$ concentration since pre-industrial times" (Denman et al., 2007). The remaining increase in atmospheric $CO_2$ concentrations is accounted for by land use change.

Via air-sea gas exchange, the ocean acts as a net sink for atmospheric $CO_2$. It is estimated, that the ocean stored about $(118 \pm 19)\,\mathrm{Pg(C)}$ ($1\,\mathrm{Pg} = 1 \times 10^{15}\,\mathrm{g} = 1\,\mathrm{Gt}$) of anthropogenic carbon dioxide from 1800 to 1994 (Sabine et al., 2004). This oceanic carbon dioxide uptake accounts for about 30 % of the anthropogenic $CO_2$ emissions, whereas almost 45 % remained in the atmosphere (Sabine et al., 2004; Denman et al., 2007). The present day total global flux of $CO_2$ into the ocean is estimated to be in the range of $1\,\mathrm{Pg(C)\,a^{-1}}$ to $3\,\mathrm{Pg(C)\,a^{-1}}$ (Takahashi et al., 2009).

Oceanic carbon sequestration does not only influence atmospheric $CO_2$ concentration, but also lowers the pH value of seawater, a process known as ocean acidification (Kleypas et al., 1999; Feely et al., 2004; Orr et al., 2005; Denman et al., 2007). A lower pH of sea-water results in a reduced $CO_2$ uptake. Ocean acidification and elevated seawater temperatures act as stressor to oceanic life-forms (e.g. Feely et al., 2004; Doney et al., 2009; Henson, 2011). An increased frequency and spatial extension of coral bleaching has been observed in the last decades, for which stress by increased ocean temperatures was accounted for (Henson, 2011). There may be interspecific

differences in levels of resistance to increased temperature and increased ocean acidification, but species may be influenced, if both processes occur simultaneously (Rodolfo-Metalpa et al., 2011). Lowered carbonate concentrations in seawater, as a consequence of a lower pH, vary regionally (Orr et al., 2005), but a "reduced diversity, structural complexity and resilience" of coral reefs can be expected, at least in the Indo-Pacific (Fabricius et al., 2011).

Coral reefs provide large ecological and economical benefits (Spurgeon, 1992; Moberg and Folke, 1999), for example by dissipating wave energy and thus providing coastal protection from waves, storms, and erosion. Bleaching and destruction of coral reefs can lead to an increased risk for land erosion and flooding of coastal areas, which also suffer from sea level rise by elevated seawater temperatures and increased glacier melting.

### 1.1.2 Nitrous oxide ($N_2O$)

Nitrous oxide ($N_2O$) is a potent GHG, with a radiative forcing potential which is about 300 times larger than that of $CO_2$ on a 100-year horizon (Forster et al., 2007). Because of its long lifetime of 114 years, $N_2O$ is transported to the stratosphere, where it forms the primary source of stratospheric nitrogen oxides ($NO_x$) via the photolytic reaction with electronically exited oxygen atoms ($O(^1D)$). In this way $N_2O$ contributes to stratospheric $O_3$ depletion (Crutzen, 1970; Solomon, 1999).

The ocean is a net source of $N_2O$, with oceanic sources rather well constrained (Rhee et al., 2009), ranging from $1.2\,\mathrm{Tg(N)\,a^{-1}}$ to $6.8\,\mathrm{Tg(N)\,a^{-1}}$ (Nevison et al., 1995). The contribution of oceanic $N_2O$ emissions to total natural $N_2O$ emissions is about 35 %, emissions from soils—especially in the tropics—contribute 60 %, and atmospheric chemistry—via the oxidation of ammonia—about 5 % (Denman et al., 2007). Anthropogenic $N_2O$ emissions account for about 38 % of the total $N_2O$ emissions. The biggest single source of anthropogenic $N_2O$ is agriculture, accounting for about 50 % of the anthropogenic emissions, the remainder stems from combustion processes and waste water treatment (Denman et al., 2007).

### 1.1.3 Dimethyl sulphide (DMS)

Dimethyl sulphide ($(CH_3)_2S$, DMS) is one of the oceanic emissions that gained largest attention in the recent decades (Kettle et al., 1999; Lana et al., 2011). Lovelock et al. (1972) and Nguyen et al. (1978) suggested that oceanic emissions of DMS close—at least partly—the total atmospheric sulphur budget and account

for the atmospheric background observations of sulphur dioxide ($SO_2$) in remote areas, not influenced by anthropogenic sulphur emissions. DMS is oxidised in the atmosphere with the the hydroxyl radical (OH) as oxidant, forming $SO_2$ and to smaller amounts methanesulphonic acid ($CH_3S(O)_2OH$, MSA), dimethyl sulfoxide, and dimethyl sulfone (Andreae and Crutzen, 1997). In the troposphere DMS oxidation supports the formation of new particles acting as CCN, in the marine boundary layer (MBL) it supports the growth of smaller particles into CCN (Andreae and Crutzen, 1997). Atmospheric particles impact the radiation budget directly by scattering of solar radiation, or indirectly by acting as CCN and changing cloud properties. Charlson, Lovelock, Andreae, and Warren (1987) formulated the CLAW hypothesis, which suggests a feedback loop between DMS production by phytoplankton, oceanic emission of DMS, formation of CCN, changes in cloud properties, and altered solar radiation available for plankton photosynthesis. However challenged by model studies, suggesting limited CCN formation (e.g. Carslaw et al., 2010), and failing to correlate DMS production directly to phytoplankton concentrations (Simó, 2001), the CLAW hypothesis stimulated research in the multidisciplinary Earth System Science, resulting in more than 1500 scientific publications on this hypothesis since its original formulation (Ayers and Cainey, 2007).

Estimated globally integrated annual DMS fluxes from the ocean are uncertain, ranging from $15\,\mathrm{Tg(S)\,a^{-1}}$ to $54\,\mathrm{Tg(S)\,a^{-1}}$ (Kettle and Andreae, 2000, and references therein). Despite the uncertain magnitude and even direction of feedbacks on the climate system via CCN production, DMS is a sulphur source to the atmosphere, where it alters atmospheric composition, chemistry, and aerosol formation. DMS is the main natural sulphur source for the marine boundary layer (Andreae and Raemdonck, 1983). Furthermore, it is regarded as main source of total atmospheric sulphur in the southern hemisphere, whereas sulphur concentrations in the northern hemisphere are dominated by anthropogenic emissions (Lana et al., 2011).

### 1.1.4 Isoprene ($C_5H_8$)

Phytoplankton emits the volatile organic compound (VOC) isoprene ($C_5H_8$) (Bonsang et al., 1992) and—to a lower extend—monoterpenes (Yassaa et al., 2008). Whereas $C_5H_8$ emissions by plants are thought to be reactions to stress—e.g. temperature and reactive oxygen—(Sharkey and Singsaas, 1995; Sharkey et al., 2008), there is no evidence for changes in $C_5H_8$ production by phytoplankton under stress (Shaw, 2001; Shaw et al., 2003). For land vegetation it is suggested that VOC emissions may also

support other biological functions of the emitting plants, like promoting flowering (Terry et al., 1995), however, the role of $C_5H_8$ in plant physiology is still not fully resolved. The function of $C_5H_8$ release from phytoplankton is even more unclear. Compared to terrestrial plants, the production rate of $C_5H_8$ relative to photosynthetic carbon fixation reported for phytoplankton is small ($10^{-4}$ % for phytoplankton vs. 2 % to 5 % for terrestrial plants), therefore $C_5H_8$ emissions from phytoplankton are thought to rather be a carbon leak than a functional release (Shaw et al., 2003).

Estimates for $C_5H_8$ emitted from the oceanic source to the atmosphere range from 0.1 to 1.2 Tg(C) $a^{-1}$ (Palmer and Shaw, 2005, and references therein), which is low compared to $C_5H_8$ emitted by plants over land, mainly from the tropical rainforest ($\approx$ 500 Tg(C) $a^{-1}$; Guenther et al., 1995). But oceanic $C_5H_8$ emissions can be the main local isoprene source to the atmosphere—especially in the MBL of remote ocean regions—because of its high reactivity and its short atmospheric lifetime of 1 to 2 h (Palmer and Shaw, 2005).

$C_5H_8$ is suggested to modify the tropospheric oxidation capacity by rapid reaction with OH and $O_3$ in unpolluted regions with low amounts of $NO_x$. This was challenged by Lelieveld et al. (2008) and Taraborrelli et al. (2012), who suggest, that OH is efficiently recycled and not depleted in unpolluted air over a pristine forest. In terms of biosphere-atmosphere interaction, this results in a stabilising effect on atmospheric chemistry and climate over the forest, because of SOA formation from oxidised VOC acting as CCN.

Nevertheless, in polluted areas $C_5H_8$ contributes to photochemical smog and produces $O_3$ and other toxic oxidants by reaction with nitric oxide (NO; Lelieveld et al., 2008). Carbonyls, like methane vinyl ketone (MVK), methacrolein (MACR), and formaldehyde (HCHO) are products of $C_5H_8$ oxidation. Further oxidation of MVK and MACR can form peroxyacetylnitrate (PAN) and peroxymethacryloylnitrate (MPAN), which can be transported over longer distances and alter local and regional atmospheric $NO_x$ concentrations, eventually affecting tropospheric $O_3$ concentrations (Shallcross and Monks, 2000).

### 1.1.5 Carbon monoxide (CO)

Photochemical production and microbial consumption determine the oceanic carbon monoxide (CO) surface concentration (Kettle, 2005a). The ocean was already suggested to be a source for atmospheric CO by Swinnerton et al. in 1970. Ocean-to-atmosphere flux of CO is estimated to be in the range of 8.5 Tg(C) $a^{-1}$ to 86 Tg(C) $a^{-1}$

(Bergamaschi et al., 2000; Ehhalt et al., 2001), with a recent study of Stubbins et al. (2006) suggesting open ocean CO emissions of $(3.7 \pm 2.6)\,\mathrm{Tg(C)\,a^{-1}}$. This is small compared to a total CO emission flux of $214\,\mathrm{Tg(C)\,a^{-1}}$ to $643\,\mathrm{Tg(C)\,a^{-1}}$, but the ocean is the main natural source. In the troposphere, CO determines the oxidation capacity of the atmosphere by reaction with OH, where almost all CO is lost in this reaction, which acts as sink for approximately 41 % of OH (von Kuhlmann et al., 2003).

### 1.1.6 Methanol ($CH_3OH$)

The oceanic net sink of methanol ($CH_3OH$) is uncertain, ranging from $0.1\,\mathrm{Tg(C)\,a^{-1}}$ to $21\,\mathrm{Tg(C)\,a^{-1}}$ (Heikes et al., 2002; Galbally and Kirstine, 2002; Jacob et al., 2005). A recent model study by Millet et al. (2008), suggests an oceanic $CH_3OH$ source of $32\,\mathrm{Tg(C)\,a^{-1}}$ and sink of $38\,\mathrm{Tg(C)\,a^{-1}}$, resulting in an oceanic $CH_3OH$ net sink of $6\,\mathrm{Tg(C)\,a^{-1}}$. The main sink of atmospheric $CH_3OH$ is ocean uptake ($38\,\mathrm{Tg(C)\,a^{-1}}$) and gas-phase oxidation by OH ($33\,\mathrm{Tg(C)\,a^{-1}}$; Millet et al., 2008).

Via the tropospheric gas-phase reaction with OH, $CH_3OH$ impacts the oxidation potential of the atmosphere and is a source of formaldehyde (HCHO; Seinfeld and Pandis, 1998) and CO (Duncan et al., 2007). The tropospheric lifetime of $CH_3OH$ is about 5 d to 10 d (Jacob et al., 2005; Millet et al., 2008).

Oceanic production, consumption, and associated processes in seawater are not well known. However, a $CH_3OH$ source via biological production by different phytoplankton cultures and bacterial sources has been proposed. Losses of $CH_3OH$ in seawater are hypothesised by photochemical destruction and microbial uptake (Dixon et al., 2011). So far, only one publication reporting measurements of $CH_3OH$ concentrations in seawater exists (Williams et al., 2004).

## 1.2 State of the art

The Earth System is characterised by a complex interplay of multiple physical and biogeochemical processes linked to and impacting each other. One key question in climate science is the future evolution of climate in the Earth System and the impact of human activity, to identify possible mitigation strategies and to quantify their influences on the future climate system.

As there is no "second Earth" to experiment with, future evolution of climate in the complex Earth System under different, assumed scenarios of (anthropogenic) forcings has to be investigated in another way. Whereas individual processes of the Earth System can be represented in laboratory, mesocosm, or free-air experiments, the interplay and impact of all processes in the Earth System on the system itself can not (Schellnhuber, 1999). Numerical models are essential tools for studying climate variability and future change, quantifying climate impacts of different processes and their interaction with each other, and determining the effect on climate of human activity and possible mitigation strategies (Flato, 2011).

Looking at the complexity of the Earth's climate system, different domains interacting with each other can be identified. From early climate models, developed directly from numerical weather prediction systems and containing only the atmosphere, complex model systems evolved, which now incorporate the hydrosphere, the cryosphere, and the biosphere. In the last decades the focus of climate systems shifted more on processes and interactions between them. With the inclusion of more model domains, climate science changed to an interdisciplinary field of work.

Various models exist in climate science, ranging from energy balance models, over models of intermediate complexity, to fully coupled climate system models. Each of these models has its own domain of application (for an overview, see e.g. McGuffie and Henderson-Sellers, 2005). Despite the increase in computational power in the last decades since the first coupled climate models in the 1960s (see Flato, 2011, for a review), even the most comprehensive climate models are far from being complete, in the sense of incorporating every single detail of the Earth's climate system.

The level of detail in numerical models is constrained by two factors. First, available computational resources are not capable of resolving processes on an arbitrary level of detail. Thus, numerical models are constrained in their spatial and temporal resolution. Processes smaller than the model resolution have to be parameterised to include their impacts in the model system. Second, not all processes of the climate system are well understood, this is especially true for feedback mechanisms between processes. Some of them are difficult to measure, or related to regions of the Earth where only sparse measurements are available. Laboratory studies and the application of simpler numerical models, focusing on a certain process or aspect of the climate system, can help to gain understanding in these processes and to implement them in complex model systems.

State of the art atmosphere-ocean general circulation models (AO-GCMs) allow simulations of the climate system's evolution with time (transient simulations). These models use prescribed GHG concentrations as boundary conditions. One key finding of transient model simulations with AO-GCMs is the role of the ocean in climate change. With increased GHG concentrations, the ocean takes up a large part of the heat from GHG forcing and stores it in the deep ocean, slowing down warming of the climate system (Flato, 2011). A further effect is a delayed stabilisation of temperature after forcings are hypothetically kept constant.

The coupling of atmosphere general circulation models (A-GCMs) and ocean general circulation models (O-GCMs) has been achieved using integrated approaches or external couplers (see (Valcke et al., 2012), for a review of coupling methods in state-of-the-art earth system models (ESMs) and Appendix A of (Kerkweg and Jöckel, 2012), for a detailed definition of coupling methods). These AO-GCMs can be used for physical climate simulations, but in general do not represent atmospheric chemistry processes, and hence there are no feedbacks between climate and biogeochemical cycles, which determine the atmospheric chemical composition (Flato, 2011).

General circulation models (GCMs) which include feedbacks between interactive atmospheric chemistry and radiation are called chemistry climate models (CCMs). These CCMs usually use emissions of GHGs as boundary conditions. CCMs include detailed stratospheric chemistry, whereas in many models tropospheric chemistry is omitted. This is done, because comprehensive tropospheric chemistry schemes consume a large amount of computational resources, and are not essential to reproduce the main stratospheric concentrations, for example stratospheric $O_3$ concentrations (e.g. Chipperfield, 1999). However, tropospheric chemistry is essential to simulate the chemical composition in the upper troposphere lower stratosphere (UTLS) region, which is the main gateway for exchange between the troposphere and the stratosphere.

The UTLS has also been identified as a region with strong temperature changes, and thus changes in chemical reactions. A changed chemical composition in this region, especially in ozone concentration, can have a big impact on radiative forcing (Lacis et al., 1990), impacting the Brewer-Dobson Circulation (BDC), and thus in turn further changing the chemical composition, both in the troposphere as well as the stratosphere (Li et al., 2008).

In the recent Chemistry-Climate Model Validation (CCMVal) project study (SPARC CCMVal, 2010) only three of the 18 contributing different models included comprehensive tropospheric chemistry. SPARC CCMVal (2010) recommends, that "[t]he next generation of CCMs should also include a better representation of

tropospheric chemical processes", because "[t]his is certainly important for science studies in the troposphere and UTLS region, but also may be important in better representing the overall climate system".

Until now, in most of the studies using CCMs the models are forced with prescribed (measured or simulated) sea surface temperatures (SSTs). The prescribed boundary conditions constrain the model system in the evolution of climate. In SPARC CCMVal (2010) only one CCM has been dynamically coupled to an interactive ocean model. Again the report recommends the coupling of CCMs to interactive ocean models, to "make the representation of climate change in the models more physically self-consistent".

The roles of the ocean in the climate system include, besides dynamical links, biogeochemical links between the ocean and climate (Bigg et al., 2003). Biogeochemical interactions between atmosphere and ocean have been identified to be important for atmospheric chemistry, and impact the climate via changing atmospheric concentrations of GHGs (Bigg et al., 2003). This gives rise to feedback mechanisms between oceanic biogeochemistry and the climate system. These interactions are addressed in the Surface Ocean – Lower Atmosphere Study (SOLAS) project[1], with activities ranging from field experiments over laboratory studies, to numerical modelling (SOLAS, 2004).

Including biogeochemical cycles, especially the oceanic and terrestrial carbon cycle, into the atmosphere-ocean model system is considered as transition from physical AO-GCMs to ESMs (Collins et al., 2011; Flato, 2011). The development of an ESM including the different domains of the climate system (atmosphere, ocean, land, cryosphere) and interactions between them is an interdisciplinary work. Usually existing models are combined as components for each domain. The inclusion of ESM components into a climate model makes the model more self consistent and the inclusion of feedbacks can have an impact on the simulated climate (Collins et al., 2011). With increasing complexity of the model system, one has to assure, that the model components work together satisfactorily and do not distort other model components and their simulation results.

An example of a complex and comprehensive ESM built up from different model components is HadGEM2 (Collins et al., 2011). This model system includes components of the atmosphere, including atmospheric chemistry and aerosols, the ocean, including the oceanic carbon cycle, and the land surface, including the terrestrial carbon cycle, as well as interactions between these components. These interactions

[1] `http://solas-int.org/` (last accessed: 01.07.2013)

are the coupling of chemistry and radiation, hydrology, and aerosols, the impact of the oceanic carbon cycle on DMS emissions, and feedbacks in the atmospheric dust cycle from vegetation and on the oceanic carbon cycle. "The focus for HadGEM2 is on terrestrial and ocean ecosystems, gas and aerosol phase composition, and the interactions between these components" (Collins et al., 2011).

The ECHAM/MESSy Atmospheric Chemistry (EMAC; Jöckel et al., 2005, 2006, 2010) model, which is used in this study, is a CCM focusing on detailed atmospheric chemistry (for details, see Chapter 3). In its process based modular concept, a component was included for calculating air-sea gas exchange from oceanic concentrations (Pozzer et al., 2006). Until now these oceanic concentration are prescribed, e.g. imported into the model system from climatological maps. Recently the physical O-GCM Max Planck Institute Ocean Model (MPIOM; Marsland et al., 2003; Jungclaus et al., 2006) was coupled to the physical atmosphere in this model system (Pozzer et al., 2011).

This study focuses on the impact of atmosphere-ocean interactions on tropospheric chemistry on short time scales of up to several years. To provide the technical basis for this analysis, in this study the model system was extended with the oceanic biogeochemistry model HAMburg Ocean Carbon Cycle model (HAMOCC; Six and Maier-Reimer, 1996; Maier-Reimer et al., 2005; Wetzel et al., 2005) to include oceanic biogeochemistry and its impact on oceanic tracer concentrations (Section 3.3). Additionally a coupling between nutrient import to the ocean by rivers was implemented (Section 3.6), as well as an option to calculate iron (Fe) and silica ($SiO_2$) input at the ocean's surface from atmospheric dust simulated "online" in the atmospheric model domain (Section 3.7).

## 1.3 Open questions addressed in this study

The goals of this study are: (1) to include the exchange of chemical compounds between ocean and atmosphere in the numerical chemistry climate model EMAC coupled to the oceanic general circulation model MPIOM and the oceanic biogeochemistry model HAMOCC by utilising the Modular Earth Submodel System (MESSy; Jöckel et al., 2010) framework; (2) to test and evaluate the chemically coupled model system in preparation for future applications in climate simulations under different scenarios (pre-industrial, IPCC scenarios, etc.).

In view of these goals, the following scientific questions are addressed in this thesis:

- **What are the differences between simulations with prescribed oceanic concentrations and simulations with "online" calculated oceanic concentrations?**
  What are the quantitative differences in air-sea fluxes in simulations with prescribed and with "online" calculated oceanic concentrations? How do the different air-sea fluxes impact atmospheric composition?

- **What is the impact of input by rivers on the oceanic chemistry and how is the atmospheric composition affected?**
  How large are the changes in oceanic biogeochemistry and, hence, in oceanic concentrations—primary in coastal areas? What are the changes in atmospheric concentrations evoked by riverine nutrient input?

- **What is the impact on oceanic chemistry and atmospheric concentrations of aeolian dust input into the ocean?**
  What are the quantitative changes in oceanic biogeochemistry, air-sea fluxes, and atmospheric composition from aeolian nutrient import calculated from "online" dust deposition replacing the climatological dust deposition map? To answer this question, the model system is extended towards a chemically self-consistent ESM by utilising the submodels for dry and wet deposition and scavenging to calculate dust deposition.

- **What is required to use the model system for long term simulations with simplified chemistry?**
  What is the optimal set of closing parameters for subgrid cloud-related parameterisations to be used for long term simulations with the model system in a configuration using simplified stratospheric chemistry?

In this study the available AO-GCM EMAC-MPIOM (Pozzer et al., 2011), which couples EMAC and MPIOM via the MESSy interface, is used as starting point. This dynamically coupled model system is extended by adding oceanic biogeochemistry and chemical air-sea interaction to form a chemically coupled atmosphere-ocean chemistry climate model (AO-CCM). The focus of this study will be on atmospheric chemistry and composition on a rather short time scale of several years in quasi steady-state for present day (year 2000) conditions.

Whereas this study concentrates on this short time scale, the coupling of a comprehensive dynamical and chemical ocean model to a comprehensive atmospheric model also enable simulations on longer time scales (centuries). Further requirements for operating the resulting model system on these longer time scales will be discussed in scope of the last question.

## 1.4 Outline

Chapter 2 gives an overview of the theoretical background on important chemical processes in the atmosphere, the ocean, and on the interaction of these domains. In Section 2.1 the impact of atmospheric composition on radiation transfer is briefly described. Section 2.2 introduces the most important chemical processes in the atmosphere. Section 2.3 gives a brief overview of oceanic biogeochemistry and how the biological cycle determines the distribution of chemical compounds in the ocean and surface seawater composition. The exchange of chemical compounds between atmosphere and ocean via air-sea gas exchange, dry and wet deposition, and by riverine input is discussed in Section 2.4.

The model system is introduced in Chapter 3. Section 3.1 introduces the MESSy interface and important submodels used in this study. The atmospheric part of the model system is briefly described in Section 3.2. In Section 3.3 the oceanic component is introduced, including some details on the implementation of oceanic biogeochemistry. The dynamical and chemical coupling between atmosphere and ocean are described in Section 3.4 and Section 3.5, respectively. Details on the implementation of nutrient import from rivers and aeolian dust can be found in Sections 3.6 and 3.7, respectively.

In Chapter 4 an overview over the simulations performed in this study and results from the sensitivity experiments are presented. Sections 4.1 gives an overview of the simulations performed for this study and introduces the different model configurations for the sensitivity experiments. Changes in oceanic chemical composition, air-sea gas exchange, and atmospheric composition between experiments with and without interactive oceanic biogeochemistry are discussed in Section 4.2. In Section 4.3 the impact of additional nutrient input to the ocean by rivers is investigated. The interactive coupling of dust deposition from the atmosphere to the oceanic biogeochemistry and its impact on atmospheric composition is discussed in Section 4.4.

The ability of the model system to perform simulations of decadal time-scales is discussed in Chapter 5. In Section 5.1 an overview of the preparations of the model system is given, further the impact of mostly cloud-related parameters on the model's climate state is discussed. The final set of parameters as optimised in the model setup used for this study are presented in Section 5.2.

A conclusion summarising the results from this study and an outlook at future work is given in Chapter 6.

# Chapter 2

# Theoretical background

This chapter gives a brief overview of radiative transfer in the atmosphere, which is important for atmospheric dynamics and for atmospheric chemistry. Further the elementary chemical reactions of the tropospheric and stratospheric chemistry are presented. The last two sections give a brief introduction to oceanic biogeochemistry and relevant processes determining the chemical composition of seawater.

## 2.1 Radiation in the atmosphere

Driver of weather and climate on Earth is absorption and loss of energy from radiation received from the sun in the atmosphere. To maintain a stable climate and a fairly constant global temperature on Earth, incoming and outgoing energy in the Earth system have to be in balance (Seinfeld and Pandis, 1998; Trenberth et al., 2009). The atmosphere is the important part in Earth's radiative transfer, determining which amount of solar radiation reaches Earth's surface, and which amount of terrestrial radiation is escaping to space (Seinfeld and Pandis, 1998). Radiative fluxes in the Earth system can be divided in solar and terrestrial radiation.

Solar radiation is the radiation reaching Earth emitted from the sun. This radiation is in the shortwave spectrum, with a maximum intensity in the visible wavelengths of electromagnetic waves at at about 500 nm (Seinfeld and Pandis, 1998; cf. Figs. 2.1, 2.2). Terrestrial radiation is coming from Earth and has a spectral distribution like a blackbody at about 300 K, with intensity peaking at about 10 µm in the infrared (Seinfeld and Pandis, 1998). The peak in intensity of terrestrial radiation is in a spectral region called the *atmospheric window* with wavelengths from 8 µm to

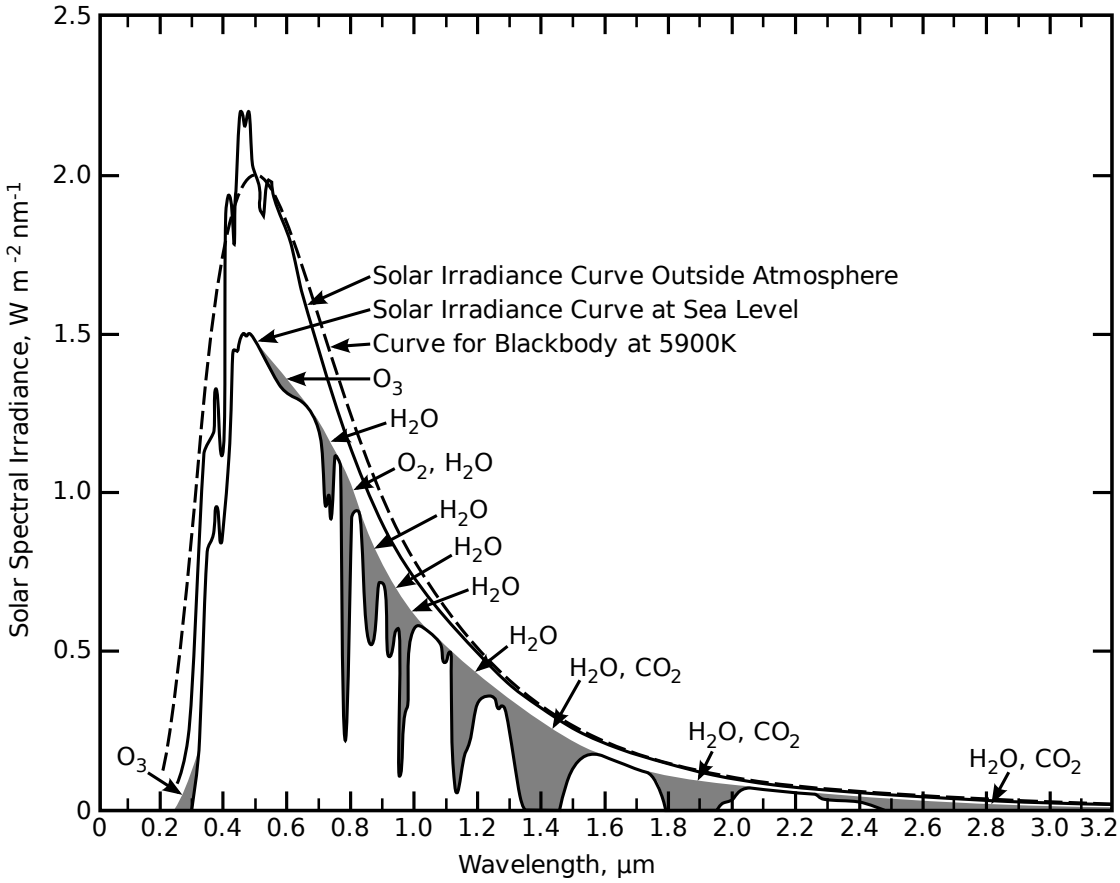


**Figure 2.1:** Solar spectral irradiance at the top of the atmosphere and at sea level. The dashed curve shows the blackbody spectral irradiance at 5900 K. Shaded areas mark absorption in the atmosphere by the molecule indicated. Adapted from Valley (1965, Fig 16.1).

12 µm (Fig. 2.2). For longwave radiation emitted from Earth in this spectral range absorption in the atmosphere is weak and nearly 80 % of the radiation escapes to space (Seinfeld and Pandis, 1998).

Absorption of radiation in the atmosphere by radiative important gases (greenhouse gases (GHGs)) is an important factor in meteorology and atmospheric chemistry (cf. Fig 1.2). Atmospheric chemical composition and the distribution of these gases determine the amount and spectral parts of solar radiation reaching Earth's surface (Fig. 2.1), the parts of terrestrial radiation escaping into space, and the temperature distribution in Earth's atmosphere. The main absorbers in the atmosphere are oxygen ($O_2$), ozone ($O_3$), water vapour ($H_2O$), and carbon dioxide ($CO_2$). Absorption of $O_2$ and $O_3$, for example, in a spectral region below 290 nm prevent solar radiation in the ultraviolet spectral range reaching Earth's surface.

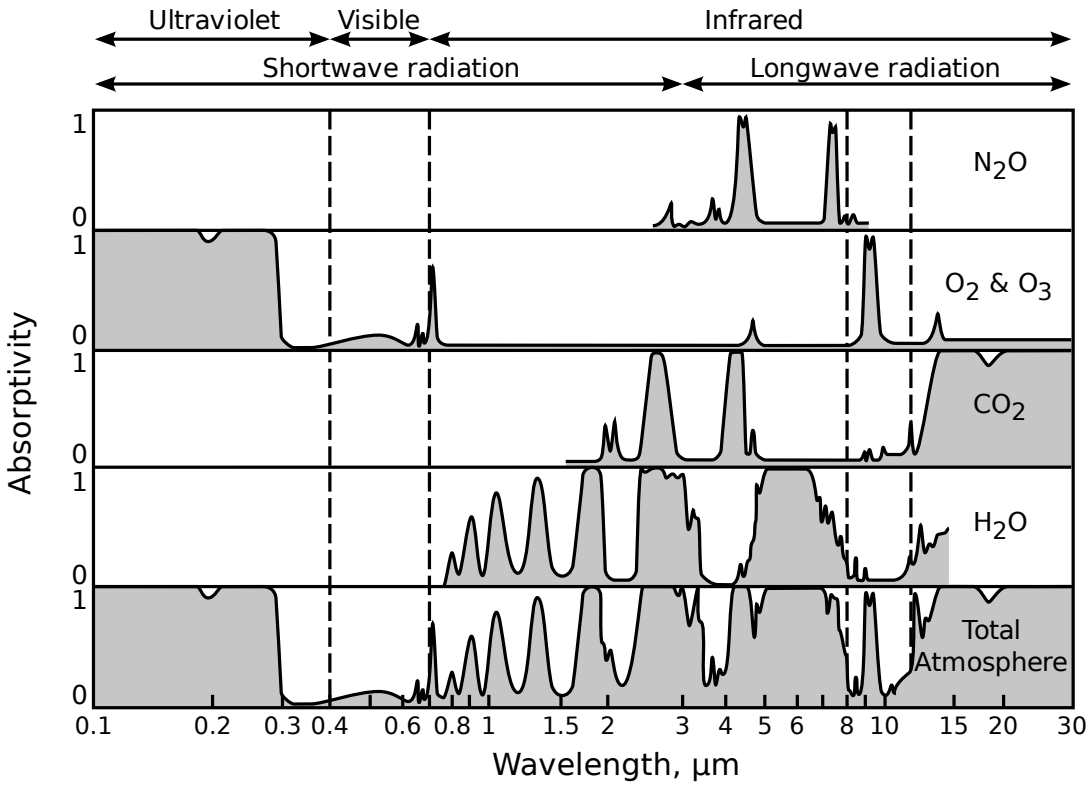


**Figure 2.2:** Absorptivity of gases in the atmosphere and the atmosphere in total. Absorptivity is given as the fraction of radiation absorbed at the respective wavelength. Dashed lines mark the visible wavelength spectrum from 400 nm to 700 nm and the atmospheric window in the infrared wavelengths from about 8 µm to 12 µm. Solar radiation reaches Earth in the shortwave spectrum (cf. Fig 2.1). Terrestrial radiation is emitted as longwave radiation in the infrared spectrum. After Goody and Robinson (1951); Fleagle and Businger (1980).

For terrestrial radiation in the infrared spectrum, with wavelengths longer than 780 nm, $H_2O$ and $CO_2$ are the main absorbers in the atmosphere (Fig. 2.2). In this region, the trace gases $O_3$, methane ($CH_4$), nitrous oxide ($N_2O$), and chlorofluorocarbons (CFCs) have strong absorption bands. Relatively small changes in concentration of these gases produce significant changes in the radiation flux in this section of the spectrum (Seinfeld and Pandis, 1998).

When the concentration of a gas reaches a level at which its absorptivity in certain wavelengths approaches unity, further increase in concentration leads to smaller effects on radiative flux. This behaviour is called band saturation effect. However, as a gas has multiple absorption bands, further rise in its concentration can effect still

other bands, unsaturated with respect to absorption. Thus, increase in concentration of a gas with band saturation effects at certain wavelengths can still have significant impacts on radiative transfer (Seinfeld and Pandis, 1998).

## 2.2 Atmospheric chemistry

### 2.2.1 Tropospheric chemistry

Tropospheric chemistry is mainly determined by emissions of species at the Earth's surface. Furthermore, for $O_3$ transport from the stratosphere in mixing events caused by tropopause foldings and transport along isentropes, and in-situ production are important for determining tropospheric concentrations (Roelofs and Lelieveld, 1997). Those species with lifetimes shorter than about one year are generally destroyed in the troposphere as transport into the stratosphere is much slower than mixing in the troposphere itself (Seinfeld and Pandis, 1998). Important factors determining tropospheric chemistry are the high concentrations of water vapour in the troposphere and photochemical reactions. Despite of solar radiation filtering of the high energetic ultra-violet wavelengths in the stratosphere, photochemistry in the troposphere is still significant (Seinfeld and Pandis, 1998). In the following, a short overview of the species relevant for this study is presented.

#### Ozone ($O_3$)

Ozone chemistry is a central part of the tropospheric chemical mechanisms. Formation of $O_3$ occurs via the photochemical cycle of nitrogen dioxide ($NO_2$), nitric oxide (NO), and $O_3$ (Seinfeld and Pandis, 1998):

$$NO_2 + h\nu\,(\lambda < 420\,\text{nm}) \longrightarrow NO + O(^3P) \qquad \text{(R 2.1)}$$

$$O(^3P) + O_2 + M \longrightarrow O_3 + M \qquad \text{(R 2.2)}$$

$$O_3 + NO \longrightarrow NO_2 + O_2 \qquad \text{(R 2.3)}$$

where M is a molecule to absorb excess vibrational energy (e.g. $N_2$ or $O_2$) without being chemically modified. Reaction R 2.2 is considered the only significant tropospheric in-situ source of $O_3$ (Seinfeld and Pandis, 1998). $O_3$ produced in Reaction R 2.2 is destroyed in Reaction R 2.3 via reaction with NO. As the main emission of nitrogen oxides ($NO_x$) is in form of NO, there is very low production of atomic

oxygen (O) and a high tendency to destroy $O_3$ via reaction with NO. Significant production of $O_3$ can only happen, if the photochemical equilibrium defined by Reactions R 2.1–R 2.3 is disturbed.

### Hydroxyl radical (OH)

The oxidation capacity of the atmosphere is determined by the highly reactive hydroxyl radical (OH). Production of the hydroxyl radical (OH) starts with photolysis of $O_3$ (Levy, 1971):

$$O_3 + h\nu\,(\lambda < 340\,\mathrm{nm}) \longrightarrow O(^1D) + O_2 \qquad \text{(R 2.4)}$$

The main destruction of the electronically excited oxygen atom ($O(^1D)$) is quenching and subsequent reaction with $O_2$ to form $O_3$:

$$O(^1D) + M \longrightarrow O(^3P) + M \qquad \text{(R 2.5)}$$

$$O(^3P) + O_2 + M \longrightarrow O_3 + M \qquad \text{(R 2.6)}$$

but up to 10 % of $O(^1D)$ produced in Reaction R 2.4 reacts with water to form OH (Seinfeld and Pandis, 1998):

$$O(^1D) + H_2O \longrightarrow 2\,OH \qquad \text{(R 2.7)}$$

### Carbon monoxide (CO)

Carbon monoxide (CO) provides the most important sink for OH. Reaction with CO does not necessarily imply depletion of OH, as OH can be recycled via reactions involving $NO_x$. Thus in $NO_x$ rich regions, reaction of OH with CO involves production of $O_3$ (Lelieveld et al., 2002):

$$CO + OH \longrightarrow CO_2 + H \qquad \text{(R 2.8)}$$

$$H + O_2 + M \longrightarrow HO_2 + M \qquad \text{(R 2.9)}$$

$$NO + HO_2 \longrightarrow NO_2 + OH \qquad \text{(R 2.10)}$$

$$NO_2 + h\nu\,(\lambda < 420\,\mathrm{nm}) \longrightarrow NO + O(^3P) \qquad \text{(R 2.11)}$$

$$O(^3P) + O_2 + M \longrightarrow O_3 + M \qquad \text{(R 2.12)}$$

---

$$\text{Net:} \qquad CO + 2\,O_2 \longrightarrow CO_2 + O_3 \qquad \text{(R 2.13)}$$

In this case the reaction chain can be terminated by the reaction of OH with $NO_2$ to form nitric acid ($HNO_3$), which is efficiently scavenged from the atmosphere:

$$OH + NO_2 + M \longrightarrow HNO_3 + M \quad \text{(R 2.14)}$$

In regions with low concentrations of $NO_x$, a net $O_3$ destruction occurs through the reaction chain (Lelieveld et al., 2002):

$$CO + OH \longrightarrow CO_2 + H \quad \text{(R 2.15)}$$
$$H + O_2 + M \longrightarrow HO_2 + M \quad \text{(R 2.16)}$$
$$O_3 + HO_2 \longrightarrow 2\,O_2 + OH \quad \text{(R 2.17)}$$

---

$$\text{Net:} \qquad CO + O_3 \longrightarrow CO_2 + O_2 \quad \text{(R 2.18)}$$

Here the termination is via self reaction of the hydroperoxyl radical ($HO_2$) forming hydrogen peroxide ($H_2O_2$), as insufficient $NO_2$ is available to terminate the reaction chain via Reaction R 2.14. $H_2O_2$ generated in this process is removed from the atmosphere by dry and wet deposition. Although some of the $HO_x$ is regenerated from $H_2O_2$ by photolysis, for about half of the $HO_x$ reacted to $H_2O_2$ deposition is a sink (Lelieveld et al., 2002).

### Nitrate radical ($NO_3$)

The nitrate radical ($NO_3$) is formed from NO stemming from natural and anthropogenic sources via the reactions:

$$NO + O_3 \longrightarrow NO_2 + O_2 \quad \text{(R 2.19)}$$
$$NO_2 + O_3 \longrightarrow NO_3 + O_2 \quad \text{(R 2.20)}$$

Because of its rapid photolysis, resulting in a lifetime of the $NO_3$ radical in sunlit conditions of $\approx 5\,s$, tropospheric $NO_3$ concentrations experience a distinct diurnal cycle with very low daytime concentrations, increasing during night (Atkinson and Arey, 2003).

### Isoprene ($C_5H_8$)

Isoprene ($C_5H_8$) reacts with OH, $O_3$, and $NO_3$, all adding initially to one of the double carbon (C) bonds in the $C_5H_8$ molecule (Atkinson, 2000). In laboratory studies, formaldehyde (HCHO), methane vinyl ketone (MVK), and methacrolein (MACR) have been identified as products of the reaction of $C_5H_8$ with OH or $O_3$ (Paulson et al., 1992a,b).

The addition of OH to the two double bonds of $C_5H_8$ results in four possible hydroxyalkyl radicals (see Fan and Zhang, 2004, for detailed reaction mechanisms of isoprene). Reaction of the hydroxyalkyl radicals with $O_2$ forms hydroxyalkyl peroxy radicals, which under further reaction with NO, self- and crossreactions form the endproducts of the reaction chain, which are HCHO, MVK, MACR and to much lower extends carbonyls and organic nitrates (Fan and Zhang, 2004). For the reaction of isoprene with OH the yields reported for HCHO, MVK, and MACR are 63 %, 32 %, and 22 %, respectively (Atkinson, 1997, and references therein).

Isoprene ozonolysis forms two primary ozonoides, decomposing into five different chemically activated carbonyl oxides called *Criegee intermediates* (Fan and Zhang, 2004). The Criegee intermediates undergo stabilisation or reactions to form dioxirane and OH (Fan and Zhang, 2004). The stabilised carbonyl oxides further react with water ($H_2O$) and NO, where the first pathway forms organic acids, $HO_2$, and OH and the second pathway HCHO, MACR, and MVK (Fan and Zhang, 2004). For the reaction with $O_3$, the yields measured in laboratory environments while OH is scavenged, are 90 % for HCHO, 39 % for MACR, and 16 % for MVK (Atkinson, 1997, and references therein).

As the other two reactions, the reaction of $C_5H_8$ with $NO_3$ also happens via addition—in this case of $NO_3$—to the isoprene double bonds. The four formed nitrooxyalkyl radicals primarily react with $O_2$ forming nitrooxyalkyl peroxy radicals, which further react to nitrooxyalkoxy radicals in the presence of NO (Fan and Zhang, 2004). Decomposition of the nitrooxyalkoxy radicals yields organic nitrates, HCHO, MVK, and MACR (Fan and Zhang, 2004). Overall the reaction of $C_5H_8$ with $NO_3$ yields 11 % of HCHO, whereas the yields for MACR and MVK are 3.5 % each (Atkinson, 1997, and references therein).

Recently the reaction of isoprene with chlorine (Cl) has gained attention, which results in the formation of 1-chloro-3-methyl-3-buten-2-one (CMBO), chloromethyl-butenal (CMBA) isomers, MVK, and chloromethyl radicals ($CH_2Cl$) (Riemer and Apel, 2001; Fan and Zhang, 2004).

### Formaldehyde (HCHO)

Formaldehyde (HCHO) is an oxidation product from hydrocarbons, like $C_5H_8$. In the atmosphere the two HCHO reaction pathways are photolysis and reaction with OH (Seinfeld and Pandis, 1998):

$$\mathrm{HCHO} + h\nu \longrightarrow \mathrm{H} + \mathrm{HCO} \quad \text{(R 2.21)}$$

$$\longrightarrow \mathrm{H_2} + \mathrm{CO} \quad \text{(R 2.22)}$$

$$\mathrm{HCHO} + \mathrm{OH} \longrightarrow \mathrm{H_2O} + \mathrm{HCO} \quad \text{(R 2.23)}$$

The hydrogen (H) atom and the formyl radical (HCO) rapidly react with $O_2$ (Seinfeld and Pandis, 1998):

$$\mathrm{H} + \mathrm{O_2} \longrightarrow \mathrm{HO_2} \quad \text{(R 2.24)}$$

$$\mathrm{HCO} + \mathrm{O_2} \longrightarrow \mathrm{HO_2} + \mathrm{CO} \quad \text{(R 2.25)}$$

In this way HCHO is a source of CO and $HO_2$.

### Dimethyl sulphide (DMS)

Oxidation of dimethyl sulphide ($(CH_3)_2S$, DMS) in the atmosphere proceeds mainly via reaction with OH and $NO_3$. The reaction of DMS with OH implies H atom abstraction or OH addition to the sulphur atom of DMS (Seinfeld and Pandis, 1998):

$$\mathrm{CH_3SCH_3} + \mathrm{OH} \longrightarrow \mathrm{CH_3SCH_2} + \mathrm{H_2O} \quad \text{(R 2.26)}$$

$$\underset{\mathrm{M}}{\overset{\mathrm{M}}{\rightleftharpoons}} \mathrm{CH_3S(OH)CH_3} \quad \text{(R 2.27)}$$

Of the two reactions R 2.26 and R 2.27, the first one is favoured at higher temperatures, whereas the addition of OH has a negative activation energy and thus is the preferred pathway for low temperatures (Seinfeld and Pandis, 1998; von Glasow and Crutzen, 2004).

Reaction of DMS with $NO_3$ is predominantly a hydrogen-abstraction reaction analogous to Reaction R 2.26 (Barnes et al., 2006):

$$\mathrm{CH_3SCH_3} + \mathrm{NO_3} \longrightarrow \mathrm{CH_3SCH_2} + \mathrm{HNO_3} \quad \text{(R 2.28)}$$

This reaction is fast enough for potentially serving as important atmospheric DMS sink (Barnes et al., 2006).

Further oxidation reactions of the sulphur containing products from Reactions R 2.26–R 2.28 result in the stable products of DMS oxidation, dimethyl sulphoxide ($CH_3S(O)CH_3$, DMSO), dimethyl sulphone ($CH_3SO_2CH_3$, $DMSO_2$), methanesulphonic acid ($CH_3S(O)_2OH$, MSA), sulphur dioxide ($SO_2$), and sulphuric acid ($H_2SO_4$). Whereas the final products of DMS oxidation are determined via measurements and rate coefficients for Reactions R 2.26 and R 2.27 are well established, the chemistry leading to the observed products, and several aspects of the chemical mechanism and its intermediate products are still not fully resolved (see Barnes et al., 2006, for a review on atmospheric DMS oxidation). DMS oxidation is further thought to be a substantial source of atmospheric carbonyl sulphide (OCS), which is observed under low $NO_x$ conditions (Barnes et al., 2006).

Oxidation of $CH_3SCH_2$ (from R 2.26 and R 2.28) and further reaction with NO produces $CH_3S$ and HCHO (Seinfeld and Pandis, 1998; Barnes et al., 2006):

$$CH_3SCH_2 + O_2 \longrightarrow CH_3SCH_2OO \quad \text{(R 2.29)}$$

$$CH_3SCH_2OO + NO \longrightarrow CH_3SCH_2O + NO_2 \quad \text{(R 2.30)}$$

$$CH_3SCH_2O \xrightarrow{M} CH_3S + HCHO \quad \text{(R 2.31)}$$

An equilibrium is established between $CH_3S$ and $CH_3SOO$. Partitioning of this equilibrium is a function of temperature, binding 20 % to 80 % of $CH_3S$ as $CH_3SOO$ under atmospheric conditions (Barnes et al., 2006):

$$CH_3S + O_2 \underset{M}{\overset{M}{\longleftrightarrow}} CH_3SOO \quad \text{(R 2.32)}$$

Further reactions of $CH_3S$ with $O_3$ and $NO_2$, and of $CH_3SOO$ with NO result after several intermediates in the production of $SO_2$, MSA, and $H_2SO_4$ (for details see Barnes et al., 2006).

Halogens and halogen oxides have been identified as important potential oxidants for DMS (von Glasow and Crutzen, 2004). In the marine boundary layer (MBL) the reaction with Cl is of importance, owing to high chlorine concentrations over the ocean (Barnes et al., 2006). However, the reaction of DMS with chlorine monoxide (ClO) seems to be too slow to be of importance for DMS oxidation under atmospheric conditions (Barnes et al., 2006). Similarly, direct reaction of DMS with bromine (Br) seems of minor importance in the atmosphere, because of its slow rate under atmospheric conditions (Barnes et al., 2006). However, via the generation of bromine monoxide (BrO), Br plays an important role as precursor for production of DMSO

(Barnes et al., 2006):

$$CH_3SCH_3 + BrO \longrightarrow CH_3S(O)CH_3 + Br \qquad (R\,2.33)$$

Finally, reactions with iodine (I) and its oxide with DMS have too slow reaction rates to be of importance in the MBL (Barnes et al., 2006).

DMSO is yielded from further oxidation from the OH addition pathway of DMS (Reaction R 2.27). Production of DMSO is the main reaction pathway for $CH_3S(OH)CH_3$ in the atmosphere (Seinfeld and Pandis, 1998; Barnes et al., 2006):

$$CH_3S(OH)CH_3 + O_2 \longrightarrow CH_3S(O)CH_3 + HO_2 \qquad (R\,2.34)$$

From reaction of DMSO and OH the products $SO_2$, $DMSO_2$, methanesulphonylperoxynitrate ($CH_3S(O)_2OONO_2$, MSPN), MSA, and methanesulphinic acid ($CH_3S(O)OH$, MSIA) have been observed (Barnes et al., 2006). Further reaction of DMSO with OH forms MSIA, which can de oxidised to form MSA. The reaction of halogens with DMSO seems to be too slow to be of relevance in the atmosphere, however detailed studies on halogen reactions are still needed (Barnes et al., 2006).

### 2.2.2 Stratospheric chemistry

#### Ozone ($O_3$)

Stratospheric $O_3$ is produced via photolysis of $O_2$.

$$O_2 + h\nu\,(\lambda < 242\,\mathrm{nm}) \longrightarrow O + O \qquad (R\,2.35)$$

$$O + O_2 + M \longrightarrow O_3 + M \qquad (R\,2.36)$$

Recombination of oxygen atoms from photolysis with oxygen atoms (R 2.36) is the only chemical source of $O_3$ in the stratosphere. With the destruction of $O_3$ via photolysis and reaction with $O_2$, Reactions R 2.35 and R 2.36 form the *Chapman mechanism* (Chapman, 1930):

$$O_3 + h\nu\,(240\,\mathrm{nm} < \lambda < 320\,\mathrm{nm}) \longrightarrow O_2 + O \qquad (R\,2.37)$$

$$O_3 + O \longrightarrow 2\,O_2 \qquad (R\,2.38)$$

When atomic oxygen is abundant (Reaction R 2.35), Reactions R 2.36 and R 2.37 are rapid, governing a steady state of stratospheric $O_3$ concentrations (Seinfeld and Pandis, 1998). The regions with highest $O_3$ production are at the equator, with increasing production with altitude. In contrast highest $O_3$ concentrations are found at high latitudes in the winter hemisphere. This phenomenon can be explained by transport of stratospheric air masses (Seinfeld and Pandis, 1998).

The Chapman mechanism alone over-predicts $O_3$ concentrations, as measurements indicated that the reaction of $O_3$ with O (Reaction R 2.38) is slower than first thought. As conclusion additional destruction pathways of $O_3$ exist, which explain the observed stratospheric concentrations (Seinfeld and Pandis, 1998).

### Nitrous oxide ($N_2O$)

The importance of biogenic $N_2O$ emissions as source of stratospheric $NO_x$ was already suggested by Crutzen (1970). The main source of $NO_x$ in the stratosphere is photolysis of $N_2O$:

$$N_2O + h\nu \longrightarrow N_2 + O(^1D) \qquad \text{(R 2.39)}$$

$$O(^1D) + N_2O \longrightarrow 2\,NO \qquad \text{(R 2.40a)}$$

$$\longrightarrow N_2 + O_2 \qquad \text{(R 2.40b)}$$

About 58 % of the reaction of $O(^1D)$ with $N_2O$ follow the pathway R 2.40a and the remaining 42 % follow the pathway R 2.40b (Seinfeld and Pandis, 1998).

### The catalytic cycles of $HO_x$, $NO_x$, $ClO_x$, and $BrO_x$

To gain significant reduction in $O_3$ concentration, the depleting species has to be abundant at high concentrations or has to be recycled in catalytic cycles. The impact of $NO_x$ on stratospheric ozone concentrations was suggested by Crutzen (1970). Stratospheric ozone depletion by chlorine-containing substances was suggested by Molina and Rowland (1974). The catalytic cycles in the stratosphere resulting in reduced $O_3$ concentrations can be written as (Seinfeld and Pandis, 1998):

$$X + O_3 \longrightarrow XO + O_2 \qquad \text{(R 2.41)}$$

$$XO + O \longrightarrow X + O_2 \qquad \text{(R 2.42)}$$

$$\text{Net:} \qquad O_3 + O \longrightarrow 2\,O_2 \qquad \text{(R 2.43)}$$

With X representing one atom or molecule from the chemical families $HO_x$ (H + OH + $HO_2$), $NO_x$ (NO + $NO_2$), $ClO_x$ (Cl + ClO), or $BrO_x$ (Br + BrO). These free radicals act as catalyst in the cycles and are recycled, so altogether there is no change in concentration of species X and low concentrations of the depleting species are sufficient for a significant ozone destruction.

## 2.3 Biogeochemistry of the ocean

The main drivers of the biological production are the photosynthetically available radiation (PAR), the availability of nutrients in surface waters, and temperature. During the process of photosynthesis phytoplankton takes up chemical elements from seawater to build organic matter, utilising energy available in form of solar radiation reaching surface oceanic waters. The chemical elements, which potentially limit photosynthesis because of their limited concentration in seawater are called nutrients (Sarmiento and Gruber, 2006).

Nutrients are distinguished between macronutrients and micronutrients depending on their relative concentrations in the biological organism (Sarmiento and Gruber, 2006). Phosphorous (P) and nitrogen (N) are (macro-)nutrients, whereas other chemical elements needed during organic cell growth, specifically H, C, and O, are generally present in adequate concentrations, and are not considered as limiting elements. Trace elements are generally abundant at much lower concentrations than macronutrients. Influencing and possibly limiting phytoplankton growth they are called micronutrients. High attention was gained by the micronutrient iron (Fe), playing an important role for phytoplankton photosynthesis (Martin et al., 1991).

In seawater, sunlight is alleviated with depth by attenuation of seawater itself and of particles suspended in seawater. The upper ocean layer, where enough light is available for photosynthesis is called the euphotic zone, with a vertical extent in the order of 100 m (Sarmiento and Gruber, 2006). The lower border of the euphotic zone is defined as the depth, where light intensity reaches 1 % of its value at the ocean's surface (Sarmiento and Gruber, 2006). If phytoplankton is transported below the euphotic zone, for example in winter, when the mixed layer is thicker than the euphotic zone, no photosynthesis can take place. When the mixed layer reaches depths larger than the euphotic zone, phytoplankton will stay out of sufficient light levels for too long and quickly die out (Sarmiento and Gruber, 2006).

Organic matter is considered to have approximately constant stoichiometric ratios of the elements it is built from. These ratios, called Redfield ratios, can be measured and are widely used in oceanic biogeochemistry models. Redfield et al. (1963) proposed a stoichiometric ratio for organic matter in phytoplankton and oxygen demands for remineralisation of P:N:C:$O_2$ equal to 1:16:106: $-$ 138. Here the value for $O_2$ is negative, as oxygen is needed in the case of remineralisation to form $CO_2$. On the other hand $O_2$ is released during the organic matter formation process as byproduct of $CO_2$ assimilation (Warneck and Williams, 2012). The ratio is based on the stoichiometric formula of the composition of marine phytoplankton:

$$106\,CO_2 + 16\,HNO_3 + H_3PO_4 + 122\,H_2O \rightleftharpoons (CH_2O)_{106}(NH_3)_{16}(H_3PO_4) + 138\,O_2 \quad \text{(R 2.44)}$$

where the reaction pathway from left to right is associated with organic matter production by photosynthesis, and the reaction pathway from right to left with remineralisation (Sarmiento and Gruber, 2006). More recent observations suggest lower O and H values in phytoplankton organic matter, resulting in more oxygen needed for respiration. Takahashi et al. (1985) propose stoichiometric ratios of P:N:C:$O_2$ of 1:16:122: $-$ 172. This stoichiometry represents the remineralisation in depths below 400 m (Sarmiento and Gruber, 2006).

The chemical composition of seawater depends on advection of chemical elements, biological production—determined by PAR and nutrients abundance—, and the efficiency of the biological pump. A diagram of interactions between nutrients (N), phytoplankton (P), zooplankton (Z), and detritus (D) in the NPZD-type ecosystem, extended by a pool of dissolved organic matter (DOM), as implemented in the HAMburg Ocean Carbon Cycle model (HAMOCC; Six and Maier-Reimer, 1996; Maier-Reimer et al., 2005; Wetzel et al., 2005) model, is shown in Fig. 2.3.

Nutrients are transported into the ocean's surface layer by advection, from upwelling, or external import from the atmosphere or from rivers. Phytoplankton uses available nutrients during the process of photosynthesis, powered by available light from solar radiation, to produce organic matter. Exudation from phytoplankton is added to DOM, dead phytoplankton goes into the detritus pool. Phytoplankton is grazed on by zooplankton, which imposes a top-down control on the NPZD-type system. A fraction of the total grazing is ingested by zooplankton to maintain life and partly leads to zooplankton growth. The remaining fraction is egested in form of fecal pellets and added to the detritus pool. Excretion from zooplankton is recycled in the euphotic zone to nutrients via remineralisation of DOM. At the end of its

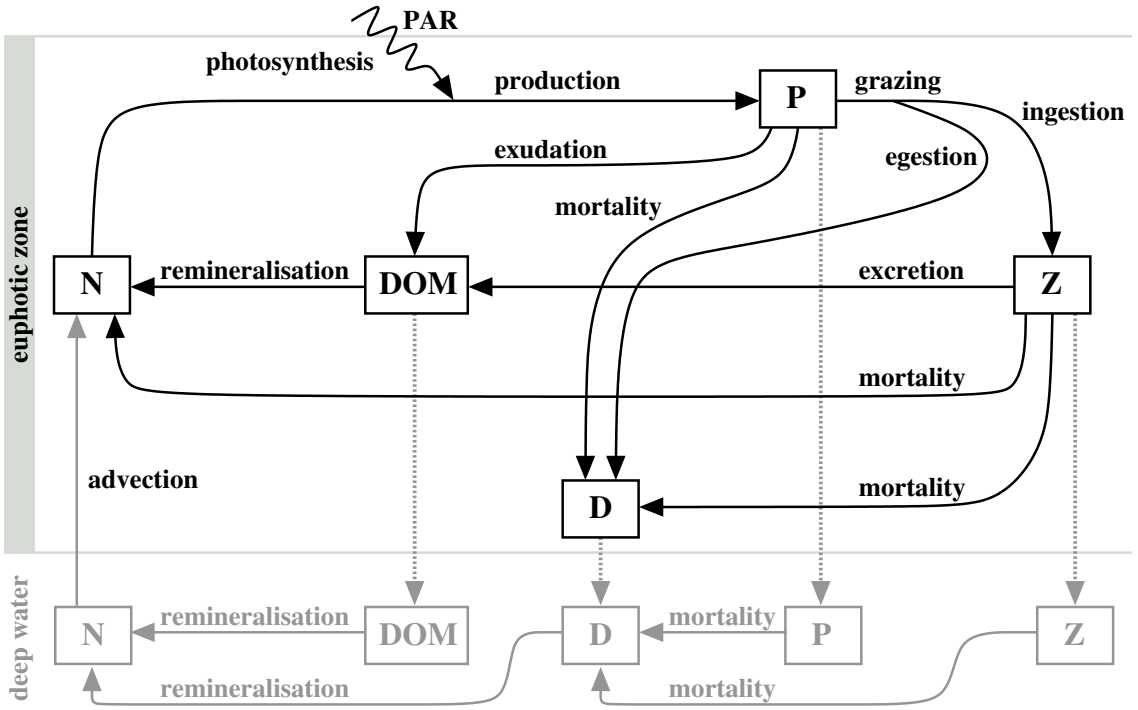


**Figure 2.3:** Schematic of the NPZD-type ecosystem as implemented in HAMOCC. Rectangles represent pools of nutrients (N), phytoplankton (P), zooplankton (Z), detritus (D), and dissolved organic matter (DOM). Processes causing changes of the pools are indicated by arrows. Broken arrows represent sinking from the euphotic zone (black pools and processes) to deep water (gray pools and processes). Interactions with the sediment are not shown. For details on the biogeochemical cycle, see the text.

lifetime zooplankton is partly remineralised into nutrients, the other part is added to the detritus pool. Remineralisation of DOM to dissolved inorganics in form of nutrients involves bacterial consumption of DOM and is called the microbial loop.

Phytoplankton and zooplankton are subject to sinking. Below the euphotic zone not enough light is available to maintain photosynthesis and phytoplankton dies. Because of the limited availability of phytoplankton to graze on, zooplankton also dies. Dead organic matter is added to the detritus pool, which is also subject to sinking. Below the euphotic zone DOM and detritus are transformed to nutrients via aerobic remineralisation.

Even when not sufficient oxygen is available, detritus can be remineralised via anaerobic remineralisation. This process includes bacteria reducing nitrate in aqueous phase ($NO_3^-$) to nitrogen ($N_2$). Nutrients from the deep ocean are advected to surface

waters by upwelling. Finally organic and inorganic matter in the deep ocean are subject to sedimentation (not shown in the figure). On longer time scales (millennia), dissolution from sediments has also to be considered a significant source of nutrients.

Photosynthesis is associated with the production of opal and calcite shells. Via production and dissolution of shell material from living and dead organisms, this process controls silicic acid ($Si(OH)_4$) and calcium carbonate ($CaCO_3$) concentration in the ocean water. Production and dissolution of $CaCO_3$ lowers or rises dissolved inorganic carbon (DIC) concentration, respectively. These processes influence the total alkalinity.

As all organisms and dead organic matter are subject to sinking, there is a transport of carbon to deeper water layers, called the biological pump. This has a big impact on the terrestrial carbon cycle, transporting efficiently carbon to deeper water and determining concentrations and alkalinity in the surface layer, and in this way uptake of atmospheric carbon in form of $CO_2$.

## 2.4 Exchange of chemical compounds between ocean and atmosphere

### 2.4.1 Air-sea gas exchange

Gas exchange at the interface between ocean and atmosphere has gained large scientific attention in the last decades, because of its impacts on biogeochemical cycles in the Earth system. Air-sea gas exchange influences the atmospheric composition of gases relevant in radiative transfer or acting as precursors for ozone and aerosol formation.

The magnitude and direction in flux of a gaseous compound between ocean and atmosphere depends on many factors. These factors can be divided into kinetic forcings and thermodynamic forcings (Wanninkhof et al., 2009). Kinetic forcings act directly on the gas transfer (gas transfer velocity), whereas thermodynamic forcings determine the concentrations of the gaseous compound in the lower atmosphere and the upper ocean.

The air-sea flux $F$ (in $\mathrm{mol\,(m^2\,s)^{-1}}$) of slightly soluble nonreactive gases can be expressed as product of a kinetic forcing function called the total transfer velocity $K_{tot}$ (in $\mathrm{m\,s^{-1}}$) and a thermodynamic driving potential $\Delta c_{wg}$. The thermodynamic driving potential is the difference between the molar concentration of the gas in the

well mixed upper water layer, $c_w$, and the molar concentration of the gas in the gas phase at the water surface, $c_g$ (both in $\mathrm{mol\,m^{-3}}$; Liss and Slater, 1974; Wanninkhof et al., 2009):

$$F = K_{tot}\Delta c_{wg} = K_{tot}(c_w - c_g). \tag{2.1}$$

The kinetic forcing factors affecting the transfer velocity, are wind, surface friction velocity, wave slope, and boundary layer dynamics. The surface friction velocity depends on the atmospheric stability. The wave slope is determined by fetch, wind direction, and surfactants influencing the ocean surface. The boundary layer dynamics includes microbreaking and bubbles (Wanninkhof et al., 2009).

Thermodynamic forcing factors determine the difference in molar concentrations on the water and gas phase side. These forcings include temperature, transport, and biology.

Air-sea gas exchange can be—depending on the solubility and reactivity of the gas in water—controlled by air side or water side processes. Gases which have a high water solubility or which react rapidly in water, are controlled by air side processes and not by hydrodynamic processes in the water (Wanninkhof et al., 2009). The contribution of air side and water side processes to control total transfer velocity can be expressed in the two-layer model by Liss and Slater (1974) as resistances against air-sea exchange on the water and gas phase side (Liss and Slater, 1974; Pozzer et al., 2006):

$$K_{tot} = (R_w + R_g)^{-1} = \left(\frac{1}{\alpha\, K_w} + \frac{k_H\, R\, T}{K_g}\right)^{-1}, \tag{2.2}$$

with $K_w$ and $K_g$ being exchange velocities on the liquid phase side and the gas phase side, respectively (both in $\mathrm{m\,s^{-1}}$). $\alpha$ is a fractional increase of the exchange velocity due to chemical reaction in the solution, $k_H$ is Henry's Law coefficient expressing solubility of the gas in water (in $\mathrm{mol\,(m^3\,Pa)^{-1}}$), $R = (8.314\,462\,1 \pm 0.000\,007\,5)\ \mathrm{J\,(mol\,K)^{-1}}$ [1] is the gas constant, and $T$ is the actual temperature in K. In the two-layer model, the transfer rate is limited by molecular diffusion through a thin water film at the air-sea interface layer.

For slightly soluble nonreactive gases, transfer velocities are controlled by aqueous phase hydrodynamics (Wanninkhof et al., 2009). $O_2$, $CO_2$, and $N_2O$ are examples of water side controlled gases. Water vapour, $O_3$, and $SO_2$, on the other hand, are highly soluble in water or, in the case of $SO_2$, react rapidly in water, and therefore are not controlled by hydrodynamics, but air side processes. DMS is a gas with an

[1] Mohr et al. (2012)

intermediate behaviour, it is controlled approximately 10 % by air phase and 90 % water phase (Wanninkhof et al., 2009). In practical applications, the transfer velocity is taken from field measurements and laboratory studies, and related to wind speed as the main energy input for driving air-sea gas exchange. Parameterisations for the transfer velocity are derived empirically from the functional form (Wanninkhof et al., 2009):

$$K_{tot} = a\, {Sc_{liq}}^{-n}\, f(Q, L, \nu), \tag{2.3}$$

which includes a model dependent constant $a$, a dependence on diffusivity ${D_{\mathrm{X}}}^{n}$ $(1/2 < n < 2/3)$ expressed in terms of the Schmidt number $Sc_{liq} = \nu / D_{\mathrm{X}}$, and a model dependent function $f(Q, L, \nu)$. Here $Q$ is a velocity scale, $L$ is a length scale, and $\nu$ is the kinematic viscosity of water.

From the above relationship, different parameterisations have been developed relating transfer velocity to the wind velocity $U$. These parameterisations are proportional to $U^m$, where $m > 1$ (for an overview, see e.g. Wanninkhof et al., 2009), because wind directly is not the driver of air-sea gas exchange, it rather affects turbulence at the interface layer (Wanninkhof et al., 2009). At least for the open ocean, wind stress is the main turbulence input, and hence controls air-sea gas exchange. In practice the 10-metre wind velocity $U_{10}$ is used to describe wind stress in the parameterisations.

The relationship between 10-metre wind and wind stress varies depending on ocean surface conditions, like wave state, boundary layer stability, and surfactants (Wanninkhof et al., 2009). In the case of surfactants, studies show a large uncertainty, because they can inhibit as well uptake as outgassing, depending on the region of the ocean, which has profound effects on the global budget, especially of $CO_2$ fluxes. Other factors influencing air-sea gas exchange are bubbles forming in dependence of the ocean's wave state and increased turbulence in presence of rain. Bubbles are generally considered to play an important role, anyway the magnitude of the effects of bubbles on gas transfer are an area of active research (Wanninkhof et al., 2009). Turbulence induced by rain has a large effect on the transfer velocity, in particular on the local scale in regions with heavy rainfall. On the global scale, however, the effect on $CO_2$ flux is estimated to be less than 5 % (Wanninkhof et al., 2009).

Parameterisations for the functional dependence of the wind speed and transfer velocity have been derived from measurements using different techniques. Deriving the parameterisation for the bulk flux $F$ on regional scales from field measurements and laboratory studies implies the need for upscaling the measurements. The

parameterisation is also dependent on the time span, over which the mean wind is calculated. The derived parameterisations are generally normalised to a Schmidt number of 660, which is the value of $Sc_{\mathrm{CO}_2}$ at a temperature of 20 °C. The transfer velocity of the gas under investigation can then be obtained by scaling with a factor of $(\frac{Sc_{liq}}{660})^{-n}$ (cf. Equation 2.3), using the actual Schmidt number $Sc_{liq}$ of the gas at the actual temperature.

In this study, the empirical parameterisation of Wanninkhof (1992) is used, which relates the transfer velocity at Schmidt number of 660 to the square of the mean 10-metre wind and includes short term variability in the wind speed (which lowers the factor in the parameterisation from 0.39 to 0.31):

$$K_{660} = 0.31\, {U_{10}}^2. \tag{2.4}$$

This is supported by theory, which relates the wind stress, $\tau$, to the quadratic wind velocity:

$$\tau = \rho_{air}\, C_d\, {U_{10}}^2, \tag{2.5}$$

with $\rho_{air}$ being air density (in $\mathrm{kg\,m^{-3}}$) and $C_d$ the dimensionless drag coefficient. This results in a transfer velocity $K$ which is proportional to the quadratic wind velocity:

$$K \approx a\, {U_{10}}^2, \tag{2.6}$$

with an empirically determined constant $a$ (Wanninkhof et al., 2009).

Practically all available parameterisations of transfer velocity are derived from measurements or laboratory studies. Although there have been advances in determining important factors impacting transfer velocity, these factors have not been fully included in the air-sea gas exchange models. In fact it is not clear, if the incorporation of more complex factors influencing forcings at the sea surface gives better estimates of air-sea fluxes than the simple parameterisations with wind speed only (Wanninkhof et al., 2009). The parameterisation, based on the theoretical background described in this subsection, used in ECHAM/MESSy Atmospheric Chemistry (EMAC; Jöckel et al., 2005, 2006, 2010) including the AIRSEA submodel (Pozzer et al., 2006) is explained in more detail in Section 3.5.

### 2.4.2 Chemical import from rivers

Coastal ocean areas are an important factor in oceanic biogeochemistry. These continental shelf seas cover about 8 % of the total ocean surface area (Bernard et al., 2010) and are characterised by biological productivity larger than that of the average oceanic surface waters (Ver et al., 1999). This high primary production rates are attributed to the high abundance of nutrients in coastal seawater, caused by resuspension from the sediments, import from rivers, and advection of nutrient rich water in the coastal upwelling regions.

Human activities impact the coastal zone directly and indirectly. As all regions on Earth, the coastal zone is impacted by changing atmospheric composition, mainly caused by fossil fuel combustion, and increasing surface temperatures. The direct impacts of human activities are deforestation and land use change, enhancing nutrient and sediment input to the coastal zone, usage of fertilisers and pesticides, accompanied by import of these substances to the coastal zone by groundwater and river fluxes, and discharge of sewage and detergents, via rivers or directly into the coastal zone (Ver et al., 1999).

Nutrient concentrations and composition of riverwater depends on the characteristics of the river network and have changed by human activities (Cotrim da Cunha et al., 2007; Mayorga et al., 2010). Processes impacting the river can be proportional of population density in the river catchment, this holds for nutrients stemming from sewage and detergent inputs to the river. Other processes scale with other factors, like changes in nutrient inputs stemming from fertiliser usage and changed land usage. Damming of rivers impacts sediment transport due to changed flow rate, but also influences silicon (Si) fluxes by enhanced diatom blooms in stagnant waters (Jickells, 1998).

The impact of oceanic biogeochemistry and gas exchange on atmospheric chemistry in coastal areas is important, as atmospheric chemistry there is also impacted by direct anthropogenic emissions.

### 2.4.3 Chemical import from the atmosphere

Deposition of mineral aerosol (“dust”) is the main input of iron to the open ocean (Martin et al., 1991; Jickells et al., 2005; Boyd et al., 2007). Iron is an important micronutrient for phytoplankton, needed for biological production during photosynthesis. Limitation of phytoplankton growth in large areas of the ocean is related

to limited iron supply (Jickells et al., 2005), also limitation of primary production by biologically available iron in high nutrient low chlorophyll (HNLC) regions was confirmed (Fung et al., 2000).

Iron supply to surface ocean waters via aeolian dust input depends on many processes in the Earth system. Starting with the emission at source regions, mainly located in the Northern Hemisphere, mineral aerosol is advected in the atmosphere by wind, moist and dry convection, and adiabatic vertical motion (Mahowald et al., 2005). Deposition of dust depends on the processes of dry and wet deposition. Close to the source regions the process of sedimentation due to gravity dominates deposition of dust, affecting larger particles more efficiently (Mahowald et al., 2005). Precipitation scavenging is the other deposition mechanism, whose efficiency also depends on aerosol size (Jickells et al., 2005). However, the interactions of dust and clouds are not well understood.

The chemical composition of dust depends on the source region. Despite of its variability, often an iron content of 3.5 % in mineral aerosol is used, representing the average iron content in Earth's crust (Mahowald et al., 2005). Not all of the iron contained in mineral aerosol is soluble in seawater. The solubility of iron is altered during atmospheric transport via photoreduction of Fe III to Fe II and processing in clouds, depending on acidity (Jickells et al., 2005). Dust deposition is also a source of various other substances to the surface water, but iron supply is the limiting factor to biological production in many ocean areas.

Atmospheric nitrogen input to the ocean potentially determines the availability of nitrogen for ocean productivity (Paerl, 1997). This effect can contribute to one third of new production in coastal areas and the open ocean (Spokes et al., 2000), when the most limiting nutrient for phytoplankton growth is $NO_3$. High nitrogen deposition in polluted coastal areas and the Atlantic Ocean, stemming from anthropogenic sources have been simulated (Tost et al., 2007b). Atmospheric nitrogen chemistry is highly influenced by anthropogenic emissions, which provides an impact of human activity to the marine ecosystem (Spokes et al., 2000).

# Chapter 3

# Description of the model system

In this study the chemistry climate model (CCM) ECHAM/MESSy Atmospheric Chemistry (EMAC; Jöckel et al., 2005, 2006, 2010) is used to simulate atmospheric dynamics and chemistry. The used version of EMAC is based on development cycle 2 of the Modular Earth Submodel System (MESSy; Jöckel et al., 2010) (Jöckel et al., 2010). An atmosphere general circulation model (A-GCM) setup of EMAC—i.e. with all processes related to atmospheric chemistry switched off—was successfully coupled to the ocean general circulation model (O-GCM) Max Planck Institute Ocean Model (MPIOM; Marsland et al., 2003; Jungclaus et al., 2006) via the MESSy interface, forming an atmosphere-ocean general circulation model (AO-GCM) by Pozzer et al. (2011).

In order to follow the vision of the MESSy developers, providing "the headstone for further model extensions from a CCM towards a comprehensive earth system model (ESM)" (Jöckel et al., 2010), in this study the extension of the CCM EMAC into an atmosphere-ocean chemistry climate model (AO-CCM) is presented. The model system now includes—in addition to the coupled atmospheric and oceanic dynamics—atmospheric chemistry, oceanic biogeochemistry, and the "online" calculated exchange of trace gases between ocean and atmosphere. Sensitivity studies quantifying the impact of air-sea gas exchange under different forcings on the oceanic biogeochemistry (Chapter 4) and a study determining reasonable parameters for closure of subgrid cloud-related processes to simulate stable climatic conditions on decadal time scales (Chapter 5) are presented, to demonstrate the applicability of the novel model system to scientific questions.

The following sections in this chapter give an overview of the specific parts of the model system and their setups. The methods for coupling between the atmospheric and oceanic domains will be presented, as well as the implementation of additional processes affecting oceanic biogeochemistry.

## 3.1 The Modular Earth Submodel System

Coupled AO-GCMs are widely used in climate research to study the past and current climate as well as projected future scenarios. AO-GCMs are composed of an A-GCM and an O-GCM, which exchange momentum, energy, and water mass between the oceanic and atmospheric domain at their interface. Including more components in the model system—e.g. chemical and biogeochemical components, vegetation models, etc.—expand the coupled AO-GCM towards an ESM. There is no strict definition when to start calling the model system ESM in terms of complexity and inclusion of processes in the model system (Collins et al., 2011). Furthermore there is no general rule from how many or which components an Earth system model should be built, and how this components are coupled.

Many approaches start by coupling atmosphere and ocean to form an AO-GCM via an external coupler, which coordinates the exchange of boundary conditions between the model components (e.g. Collins et al., 2006; Wetzel et al., 2006). The components of this coupled model system are running in parallel, usually as separate tasks. In that way, using a flexible external coupler (see Valcke et al., 2012, for a review of coupling techniques in ESMs), additional Earth system components, like a surface and vegetation model, can be added during ongoing model development.

Another approach is an internal coupling strategy, where coupling is included in the model system (e.g. Collins et al., 2005; Gent et al., 2011). In these setups the components are compiled into one executable and share the same parallel decomposition topology (Pozzer et al., 2011).

Both approaches of coupling are based on the concept of operator splitting (Janenko, 1969; Marchuk, 1971). Operator splitting is a method to divide the temporal evolution of a state variable into smaller steps. In terms of a partial differential equation, the changing of the state variable $u$ with time $t$ can be expressed as:

$$\frac{\partial u}{\partial t} = \mathcal{L}\, u, \tag{3.1}$$

with an operator $\mathcal{L}$, which can be written as linear sum of $m$ pieces (Press et al., 2007, Section 20.3.3). Equation 3.1 can then be written as:

$$\mathcal{L}\, u = \mathcal{L}_1\, u + \mathcal{L}_2\, u + \cdots + \mathcal{L}_m\, u. \tag{3.2}$$

In an ESM, the $m$ pieces of the operator correspond to $m$ different processes acting on the state variable $u$. For each of these processes it is known, how the state variable $u$ has to be updated from time step $n$ to time step $n + 1$. These known updates of the state variable $u$ are performed sequentially. Each process (or operator) is calculating a tendency of the state variable $u$, which is updated with this tendency and then passed to the next process until all processes have updated the state variable and the model advances to the next time step. In that way, using an operator splitting approach, the update of the variable $u$ is not calculated in one step, but rather as sequence of multiple ($m$) steps, with multiple processes expressed as operators (Jöckel, 2012).

ESMs can be thought of being built up from many processes (operators), which update state variables to advance the models system to the next time step. The complexity of such a processes can vary between different model systems and different processes of a model system. An ESM built up from different models for the different domains, coupled via an external coupler, has a coarse granularity. Each model can be thought of as one piece of the operator, despite of model internal implementations, which are based on the operator splitting approach. Providing a framework for the model time stepping and the representation of state variables, one can built an ESM with a much finer granularity, composed of submodels each describing one process of the natural system and the resulting update of the state variables.

The MESSy interface[1] (Jöckel et al., 2005) provides and implements a standard for coupling at a process based scale. It provides the possibility to couple representations of processes (called submodels) to a model system. All dynamical and chemical processes (submodels) can be connected in a flexible manner and switched on or off independently from each other. Submodels of processes can also be replaced by submodels implementing the same processes in a different way. The user interface via namelists provides a powerful tool for changing model parameters of the submodels and for switching processes on or off with no need to recompile the model code at changes in the model setup. In that way the model system can be used in various scientific applications—ranging from the Quasi Chemistry-Transport Model (QCTM)

[1] `http://www.messy-interface.org/` (last accessed: 01.07.2013)

mode (Deckert et al., 2011), over CCM (Jöckel, 2006), to AO-GCM (Pozzer et al., 2011)—, depending on the setup of the model system, the used submodels, and the included feedbacks between the active submodels.

Using the MESSy interface specifications, the atmospheric chemistry climate model EMAC was developed (Jöckel, 2006). It includes atmospheric dynamical processes from the general circulation model ECHAM5 re-implemented as submodels and couples additional submodels for atmospheric chemical processes.

Whereas the development of EMAC was strongly based on a base model (ECHAM5) (Jöckel, 2006), the vision was formulated, to form a comprehensive ESM, where all processes are implemented as (a multitude of) submodels and "a base model which contains only a central clock and runtime control" (Jöckel et al., 2005). The second development cycle of the Modular Earth Submodel System (MESSy2; Jöckel et al., 2010) follows this vision by providing an extended and base model independent infrastructure for the coupling of submodels. The MESSy infrastructure provides generic (base model independent) submodels for time control (TIMER), for submodel control (SWITCH, CONTROL), for memory management and data output (CHANNEL), for management of prognostic variables including constituents (TRACER (Jöckel et al., 2008, 2010)), for data import and re-discretisation (IMPORT, NCREGRID), and for grid-transformation (GRIDTRAFO).

A schematic representation of the model system as used in this study is given in Figure 3.1. The model system can be visualised as consisting of four domains (rectangles), atmospheric physics, atmospheric chemistry, oceanic physics, and oceanic biogeochemistry. Between these domains couplings exist (open arrows). Processes of the domains as well as of the couplings are implemented as submodels (ellipses) obeying the MESSy interface standard (as indicated with the filled arrows for the coupling processes). The MESSy interface also provides infrastructural submodels (abstracted as the central rounded rectangle), which interact with other submodels (indicated for some of the submodels with filled arrows). The Figure shows the schematic of the model system configuration as used in this study. Several submodels are involved in atmospheric dynamics and atmospheric chemistry (for an overview of the submodels used in this study, see Table 3.1). The coupling between atmospheric dynamics and atmospheric chemistry is introduced in EMAC via the submodels RAD4ALL, H2O, and MSBM (Deckert et al., 2011). The RAD4ALL submodel calculates atmospheric radiative transfer depending on atmospheric chemical composition. The H2O submodel synchronises the water ($H_2O$) tracer used in the atmospheric chemistry and the specific humidity used in the atmospheric dynamics sub-domain of the model

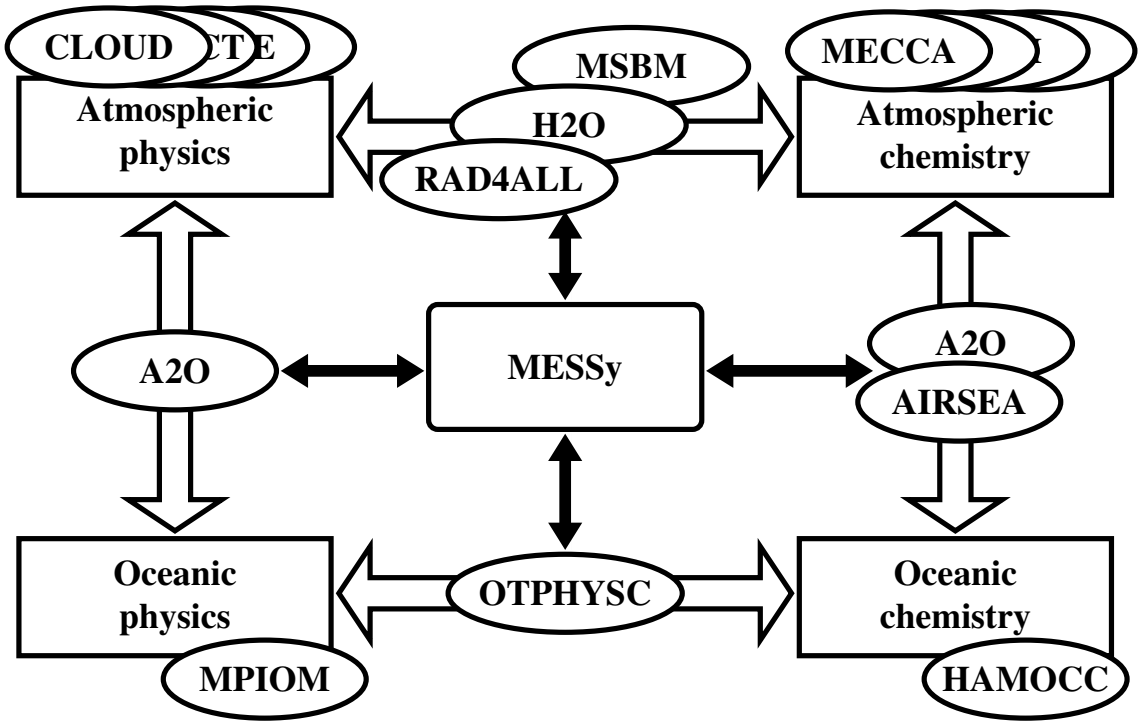


**Figure 3.1:** Schematic overview of the model system. The four sub-domains included in the model system (rectangles) are build up from different submodels (ellipses). Between the sub-domains couplings exist (open arrows) via submodels, implementing the MESSy interface standard and interact with structural submodels (abstracted as central rounded rectangle; interactions are indicated as filled arrows for some of the submodels). See text for details on the model system and coupling between sub-domains.

system. The MSBM submodel accounts for polar stratospheric clouds (PSCs) and associated heterogenous reactions, as well as dehydration and denitrification in the stratosphere, changing the $H_2O$ and nitric acid ($HNO_3$) distributions.

Ocean dynamics was included in the MESSy infrastructure by Pozzer et al. (2011), implementing MPIOM as MESSy conform submodel. An implementation of the HAMburg Ocean Carbon Cycle model (HAMOCC; Six and Maier-Reimer, 1996; Maier-Reimer et al., 2005; Wetzel et al., 2005) as submodel to be used to calculate oceanic chemical composition depending on oceanic biogeochemistry has been developed in this study. Ocean dynamics and ocean chemistry are coupled via the submodel OTPHYSC (Ocean Tracer PHYsiCs), providing transport of chemical tracers conform to ocean dynamics. The coupling between ocean and atmosphere involves grid transformations performed by the A2O (Pozzer et al., 2011) submodel

| name | description | reference(s) |
|---|---|---|
| A2O | coupling between atmosphere and ocean | Pozzer et al. (2011) |
| AIRSEA | air-sea gas exchange | Pozzer et al. (2006) |
| CLOUD | ECHAM5 cloud scheme | Roeckner et al. (2006); Jöckel et al. (2006) |
| CONVECT | convection | Tost et al. (2006b) |
| CVTRANS | convective tracer transport | Tost (2006) |
| DDEP | dry deposition | Kerkweg et al. (2006a) |
| GWAVE | non-orographic gravity waves | Hines (1997a,b); Manzini and McFarlane (1998); A. Baumgaertner, pers. comm. |
| H2O | stratospheric water vapour and feedback | Jöckel et al. (2006); Lelieveld et al. (2007) |
| HD | hydrological discharge | Hagemann and Dümenil (1998); A. Pozzer, pers. comm. |
| HAMOCC | oceanic biogeochemistry | Maier-Reimer et al. (2005); Wetzel et al. (2005); A. Pozzer, pers. comm.; **this study, Section 3.3, Appendix A** |
| JVAL | photolysis rates | Landgraf and Crutzen (1998); Jöckel et al. (2006); R. Sander, pers. comm. |
| LNOX | lightning nitrogen oxides ($NO_x$) | Grewe et al. (2001); Tost et al. (2007b); Jöckel et al. (2010) |
| M7 | aerosol microphysics | Vignati et al. (2004); Stier et al. (2005); Kerkweg et al. (2008); Gläser et al. (2012) |
| MECCA | tropospheric and stratospheric chemistry | Sander et al. (2011) |
| MPIOM | ocean dynamics | Marsland et al. (2003); Jungclaus et al. (2006); Pozzer et al. (2011) |
| MSBM | multi-phase stratospheric box model | Jöckel et al. (2010) |
| OFFEMIS | offline emissions | Kerkweg et al. (2006b) |
| ONEMIS | online emissions | Kerkweg et al. (2006b) |
| OTPHYSC | oceanic tracer physics | A. Pozzer, pers. comm.; **this study, Section 3.6, Appendix B** |
| RAD4ALL | ECHAM5 radiation scheme | Roeckner et al. (2006); Jöckel et al. (2006) |
| SCALC | simple calculations | **this study, Section 3.7, Appendix C** |
| SCAV | scavenging | Tost et al. (2006a) |
| SEDI | sedimentation | Kerkweg et al. (2006a) |
| TNUDGE | tracer nudging | Kerkweg et al. (2006b) |
| TROPOP | tropopause and diagnostics | Jöckel et al. (2006) |

**Table 3.1:** MESSy submodels used in this study.

(see also Section 3.4). The chemical coupling between ocean and atmosphere via air-sea gas exchange is implemented by the submodel AIRSEA (Pozzer et al., 2006; see also Section 3.5).

## 3.2 Atmosphere

The EMAC model is a numerical model system, consisting of submodels for simulating tropospheric and middle atmospheric (stratospheric and mesospheric) dynamical and physical processes, and their interaction with oceans, land, and human influences (Jöckel et al., 2010). The model system used in this study is based on version 2 of the MESSy interface and the 5th generation of European Centre HAMburg general circulation model (ECHAM; Roeckner et al., 2003, 2006; version 5.3.02). Simulations are performed, using a spherical truncation of T42, corresponding to a quadratic Gaussian grid spacing of approximately $2.8° \times 2.8°$ in latitude and longitude. In the vertical dimension 47 hybrid pressure levels are used, extending from Earth's surface up to a pressure of 0.01 hPa (at the mid of the top model layer).

Atmospheric chemistry is calculated using the MESSy submodel MECCA (Module Efficiently Calculating the Chemistry of the Atmosphere; Sander et al., 2005, 2011). The comprehensive atmospheric chemistry follows Jöckel et al. (2010), with the exception of mercury, which is not included in the chemical mechanism used in the present study.

Atmospheric aerosol is simulated using the implementation of the microphysical aerosol model M7 (Vignati et al., 2004) as MESSy submodel (Kerkweg et al., 2008). The aerosol model uses seven aerosol classes, representing nucleation, Aitken, accumulation, and coarse mode for soluble particles and Aitken, accumulation, and coarse mode for insoluble particles. The simulated aerosol consists of mineral dust, black carbon, primary organic carbon, sulphate, and sea salt. The aerosol model represents the processes of nucleation, accumulation, and condensation of sulphuric acid. Scavenging, dry deposition, sedimentation, and wet deposition of aerosols are not included in the microphysical aerosol model and calculated via the submodels DDEP (Dry DEPosition; Kerkweg et al., 2006a), SEDI (SEDImentation; Kerkweg et al., 2006a), and SCAV (SCAVenging; Tost et al., 2006a), respectively.

For the sensitivity study using "online" calculated dust deposition (Section 4.4), the dust emission scheme after Tegen et al. (2002) is used, implemented in EMAC by Gläser et al. (2012) into the ONEMIS (ONline tracer EMISsions; Kerkweg et al., 2006b) submodel. The total dust deposition flux is summed up from partial dust

deposition fluxes calculated by the submodels DDEP, SEDI and SCAV via a newly implemented submodel SCALC (Simple CALCulations) and then passed to the oceanic domain. Details on the inclusion of online calculated dust deposition fluxes in the model system are presented in Section 3.7.

For calculation of radiative transfer the radiation submodel RAD4ALL is used, which is a re-implementation of the original ECHAM5 radiation scheme (Roeckner et al., 2006) as MESSy submodel. The radiation code is coupled interactively to online calculated fields provided from various submodels. These fields are cloud water, cloud ice, and fractional cloud cover (submodel CLOUD), prognostic specific humidity (submodels H2O, MSBM), radiatively active chemical compounds ($CO_2$, $O_3$, $CH_4$, $N_2O$, CFC-11, and CFC-12; submodel MECCA) and aerosols (internal Tanre climatology; Tanre et al., 1984) in the atmosphere.

For this study time-slice experiments with prescribed greenhouse gas conditions at year-2000 levels were performed. To decouple atmospheric dynamics from atmospheric composition, the QCTM mode (Deckert et al., 2011) is used in the simulations. In this mode, the radiation scheme operates with the identical (offline) prescribed atmospheric composition for the relevant chemical species in every sensitivity simulation. In this way, the meteorological situation at a given time is identical in every single simulation, independent of the altered atmospheric composition caused by changed emissions. This allows for the identification of small signals in atmospheric chemical composition, otherwise masked by changed atmospheric dynamics.

To operate the model system in QCTM mode, a preparatory model simulation has to be performed with output of monthly mean fields of atmospheric concentrations of carbon dioxide ($CO_2$), methane ($CH_4$), ozone ($O_3$), nitrous oxide ($N_2O$), $CCl_3F$ (trichlorofluoromethane, CFC-11), $CCl_2F_2$ (dichlorodifluoromethane, CFC-12), $HNO_3$, and $HNO_3$ in NAT phase ($HNO_{3nat}$). These tracer fields are used in subsequent simulations to calculate atmospheric radiative transfer (in case of $CO_2$, $CH_4$, $O_3$, $N_2O$, CFC-11, and CFC-12) in the RAD4ALL submodel. This ensures, that radiative transfer is equal in space and time in all model simulations using the offline provided tracer fields, and in this way all model simulations experience the same feedback on atmospheric dynamics.

Offline provided total $HNO_3$ (the sum of the tracers $HNO_3$ and $HNO_{3nat}$) is used to calculate water vapour tendencies, particle radii, and thermodynamic phase of PSCs in the MSBM submodel (Deckert et al., 2011). That gives consistent $H_2O$ tracer fields in all sensitivity experiments, as all simulations are subject to the same processes and regions of PSC occurrence. Further the H2O submodel is

configured to use climatological $H_2O$ tendencies to account for stratospheric methane oxidation, ensuring consistent feedbacks on the model system's specific humidity for all sensitivity experiments. The model constraints are limited to the dynamical part of the model, suppressing any feedbacks from model chemistry on the model system's dynamics. Further details on the QCTM mode in the EMAC model can be found in Deckert et al. (2011).

## 3.3 Ocean

Version 1.3 of MPIOM (Marsland et al., 2003; Jungclaus et al., 2006) in an implementation as MESSy submodel (Pozzer et al., 2011) is used. The oceanic biogeochemistry model HAMOCC5.1 (Maier-Reimer et al., 2005; Wetzel et al., 2005) is coupled to the model system via the MESSy interface in this study.

MPIOM is an O-GCM based on the Boussinesq approximated primitive equations for a hydrostatic fluid with a free surface, discretised on a horizontal staggered Arakawa C-grid with velocity components residing on the centres of the grid-cell edges (Arakawa and Lamb, 1977) and a vertical z-coordinate (Marsland et al., 2003). The model setup uses a bipolar orthogonal curvilinear grid with shifted poles, one located at 72° N, 40° W over Greenland and the other one located at 84° S, 60° E over Antarctica. The ocean grid GR30 has an average grid spacing of $3.0° \times 3.0°$ in latitude and longitude. In the vertical dimension the model operates on 40 unevenly spaced levels, reaching down to 6000 m. Bathymetry is resolved using partial grid cells.

The subgrid-scale parameterisations include bottom boundary layer slope convection (Marsland et al., 2003) and isopycnal diffusion (Redi, 1982; Gent et al., 1995; Griffies, 1998). Vertical eddy viscosity is parameterised using a Richardson number dependent mixing term following Pacanowski and Philander (1981) with additional near surface wind mixing proportional to the cubed 10-metre wind speed, decaying exponentially with depth (Marsland et al., 2003). An operator splitting method is used for time-stepping, momentum advection of tracers is done by a mixed central-difference and upstream integration scheme (Marsland et al., 2003).

External forcing at the ocean surface is provided by heat, freshwater, and momentum fluxes. Freshwater input from rivers to the ocean is calculated by an implementation of the HD (Hydrological Discharge) model (Hagemann and Dümenil, 1998) as MESSy submodel. River discharge is calculated from drainage and runoff provided by atmospheric submodels and passed to the ocean via summation to the

freshwater forcing field. Tracer dilution by freshwater discharge in the oceanic tracer field is included in the OTPHYSC submodel. In OTPHYSC an extension has been developed in this study, to add molar tracer concentrations to the freshwater flux from the HD submodel. Section 3.4 gives some details on the forcing at the air-sea interface provided via the MESSy infrastructure. Details of nutrient input to the ocean by river discharge are described in Section 3.6. Further details of the ocean and sea ice model can be found in Marsland et al. (2003).

HAMOCC operates on the same grid and at the same time step as the O-GCM and is coupled to the ocean model dynamics. For application of HAMOCC in the MESSy framework, it was re-implemented as submodel in this study.

Oceanic tracers are set-up using the generic MESSy submodel TRACER. Oceanic tracer fields are represented at the same horizontal and vertical grid as used by the O-GCM. For advection, convection, diffusion, and dilution of oceanic tracers the MESSy submodel OTPHYSC is used. The MESSy based oceanic tracer fields are subject to the same processes as the generic tracers in the original HAMOCC model. The same advection scheme for oceanic tracers in HAMOCC as for salinity and temperature in MPIOM is used.

HAMOCC includes an ecosystem of the NPZD-type extended by a pool of dissolved organic matter (DOM) (Six and Maier-Reimer, 1996; Maier-Reimer et al., 2005), i.e. it is based on the functional groups nutrients, phytoplankton, zooplankton, detritus, and DOM. An overview of interactions between the different compartments of the ecosystem model is given in Fig. 2.3. The nutrient pool is composed of orthophosphate ($PO_4^{3-}$), nitrate in aqueous phase ($NO_3^-$), silicic acid ($Si(OH)_4$), and iron (Fe). The model includes processes for denitrification and nitrogen fixation, formation of calcium carbonate ($CaCO_3$) and opaline shells, dimethyl sulphide ($(CH_3)_2S$, DMS) production, dissolved iron uptake, dust deposition, and sinking (Wetzel et al., 2005). Phytoplankton is assumed to be implicitly composed of two types. One type (diatoms) producing opal and growing fastest, when silicate is available, and the other type (coccolithophorides) producing calcite up to a maximum fraction of total photosynthesis (Maier-Reimer et al., 2005). Biological production, with changes in the phosphorous pool and production of calcium carbonate is associated with uptake of dissolved organic carbonate and directly impacts alkalinity. Inorganic carbon chemistry is represented according to Maier-Reimer and Hasselmann (1987). Ocean surface concentrations of $CO_2$ are calculated from the prognostic variables temperature, salinity, dissolved inorganic carbon, and total alkalinity.

The sediment module follows the approach of Heinze and Maier-Reimer (1999) and contains pore water and solid sediments. Sediments and their interaction with the bottom layer ocean water via processes like dissolution from sediments and burial, however, only become relevant on very long time scales (more than 1000 years).

The implementation of the HAMOCC submodel is based on an updated version of HAMOCC5.1 (Maier-Reimer et al., 2005), comparable to a model version used in Assmann et al. (2010). For an updated model description of HAMOCC see also Ilyina et al. (2013). However, because of some deviations in the implementation as MESSy submodel, some general details and main differences between the original release as described in Maier-Reimer et al. (2005) and the version used in this study are discussed below. Table 3.2 lists an overview of the parameters used in this study for the oceanic biogeochemistry model. A compilation of all model parameters in the HAMOCC submodel available via user namelist, and their default and used values, can be found in Appendix A.

The original HAMOCC model consists of three different parts of the carbon cycle. It is implemented to simulate the carbon cycle of air, water and sediment, as well as the interactions between them. The atmospheric component of HAMOCC is a simple diffusive slab atmosphere for the calculation of changes in atmospheric tracer concentrations of $CO_2$, $O_2$, and $N_2$. The model also contains a module for the calculation of air-sea gas exchange for these tracers. As we intend to use the model only coupled to an atmospheric chemistry model, this part was not implemented in the MESSy submodel version of HAMOCC and is not described further. Air-sea gas exchange in the EMAC model is simulated using the submodel AIRSEA, which is explained in more detail in Section 3.5.

Two coupling processes to the atmospheric domain exist, which are not simulated by the AIRSEA submodel but are directly accounted for in HAMOCC: (1) Nitrogen fixation by diazotrophs is accounted for in the surface layer water. In this way, diazotrophs can directly "take up" atmospheric nitrogen. (2) Iron import via dust deposition is simulated in the surface ocean layer. In the standard implementation, the dust deposition is provided by a climatological input field of monthly means (Timmreck and Schulz, 2004). The solubility of iron from dust deposition is fixed at 1%, whereas a fixed mass fraction of iron in dust of 3.5% is assumed. In addition to the original HAMOCC code, dust is also considered as source of silicon (Si) here. For silica ($SiO_2$), a mass fraction of 30.8% and a solubility of 7.5% is assumed (Cotrim da Cunha et al., 2007). Extensions to include "online" calculated dust deposition are described in Section 3.7.

| description | symbol | variable | value and units |
|---|---|---|---|
| Euphotic zone (0 to 90 m) | | | |
| Phytoplankton | | | |
| initial slope of the P-I curve | $\alpha_{PI}$ | pi_alpha | $0.008\,\mathrm{d}^{-1}(\mathrm{W\,m}^{-2})^{-1}$ |
| light extinction coefficient of water | $k_w$ | atten_w | $0.04\,\mathrm{m}^{-1}$ |
| specific light extinction of chlorophyll | $k_c$ | atten_c | $0.03 \times 10^6\,\mathrm{m}^{-1}\,(\mathrm{kg(Chl)\,m}^{-3})^{-1}$ |
| half-saturation constant for $PO_4$ | $K_{\mathrm{Phy}}^{\mathrm{PO_4}}$ | bkphy | $1 \times 10^{-8}\,\mathrm{kmol(P)\,m}^{-3}$ |
| half-saturation constant for $Si(OH)_4$ | $K_{\mathrm{Phy}}^{\mathrm{Si(OH)_4}}$ | bkopal | $1 \times 10^{-6}\,\mathrm{kmol(P)\,m}^{-3}$ |
| Fe:P uptake ratio | $R_{\mathrm{Fe:P}}$ | riron | $3 \times 10^{-6} \times 122\,\mathrm{mol(Fe)\,mol(P)}^{-1}$ |
| Opal:P uptake ratio | $R_{\mathrm{Si:P}}$ | ropal | $25\,\mathrm{mol(Si)\,mol(P)}^{-1}$ |
| $CaCO_3$:P uptake ratio | $R_{\mathrm{CaCO_3:P}}$ | rcalc | $35\,\mathrm{mol(C)\,mol(P)}^{-1}$ |
| remineralisation rate | $\lambda^{\mathrm{surf}}_{\mathrm{DOM,PO_4}}$ | remido | $0.025\,\mathrm{d}^{-1}$ |
| mortality rate | $\lambda^{\mathrm{surf}}_{\mathrm{Phy,Det}}$ | dyphy | $0.008\,\mathrm{d}^{-1}$ |
| exudation rate | $\lambda_{\mathrm{Phy,DOM}}$ | gammap | $0.03\,\mathrm{d}^{-1}$ |
| Zooplankton | | | |
| maximum grazing rate | $\mu_{\mathrm{Zoo}}$ | grazra | $1.0\,\mathrm{d}^{-1}$ |
| half-saturation constant for grazing | $K_{\mathrm{Zoo}}$ | bkzoo | $4 \times 10^{-8}\,\mathrm{kmol(P)\,m}^{-3}$ |
| mortality rate | $\lambda^{\mathrm{surf}}_{\mathrm{Zoo}}$ | spemor | $3 \times 10^6\,\mathrm{d}^{-1}$ |
| excretion rate | $\lambda_{\mathrm{Zoo,DOM}}$ | gammaz | $0.06\,\mathrm{d}^{-1}$ |
| Deep ocean (> 90 m) | | | |
| Detritus remineralisation rate | $\lambda^{\mathrm{deep}}_{\mathrm{Det,PO_4}}$ | drempoc | $0.1\,\mathrm{d}^{-1}$ (AGG) |
| DOM remineralisation rate | $\lambda^{\mathrm{deep}}_{\mathrm{DOM,PO_4}}$ | dremdoc | $0.03\,\mathrm{d}^{-1}$ |
| Opal dissolution rate | $\lambda_{\mathrm{Opal,Si(OH)_4}}$ | dremopal | $3.3 \times 10^{-3}\,\mathrm{d}^{-1}$ (AGG) |
| Calcium carbonate dissolution rate | $\lambda_{\mathrm{CaCO_3},C_T^{12}}$ | dremcalc | $0.075\,\mathrm{d}^{-1}$ |
| Phytoplankton mortality rate | $\lambda^{\mathrm{deep}}_{\mathrm{Phy,Det}}$ | dphymor | $0.2\,\mathrm{d}^{-1}$ (AGG) |
| Zooplankton mortality rate | $\lambda^{\mathrm{deep}}_{\mathrm{Zoo,Det}}$ | dzoomor | $0.02\,\mathrm{d}^{-1}$ |

**Table 3.2:** Parameters of the oceanic biogeochemistry in HAMOCC, their symbols and values as used in this study (cf. Maier-Reimer et al., 2005; Assmann et al., 2010). The column "variable" lists the name of the variable used in the model code. (AGG) denotes values, which were chosen, because variable sinking velocities for detritus, opal, and calcium carbonate following the aggregation model by Kriest and Evans (2000); Kriest (2002) are used.

The water component of the biogeochemistry model contains an ecosystem model of NPZD-type. This ecosystem is build from two phytoplankton (opal and calcite producers) and one zooplankton species (Schneider et al., 2008). Uptake and re-dissolution of nutrients, carbon, and oxygen are calculated using constant Redfield

stoichiometric ratios of P:N:C:$O_2$:Fe of 1:16:122: − 172:3.7 × $10^{-4}$ (Takahashi et al., 1985; Maier-Reimer et al., 1996). Biological production and grazing of zooplankton only take place in the upper 90 m of the model, the euphotic zone, where sufficient light is assumed to be available. Below the euphotic zone all organic matter is re-mineralised to nutrients (Maier-Reimer et al., 2005). Phytoplankton growth is limited by availability of light, availability of nutrients, and temperature.

Light intensity decreases with ocean depth by attenuation due to seawater, expressed by the extinction coefficient $k_w$ (in $\mathrm{m}^{-1}$). Light attenuation by phytoplankton depends on the mass of chlorophyll per volume of seawater. $k_c$ is the specific extinction coefficient for chlorophyll in $\mathrm{m}^{-1}\,(\mathrm{kg(Chl)\,m^{-3}})^{-1}$. The mass concentration of chlorophyll is calculated from the molar concentration of phytoplankton [Phy] using the Redfield stoichiometric C:P ratio $R_{\mathrm{C:P}}$ (in $\mathrm{mol(C)\,mol(P)}^{-1}$), the ratio of carbon to chlorophyll in phytoplankton $R_{\mathrm{C:Chl}}$ (in $\mathrm{g(C)\,g(Chl)}^{-1}$), and the molar mass of carbon $M_{\mathrm{C}} = 12\,\mathrm{g/mol(C)}$. Available irradiance $I$ at depth $z$ and at time $t$ is calculated from the total solar irradiance at the ocean's surface $I_0$:

$$I(z,t) = a_f\, I_0(t)\, e^{-(k_w + k_c[\mathrm{Phy}]\, M_{\mathrm{C}}\, R_{\mathrm{C:P}}/R_{\mathrm{C:Chl}})z} \tag{3.3}$$

(Maier-Reimer et al., 2005). At the ocean surface absorption is taken into account via a constant attenuation coefficient of $a_f = 0.4$.

The light limited growth rate of phytoplankton $J(I)$ (in $\mathrm{d}^{-1}$) is calculated as product of the slope of the P-I-curve (production versus light intensity) $\alpha_{PI}$ (in $\mathrm{d}^{-1}\,(\mathrm{W\,m^{-2}})^{-1}$) and the available solar irradiance $I$ (in $\mathrm{W\,m^{-2}}$) at depth $z$ and time $t$:

$$J(I(z,t)) = \alpha_{PI} \times I(z,t). \tag{3.4}$$

The maximum growth rate of phytoplankton $\mu_\vartheta$ limited by temperature $\vartheta$ is expressed as an empirical relationship following Eppley (1972):

$$\mu_\vartheta(z,t) = 0.6 \times 1.066^{\vartheta(z,t)}, \tag{3.5}$$

with $\vartheta$ in °C and $\mu_\vartheta$ in $\mathrm{d}^{-1}$.

Light and temperature limited growth rates are combined to a total growth rate $J_{tot}(I,\vartheta)$ of phytoplankton (in $\mathrm{d}^{-1}$):

$$J_{tot}(I(z,t),\vartheta(z,t)) = \frac{J(I(z,t)) \times \mu_\vartheta(z,t)}{\sqrt{J(I(z,t))^2 + \mu_\vartheta(z,t)^2}}. \tag{3.6}$$

Nutrient co-limitation by phosphate, nitrate and iron is accounted for by using

$$[\mathrm{X}] = min\left([\mathrm{PO_4}], \frac{[\mathrm{NO_3}]}{R_{\mathrm{N:P}}}, \frac{[\mathrm{Fe}]}{R_{\mathrm{Fe:P}}}\right), \tag{3.7}$$

to calculate the molar concentration of the limiting nutrient [X]. Here the stoichiometric uptake ratios for nitrogen $R_{\mathrm{N:P}}$ and iron $R_{\mathrm{Fe:P}}$ are taken into account, to get the molar concentration of the limiting nutrient in units of $\mathrm{kmol(P)\,m^{-3}}$.

The total phytoplankton production by photosynthesis $\rho_p$ (in $\mathrm{kmol(P)\,m^{-3}\,d^{-1}}$) is expressed by Michaelis-Menten kinetics (Maier-Reimer, 1993), including limitations by available nutrients, light, and temperature:

$$\rho_p = \frac{[\mathrm{Phy}]\, J_{tot}(I, \vartheta)\, [\mathrm{X}]}{K_{Phy}^{\mathrm{PO_4}} + [\mathrm{X}]} \tag{3.8}$$

(Maier-Reimer et al., 2005).

Sulphate reduction in oxygen-poor waters and sediments was added in a recent version of HAMOCC5.1. Zooplankton mortality is now parameterised as quadratic relationship of zooplankton concentration (Assmann et al., 2010). In addition to remineralisation of particulate organic carbon (POC) and dissolved organic carbon (DOC), remineralisation of dying phytoplankton is taken into account.

The oceanic biogeochemistry model already includes tracers for the dissolved gases oxygen ($O_2$), $N_2O$, nitrogen ($N_2$), $CO_2$, and DMS in water. In order to simulate air-sea gas exchange of isoprene ($C_5H_8$) and carbon monoxide (CO), and to assess its impact on atmospheric chemistry and chemical composition, additional parameterisations for seawater concentrations of these gases have been implemented in the model system for this study. Seawater concentration of $C_5H_8$ is parameterised following Broadgate et al. (1997), CO concentration is simulated following the approach of Kettle (2005a).

The parameterisation of Broadgate et al. (1997) deduce the molar concentration of $C_5H_8$ in seawater directly from the mass concentration of chlorophyll. Chlorophyll mass concentration [Chl] is calculated diagnostically from the phytoplankton molar concentration [Phy] expressed in units of $\mathrm{kmol(P)\,m^{-3}}$, the carbon to phosphorous ratio $R_{\mathrm{C:P}}$ (in $\mathrm{mol(C)\,mol(P)^{-1}}$), and the carbon to chlorophyll ratio $R_{\mathrm{C:Chl}}$ (in $\mathrm{g(C)\,g(Chl)^{-1}}$), analogous to Moore et al. (2001):

$$[\mathrm{Chl}] = R_{\mathrm{C:P}} \times \frac{M_{\mathrm{C}}}{R_{\mathrm{C:Chl}}} \times 10^3 \times [\mathrm{Phy}], \tag{3.9}$$

where $M_C$ is the molar mass of carbon (C) and the factor $10^3$ enters the equation, to yield [Chl] as mass concentration in $\mathrm{mg\,l^{-1}}$. HAMOCC uses a constant carbon to phosphorous Redfield ratio of $R_{C:P} = 122\,\mathrm{mol(C)\,mol(P)^{-1}}$, and a constant carbon to chlorophyll ratio of $R_{C:Chl} = 60\,\mathrm{g(C)\,g(Chl)^{-1}}$.

The $C_5H_8$ molar concentration [Isop] is calculated following the diagnostics by Broadgate et al. (1997), who parameterise [Isop] via an empirical relationship to [Chl]:

$$[\mathrm{Isop}] = (6.43 \times [\mathrm{Chl}] \times 10^3 + 1.2) \times 10^{-12}. \tag{3.10}$$

The factors $10^3$ and $10^{-12}$ are introduced to yield molar concentrations of [Isop] in $\mathrm{kmol(Isop)\,m^{-3}}$.

The molar concentration of CO is calculated following the approach of Kettle (2005a), which takes into account photochemical production and microbial consumption of CO. The temporal evolution of the upper ocean CO concentration can be expressed as continuity equation. The continuity equation of [CO] is written (in its one-dimensional form and with upper ocean CO concentration denoted as $\chi(z,t)$ in $\mathrm{\mu mol\,m^{-3}}$ at depth $z$ and at time $t$) as (Kettle, 2005a, Equation 1):

$$\frac{\partial \chi(z,t)}{\partial t} + \mathfrak{R}_S[\chi(z,t)] = J(z,t) + \mathfrak{M}(z,t) + \mathfrak{D}, \tag{3.11}$$

where the change of concentration $\chi(z,t)$ with time $t$ is affected by turbulent mixing in the upper oceanic boundary layer expressed by a linear transport operator $\mathfrak{R}_S$, photochemical production rate $J$, microbial consumption rate $\mathfrak{M}$, and dark production rate $\mathfrak{D}$, accounting for abiotic CO production (see e.g. Zhang et al., 2008).

The photochemical CO production rate depends on the wavelength of light ($\lambda$) and is the product of attenuation of down-welling irradiance $E_d$ (Kettle, 2005b, Appendix A, Equation A.1), fraction of energy absorption by coloured dissolved organic matter (CDOM) to total energy absorption $f_g(\lambda)$, the apparent quantum yield for CO formation $\Phi(\lambda)$, and a constant $\frac{\lambda}{hc}$ to convert from energy units of $\mathrm{J\,m^{-3}\,s^{-1}}$ to CO production in $\mathrm{\mu mol(CO)\,m^{-3}\,s^{-1}}$ (Kettle, 2005a, Appendix A, Equation A.1):

$$J_\lambda(z,t,\lambda) = -\frac{dE_d(z,t,\lambda)}{dz} f_g(\lambda)\Phi(\lambda)\frac{\lambda}{hc}. \tag{3.12}$$

Here $h = (6.626\,069\,57 \pm 0.000\,000\,29) \times 10^{-34}\,\mathrm{J\,s}$ [2] is Planck's constant and $c = 299\,792\,458\,\mathrm{m\,s^{-1}}$ [2] is speed of light in vacuum. With $\lambda = \lambda_0 = 320\,\mathrm{nm}$ and using the solar irradiance $I(z,t)$ at depth $z$, $J(z,t)$ becomes:

$$J(z,t) = I(z,t)\, a_g\,[\mathrm{DOM}]\, \frac{M_\mathrm{C}}{M_\mathrm{P}}\, \Phi(\lambda_0)\, \frac{\lambda_0}{hc}\, \frac{N_A}{10^3\,\mathrm{kmol\,mol^{-1}}}. \tag{3.13}$$

The absorption coefficient $a_{320} = 0.87$, measured offshore by Retamal et al. (2007) at a wavelength of $\lambda = 320\,\mathrm{nm}$ and salinity of 30.09, is normalised to the measured DOC concentration of $[\mathrm{DOC}] = 1.15\,\mu\mathrm{g(C)\,l^{-1}} = 9.58 \times 10^{-5}\,\mathrm{kmol(C)\,m^{-3}}$ to form the absorption coefficient of CDOM, $a_g$. The factor $M_\mathrm{C}/M_\mathrm{P}$, with the molar mass of C $M_\mathrm{C} = 12\,\mathrm{g/mol(C)}$ and the molar mass of phosphorous (P) $M_\mathrm{P} = 30\,\mathrm{g/mol(P)}$, transforms from "phosphorous units" to "carbon units". The factor $N_A/(10^3\,\mathrm{kmol\,mol^{-1}})$ is included to yield a CO production in $\mathrm{kmol(C)\,m^{-3}\,s^{-1}}$. $N_A = (6.022\,141\,29 \pm 0.000\,000\,27) \times 10^{23}\,\mathrm{mol^{-1}}$ [2] is Avogadro's constant. For the apparent quantum yield of CO formation at $\lambda = \lambda_0 = 320\,\mathrm{nm}$ a value of $\Phi(\lambda_0) = 4.7 \times 10^{-5}$ is used. It is linearly interpolated from measured values of $\Phi(\lambda)$ for $\lambda = 313\,\mathrm{nm}$ and $\lambda = 325\,\mathrm{nm}$ of Kettle (2005a, Appendix A, Table 3).

Particles in the water column are subject to settling, which provides a vertical redistribution of marine snow and dust. The sinking speed of particles is variable and depends on the particle size. Particle size distribution of phytoplankton and detritus (marine snow) is variable in time and with depth, depending on aggregation, sinking, and zooplankton mortality (Maier-Reimer et al., 2005). Aggregation follows the approach of Kriest and Evans (2000) and Kriest (2002). Details can be found there, modifications specific to HAMOCC5.1 are described in Maier-Reimer et al. (2005).

The sediment module collects all particles, which are not re-mineralised during their way trough the water below the euphotic zone. Re-dissolution from the sediments is simulated in the model. The sediment model is based on Heinze and Maier-Reimer (1999), details can also be found in Maier-Reimer et al. (2005).

[2] Mohr et al. (2012)

## 3.4 Dynamical coupling between ocean and atmosphere

Using the MESSy2 framework, EMAC was coupled to MPIOM, and the coupled AO-GCM (i.e. with atmospheric chemistry submodels switched off) was evaluated (Pozzer et al., 2011). As the structure of the MESSy interface suggest a process based approach for coupling, MPIOM is implemented as submodel. A submodel interface layer (SMIL) module is provided, acting as interface between calls of the main entry points from submodel CONTROL and the original MPIOM subroutines calculating ocean dynamics. The original MPIOM code containing these subroutines is linked as library to the executable. Minor changes had to be performed in the MPIOM code, which are enclosed by preprocessor directives. Further details can be found in Pozzer et al. (2011).

The exchange of momentum, energy, and water mass at the interface between the atmospheric and oceanic domain is implemented as separate submodel A2O. As the atmospheric and oceanic model in general are operated with different time step lengths, independent from the coupling time step between the domains, A2O has to accumulate and average the fields needed for exchange with respect to time.

As EMAC uses a quadratic Gaussian grid and MPIOM operates on a rotated curvilinear grid, exchanged fields have to be transformed between their source and destination grid. A2O uses the generic submodel GRIDTRAFO to transform gridded fields between different grids in the atmospheric and oceanic domain. GRIDTRAFO is based on the SCRIP (Spherical Coordinate Remapping and Interpolation Package; Jones, 1999) library, which includes first- and second-order conservative remapping, bilinear interpolation with local bilinear approximation, bicubic interpolation, and inverse-distance-weighted averaging.

Scalar fields are interpolated using the bilinear method, whereas fluxes are interpolated using a first-order conservative remapping to conserve total fluxes. The fields exchanged between atmosphere and ocean—and vice versa—as well as the transformation method used are listed in Table 3.3.

| variable name | description | units | transformation method |
|---|---|---|---|
| atmosphere to ocean | | | |
| aofltxwo | zonal wind stress over water | Pa/1025 | bilinear |
| aofltywo | meridional wind stress over water | Pa/1025 | bilinear |
| aofltxio | zonal wind stress over ice | Pa/1025 | bilinear |
| aofltyio | meridional wind stress over ice | Pa/1025 | bilinear |
| aoflfrwo | solid freshwater flux | $\mathrm{m\,s^{-1}}$ | conservative |
| aoflfrio | liquid freshwater flux | $\mathrm{m\,s^{-1}}$ | conservative |
| aoflnhwo | net heat flux over water | $\mathrm{m\,s^{-1}}$ | conservative |
| aoflshwo | downward short-wave radiation | $\mathrm{m\,s^{-1}}$ | conservative |
| aoflchio | conductive heat flux over ice | $\mathrm{m\,s^{-1}}$ | conservative |
| aoflrhio | residual heat flux over ice | $\mathrm{m\,s^{-1}}$ | conservative |
| aoflwsvo | 10-metre wind speed | $\mathrm{m\,s^{-1}}$ | bilinear |
| ocean to atmosphere | | | |
| tho | sea surface temperature | K | bilinear |
| sictho | sea ice thickness | m | bilinear |
| sicomo | sea ice compactness (ice fraction) | 1 | bilinear |
| sicsno | snow thickness | m | bilinear |
| socu | zonal surface water velocity | $\mathrm{m\,s^{-1}}$ | bilinear |
| socv | meridional surface water velocity | $\mathrm{m\,s^{-1}}$ | bilinear |

**Table 3.3:** Exchanged fields for dynamical coupling between ocean and atmosphere (Pozzer et al., 2011, modified).

## 3.5 Air-sea gas exchange

Air-sea gas exchange is calculated following the two-layer model by Liss and Slater (1974). It is implemented as MESSy submodel AIRSEA (Pozzer et al., 2006). The model is based on the assumption, that the uppermost ocean layer and the lowermost atmospheric layer are well mixed, and the only driver of air-sea gas exchange at the interface is molecular diffusion. The bulk flux $F$ in $\mathrm{mol\,(m^2\,s)^{-1}}$ across the oceanic and atmospheric interface can be written as:

$$F = K_{tot}\,(c_w - k_H p_g), \tag{3.14}$$

with the transfer velocity $K_{tot}$ (in $\mathrm{m\,s^{-1}}$), the seawater tracer concentration in the uppermost oceanic layer $c_w$ (in $\mathrm{mol\,m^{-3}}$), Henry's Law coefficient $k_H$ (in $\mathrm{mol\,(m^3\,Pa)^{-1}}$) and the partial pressure of the gas in the lowermost atmospheric layer $p_g$ (in Pa).

Henry's Law coefficient is defined as the ratio of the molar concentration of a species in the aqueous phase ($c_a$, in $\mathrm{mol\,m^{-3}}$) to its partial pressure in the gas phase ($p_g$, in Pa):

$$k_H = c_a / p_g \tag{3.15}$$

(Sander, 1999a,b).

The temperature dependence of the Henry's Law coefficient is described as:

$$k_H = k_H^{\ominus} \times \exp\left(\frac{-\Delta_{soln}H}{R}\left(\frac{1}{T} - \frac{1}{T^{\ominus}}\right)\right), \tag{3.16}$$

where $k_H^{\ominus}$ is the (measured) Henry's Law coefficient at standard temperature $T^{\ominus} = 298.15\,\mathrm{K}$ (Sander, 1999b). Henry's Law coefficient depends on the molar enthalpy of the solution $\Delta_{soln}H$ in $\mathrm{J\,mol^{-1}}$, $R = (8.314\,462\,1 \pm 0.000\,007\,5)\,\mathrm{J\,(mol\,K)^{-1}}$ [3] the gas constant, and the actual temperature $T$ in K.

From Equation 3.16, the temperature dependence is:

$$\frac{-\mathrm{d}\ln k_H}{\mathrm{d}(1/T)} = \frac{\Delta_{soln}H}{R}. \tag{3.17}$$

Commonly $k_H$ is expressed in units of $\mathrm{M/atm} = \mathrm{mol\,dm^{-3}/atm}$, where $1\,\mathrm{atm} = 101\,325\,\mathrm{Pa}$. The conversion between the two representations of $k_H$ is (Sander, 1999a):

$$\frac{k_H}{\mathrm{M/atm}} = 101.325\,\frac{k_H}{\mathrm{mol\,m^{-3}\,Pa}}. \tag{3.18}$$

The total transfer velocity $K_{tot}$ in Equation 3.14 is expressed in terms of resistances against air-sea gas exchange in water ($R_w$, in $\mathrm{s\,m^{-1}}$) and in the gas phase ($R_g$, in $\mathrm{s\,m^{-1}}$) (Liss and Slater, 1974; Pozzer et al., 2006):

$$K_{tot} = (R_w + R_g)^{-1} = \left(\frac{1}{\alpha\,K_w} + \frac{k_H\,R\,T}{K_g}\right)^{-1}, \tag{3.19}$$

[3] Mohr et al. (2012)

where $K_w$ and $K_g$ are exchange velocities on the liquid phase side and the gas phase side, respectively (both in $\mathrm{m\,s^{-1}}$). When considering a chemically reactive gas, exchange can not be described by molecular diffusion alone. Therefore a fractional increase $\alpha$ in exchange velocity due to chemical reaction in the solution is included (Liss and Slater, 1974; Pozzer et al., 2006).

The solubility of a gas in pure water is larger than its solubility in salty water. The actual value of Henry's Law coefficient for a specific gas in salty water $k_H$ is therefore lower than the Henry's Law coefficient of this gas in pure water $k_H^0$. This effect, usually called "salting-out", is taken into account using the Setschenow equation (Sander, 1999b; Pozzer et al., 2006):

$$\ln\left(\frac{k_H}{k_H^0}\right) = k_s\, c_s, \tag{3.20}$$

where $k_s$ (in $\mathrm{l\,mol^{-1}}$) is the Setschenow constant for the specific gas and $c_s$ (in $\mathrm{mol\,l^{-1}}$) is the molar concentration of salt in the solution. The "salting-out effect" on the Henry's Law coefficient is accounted for in the submodel AIRSEA. Via namelist, the user can define a value for the Setschenow constant of a specific species. If a value of 0 is assigned, the Setschenow constant is approximated from the species' molar volume at boiling point $V_\mathrm{X}$ using the relation established by Xie et al. (1997), see also Pozzer et al. (2006):

$$k_s = 0.0018\, V_\mathrm{X}. \tag{3.21}$$

An overview of the species, for which air-sea gas exchange is calculated in this study, and values for their molar mass, their Henry's Law coefficient and temperature dependence, the fractional increase in exchange velocity due to the species chemical reaction, their molar volume at boiling point, and their Setschenow constant, as used in the submodel AIRSEA, are listed in Table 3.4.

For calculating the water side exchange velocity $K_w$ different parameterisations are available in the submodel AIRSEA. The parametrisations of $K_w$ mainly combine field and laboratory measurements, and are normalised to a Schmidt number of 660 (Pozzer et al., 2006).

In this study the parameterisation by Wanninkhof (1992) is used, which relates the normalised water side exchange velocity $\hat{K}_w$ in $\mathrm{cm\,h^{-1}}$ to the quadratic 10-metre wind velocity $U_{10}$ in $\mathrm{m\,s^{-1}}$:

$$\hat{K}_w = 0.31\, {U_{10}}^2. \tag{3.22}$$

| species | molar mass $\frac{M}{\mathrm{g\,mol^{-1}}}$ | Henry's Law coefficient $\frac{k_H^{\ominus}}{\mathrm{M\,atm^{-1}}}$ | temperature dependence $\frac{\mathrm{d}\ln k_H}{\mathrm{d}(1/T)}$ $\frac{}{\mathrm{J\,mol^{-1}}}$ | increase due to chemical reaction $\alpha$ | molar volume at boiling point $\frac{V_\mathrm{X}}{\mathrm{cm^3\,mol^{-1}}}$ | Setschenow constant $\frac{k_s}{\mathrm{l\,mol^{-1}}}$ |
|---|---|---|---|---|---|---|
| $N_2$ | 28.013[a] | $6.5 \times 10^{-4}$[b] | 1300[b] | 1 | 34.84[c] | 0[d] |
| CO | 28.010[a] | $9.9 \times 10^{-4}$[b] | 1300[b] | 1 | 34.88[c] | 0[d] |
| $O_2$ | 31.999[a] | $1.2 \times 10^{-3}$[b] | 1700[b] | 1 | 27.85[c] | 0[d] |
| $CO_2$ | 44.010[a] | $3.6 \times 10^{-2}$[b] | 2200[b] | 1 | 37.3[e] | 0[d] |
| $N_2O$ | 44.013[a] | $2.4 \times 10^{-2}$[b] | 2700[b] | 1 | 35.9[c] | 0[d] |
| DMS | 62.134[a] | $4.8 \times 10^{-1}$[b] | 3100[b] | 1 | 75.16[f] | 0[d] |
| $C_5H_8$ | 68.117[a] | $1.3 \times 10^{-2}$[b] | 0[b] | 1 | 105.12[f] | 0[d] |
| $CH_3OH$ | 32.042[a] | $2.2 \times 10^{2}$[b] | 5600[b] | 1 | 42.5[e] | 0[d] |

[a] NIST (2011).
[b] Sander (1999a, and references therein).
[c] Poling et al. (2001, and references therein).
[d] for $k_s = 0$ the theoretical value of $k_s$ calculated from Equation 3.21 is used.
[e] Hayduk and Laudie (1974, and references therein).
[f] theoretical value, calculated from Poling et al. (2001, Eq. 4-11.4a); Yamada and Gunn (1973).

**Table 3.4:** Parameters used for species in AIRSEA in this study.

The actual water side exchange velocity $K_w$ (in $\mathrm{m\,s^{-1}}$) is obtained by scaling the normalised exchange velocity $\hat{K}_w$ with the actual Schmidt number of the tracer in the liquid phase $Sc_{liq}$:

$$K_w = \beta_{Sc}\,\hat{K}_w\,\left(\frac{Sc_{liq}}{660}\right)^{-n}, \tag{3.23}$$

where a scaling factor $\beta_{Sc} = 2.8 \times 10^{-6}\,(\mathrm{m\,s^{-1}})/(\mathrm{cm\,h^{-1}})$ is used to convert into $\mathrm{m\,s^{-1}}$. The exponent $n$ has a value between 1/2 for rough sea and 2/3 for a calm water surface, in this study AIRSEA operates with a constant value of $n = 1/2$ (Pozzer et al., 2006).

The actual Schmidt number for the tracer in the liquid phase ($Sc_{liq}$) is estimated from the Schmidt number of $CO_2$ in sea water ($Sc_{CO_2}$), calculated according to Wanninkhof (1992):

$$Sc_{CO_2} = k_0 - k_1\,\vartheta + k_2\,\vartheta^2 - k_3\,\vartheta^3, \tag{3.24}$$

with $k_0 = 2073.1$, $k_1 = 125.62\,^\circ\mathrm{C}^{-1}$, $k_2 = 3.6276\,^\circ\mathrm{C}^{-2}$, $k_3 = 0.043\,219\,^\circ\mathrm{C}^{-3}$, and temperature $\vartheta$ given in °C.

The Schmidt number of a tracer X is defined as ratio of the kinematic viscosity of sea water $\nu$ and the tracer's molecular diffusivity $D_{\mathrm{X}}$, and can be expressed in terms of the Schmidt number of $CO_2$ in sea water $Sc_{\mathrm{CO_2}}$ and the molecular diffusivity of $CO_2$ ($D_{\mathrm{CO_2}}$) as:

$$Sc_{liq} = \frac{\nu}{D_{\mathrm{X}}} = Sc_{\mathrm{CO_2}} \left( \frac{D_{\mathrm{CO_2}}}{D_{\mathrm{X}}} \right). \tag{3.25}$$

AIRSEA calculates $D_{\mathrm{CO_2}}/D_{\mathrm{X}}$ from the molar volumes at boiling point, using the proportionality of $D_{\mathrm{X}}$ to ${V_{\mathrm{X}}}^{0.6}$ as suggested by Wilke and Chang (1955):

$$\frac{D_{\mathrm{CO_2}}}{D_{\mathrm{X}}} = \left( \frac{V_{\mathrm{X}}}{V_{\mathrm{CO_2}}} \right)^{0.6}, \tag{3.26}$$

where $V_{\mathrm{X}}$ and $V_{\mathrm{CO_2}}$ are the molar volumes at boiling point of the tracer X and $CO_2$, respectively (Pozzer et al., 2006).

A gas is called liquid side controlled, when the water side resistance $R_w$ against air-sea gas exchange is much bigger than the gas phase side resistance $R_g$. For very soluble gases, the resistance on the gas phase side plays the key role, so the gas is gas phase side controlled. The gas phase side exchange velocity $K_g$ can be written as the reciprocal of two resistances on the gas phase side:

$$K_g = \frac{1}{R_a + R_{qbr}}, \tag{3.27}$$

with $R_a$ the aerodynamic resistance and $R_{qbr}$ the quasi-laminar boundary layer resistance. $R_a$ and $R_{qbr}$ are calculated following Kerkweg et al. (2006a) for consistency with the MESSy submodel DDEP (Pozzer et al., 2006).

## 3.6 Riverine nutrient input into the ocean

Import from rivers is a major source of nutrients in the coastal zone. Recent studies showed the effect of nutrient import on oceanic biogeochemistry (Cotrim da Cunha et al., 2007) and on the oceanic Si cycle (Bernard et al., 2010).

The MESSy submodel OTPHYSC calculates advection, convection, diffusion, and dilution of oceanic tracers using the same advection scheme as the dynamical ocean system. Nutrient import from rivers is considered in OTPHYSC and added to the molar concentration [X] of tracer X at the new time level $t + 1$ in the uppermost

ocean level:

$$[\mathrm{X}](x,y,t+1) = [\mathrm{X}](x,y,t) + \mathcal{D}(x,y,t) \times [\mathrm{X}]_{riv}(x,y,t) \times \frac{1}{V_{box}(x,y,t)} \times \Delta t, \quad (3.28)$$

with $[\mathrm{X}](x,y,t)$ the molar concentration of tracer X in the uppermost ocean level at time $t$ and location $(x,y)$ in $\mathrm{kmol\,m^{-3}}$. $\mathcal{D}$ is discharge in $\mathrm{m^3\,s^{-1}}$, $[\mathrm{X}]_{riv}$ the molar concentration of tracer X in the river—which generally can be variable in space and time—, $V_{box}$ the volume of the uppermost ocean grid box in $\mathrm{m^3}$, and $\Delta t$ the model time step in s.

Two different methods exist for determining molar concentrations of tracers in rivers in OTPHYSC, which can be selected via namelist parameters (see Appendix B for an example namelist). A globally constant molar concentration can be set by the user for each tracer individually, or an input field can be selected, which contains the molar concentration of a tracer in a global 2D-field. By using channel objects, provided by the generic MESSy submodel CHANNEL (see Section 2 of Jöckel et al., 2010), any field (represented on a 2D ocean grid) from other submodels can be used as riverine molar concentration. Both methods can be mixed for different tracers. A sensitivity study with globally constant molar concentrations in rivers comparable to Cotrim da Cunha et al. (2007) has been performed.

## 3.7 Aeolian dust input into the ocean

In open ocean regions dust deposition is the main input mechanism for iron (Martin et al., 1991; Jickells et al., 2005; Boyd et al., 2007). HAMOCC accounts for iron limitation of photosynthesis, iron release at remineralisation, and iron complexation by organic substances (Maier-Reimer et al., 2005). Iron uptake and release is represented using a constant Fe:P ratio $R_{\mathrm{Fe:P}}$. Iron complexation is taken into account using an iron relaxation with a relaxation time constant $\lambda_{\mathrm{Fe}}$ to iron concentrations of $0.6\,\mathrm{nmol\,l^{-1}}$. Any iron beyond this limit is assumed to be complexed and not bio-available (Maier-Reimer et al., 2005).

Dust in HAMOCC is considered to be chemically inert with its only sinks settling and sedimentation. Dust is assumed to have a constant particle size, and in that way has a constant sinking speed. Aggregation of dust is only considered with marine snow, after aggregation dust particles sink at the speed of marine snow (Kriest and Evans, 2000; Maier-Reimer et al., 2005).

In the upper ocean level dissolved iron is released from dust, this release happens immediately after deposition. A fixed mass fraction of iron in dust and a constant solubility are assumed (Maier-Reimer et al., 2005), the molar concentration of iron [Fe] at time $t+1$ can be written as:

$$[\mathrm{Fe}](x,y,t+1) = [\mathrm{Fe}](x,y,t) + \frac{F_{Dust}(x,y,t)}{\Delta z_{surf}} \frac{1}{M_{\mathrm{Fe}}} \frac{1}{3.1536 \times 10^7\,\mathrm{s\,a^{-1}}} \epsilon_{\mathrm{Fe}}\, S_{\mathrm{Fe}}\, \Delta t, \tag{3.29}$$

where $F_{Dust}$ is the dust deposition flux in $\mathrm{kg\,(m^2\,a)^{-1}}$, $\Delta z_{surf}$ the thickness of the ocean surface layer (in m), $\epsilon_{\mathrm{Fe}} = 0.035$ the mass fraction of iron in dust, $S_{\mathrm{Fe}} = 0.01$ the dimensionless iron solubility, and $\Delta t$ the time step (in s). Division by the molar mass of iron $M_{\mathrm{Fe}} = 55.85\,\mathrm{g\,mol^{-1}}$ and the constant $3.1536 \times 10^7\,\mathrm{s\,a^{-1}}$ result in an iron concentration in units of $\mathrm{kmol(Fe)\,m^{-3}}$.

Dust deposition is also a source of Si to the ocean. In the implementation of HAMOCC as MESSy submodel a $SiO_2$ import from dust deposition analogous to iron import in Equation 3.29 was added. In this study a constant mass fraction of $SiO_2$ in dust of $\epsilon_{\mathrm{SiO_2}} = 0.308$ and a solubility of $S_{\mathrm{SiO_2}} = 0.075$ are assumed (Cotrim da Cunha et al., 2007). Using the molar mass of $SiO_2$ of $M_{\mathrm{SiO_2}} = 60\,\mathrm{g\,mol^{-1}}$, the equation for molar concentration of $SiO_2$ [$SiO_2$] at time $t+1$ reads:

$$\begin{aligned}[\mathrm{SiO_2}](x,y,t+1) = {} & [\mathrm{SiO_2}](x,y,t) \\ & + \frac{F_{Dust}(x,y,t)}{\Delta z_{surf}} \frac{1}{M_{\mathrm{SiO_2}}} \frac{1}{3.1536 \times 10^7\,\mathrm{s\,a^{-1}}} \epsilon_{\mathrm{SiO_2}}\, S_{\mathrm{SiO_2}}\, \Delta t.\end{aligned} \tag{3.30}$$

The dust deposition flux at the ocean surface in HAMOCC is read from a file containing monthly mean values, or can be passed from the atmospheric domain to the ocean when coupling the models via Ocean Atmosphere Sea Ice Soil (OASIS) (Kloster et al., 2006). The HAMOCC implementation as MESSy submodel provides the possibility for the user to define any channel object provided by a submodel via CHANNEL as dust deposition flux field. Different parts of the total dust deposition flux are calculated in the different submodels in MESSy. Dry deposition fluxes and sedimentation fluxes are calculated by the submodels DDEP and SEDI, respectively, wet deposition fluxes by SCAV.

Mineral dust is represented in the M7 submodel as dust particles in Aitken and coarse mode, in each mode distinguished between soluble and insoluble particles. DDEP and SEDI calculate dry deposition and sedimentation fluxes for dust particles

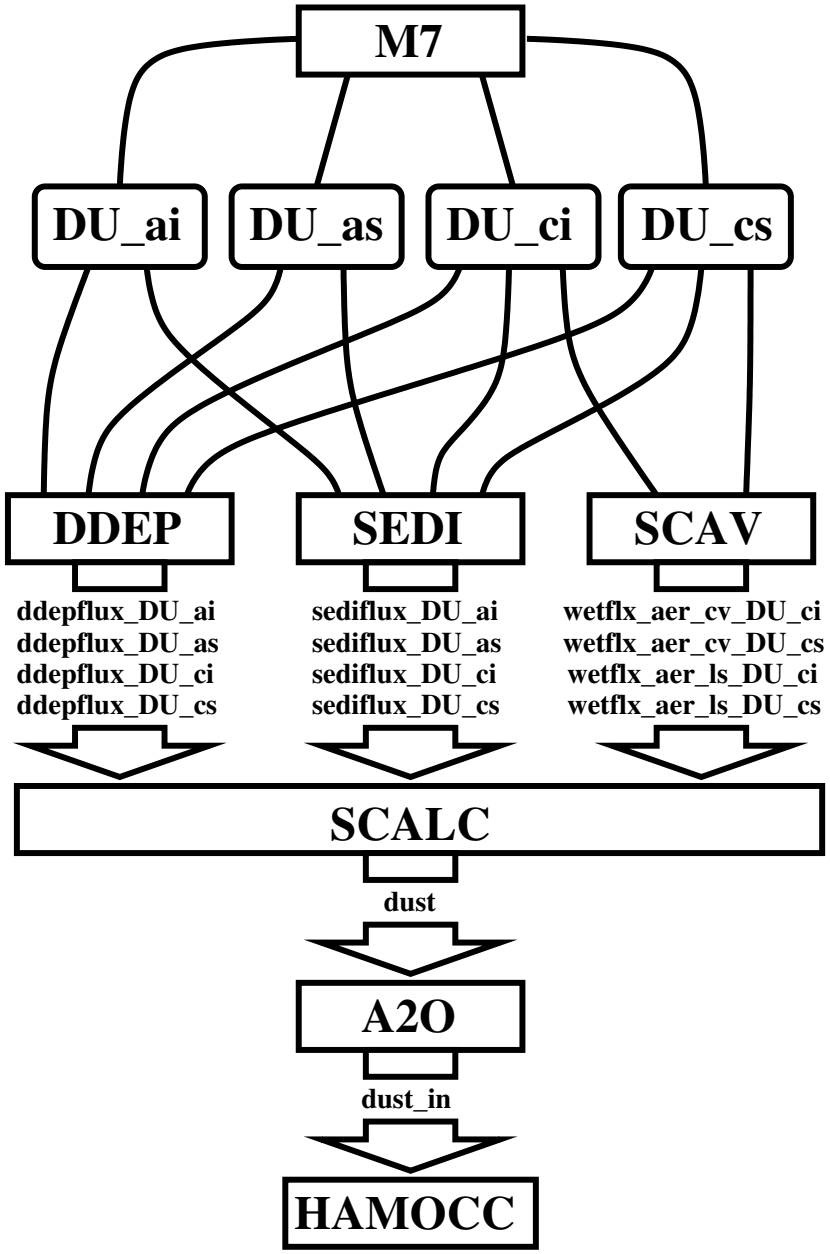


**Figure 3.2:** Flow chart of processing dust deposition fields in MESSy submodels. DDEP, SEDI, and SCAV calculate partial dust deposition fluxes of M7 dust particles (DU) in different deposition classes. Dust particles are divided in soluble particles in Aitken mode (as), insoluble particles in Aitken mode (ai), soluble particles in coarse mode (cs), and insoluble particles in coarse mode (ci). From these particle concentrations in the atmosphere, the partial deposition fluxes are calculated for the different particle classes in the submodels DDEP, SEDI, and SCAV. In SCAV, fluxes are partitioned in flux from convective precipitation (cv) and flux from large scale precipitation (ls). SCALC calculates the sum over the partial dust deposition flux fields and scales to the appropriate units, providing the result as channel object (dust). A2O performs a grid transformation to get a scaled total dust deposition field (dust_in) on the ocean model grid. Total dust deposition is used in HAMOCC as dust deposition input field.

in all modes, respectively. SCAV calculates wet deposition fluxes stemming from convective and large scale precipitation, in both cases coarse soluble and coarse insoluble dust particles are discriminated.

Figure 3.2 shows a flow chart of dust deposition flux fields between different MESSy submodels, to calculate total dust deposition. To collect the twelve partial dust deposition flux fields and to transfer them into units of $\mathrm{kg\,(m^2\,a)^{-1}}$, a new submodel SCALC was implemented for this study. SCALC performs simple calculations on any channel objects and provide the result as new channel object (see Appendix C for an example user interface namelist). For now arithmetic operations for summation and scaling are implemented, which is sufficient to calculate the total sum of the twelve partial dust deposition flux fields from DDEP, SEDI, and SCAV, scale them to the appropriate units, and provide the result as a new channel object (dust). This field is interpolated to the ocean grid by the submodel A2O, which in turn provides the transformed scaled total dust deposition as channel object (dust_in). The channel object of the transformed and scaled total dust deposition flux field is used in HAMOCC as source of dust deposition flux at the ocean surface.

Dust burden and dust deposition fluxes depend on dust emissions, which are simulated in a CCM by an emission scheme or prescribed by emission fields. In this study, prescribed dust deposition flux fields provided by HAMOCC as well as "online" calculated dust deposition fluxes are used. In the sensitivity study investigating the impact of interactive dust deposition, dust emissions are simulated using the dust emission scheme by Tegen et al. (2002), implemented in EMAC by Gläser et al. (2012).

## 3.8 Summary of the model system expansions

This section gives an overview of the extentions and developments in the coupled EMAC-MPIOM model system implemented in this study. An overview of the parts of the model system associated with biogenic oceanic emissions is presented in Fig. 3.3. Before the implementation of the AIRSEA submodel (Pozzer et al., 2006; Pozzer, 2007), the only way to include chemical interaction between the ocean and atmosphere in the model system was the specification of emissions at the lower boundary of the atmospheric domain (Fig. 3.3, left). These emissions are only in one direction, more precisely from the ocean into the atmosphere.

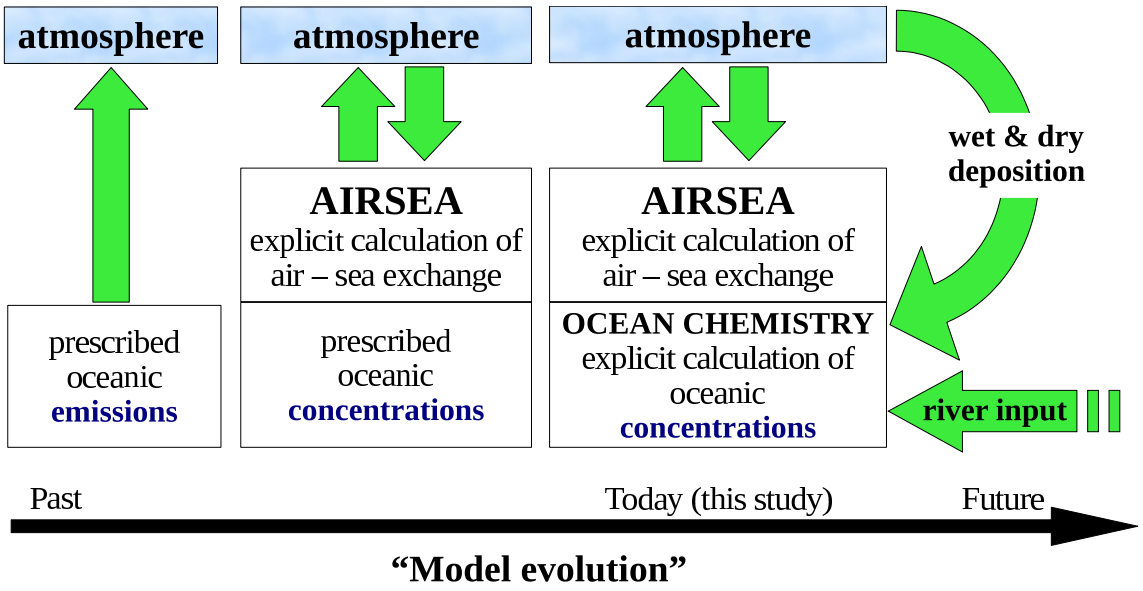


**Figure 3.3:** Evolution of the model system used in this study. From left to right three stages of the model system during its evolution are shown. The upper boxes depict the atmospheric model domain, the lower boxes the oceanic model domain. Arrows denote exchanges between the model domains. In the past (left), the model was an atmospheric model only. Biogenic oceanic emission had to be prescribed, only a gas exchange from the ocean into the atmosphere with related changes in concentrations in the atmosphere was possible. After the inclusion of the AIRSEA submodel (middle), gas exchange between ocean and atmosphere in both directions became possible. As the oceanic concentrations were prescribed, only atmospheric concentrations were subject to interactive change. In the present study (right), an interactive oceanic biogeochemistry has been included into the model system. Via the AIRSEA submodel gas exchange between ocean and atmosphere is calculated. Changes in concentrations via exchange of gaseous compounds are now possible in both model domains. Additional feedbacks have been included in the model system. Atmospheric dust and input of nutrients from rivers affect oceanic biogeochemistry and change oceanic concentrations. Changes in oceanic concentrations impact air-sea gas exchange and, hence, atmospheric concentrations.

With the inclusion of AIRSEA into the model system (Fig. 3.3, middle), air-sea gas exchange could be calculated "online" from prescribed oceanic concentrations and the actual (prescribed or interactive) concentrations in the atmospheric model domain. The calculated air-sea gas fluxes can be positive or negative, i.e. from the ocean into the atmosphere or from the atmosphere into the ocean. However, as the oceanic concentrations are prescribed, this kind of air-sea exchange only affects atmospheric concentrations. EMAC can in both cases be used in configurations as "atmosphere only" model or coupled to an interactive dynamical ocean.

In this study, the model system is extended to include interactive calculations of the oceanic biogeochemistry (Fig. 3.3, right). The oceanic biogeochemistry determines oceanic concentrations, and from these AIRSEA calculates the actual air-sea gas exchange. These air-sea gas fluxes are used to update atmospheric and oceanic concentrations, respectively.

Further feedback mechanisms are included in this model system configuration, stemming from dry and wet deposition from the atmosphere and from input of chemical compounds from rivers, which both eventually alter oceanic biogeochemistry and, hence, oceanic tracer concentrations. For the calculation of oceanic biogeochemistry, the model system has to be used in a configuration with a coupled dynamical ocean model, as the biogeochemistry is also affected by ocean dynamics.

The extensions of the model system implemented in this study base upon the coupled AO-GCM EMAC-MPIOM (Pozzer et al., 2011). The major expansion of the model system is the inclusion of oceanic biogeochemistry. The novel developed submodel is an implementation of HAMOCC (Maier-Reimer et al., 2005; Wetzel et al., 2005) conform to the MESSy interface (Jöckel et al., 2005, 2010). An overview of the biogeochemical processes in HAMOCC and the implementation of HAMOCC as MESSy submodel can be found in Sections 2.3 and 3.3, respectively. The submodel provides an extended interface for user defined values of the variables used in the oceanic biogeochemistry module. Appendix A lists the variables controllable in this submodel by the user. The user interface is provided via the mechanism of standard FORTRAN namelists in accordance with the MESSy standard. A commented example of such a namelist is shown in Appendix A.

The submodel OTPHYSC, which couples the tracer fields of the oceanic biogeochemistry to the oceanic dynamics provided by the MPIOM submodel, was extended to update oceanic biogeochemical tracers with fluxes of theses tracers from riverine origin. For the calculation of tracer fluxes from river input into the ocean, constant molar concentrations for all rivers, 2D fields of molar concentrations, or a combination of both for different tracers can be chosen. The input source for freshwater fluxes needed for the calculation can be chosen via the user interface. In the coupled model system EMAC-MPIOM-HAMOCC used in this study, the calculated freshwater fluxes from the HD submodel have been used. An overview of the inclusion of nutrient import from rivers to the ocean model is presented in Section 3.6. A commented example of the user interface namelist of the OTPHYSC submodel is included in Appendix B. The HD submodel has been updated to a more recent version as used in ECHAM6 (Stevens et al., 2013).

For “online” coupling of the deposition of atmospheric mineral dust to the oceanic biogeochemistry, the new MESSy submodel SCALC has been developed. This submodel provides the possibility to perform simple calculations on arbitrary channel objects as provided by the MESSy generic submodel CHANNEL. For this study summation and scaling of fields have been implemented. The technical implementation of the interplay between the atmospheric dust deposition and the oceanic biogeochemistry is shown in Section 3.7. A schematic overview of the interaction of SCALC, as used in this study’s model setup, with other submodels is presented in Fig 3.2. A commented example of the user interface namelist can be found in Appendix C.

# Chapter 4

# Investigation of the chemical coupling mechanisms between ocean and atmosphere

The chemical feedback mechanisms between ocean and atmosphere are analysed next by conducting sensitivity studies. Sensitivity analyses can be performed in different ways by changing model parameters or using different input data or boundary conditions. The impact of changes in model parameters and input data on the simulation results can be determined in two ways. Either in simulation experiments with only one changed parameter, or in experiments with multiple changed parameters, to assess the impact of individual processes or a combination of them, respectively. During a sensitivity analysis of a model system multiple sensitivity studies can be performed, depending on the complexity of the model system and the questions to be answered by this analysis. Common questions to be answered with sensitivity studies are about the robustness of the model system under uncertain conditions, sensitive and important model variables, changes under different assumptions, the relationship between input and output variables, finding model errors, or model calibration (see Pannell, 1997, for an overview[1]).

In this study, sensitivity experiments are used to test the novel model system for validity and robustness. Furthermore, the response of the model system's atmospheric domain on changed input data, in form of changed chemical fluxes at the ocean interface, is assessed.

[1] available via `http://dpannell.fnas.uwa.edu.au/dpap971f.htm` (last accessed: 06.07.2013)

## 4.1 Methodology

To analyse the impact of oceanic emissions on atmospheric chemistry in the coastal and marine boundary layer, the free troposphere, and the stratosphere, numerical sensitivity experiments with the ECHAM/MESSy Atmospheric Chemistry (EMAC; Jöckel et al., 2005, 2006, 2010) model coupled to the Max Planck Institute Ocean Model (MPIOM; Marsland et al., 2003; Jungclaus et al., 2006) and the HAMburg Ocean Carbon Cycle model (HAMOCC; Six and Maier-Reimer, 1996; Maier-Reimer et al., 2005; Wetzel et al., 2005) were performed. All model simulations have been "year-2000 time-slice" experiments. In the "time-slice" setup, climatic forcings from boundary conditions, such as emissions of radiatively active substances and their precursors, have been prescribed from a dataset for the specific time interval and have been perpetually repeated throughout the simulation. In case of "year-2000 time-slices", the boundary conditions are representative for the year 2000 and recurrent for every simulated year. To exclude the influence of inter-annual changes in the solar cycle on the simulations, a constant medium solar activity has been set up.

In Figure 4.1 an overview of all simulations performed in this study is given. To provide a realistic state of the upper ocean layers as initial condition for the subsequent simulations with the fully coupled atmosphere-ocean chemistry climate model (AO-CCM), a simulation with the coupled atmosphere-ocean general circulation model (AO-GCM) EMAC-MPIOM over 100 simulation years was performed. Bearing in mind, that with a simulation time of 100 years the model is not able to dynamically equilibrate the complete deep circulation in the ocean, yet a realistic upper ocean circulation, suitable for short term simulation experiments, has been reached. This dynamical spin-up phase was followed by a simulation of 30 years with additional oceanic biogeochemistry to equilibrate air-sea gas fluxes. All subsequent sensitivity experiments were initialised from this spin-up simulation. From the seven years simulation time of the sensitivity experiments, the last five years are used for evaluation.

Identifying changes in atmospheric chemical composition stemming from altered emissions between two sensitivity experiments is challenging, as intrinsic variability is able to obscure small perturbations. It is therefore advantageous to suppress feedbacks of changed atmospheric composition on atmospheric dynamics, to obtain the identical meteorological situation in all sensitivity studies. This is achieved using the Quasi Chemistry-Transport Model (QCTM) mode (Deckert et al., 2011; Section 3.2) in the sensitivity experiments. Suppressing the noise introduced by feedbacks of

the chemical composition on the model system's meteorological state, identification of small signals, caused by changes between the sensitivity experiments, with statistical tools is possible using shorter simulation times.

In order to decouple atmospheric composition and chemistry from atmospheric dynamics, a preparatory simulation (PREP) was performed with the fully coupled AO-CCM, including atmospheric chemistry and oceanic biogeochemistry. In this simulation, oceanic concentrations of isoprene ($C_5H_8$) and dimethyl sulphide ($(CH_3)_2S$, DMS) have been prescribed. An under-saturation of oceanic methanol ($CH_3OH$) concentrations, with values of 94 % with respect to atmospheric concentrations, has been used (Singh et al., 2003; Pozzer, 2007). Biogenic oceanic emissions of carbon monoxide (CO) have been prescribed from the Global Emissions InitiAtive (GEIA) database (Guenther et al., 1995)[2] as described by Jöckel et al. (2006). Air-sea gas exchange has been calculated from the prescribed oceanic concentrations via the AIRSEA submodel (Pozzer et al., 2006).

From the simulation PREP, monthly mean distributions of the atmospheric radiatively active tracer fields and the distribution of total nitric acid ($HNO_3$), influencing the polar stratospheric cloud (PSC) related effects of sedimentation, dehydration, and denitrification, were written out. These tracer fields have been used as input fields for the subsequent simulations BASE, SOCX, SRFIX, and SDUST in QCTM mode.

The radiative active fields provided from the simulation PREP have been carbon dioxide ($CO_2$), methane ($CH_4$), ozone ($O_3$), nitrous oxide ($N_2O$), $CCl_3F$ (trichlorofluoromethane, CFC-11), and $CCl_2F_2$ (dichlorodifluoromethane, CFC-12). These offline provided fields have been used to calculate the atmospheric radiative transfer in the RAD4ALL (implementation of the ECHAM5 radiation scheme as MESSy submodel; Roeckner et al., 2006; Jöckel et al., 2006) submodel. The field of total $HNO_3$ obtained from the simulation PREP has been used as input field for the submodel MSBM (multi-phase stratospheric box model; Jöckel et al., 2010). From this input field, water vapour tendencies, particle radii, and the thermodynamic phase of PSCs have been calculated. Dehydration and denitrification due to sedimentation of ice particles and sedimentation of nitric acid trihydrate (NAT) particles, respectively, have also been accounted for (see Section 3.2 and Deckert et al. (2011) for details on the QCTM mode).

[2] `http://www.geiacenter.org/` (last accessed: 08.07.2013)

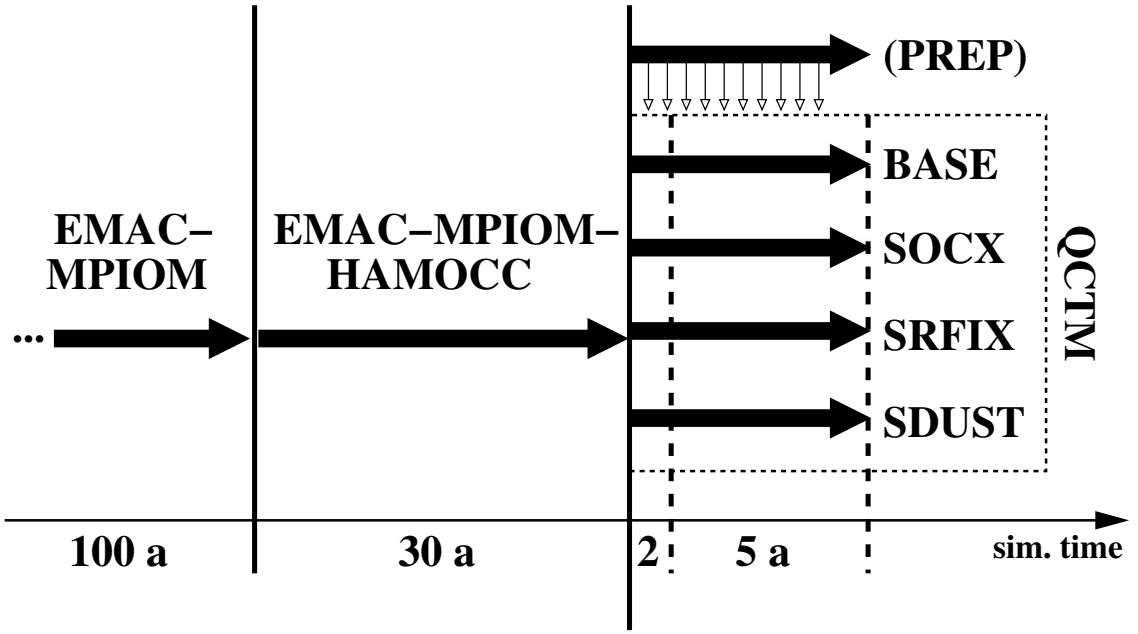


**Figure 4.1:** Overview of model simulations performed for this study. The horizontal axis denotes simulation time. A 100-year dynamical simulation with the coupled model system EMAC-MPIOM was performed as spin-up for ocean dynamics to achieve a realistic upper ocean state. From this simulation a 30-year simulation including the submodel HAMOCC for oceanic biogeochemistry was performed to reach realistic chemical surface water concentrations. The preparatory simulation (PREP), the baseline simulation (BASE), and the three sensitivity studies (SOCX, SRFIX, SDUST) have been initialised from the coupled EMAC-MPIOM-HAMOCC simulation. PREP provides fields for atmospheric chemical tracer distribution for the model simulations in QCTM mode (denoted by small open arrows). The simulated time for BASE, SOCX, SRFIX, and SDUST is seven years, the last five years of the simulations are analysed in this study. For more details see the text and Table 4.1.

An overview of all simulations performed and the differences in the model setups between the sensitivity experiments are listed in Table 4.1. Tracer fields used in the radiation transfer calculation (submodel RAD4ALL) and the PSC calculation (submodel MSBM) have been provided for all sensitivity experiments from monthly mean fields derived from PREP. In all simulations, the model time step in the atmospheric part has been 720 s, the oceanic model time step has been 2 h. The time step for coupling between ocean and atmosphere has been 2 h, to account for diurnal variations in forcing fields between the two domains.

| simulation | properties |
|---|---|
| PREP | • fully coupled, year-2000 time-slice, air-sea gas exchange from AIRSEA |
| | • prescribed oceanic concentrations of $C_5H_8$, DMS and oceanic emission of CO |
| | • saturation coefficient for oceanic concentration of $CH_3OH$[a] |
| | • no riverine nutrient import |
| | • constant aeolian import of Fe and Si from climatological dust deposition map |
| BASE | • QCTM, year-2000 time-slice, air-sea gas exchange from AIRSEA |
| | • prescribed oceanic concentrations of $C_5H_8$, DMS and oceanic emission of CO |
| | • saturation coefficient for oceanic concentration of $CH_3OH$[a] |
| | • no riverine nutrient import |
| | • constant import of aeolian Fe and Si from climatological dust deposition map |
| SOCX | • QCTM, year-2000 time-slice, air-sea gas exchange from AIRSEA |
| | • **online oceanic concentrations of $C_5H_8$, DMS, CO, $N_2O$, $CO_2$, $O_2$, $N_2$** |
| | • saturation coefficient for oceanic concentration of $CH_3OH$[a] |
| | • no riverine nutrient import |
| | • constant import of aeolian Fe and Si from climatological dust deposition map |
| SRFIX | • QCTM, year-2000 time-slice, air-sea gas exchange from AIRSEA |
| | • online oceanic concentrations of $C_5H_8$, DMS, CO, $N_2O$, $CO_2$, $O_2$, $N_2$ |
| | • saturation coefficient for oceanic concentration of $CH_3OH$[a] |
| | • **constant riverine nutrient import of Fe, Si, $CO_2$, $N_2$** |
| | • constant import of aeolian Fe and Si from climatological dust deposition map |
| SDUST | • QCTM, year-2000 time-slice, air-sea gas exchange from AIRSEA |
| | • online oceanic concentrations of $C_5H_8$, DMS, CO, $N_2O$, $CO_2$, $O_2$, $N_2$ |
| | • saturation coefficient for oceanic concentration of $CH_3OH$[a] |
| | • no riverine nutrient import |
| | • **import of aeolian Fe and Si from online dust deposition** |

[a] see Chapter 3.5, Singh et al. (2003), Pozzer (2007).

**Table 4.1:** Overview of sensitivity experiments. Differences of the sensitivity experiments SOCX vs. BASE, and the sensitivity experiments SRFIX and SDUST vs. SOCX are typeset in bold.

For the baseline experiment (BASE) a simulation was performed with the AO-CCM in QCTM mode and oceanic emissions calculated as described for the preparatory simulation (PREP).

In the first sensitivity experiment the impact of air-sea gas exchange on the atmospheric composition is evaluated (SOCX). For this experiment the same AO-CCM as in the baseline case was run for seven years, replacing the prescribed oceanic concentration for $C_5H_8$ and DMS with interactively calculated oceanic concentrations for this chemicals from the HAMOCC submodel. Furthermore, prescribed oceanic biogenic CO emissions have been replaced by air-sea gas exchange calculated via the AIRSEA submodel, using the oceanic CO concentrations interactively simulated by the HAMOCC submodel. In addition, air-sea gas exchange has been calculated from online oceanic concentrations of $CO_2$, $N_2O$, oxygen ($O_2$), and nitrogen ($N_2$), all provided from the submodel HAMOCC. Whereas $O_2$ and $N_2$ have been assumed to be fixed in the atmospheric chemistry module MECCA (Module Efficiently Calculating the Chemistry of the Atmosphere; Sander et al., 2005, 2011), emissions of $C_5H_8$, DMS, and CO did impact atmospheric concentrations.

$CO_2$ and $N_2O$ are radiatively active gases, but do not affect tropospheric chemistry directly. The stratospheric chemistry is affected by $N_2O$ as source of nitric oxide (NO) by reaction with the electronically excited oxygen atom ($O(^1D)$; Reaction R 2.40a). As the focus of this study is on changes in the tropospheric chemical composition on short time-scales in the order of years, and since all sensitivity experiments were performed with atmospheric dynamics decoupled from the chemical composition, atmospheric mixing ratios of $CO_2$ and $N_2O$ have been prescribed by a relaxation method via the submodel TNUDGE (Tracer NUDG(E)ing; Kerkweg et al., 2006b) with a time constant of 10 800 s. In this way, air-sea gas fluxes of $CO_2$ and $N_2O$ could be assessed as diagnostic quantities without any impact on atmospheric chemical composition from the calculated fluxes.

To evaluate the impact of nutrient import from rivers on air-sea gas exchange and atmospheric composition, the sensitivity SRFIX has been performed. In this sensitivity study, globally constant concentrations of tracers per volume of riverine freshwater input to the ocean have been assumed. Freshwater fluxes from rivers have been calculated interactively by the HD (Hydrological Discharge; Hagemann and Dümenil, 1998) submodel.

With the last sensitivity experiment the impact of aeolian nutrient import to the ocean, in form of iron (Fe) and silicon (Si) from dust deposition (see Section 3.7), on air-sea gas exchange and atmospheric composition is evaluated (SDUST). In this

simulation the aerosol submodel M7 (Vignati et al., 2004; Kerkweg et al., 2008) and the dust emission scheme of Tegen et al. (2002) implemented in EMAC by Gläser et al. (2012) into the submodel ONEMIS (ONline tracer EMISsions; Kerkweg et al., 2006b) have been included. A new submodel SCALC (Simple CALCulations) was implemented as part of the present study to provide an accumulated dust deposition source consisting of the fractions of dust deposition from dry deposition (calculated by the submodel DDEP, Dry DEPosition; Kerkweg et al., 2006a), scavenging (calculated by SCAV, SCAVenging; Tost et al., 2006a), and sedimentation (calculated by SEDI, SEDImentation; Kerkweg et al., 2006a) to the oceanic biogeochemistry model (see Section 3.7). Total dust deposition fluxes from the submodel SCALC—averaged over the coupling time step between ocean and atmosphere—have been passed over to HAMOCC instead of the climatological map of dust deposition fluxes (Timmreck and Schulz, 2004; Maier-Reimer et al., 2005), allowing for a variable dust deposition, according to the meteorological situation in the model. Furthermore, by including the calculation of dust import to the ocean from dust deposition fluxes in the atmospheric model domain, the model system obtains a more consistent representation of processes and accounts for additional potentially important feedback mechanisms between ocean and atmosphere.

The remainder of this Chapter is organised as follows: In Section 4.2 the impact of interactive oceanic biogeochemistry and air-sea gas exchange in the model system is presented. Section 4.3 focuses on the impact of nutrient input to the ocean from rivers and the related changes in oceanic biogeochemistry, air-sea gas exchange, and atmospheric composition. The impact of nutrient input to the ocean from deposition of aeolian mineral aerosol (dust) is investigated in Section 4.4.

## 4.2 Gas exchange between ocean and atmosphere

Oceanic emissions can be provided to the atmospheric domain of the model system in two different ways. On one hand, emissions can be prescribed “offline” as fluxes at the lower atmospheric boundary by emission datasets. On the other hand, emissions from the ocean can be calculated “online” from atmospheric concentrations, oceanic concentrations, and the meteorological situation via the AIRSEA submodel.

For the online calculation, until now, the oceanic surface water concentrations had to be provided by "offline" datasets, for example from climatologies. The implementation of HAMOCC as MESSy submodel provides the ability to calculate oceanic chemical concentrations "online" and use these tracer fields for the calculation of air-sea gas exchange.

To provide realistic input fields of oceanic chemical composition to the AIRSEA submodel, the oceanic biogeochemistry has to simulate the oceanic biogeochemical cycles in a realistic way. A thorough evaluation of the latest version of HAMOCC, which is comparable to the implementation of the oceanic biogeochemical cycle as used in this study, can be found in Ilyina et al. (2013). Here, only a short analysis of surface water concentrations of the most important oceanic tracers is presented, as these determine the air-sea gas exchange, and thus influence atmospheric chemical composition.

### 4.2.1 Evaluation of the oceanic biogeochemistry

A realistic representation of physical processes in the ocean model is important to simulate realistic oceanic biogeochemistry (Doney et al., 2004). Feedbacks of the oceanic biogeochemistry on physical ocean processes via absorption of solar radiation by phytoplankton is switched off in all sensitivity experiments, to simulate identical ocean circulation, and hence temperature and salinity distributions in the ocean (comparable to the QCTM mode in the atmosphere). Figure 4.2 shows a Taylor diagram (Taylor, 2001) providing a statistical summary of how well simulated sea surface temperature (SST), sea surface salinity (SSS), surface ocean phosphate ($PO_4$) and silicate ($Si(OH)_4$) concentrations, and net primary production (NPP) in the water column are represented in the model system (sensitivity experiment SOCX) compared to observation based estimates from the World Ocean Atlas (WOA; Locarnini et al., 2010; Antonov et al., 2010; Garcia et al., 2010)[3] and the Carbon-based Productivity Model (CbPM; Behrenfeld et al., 2005; Westberry et al., 2008)[4]. The Taylor diagram in Fig 4.2 shows the spatial area weighted correlation $R$ between the simulated quantity $f$ and the observation based estimate $r$ for $N$ cells of the

[3] data available from `http://www.nodc.noaa.gov/OC5/WOA09/pr_woa09.html` (last accessed 13.08.2013)

[4] data available from `http://www.science.oregonstate.edu/ocean.productivity/` (last accessed 13.08.2013)

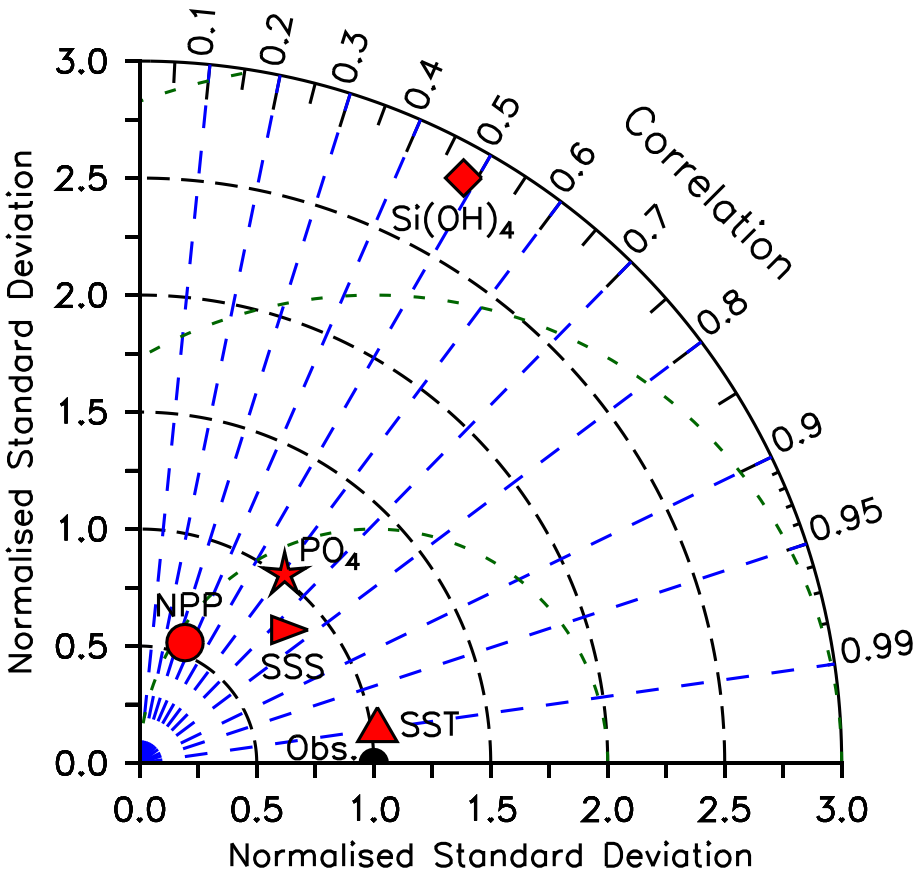


**Figure 4.2:** Taylor diagram of area-weighted pattern statistics of annual mean surface fields between model simulation SOCX (over five years) and observation based estimates. Shown are the Pearson's correlation coefficient $R$ between model simulations and observations (Obs.), and the standard deviation of model simulations normalised with respect to the standard deviation of observations $\hat{\sigma}_f = \sigma_f/\sigma_r$. Symbols denote SST, SSS, surface phosphate concentrations ($PO_4$), surface silicate concentrations ($Si(OH)_4$) and water column NPP. Estimates for SST, SSS, $Si(OH)_4$ and $PO_4^{3-}$ are from WOA, NPP is calculated from SeaWiFS data with the CbPM model. The black dot represents the observation based estimates. Dashed green contours denote the root mean square error normalised with respect to the observed standard deviation with an interval of 1 between contour lines.

model grid, with associated means $\overline{f}$ and $\overline{r}$, respectively:

$$R = \frac{\frac{1}{N}\sum_{n=1}^{N} w_n'^2 (f_n - \overline{f})(r_n - \overline{r})}{\sigma_f \sigma_r}. \tag{4.1}$$

The weighting coefficients are defined as:

$$w'_n = \frac{A_n}{\sum_{n=1}^{N} A_n}, \tag{4.2}$$

where $A_n$ is the area of the respective grid cell. Standard deviations of simulated values $\sigma_f$ and of the observation based values $\sigma_r$ are:

$$\sigma_f = \sqrt{\frac{1}{N}\sum_{n=1}^{N} w'_n (f_n - \overline{f})^2}, \tag{4.3}$$

$$\sigma_r = \sqrt{\frac{1}{N}\sum_{n=1}^{N} w'_n (r_n - \overline{r})^2}. \tag{4.4}$$

$$\tag{4.5}$$

The normalised standard deviation of simulated values with respect to observation based estimates, as used in the Taylor diagram is defined as:

$$\hat{\sigma}_f = \frac{\sigma_f}{\sigma_r}. \tag{4.6}$$

In the Taylor diagram observations are located at $\hat{\sigma}_f = 1$, $R = 1$.

### Sea surface temperature (SST)

The annual mean spatial variability and distribution of the SST is realistically represented in the model system compared to the WOA data (Locarnini et al., 2010). With a correlation coefficient $R = 0.99$ and a standard deviation of the model normalised with respect to the standard deviation of the WOA reference of $\hat{\sigma}_f = \sigma_f/\sigma_r = 1.025$, the simulated SSTs are close to the observed (Fig. 4.2). This can also be seen in the global map of simulated SSTs and the differences in SST between the model system and WOA estimates in Figure 4.3.

Whereas in large parts of the ocean the differences in SST between the simulation and the WOA analysis are below 1 K, regionally stronger deviations exist. The spatial deviation patterns in SST are comparable to the results found by Pozzer et al. (2011), comparing the physically coupled AO-GCM EMAC-MPIOM to AMIP II (Atmospheric Model Intercomparison Project; Taylor et al., 2000; Hurrell et al., 2008) data, and the results obtained by Jungclaus et al. (2006) with the coupled ECHAM5-MPIOM model system. The results are also in line with simulation studies by Assmann et al. (2010) and Tjiputra et al. (2013), who used the isopycnal

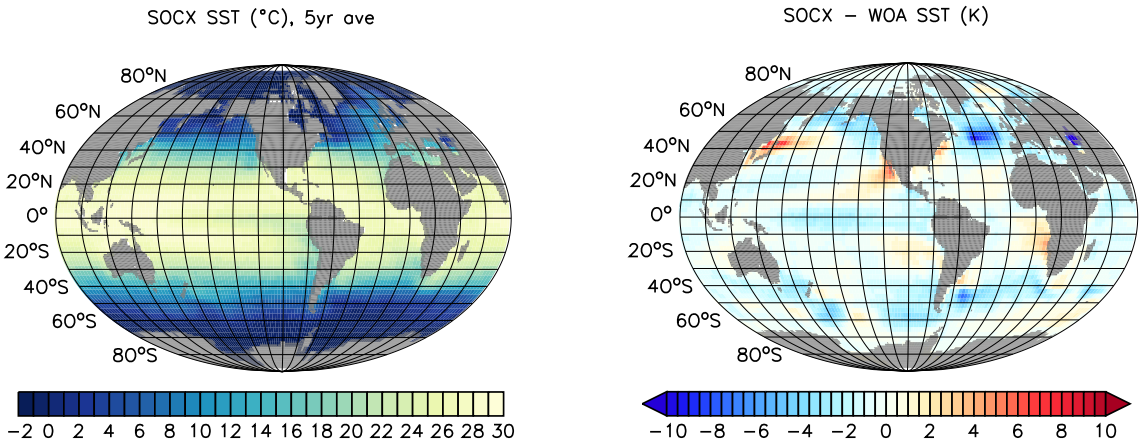


**(a)** sea surface temperature (SOCX)

**(b)** sea surface temperature difference (SOCX - WOA)

**Figure 4.3:** (a) Averages of SST in °C over five years in the simulation SOCX. (b) Differences in SST between the 5-year average in SOCX and the climatology from WOA in K.

ocean model Miami Isopycnic Coordinate Model (MICOM; Bleck and Smith, 1990; Bleck et al., 1992) forced by National Centers for Environmental Prediction (NCEP) reanalysis (Kalnay et al., 1996) data, and coupled to a modified version of the Community Atmosphere Model (CAM4; Neale et al., 2013; Kirkevåg et al., 2013), respectively.

The cold bias in the North Atlantic was identified to be caused by a deviation in the path of the North Atlantic Current (Marsland et al., 2003; Jungclaus et al., 2006; Assmann et al., 2010). A similar effect can be observed in the Kuroshio region, leading to higher SSTs in the simulation (Jungclaus et al., 2006) compared to observations. These deviations of the simulated circulation patterns are common to ocean models of comparable resolution (Assmann et al., 2010).

Too high SSTs compared to observations at the western coasts of Africa and the Americas, as found in this study, have also been previously observed in model simulations. These deviations can be explained by an underestimation of stratocumulus clouds (Jungclaus et al., 2006; Pozzer et al., 2011) and too weak coastal upwelling (Assmann et al., 2010; Pozzer et al., 2011) in these regions in the model system.

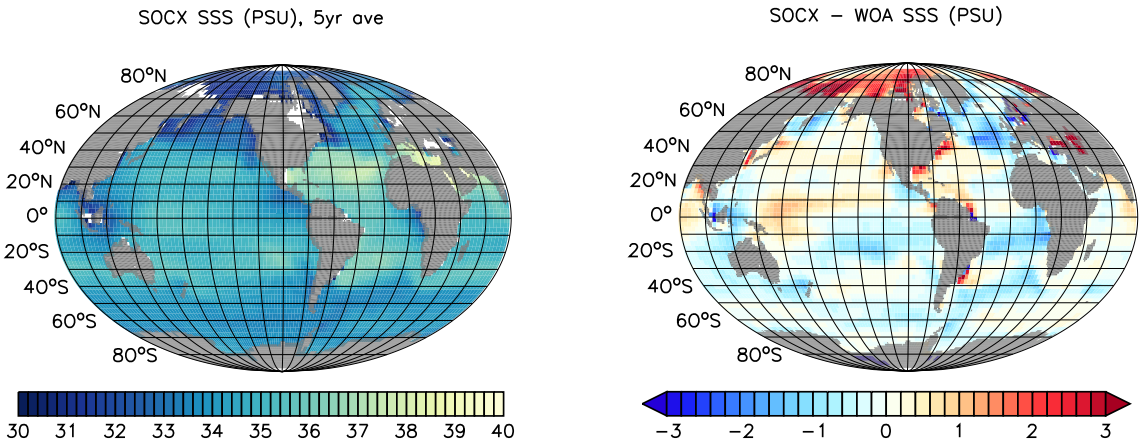


**(a)** sea surface salinity (SOCX)

**(b)** sea surface salinity difference (SOCX - WOA)

**Figure 4.4:** (a) 5-year averages of SSS in PSU obtained in the simulation SOCX. (b) Differences in SSS between the 5-year average in SOCX and the climatology from WOA in PSU.

### Sea surface salinity (SSS)

The spatial distribution of SSS is less well represented in the model system as the SST, yielding a spatial correlation with WOA observations (Antonov et al., 2010) of $R = 0.748$ and a simulated standard deviation normalised with respect to the observed standard deviation of $\hat{\sigma}_f = 0.858$ (Fig. 4.2). This deviation in model simulations is well known and attributed to deficiencies in the simulated hydrological cycle of the atmospheric (sub-)model (Schneider et al., 2007, 2008). The spatial distribution of simulated SSS is shown in Figure 4.4 (a), the differences of SSS between the model system and estimates from WOA (Antonov et al., 2010) are presented in Figure 4.4 (b). The deviation of the global mean SSS in the model system compared to observations is $-0.03$ PSU (Practical Salinity Units)[5]. The spatial distribution reveals small, predominantly negative, deviations in the simulation throughout the Southern Hemisphere and overestimates in the Northern Hemisphere Pacific and Indic. Stronger positive deviations in simulated SSS can be found in the Kuroshio region and at the western coast of North America. A strong negative bias is simulated in the Atlantic north of 40 °N. These patterns are similar to those found in comparison of the simulated SST with WOA data, associated with displaced circulation paths

[5] Practical Salinity $S$ is defined in terms of $K_{15}$, the ratio of conductivity of a seawater sample to the conductivity of a potassium chloride (KCl) solution with a mass fraction of $32.4356 \times 10^{-3}$ measured at 15 °C and 1013.25 hPa, as: $S = 0.0080 - 0.1692\,K_{15}^{1/2} + 25.3851\,K_{15} + 14.0941\,K_{15}^{3/2} - 7.0261\,K_{15}^{2} + 2.7081\,K_{15}^{5/2}, 2 \leq S \leq 42$. $K_{15} = 1$ corresponds to 35 PSU (Dauphinée et al., 1981).

in coarse resolution global ocean models (Marsland et al., 2003; Jungclaus et al., 2006; Assmann et al., 2010). Furthermore the model overestimates SSS in the Arctic by up to 3 PSU, with an even higher overestimation at the Siberian coast. The too high SSS in the Artic region is related to deficiencies in the representation of the Arctic large scale freshwater cycle (Serreze et al., 2006), due to the model's inability to adequately represent the freshwater import from the Pacific through the Bering Strait and the freshwater export through the Canadian Archipelago because of the coarse resolution. However, these model results are in line with earlier simulations of different model systems (Marsland et al., 2003; Tjiputra et al., 2013).

### Net primary production (NPP) and export production (EP)

Oceanic biogeochemistry largely depends on its biological component phytoplankton. Simulated phytoplankton concentrations are determined by production and decay calculated in the biogeochemical submodel. Phytoplankton production by photosynthesis is expressed in terms of Michael-Menten kinetics and includes limitations by available nutrients, light, and temperature (for details, see Section 3.3).

At each coupling time step the total solar irradiance at the ocean's surface, averaged over the time span between the last and the current coupling time step (two hours in the present study), is passed to the oceanic model domain. From the total solar irradiance at a certain location, the available irradiance at all ocean depths can be calculated (Eq. 3.3). The light limitation of the phytoplankton growth rate is then calculated via the product of photosynthetically available radiation (PAR) and the slope of the P-I-curve (production versus light intensity, Eq. 3.4). The initial slope of the P-I-curve $\alpha_{PI}$ is a model parameter in the biogeochemistry code, whose value can be defined by the user at runtime (Appendix A). To keep the changes in the model code as small as possible, in this study, the slope of the P-I-curve has been the only model parameter changed in the submodel compared to the original HAMOCC code (Appendix A lists an overview of all parameters used in the HAMOCC submodel in this study).

For the irradiation at the ocean's surface the value passed every two hours from the atmosphere to the ocean domain is used. In the original HAMOCC code, however, daily averages of the total irradiation are expected. Consequently, the initial slope of the P-I-curve in this study was lowered from the original value of $\alpha_{PI} = 0.02\,\mathrm{d}^{-1}\,(\mathrm{W\,m}^{-2})^{-1}$ to $\alpha_{PI} = 0.008\,\mathrm{d}^{-1}\,(\mathrm{W\,m}^{-2})^{-1}$. This value has been derived by performing several test simulations with different values for $\alpha_{PI}$, aiming at

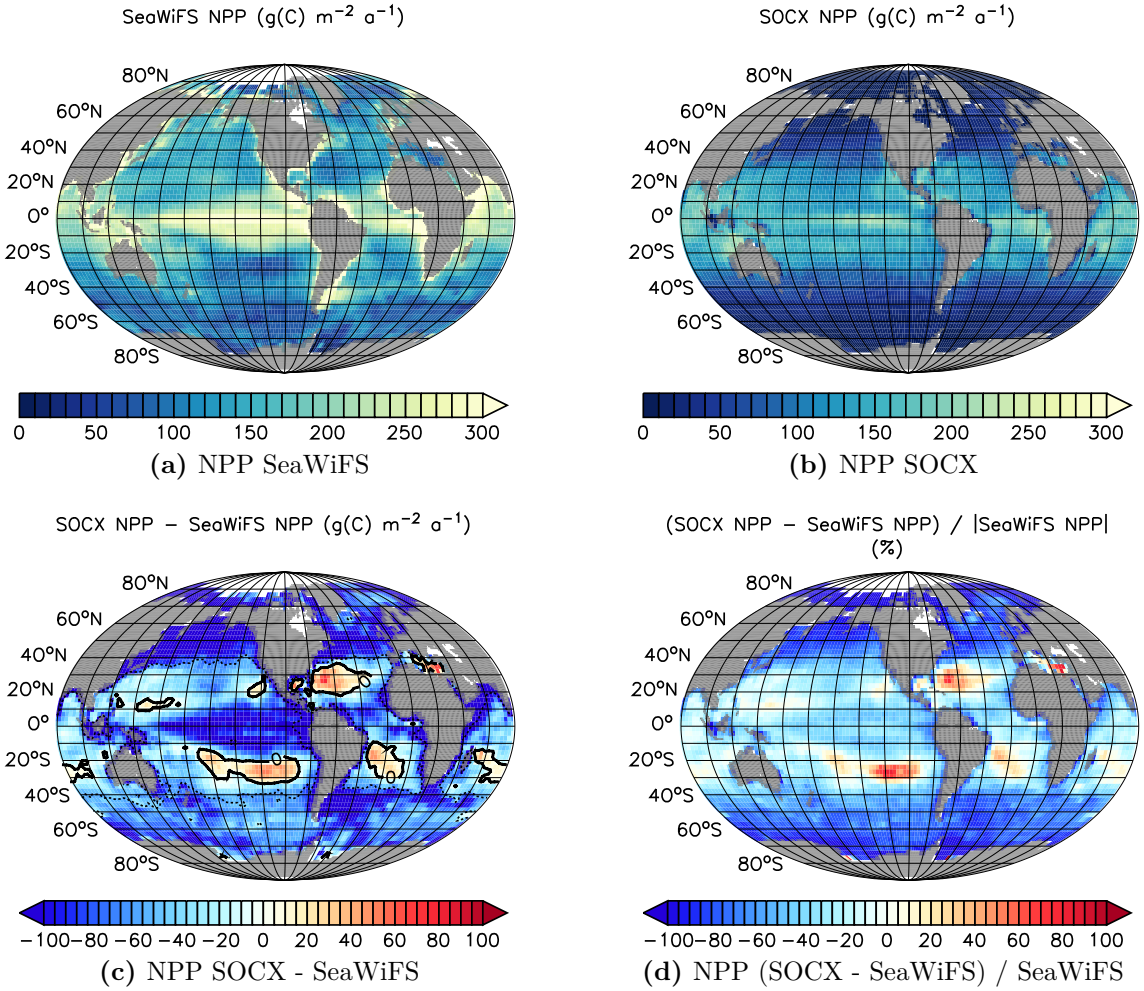


**Figure 4.5:** Averages of water column NPP in g(C) m$^{-2}$ a$^{-1}$ from (a) SeaWiFS data calculated with CbPM for 1998 to 2002 and (b) in SOCX for five years of simulation. (c) absolute difference and (d) relative difference in water column NPP between SOCX and SeaWiFS in g(C) m$^{-2}$ a$^{-1}$ and %, respectively. Contours denote relative differences. The broken contour indicates −50 %, the interval between solid contour lines is 100 %.

achieving a primary production from photosynthesis, which is comparable to values from the literature, and likewise a reasonable export production. The finally chosen value of $\alpha_{PI} = 0.008\,\mathrm{d}^{-1}\,(\mathrm{W\,m}^{-2})^{-1}$ yields an average NPP of 36.3 Pg(C) a$^{-1}$.

The annual mean net primary production (NPP) integrated over the water column calculated from ocean colour retrievals of the Sea-viewing Wide Field-of-view Sensor (SeaWiFS; O'Reilly et al., 1998) with the Carbon-based Productivity Model (CbPM; Behrenfeld et al., 2005; Westberry et al., 2008) and simulated in the SOCX sensitivity simulation are presented in Figures 4.5 (a) and 4.5 (b), respectively.

The simulated global NPP from photosynthesis in SOCX of $(36.3 \pm 5.8)\,\mathrm{Pg(C)\,a^{-1}}$ is at the lower end of the range from $33\,\mathrm{Pg(C)\,a^{-1}}$ to $71\,\mathrm{Pg(C)\,a^{-1}}$ from model simulations by Carr et al. (2006) and lower than values estimated from satellite data ($43\,\mathrm{Pg(C)\,a^{-1}}$ to $58\,\mathrm{Pg(C)\,a^{-1}}$; Behrenfeld et al., 2006), with $52\,\mathrm{Pg(C)\,a^{-1}}$ calculated from the expanded CbPM by Westberry et al. (2008). The primary production in this study is also lower compared to the simulated values by HAMOCC in different Coupled Model Intercomparison Project (CMIP5) experiments for the year 1850 ranging from $55.83\,\mathrm{Pg(C)\,a^{-1}}$ to $61.63\,\mathrm{Pg(C)\,a^{-1}}$, using the original value of $\alpha_{PI}$ and a daily-mean solar irradiation at the ocean surface (Ilyina et al., 2013).

As can bee seen in the Taylor diagram (Fig. 4.2) the spatial correlation between the annual averaged water column NPP in SOCX and the values derived from SeaWiFS data is $R = 0.352$. The standard deviation in the simulation normalised with respect to the standard deviation of the observation based estimate is $\hat{\sigma}_f = 0.55$. This low spatial correlation is caused by large differences between the NPP distributions in the model system and observations (Fig. 4.5). In the model system, less than half of the NPP calculated from satellite ocean colour retrievals is simulated poleward of 40 °N and 40 °S. Whereas between 40 °S and 40 °N, the observed spatial pattern in NPP is well represented by the simulation, the amplitude is not, underestimating observed maxima and overestimating observed minima. This clearly points to deficiencies in the representation of phytoplankton growth in the model system.

The overall underestimation of the annually integrated global water column NPP can be compensated with an increased value for the initial slope of light depended photosynthesis $\alpha_{PI}$. Additional corrections may have to be applied to the temperature dependency of phytoplankton growth (Eq. 3.5) and the half saturation constant for $PO_4^{3-}$ uptake $K_{Phy}^{PO_4}$ (Eq. 3.8) to match model results to the observed spatial distribution of NPP and surface ocean $PO_4^{3-}$ concentrations.

In the submodel HAMOCC export production (EP) is defined as the amount of particulate organic carbon (POC) transported out of the euphotic zone, i.e. transported through the depth of 90 m. The model system simulates an average global EP of $7.3\,\mathrm{Pg(C)\,a^{-1}}$. This value is lower than estimates ranging from $10\,\mathrm{Pg(C)\,a^{-1}}$ to $21\,\mathrm{Pg(C)\,a^{-1}}$ (Schlitzer, 2002; Laws et al., 2000) and the EP of $8.23\,\mathrm{Pg(C)\,a^{-1}}$ to $9.07\,\mathrm{Pg(C)\,a^{-1}}$ simulated by HAMOCC in the Max Planck Institute Earth System Model (MPI-ESM; Ilyina et al., 2013). As EP can be related as a first approximation to NPP in the euphotic zone (Schneider et al., 2008), it is expected to increase with

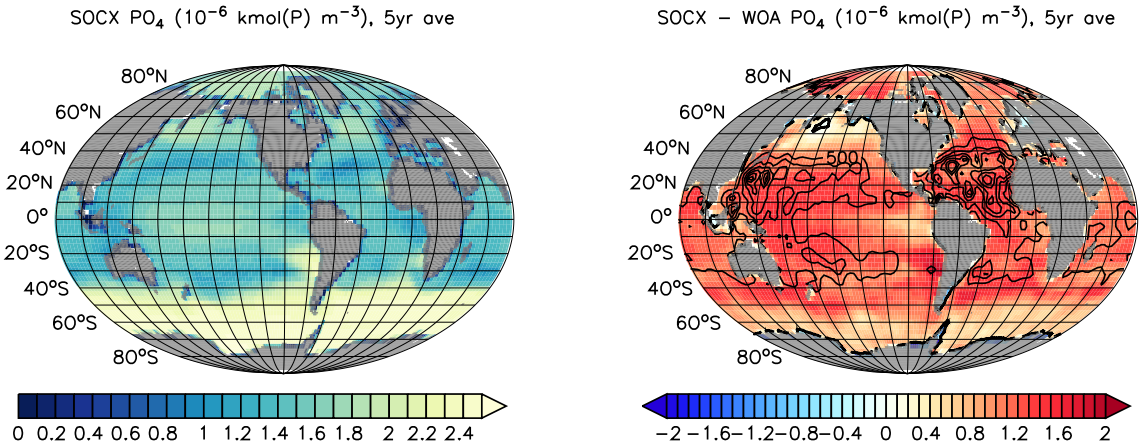


**(a)** $PO_4$ SOCX **(b)** $PO_4$ SOCX - WOA

**Figure 4.6:** (a) Averages of surface ocean molar $PO_4^{3-}$ concentrations in $10^{-6}$ kmol(P) $m^{-3}$ over five years in the simulation SOCX. (b) Differences in surface ocean molar $PO_4^{3-}$ concentrations between the 5-year average in SOCX and the climatology from WOA in $10^{-6}$ kmol(P) $m^{-3}$.

an increased global NPP. Thus an optimisation of phytoplankton growth may be sufficient to simultaneously obtain a more realistic global NPP and global EP in the model system.

### Phosphate ($PO_4$)

With a correlation coefficient of $R = 0.61$ and a normalised standard deviation of $\hat{\sigma}_f = 1.015$ (Fig. 4.2), the spatial distribution of surface ocean orthophosphate ($PO_4^{3-}$) concentrations is moderately well represented in the model system compared to WOA observations (Garcia et al., 2010). In the spatial distribution (Fig. 4.6 (a)), regions of high surface ocean $PO_4^{3-}$ concentrations are associated with regions of strong upwelling and mixing, e.g. at the east coasts of South America and Africa, in the Southern Ocean, the North Pacific, and the North Atlantic. However, the absolute surface ocean $PO_4^{3-}$ concentration is overestimated in the model system by $0.979 \times 10^{-6}$ kmol(P) $m^{-3}$ on global average (Fig. 4.6 (b)). This overestimation is obvious at mid latitudes, where surface ocean $PO_4^{3-}$ concentrations are low. Here the relative differences exceed more than 20 times the observed concentrations in the eastern Pacific and the Atlantic. Low $PO_4^{3-}$ sea surface concentrations at mid latitudes are associated with a steady nutrient consumption by phytoplankton in this region, where no light and temperature limitation for phytoplankton growth is

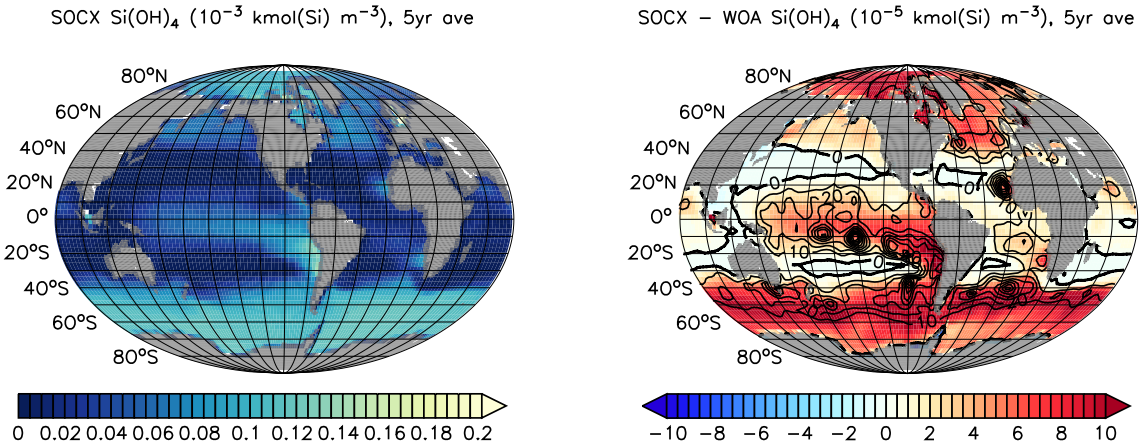


**(a)** $Si(OH)_4$ SOCX **(b)** $Si(OH)_4$ SOCX - WOA

**Figure 4.7:** (a) 5-year averages of surface ocean molar $Si(OH)_4$ concentrations in $10^{-3}$ kmol(Si) $m^{-3}$ in the simulation SOCX. (b) Differences in surface ocean molar $Si(OH)_4$ concentrations between the 5-year average in SOCX and the climatology from WOA in $10^{-5}$ kmol(Si) $m^{-3}$. Contour lines denote relative differences between SOCX and WOA. The interval between contour lines is 1000 %

expected throughout the year (Tjiputra et al., 2013). This points to deficiencies in the simulation of phytoplankton growth and decay in the current model setup and is in line with the above analysis of NPP.

### Silicate ($Si(OH)_4$)

Likewise, surface ocean concentrations of silicic acid ($Si(OH)_4$) are overestimated in the model simulation (Fig. 4.7), as too low NPP is simulated, resulting in lower $Si(OH)_4$ uptake. As in previous simulations of HAMOCC in the MPI-ESM (Ilyina et al., 2013) and the Norwegian Earth System Model (NorESM; Tjiputra et al., 2013), the model overestimates surface ocean $Si(OH)_4$ concentrations in the Southern Ocean. However, the absolute concentrations simulated in the present study are about twice the values obtained from the other studies. Furthermore, the model system overestimates $Si(OH)_4$ concentrations in the tropical and subtropical oceans, attributed to the underestimated NPP. These deficiencies are reflected in the low correlation of $R = 0.484$ between the simulation and observations, and the standard deviation of the simulation normalised with respect to observations of $\hat{\sigma}_f = 2.858$ (Fig. 4.2).

### Dimethyl sulphide (DMS)

DMS production is described according to Kloster et al. (2006) taking into account the temperature dependent DMS production from phytoplankton, separated in opal- and calcium carbonate-producing species in the detritus pool (Maier-Reimer et al., 2005; Ilyina et al., 2013). Destruction of DMS is described as function of irradiance (photolysis) and temperature dependent bacterial consumption. Because of the production from phytoplankton, surface water DMS concentration depends indirectly on photosynthesis.

For surface water DMS concentrations in the SOCX study a distinct annual cycle of high concentrations, following the latitudes with highest irradiance can be seen, which is also visible in the two climatologies of Kettle and Andreae (2000, used as surface water DMS concentrations for BASE) and Lana et al. (2011, not shown). Annual averages of surface water DMS concentrations of the BASE simulation, the SOCX study, the Lana et al. (2011) climatology, and differences between these are presented in Figure 4.8.

The Lana et al. (2011) climatology[6] is an update of the Kettle and Andreae (2000) climatology[7]. An obvious change is the reduction in annual average surface water DMS concentrations in the polar regions, the Atlantic, the east equatorial and west Pacific. Especially in the polar regions Kettle and Andreae (2000) overestimate surface water DMS concentrations, in west Antarctica up to a factor of two compared to the updated climatology. At the Malay Archipelago and in the Indian Ocean Lana et al. (2011) have more than 1.5 times higher values compared to Kettle and Andreae (2000).

Surface water DMS concentrations in the SOCX experiment are generally 50 % lower in the polar regions compared to either of the climatologies. However, the differences in SOCX to the more recent DMS climatology of Lana et al. (2011) are smaller in the polar regions, than the difference of SOCX to the Kettle and Andreae (2000) DMS climatology. DMS surface water concentrations are still overestimated in the SOCX study compared to Lana et al. (2011) at the Malay Archipelago, the subtropic Pacific, the Atlantic, and the tropic Indic. Compared to the differences to the Kettle and Andreae (2000) climatology, these overestimations of SOCX are, however, lower, especially in the Malay Archipelago, in the southern subtropical

[6] data available from `http://www.bodc.ac.uk/solas_integration/implementation_products/group1/dms/` (last accessed: 01.07.2013)

[7] data available from `http://saga.pmel.noaa.gov/dms/` (last accessed: 01.07.2013)

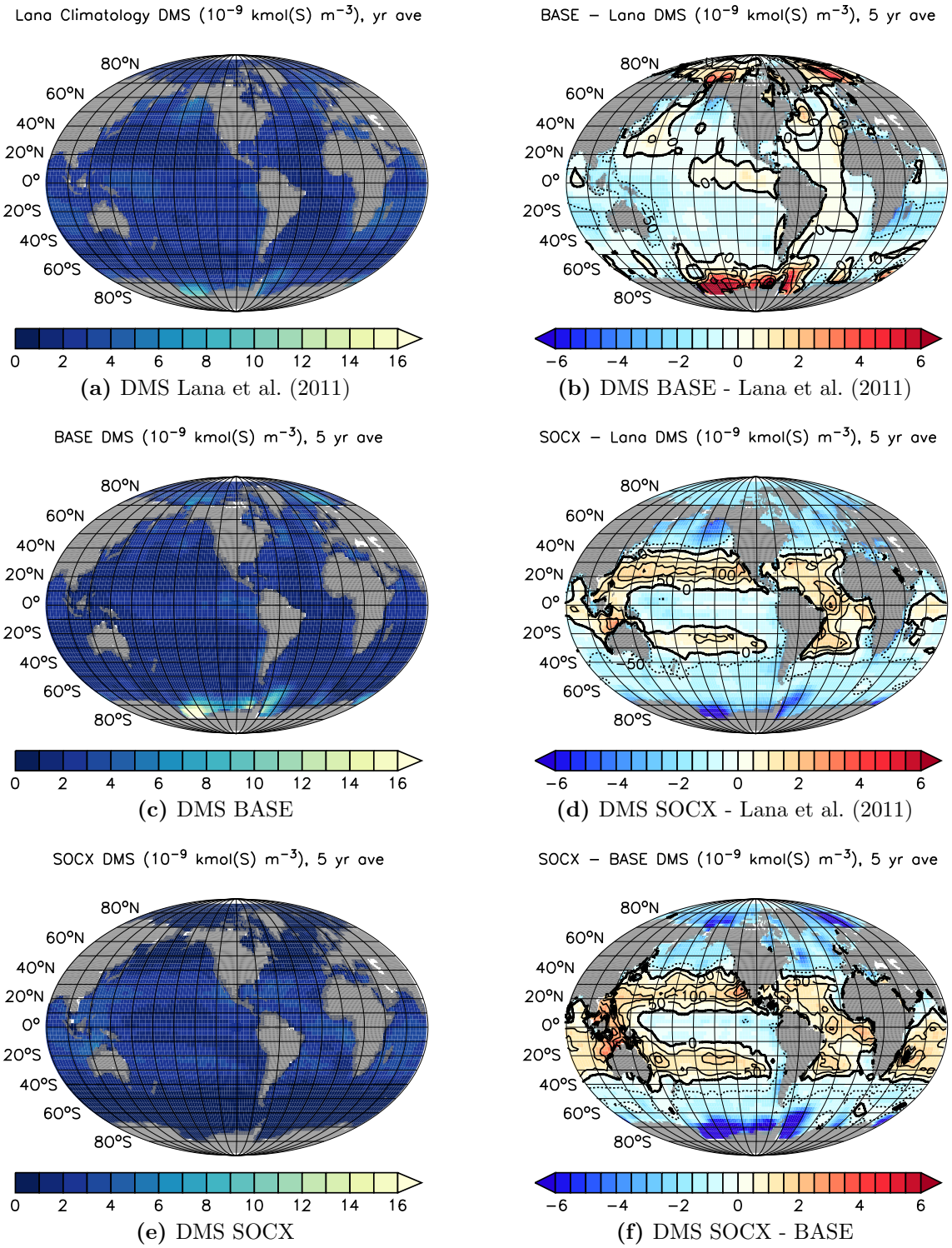


**(a)** DMS Lana et al. (2011)

**(b)** DMS BASE - Lana et al. (2011)

**(c)** DMS BASE

**(d)** DMS SOCX - Lana et al. (2011)

**(e)** DMS SOCX

**(f)** DMS SOCX - BASE

**Figure 4.8:** (a), (c), (e): 5-year averages of surface water DMS molar concentrations in $10^{-9}$ kmol(S) $m^{-3}$. (b), (d), and (f): differences in surface water DMS molar concentrations in $10^{-9}$ kmol(S) $m^{-3}$. Contours denote relative differences, the interval between contour lines is 50 %.

Pacific, and at the west coast of Northern America. In the southern subtropical Indic the annual averaged DMS concentrations of SOCX compare quite well to the values from Lana et al. (2011).

As simulated DMS concentrations depend on a production term, taking into account production from opaline and calcium carbonate producing species in the detritus pool, DMS is related to the simulated NPP. Thus, a clear similarity of underestimation of both variables with respect to observations is visible in the polar oceans poleward of 40° (cf. Figs. 4.5 (c) and 4.8 (d)). Overestimations of sea surface DMS concentrations in the subtropical Pacific, the Atlantic, and the Indic Ocean have, however, larger extends than the areas of overestimated NPP. Not only an improvement of NPP in the model system is needed to obtain simulated DMS concentrations closer to observation based estimates, but further adaption of parameters describing DMS production and decay in the model system may be necessary as well. This holds especially for the photolysis term in the parameterisation, as a changed, more variable (two hourly) solar radiation is passed to the biogeochemistry submodel compared to the original implementation of HAMOCC (daily).

### Carbon dioxide ($CO_2$)

In the SOCX sensitivity study annual averaged surface water concentrations of $CO_2$ (Fig. 4.9) are overestimated in all regions compared to the climatology of Takahashi et al. (2009)[8]. The highest overestimates occur in the tropical Pacific and the tropical Atlantic, especially at the west coast of South America and the west coast of Africa. Further overestimations, larger than 30 % compared to Takahashi et al. (2009) are at the latitudes poleward of 70° in both hemispheres. Despite the general overestimation in the model simulation, the pattern of the surface ocean $CO_2$ concentrations form the climatology is well represented by the simulation. The $CO_2$ concentration shows a maximum in the tropics, surrounded by minima in the subtropics, and small secondary maxima at higher latitudes.

The overestimation of surface water $CO_2$ concentrations has several reasons. First, the spatial extend of high $CO_2$ concentrations is generally overestimated in the model system (as shown by Ilyina et al., 2013). Second, specifically for the present study, the spin-up phase for the oceanic biogeochemistry and air-sea gas exchange of 30 years was too short to equilibrate the oceanic $CO_2$ concentrations in the model system,

[8] data available from `http://www.ldeo.columbia.edu/res/pi/CO2/carbondioxide/pages/air_sea_flux_2010.html` (last accessed: 01.07.2013)

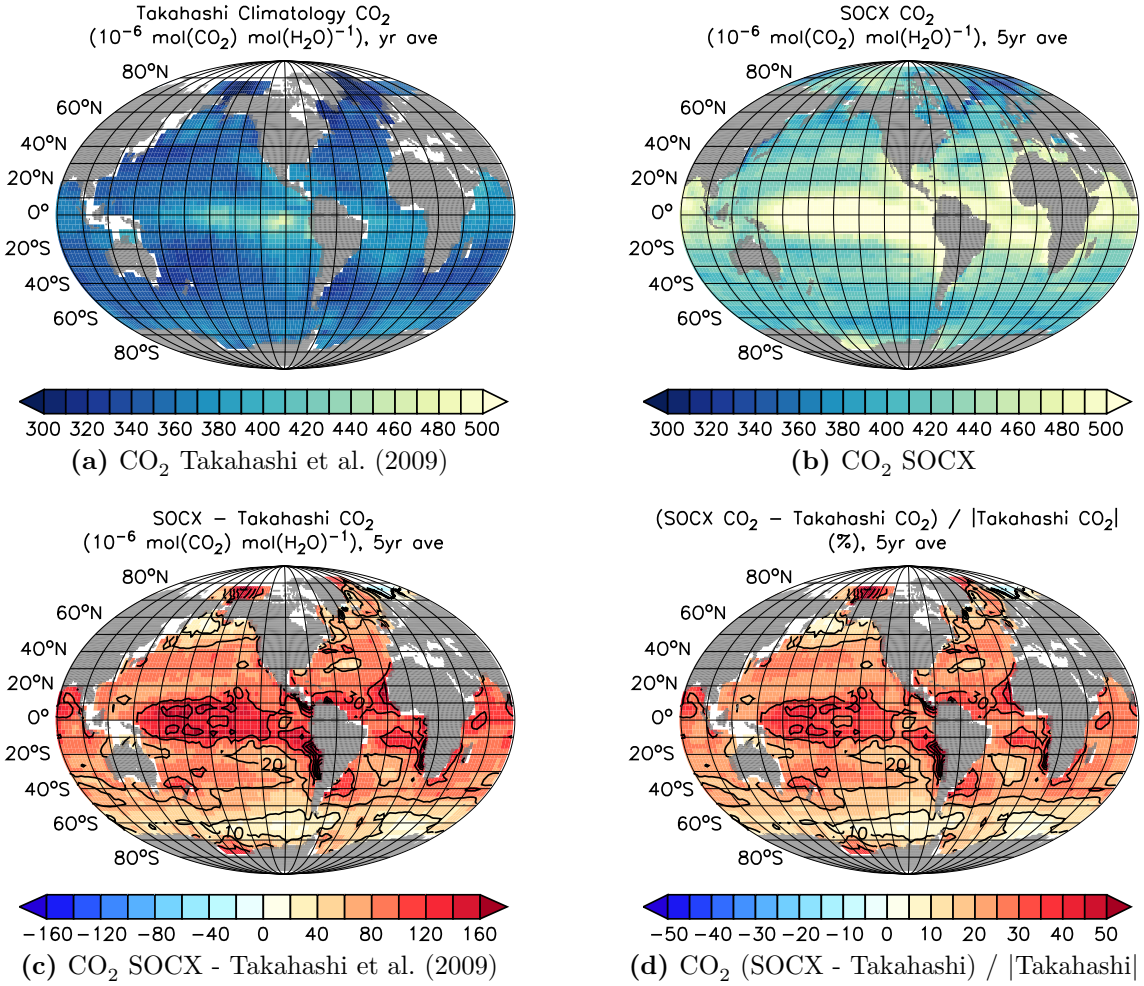


**(a)** $CO_2$ Takahashi et al. (2009)

**(b)** $CO_2$ SOCX

**(c)** $CO_2$ SOCX - Takahashi et al. (2009)

**(d)** $CO_2$ (SOCX - Takahashi) / |Takahashi|

**Figure 4.9:** Averages of surface water $CO_2$ molar mixing ratios in $10^{-6}\,\mathrm{mol}(CO_2)\,\mathrm{mol}(H_2O)^{-1}$ from (a) the Takahashi et al. (2009) climatology and (b) over five years of SOCX. (c) absolute difference and (d) relative difference in surface water $CO_2$ molar mixing ratios between SOCX and the Takahashi et al. (2009) climatology in $10^{-6}\,\mathrm{mol}(CO_2)\,\mathrm{mol}(H_2O)^{-1}$ and %, respectively. Contours denote relative differences, the interval between contour lines is 10 %.

which was started from a non-equilibrated state between ocean and atmosphere. A further aspect for the overestimation of $CO_2$ concentrations is the reduced NPP in the simulation compared to other studies.

### Isoprene ($C_5H_8$)

Annually averaged surface water concentrations of $C_5H_8$ are shown in Figure 4.10. In both simulations $C_5H_8$ concentrations are calculated via the empirical relationship to chlorophyll concentrations from Eq. 3.10 (Broadgate et al., 1997). For the BASE

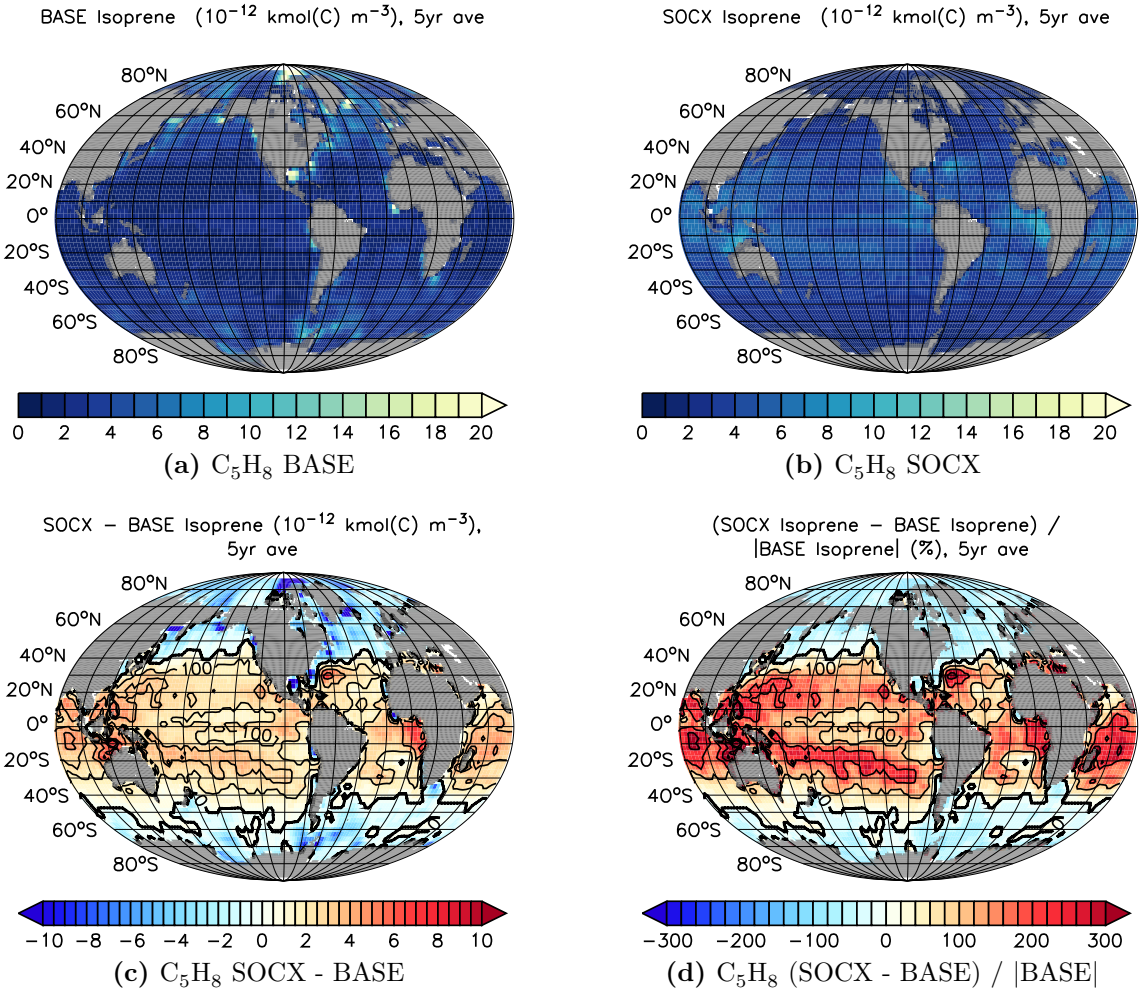


**(a)** $C_5H_8$ BASE **(b)** $C_5H_8$ SOCX

**(c)** $C_5H_8$ SOCX - BASE **(d)** $C_5H_8$ (SOCX - BASE) / |BASE|

**Figure 4.10:** Averages of surface water $C_5H_8$ molar concentrations in $10^{-12}$ kmol(C) $m^{-3}$ over five years of (a) BASE and (b) SOCX. (c) absolute difference and (d) relative difference in surface water $C_5H_8$ molar concentration SOCX and BASE in $10^{-12}$ kmol(C) $m^{-3}$ and %, respectively. Contours denote relative differences, the interval between contour lines is 100 %.

simulation prescribed chlorophyll concentrations from the World Ocean Atlas (WOA; Conkright et al., 2002[9]) are used. In SOCX the chlorophyll concentrations are calculated from the simulated phytoplankton concentrations (Eq. 3.9). As chlorophyll is overestimated in SOCX in the tropics (not shown), a similar overestimation is visible in the $C_5H_8$ concentrations. In the subtropical regions of the Pacific, in the subtropical Indic, and at the western coast of Africa the overestimation in SOCX reaches a factor of two compared to the BASE simulation.

[9] data available from `http://www.nodc.noaa.gov/OC5/WOA01/pr_woa01.html` (last accessed 10.08.2013)

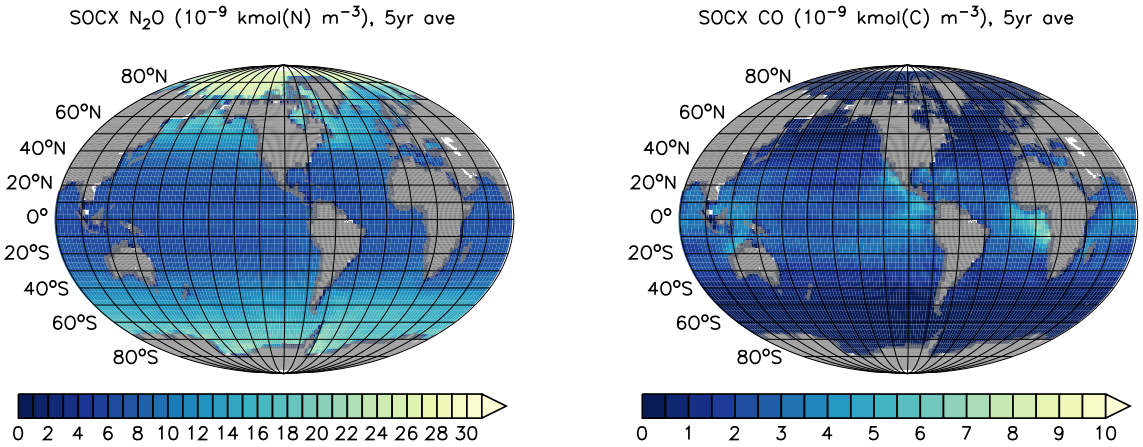


**(a)** $N_2O$ SOCX **(b)** CO SOCX

**Figure 4.11:** Averages of surface water molar concentrations of (a) $N_2O$ and (b) CO in SOCX over five years. Units are $10^{-9}$ kmol(N) $m^{-3}$ and $10^{-9}$ kmol(C) $m^{-3}$, respectively.

The deficiencies in the model's representation of surface water $C_5H_8$ concentrations are related to the simulation of NPP and the diagnostic relationship of $C_5H_8$ to chlorophyll concentrations. As chlorophyll concentration is no prognostic model variable, it is calculated via a simple relationship from the model system's phytoplankton concentration (Eq. 3.9). However, for this relationship a constant carbon to chlorophyll ratio $R_{\mathrm{C:Chl}}$ is assumed. Whereas $R_{\mathrm{C:Chl}} = 60$ resembles observations ranging from 27 to 67, in reality the phytoplankton chlorophyll content varies with the availability of light and nutrients (Riemann et al., 1989). To improve the representation of chlorophyll in the future model system, these variations have to be taken into account for the parameterisation.

### Nitrous oxide ($N_2O$)

Surface water concentrations of $N_2O$ comprise maxima in the polar regions and a minimum in the tropics (Fig. 4.11 (a)). Compared to the work of Freing et al. (2012), who parameterise $N_2O$ production depending on apparent oxygen utilisation (AOU), temperature, and depth, the SOCX simulation lacks maxima in the tropical high productivity zones. This deficiency is directly related to the apparent underestimation of NPP in the simulation.

#### Carbon monoxide (CO)

CO concentrations in surface water show minima at high latitudes and maxima in tropical waters (Fig. 4.11 (b)). This distribution is reasonable, as the production of CO in seawater is a photochemical source (Eq. 3.11). The results of this model simulation are in line with the spatial distribution of CO obtained from a simulation study by Chu et al. (2007).

#### Discussion

Even with these partly profound deviations in oceanic concentrations from observation based estimates of the chemical species in focus, caused by deficiencies in the representation of oceanic biogeochemistry in the model system, further analysis of the data obtained by the sensitivity studies is useful to evaluate the response of the model system to modified forcings. Deficiencies in the oceanic concentrations of climatologies derived from observations and aiming at reproducing the reality have also to be taken into account, as in-situ measurements in the ocean are very sparse. To overcome this sparseness in measurements, usually interpolation methods in space and time are applied to the data. For instance, despite a threefold increase of reported in-situ measurements of DMS used by Lana et al. (2011) compared to Kettle and Andreae (2000), a temporal interpolation and substitution of undersampled regions based on biogeographic provinces have been applied to fill gaps in the annual cycle. Despite the increase in reported data from in-situ measurements, temporal and spatial sparseness remaines a problem for oceanic data.

Therefore, analysing differences between the sensitivity simulations and the baseline simulations provide further insight into the robustness of the model system and the ability of the model to simulate reasonable responses to modified forcings in terms of different oceanic concentrations and, hence, ocean-to-atmosphere fluxes. Furthermore, upper estimates for impacts under heavily modified forcings may be assessed. Focusing on relative differences between sensitivity studies, feedbacks of individual processes acting in the coupled system can be investigated.

### 4.2.2 Evaluation of the fluxes between ocean and atmosphere

Total annual global integrals of ocean-to-atmosphere gas fluxes in the BASE simulation, in the sensitivity studies, and from literature are presented in Table 4.2. The direction of fluxes between ocean and atmosphere are defined to be positive

| | BASE | SOCX | SRFIX | SDUST | Literature |
|---|---|---|---|---|---|
| DMS<br>$\mathrm{Tg(S)\,a^{-1}}$ | $24.78 \pm 5.64$ | $23.57 \pm 2.96$ | $23.57 \pm 2.95$ | $23.64 \pm 2.93$ | 15–54[a] |
| $CO_2$<br>$\mathrm{Pg(C)\,a^{-1}}$ | – | $3.50 \pm 1.28$ | $3.63 \pm 1.31$ | $3.46 \pm 1.26$ | $-(1–3)$[b] |
| $C_5H_8$<br>$\mathrm{Tg(C)\,a^{-1}}$ | $0.069 \pm 0.004$ | $0.097 \pm 0.014$ | $0.097 \pm 0.014$ | $0.097 \pm 0.014$ | 0.1–1.2[d]<br>0.18–0.45[e] |
| $N_2O$<br>$\mathrm{Tg(N)\,a^{-1}}$ | – | $0.643 \pm 0.252$ | $0.643 \pm 0.252$ | $0.644 \pm 0.252$ | 1.2–6.8[c] |
| CO<br>$\mathrm{Tg(C)\,a^{-1}}$ | 9.8[f] | $10.25 \pm 0.99$ | $10.26 \pm 0.99$ | $10.28 \pm 0.98$ | 8.5–86[g]<br>$3.7 \pm 2.6$[h] |
| $CH_3OH$<br>$\mathrm{Tg(C)\,a^{-1}}$ | $-1.52 \pm 0.18$ | $-1.48 \pm 0.18$ | $-1.48 \pm 0.18$ | $-1.49 \pm 0.18$ | $-(0.1–21)$[i]<br>$-6$[j] |

[a] Kettle and Andreae (2000), and references therein.
[b] Takahashi et al. (2009).
[c] Nevison et al. (1995).
[d] Palmer and Shaw (2005), and references therein.
[e] Arnold et al. (2009).
[f] Constant prescribed biogenic oceanic CO emissions.
[g] Bergamaschi et al. (2000); Ehhalt et al. (2001).
[h] Stubbins et al. (2006).
[i] Heikes et al. (2002); Galbally and Kirstine (2002); Jacob et al. (2005).
[j] Millet et al. (2008).

**Table 4.2:** 5-year averages and inter-annual standard deviations of the total global ocean-to-atmosphere gas fluxes. Positive values are net fluxes from the ocean to the atmosphere, negative values denote net uptake by the ocean.

for outgassing from the ocean and negative for ocean uptake throughout this study. Comparing the total ocean-to-atmosphere gas fluxes of the sensitivity studies, only small changes can be seen in the global integrals between different simulations.

This subsection focuses on the differences in the ocean-to-atmosphere fluxes between the SOCX sensitivity study, the BASE study, measurements, and literature values. Compared to the BASE simulation the SOCX study simulates interactive oceanic biogeochemistry with the HAMOCC submodel. The air-sea gas exchange in SOCX is calculated from the interactively calculated ocean's surface chemical concentrations, whereas in the BASE simulation these concentrations have been prescribed.

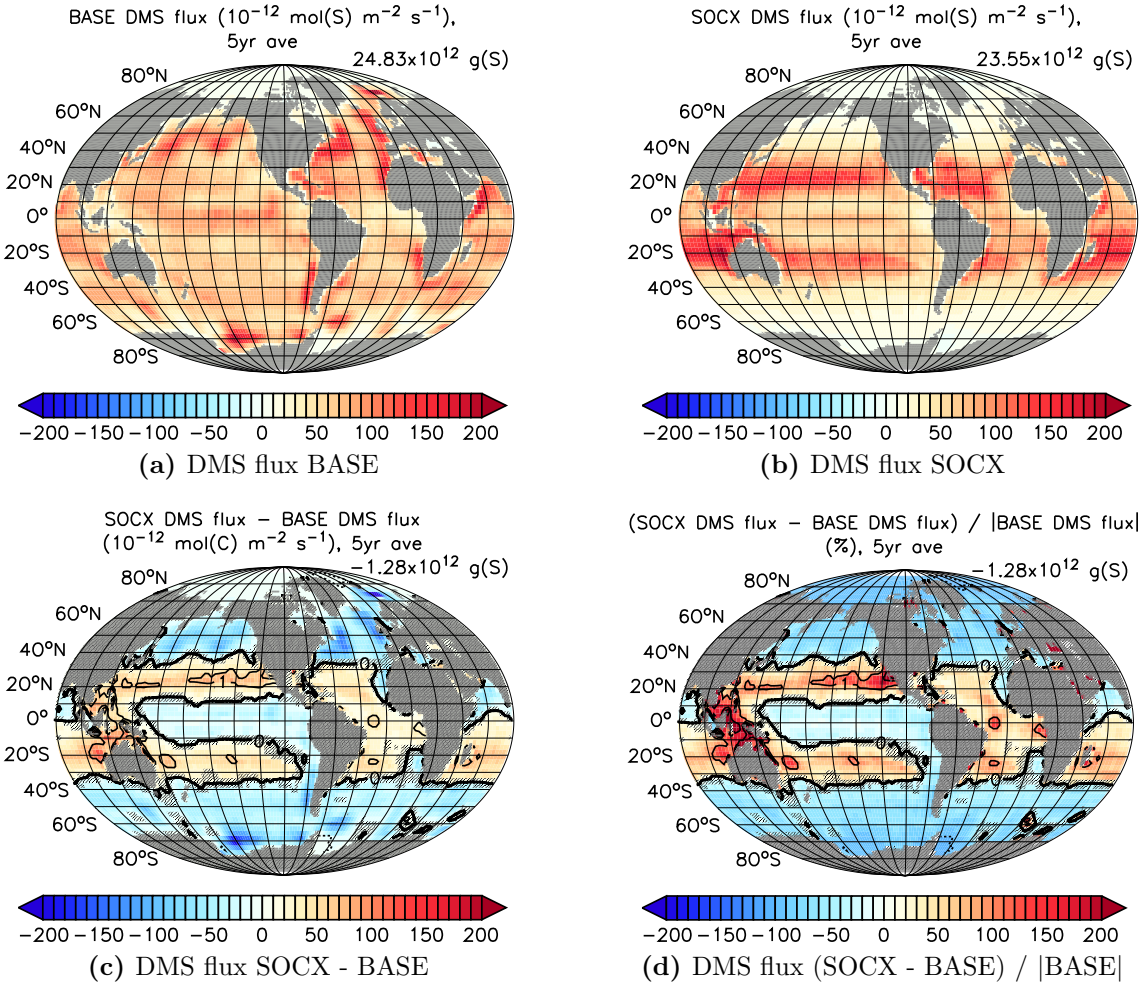


**(a)** DMS flux BASE

**(b)** DMS flux SOCX

**(c)** DMS flux SOCX - BASE

**(d)** DMS flux (SOCX - BASE) / |BASE|

**Figure 4.12:** 5-year averages of ocean-to-atmosphere gas fluxes for DMS in the (a) BASE and in the (b) SOCX simulation. Units are $10^{-12}$ mol(S) $m^{-2}$ $s^{-1}$, positive values are fluxes from the ocean into the atmosphere, negative values denote ocean uptake. The annual total global ocean-to-atmosphere gas flux is given in g(S). (c) absolute and (d) relative differences in 5-year averaged ocean-to-atmosphere gas flux of DMS between SOCX and BASE. Units are $10^{-12}$ mol(S) $m^{-2}$ $s^{-1}$ and %, respectively. The difference in the annual total global ocean-to-atmosphere gas flux between SOCX and BASE is given in g(S). Contours denote the relative difference in %, the interval between contour lines is 100 %. Differences in ocean-to-atmosphere gas fluxes in gray shaded areas are not significant on a 99 % level according to a two-sided Student's t-test.

### Dimethyl sulphide (DMS)

The globally integrated annual ocean-to-atmosphere gas fluxes of DMS in the sensitivity simulations are comparable to the value obtained in the BASE simulation. The DMS flux in BASE shows a higher inter-annual variablity than the simulated

fluxes in the sensitivity studies. This is caused by larger monthly variation of DMS fluxes calculated from the prescribed monthly oceanic DMS concentrations in BASE compared to the sensitivity studies, based on interactively calculated oceanic DMS concentrations (cf. Figs. 4.13, 4.14). The total global ocean-to-atmosphere gas fluxes of DMS in all simulations are within the range of the values from literature (Tab. 4.2).

The spatial distribution of the ocean-to-atmosphere gas flux averaged over 5 simulated years for DMS in the BASE simulation and the SOCX sensitivity simulation is presented in Figure 4.12. The DMS flux in the BASE simulation is calculated from prescribed oceanic surface concentrations of DMS obtained from the Kettle and Andreae (2000) climatology (Fig. 4.8 (c)). In the sensitivity simulation SOCX, surface water DMS concentrations (Fig. 4.8 (e)) are calculated interactively by the HAMOCC submodel based on the method implemented by Kloster et al. (2006).

Compared to BASE, the ocean-to-atmosphere DMS flux between 20° to 30° in the Pacific in both hemispheres is more than twice as large in the SOCX sensitivity simulation. Furthermore there are larger fluxes in the whole tropical and subtropical Atlantic and in the southern tropical and subtropical Indic. These increased ocean-to-atmosphere fluxes of DMS are in correspondence with the higher DMS surface water concentrations in SOCX compared to BASE (Fig. 4.8 (f)).

Lower ocean-to-atmosphere fluxes of DMS in SOCX are apparent in the North Pacific, the North Atlantic, and the Southern Ocean. These decreased ocean-to-atmosphere fluxes in SOCX compared to BASE likewise correspond to the lower DMS concentrations simulated by the interactive oceanic biogeochemistry module compared to the prescribed values in the baseline simulation (Fig. 4.8 (f)). However, in the BASE experiment the prescribed surface water DMS concentrations in the Southern Ocean are too high compared to the more recent climatology of Lana et al. (2011).

As differences in ocean-to-atmosphere gas fluxes of DMS are directly linked to differences in the ocean surface DMS concentrations between the two simulations (Fig. 4.8 (f)), the results show that ocean-to-atmosphere fluxes of DMS are realistically represented in the model system under changed ocean surface concentrations of DMS. Global integrated annual air-sea fluxes for DMS in SOCX are comparable to observations and the baseline simulation. The shift in spatial distribution from BASE to SOCX provides a modified forcing on the atmospheric domain of the model system. Despite the deficiencies in the model system to reproduce observations, it is possible to assess the model system's robustness, responses in atmospheric

chemistry, and relative changes in atmospheric composition under changed forcings. However, to simulate results close to observation based estimates, it is necessary to achieve a better representation of NPP in the model system, to yield more realistic ocean surface DMS concentration patterns. Furthermore, a revision of the DMS parameterisation in the model is needed to obtain DMS concentrations, and thus ocean-to-atmosphere fluxes of DMS, which are closer to observation based estimates.

A strong dependence on solar radiation can be seen in the BASE simulation (Fig. 4.13) and in the SOCX sensitivity experiment (Fig. 4.14) showing the annual cycle of the DMS ocean-to-atmosphere gas flux. The monthly patterns in both simulations are similar, indicating a reasonable simulation of the DMS ocean-to-atmosphere flux in the model setup with interactive oceanic biogeochemistry. The intra-annual variations in global integrated monthly DMS ocean-to-atmosphere gas fluxes are comparable, with lower values in the SOCX simulation. This is mainly caused by the lower DMS ocean-to-atmosphere fluxes in the Southern Ocean during December to March (Figs. 4.15 (l), (a)–(c)), resulting in lower global integrated monthly fluxes in these months, in the SOCX simulation compared to BASE. However, according to the updated climatology of surface water DMS concentrations by Lana et al. (2011), the climatology used in BASE (Kettle and Andreae, 2000) seems to overestimate DMS concentrations in this region (Fig. 4.8 (b)).

Significantly higher DMS ocean-to-atmosphere gas fluxes in the SOCX simulation are associated with the sun's zenith (Fig. 4.15), affecting mainly latitudes from 0° to 40° in both hemispheres. Maxima of DMS fluxes are simulated in September and October between 30 °S and 40 °S.

Throughout the year, in SOCX reduced oceanic sources of DMS emissions are simulated in the polar and subpolar regions compared to the baseline experiment (Fig. 4.15). These reductions are significant in summer and autumn of both hemispheres. From December to April at the Southern Ocean (Figs. 4.15 (l) and (a)–(d)) and from May to October in the northern parts of the Atlantic and Pacific (Figs. 4.15 (e)–(j)).

The simulated surface ocean DMS concentrations are closer to the updated DMS climatology of Lana et al. (2011) as to the Kettle and Andreae (2000) climatology used in BASE (Fig. 4.8), so the differences in DMS flux in SOCX are lower when compared to the updated climatology. However, as noted before, there is room for improvement of simulated sea surface DMS concentrations in the model system by an improved representation of NPP adapted to the increased coupling frequency of solar radiation from the atmospheric model domain.

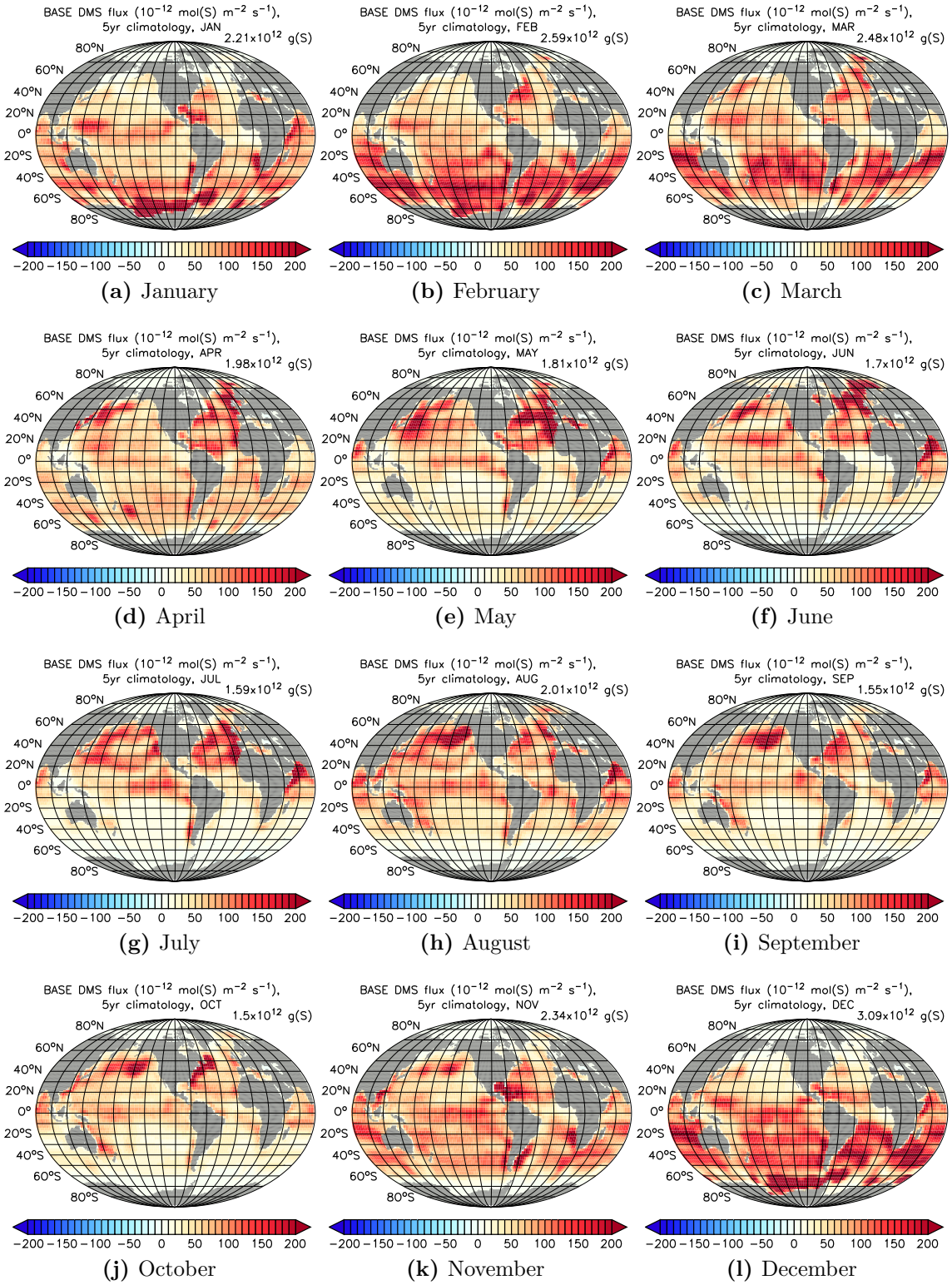


**Figure 4.13:** 5-year monthly climatology of DMS ocean-to-atmosphere gas fluxes in $10^{-12}$ mol(S) $m^{-2}$ $s^{-1}$ derived from the BASE simulation. 5-year averages of the monthly total global ocean-to-atmosphere gas fluxes are listed in g(S).

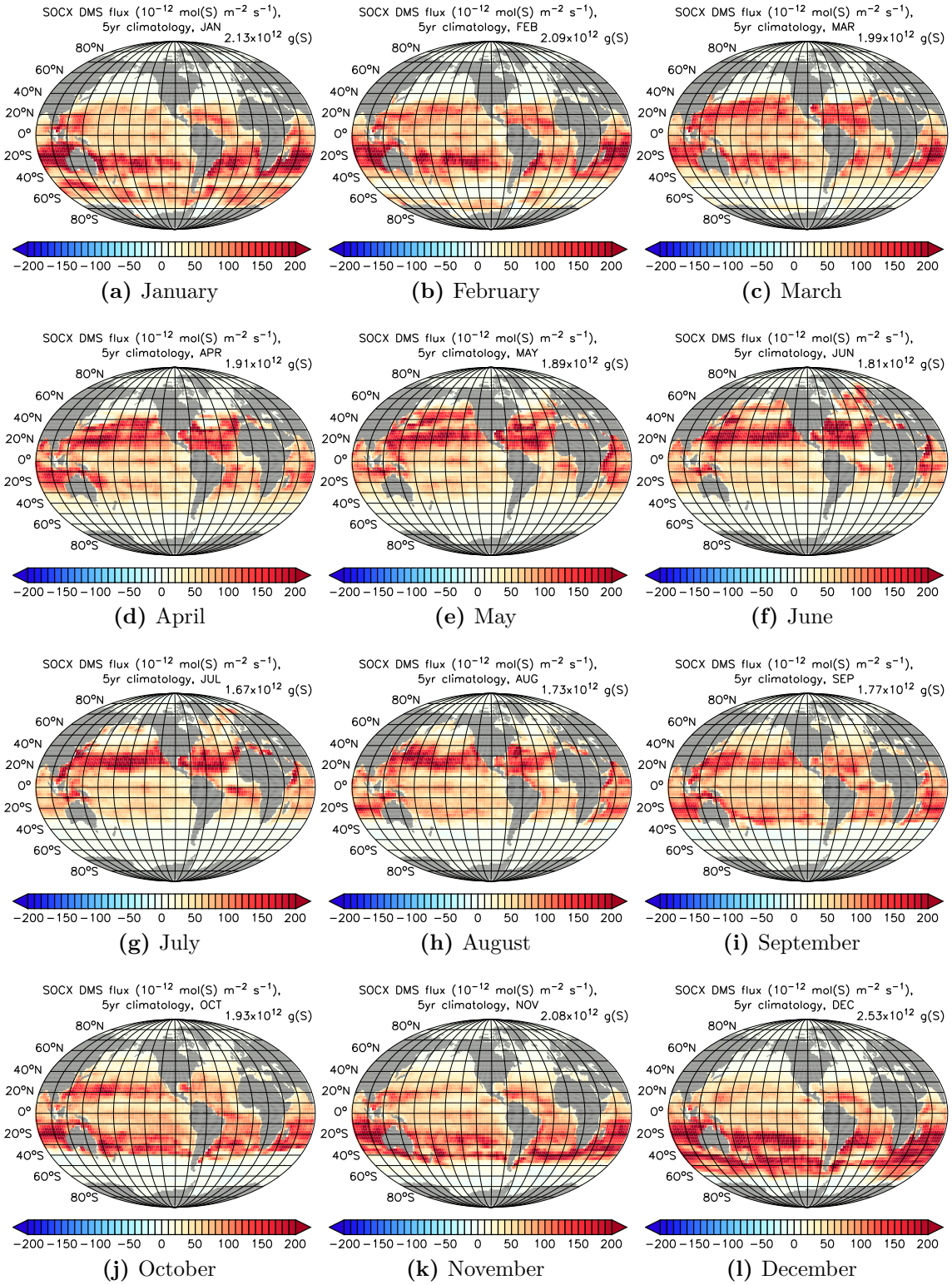


**(a)** January **(b)** February **(c)** March

**(d)** April **(e)** May **(f)** June

**(g)** July **(h)** August **(i)** September

**(j)** October **(k)** November **(l)** December

**Figure 4.14:** 5-year monthly climatology of DMS ocean-to-atmosphere gas fluxes in $10^{-12}$ mol(S) $m^{-2}$ $s^{-1}$ derived from the SOCX simulation. 5-year averages of the monthly total global ocean-to-atmosphere gas fluxes are listed in g(S).

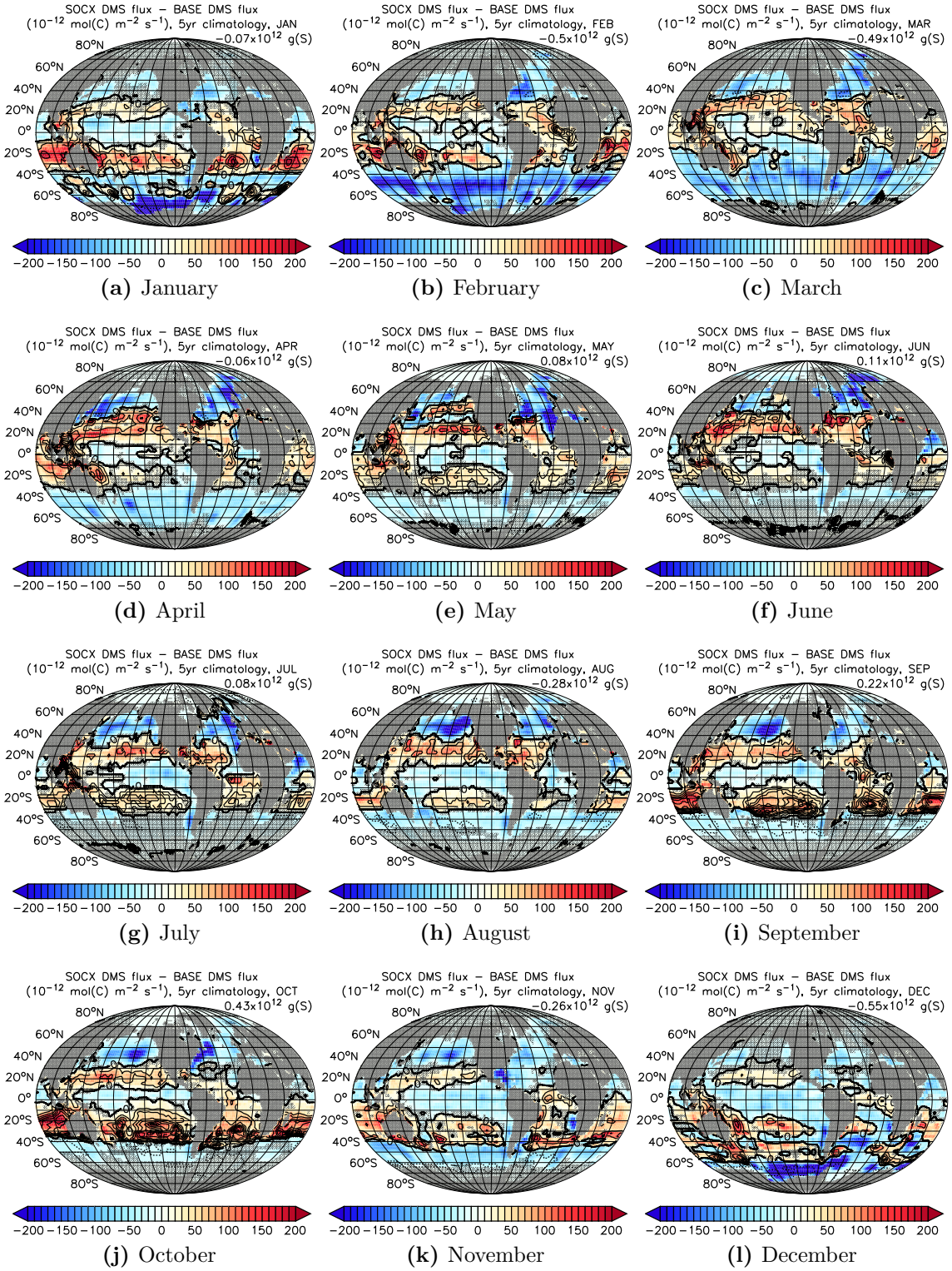


**(a)** January **(b)** February **(c)** March

**(d)** April **(e)** May **(f)** June

**(g)** July **(h)** August **(i)** September

**(j)** October **(k)** November **(l)** December

**Figure 4.15:** Differences in 5-year monthly climatology of DMS ocean-to-atmosphere gas fluxes in $10^{-12}$ mol(S) $m^{-2}$ $s^{-1}$ between SOCX and BASE. Differences in the 5-year averages of the monthly total global ocean-to-atmosphere gas fluxes are given in g(S). Contours denote relative differences in %, the interval between contour lines is 100 %. Differences in ocean-to-atmosphere gas fluxes in gray shaded areas are not significant on a 99 % level according to a two-sided Student's t-test.

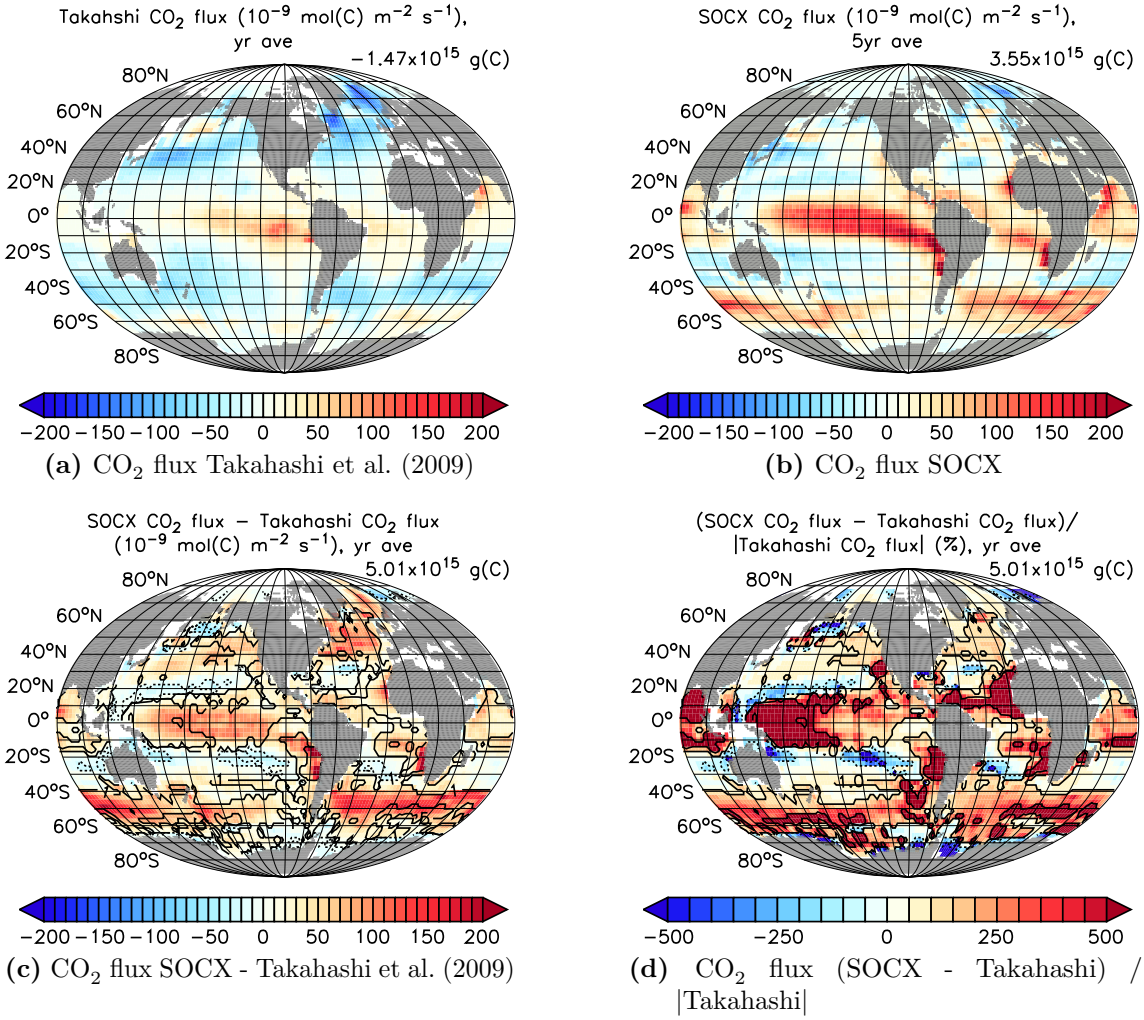


**(a)** $CO_2$ flux Takahashi et al. (2009)

**(b)** $CO_2$ flux SOCX

**(c)** $CO_2$ flux SOCX - Takahashi et al. (2009)

**(d)** $CO_2$ flux (SOCX - Takahashi) / |Takahashi|

**Figure 4.16:** Averages of ocean-to-atmosphere gas fluxes for $CO_2$ from (a) the Takahashi et al. (2009) climatology and (b) five years SOCX simulation. Units are $10^{-9}\,\mathrm{mol(C)\,m^{-2}\,s^{-1}}$, positive values are fluxes from the ocean into the atmosphere, negative values denote ocean uptake. Annual total global ocean-to-atmosphere gas fluxes are given in g(C). (c) absolute and (d) relative differences in averaged ocean-to-atmosphere gas flux of $CO_2$ between the Takahashi et al. (2009) climatology and SOCX. Units are $10^{-9}\,\mathrm{mol(C)\,m^{-2}\,s^{-1}}$ and %, respectively. Differences in annual total global ocean-to-atmosphere gas fluxes between SOCX and Takahashi et al. (2009) are given in g(C). Contours denote relative differences in %, contour lines are at −500 %, −100 %, 100 % and 500 %.

### Carbon dioxide ($CO_2$)

Figure 4.16 shows the averaged ocean-to-atmosphere gas fluxes of $CO_2$ from the Takahashi et al. (2009) climatology and the 5-year simulation SOCX. In agreement with the overestimation of $CO_2$ surface water concentrations in the sensitivity

simulation (Fig. 4.9), ocean-to-atmosphere gas fluxes are increased in most regions over the global ocean (Figs. 4.16 (c), 4.16 (d)). Most prominent are the largely overestimated strengths and extends of $CO_2$ outgassing over the tropics and the Southern Ocean. Despite the overestimation of surface water $CO_2$ concentrations, regions of ocean uptake of $CO_2$ are apparent in the model system (Fig. 4.16 (b)). The overall pattern, with only small annual variation (not shown) is reproduced by the model system. However, the annual global total ocean-to-atmosphere flux in the model system is $3.5\,\mathrm{Pg(C)\,a^{-1}}$ (see also Table 4.2), compared to $-1.5\,\mathrm{Pg(C)\,a^{-1}}$ calculated from the Takahashi et al. (2009) climatology. Thus the $CO_2$ air-sea flux is not only overestimated in the SOCX sensitivity study, but also represents a net source to the atmosphere, whereas an oceanic sink for atmospheric $CO_2$ is expected (Table 4.2).

This discrepancy in the model system is caused by the poor representation of NPP in the model system. Furthermore, the limited spin-up phase of the oceanic concentrations, starting from non-equilibrated $CO_2$ air-sea gas fluxes, and the constant atmospheric $CO_2$ concentrations used in the time-slice experiments contributes to the deficiencies in the presented simulations. It is important to note, however, that in this study atmospheric concentrations of $CO_2$ are prescribed and the model system is operated in QCTM mode. Thus ocean-to-atmosphere fluxes of $CO_2$ are purely diagnostic and have no impact on neither the simulated climate, nor the atmospheric chemistry.

For the simulation of realistic surface water $CO_2$ concentrations, as well as ocean-to-atmosphere gas fluxes, special care has to be taken at the initialisation and the spin-up phase to reach distributions close to the equilibrium state (Tjiputra et al., 2013). Furthermore, a transient simulation with changing atmospheric $CO_2$ concentrations, or changing anthropogenic $CO_2$ emissions over time has to be performed in a future study to evaluate the model system with respect to $CO_2$ air-sea gas exchange. Such a simulation, starting from pre-industrial conditions with a carefully equilibrated model system, including a compiled $CO_2$ emission database from the model start to present conditions, however, is beyond the scope of this study.

### Isoprene ($C_5H_8$)

The $C_5H_8$ ocean-to-atmosphere gas flux is presented in Figure 4.17 for the baseline and the sensitivity simulation including interactive oceanic biogeochemistry. In SOCX the 5-year averaged ocean-to-atmosphere gas flux of $C_5H_8$ is significantly

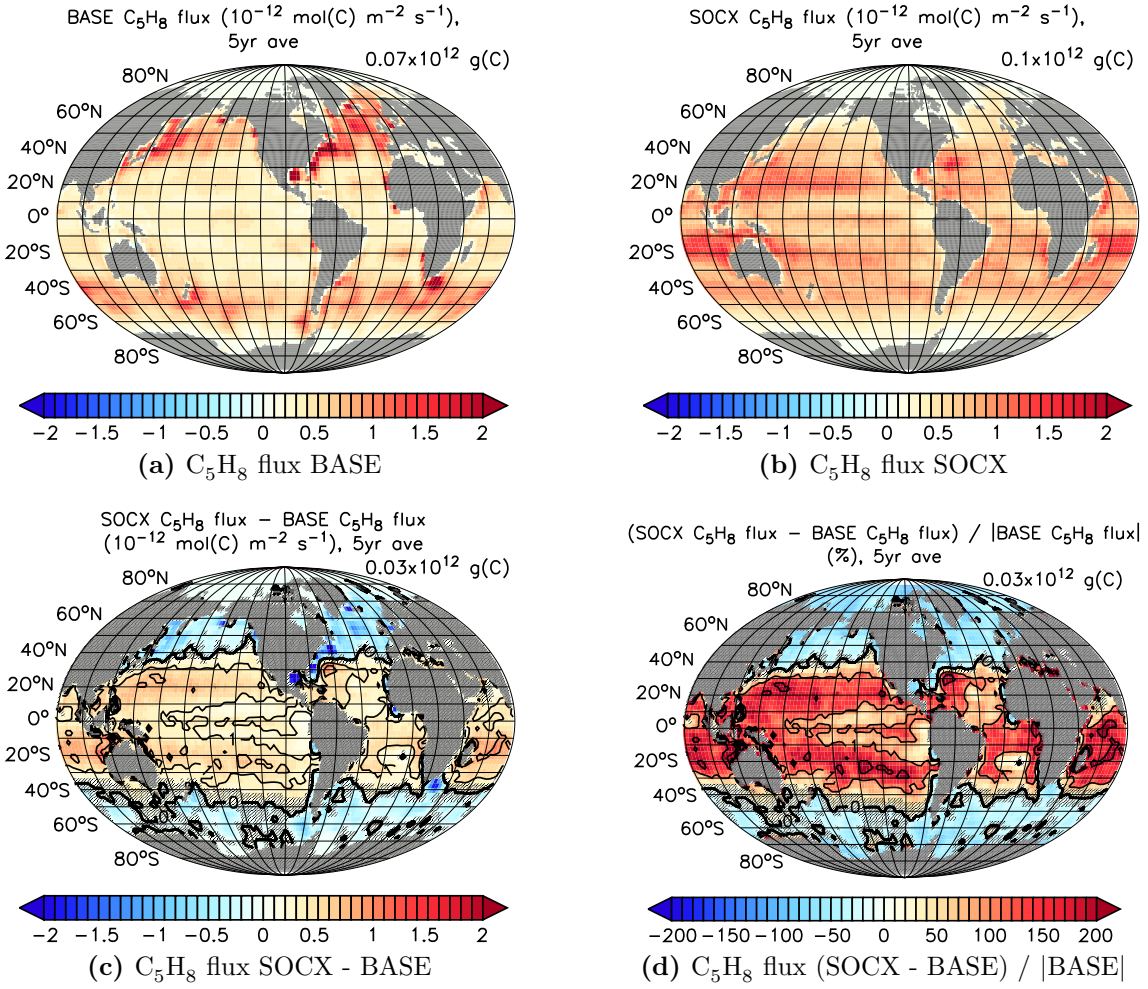


**(a)** $C_5H_8$ flux BASE

**(b)** $C_5H_8$ flux SOCX

**(c)** $C_5H_8$ flux SOCX - BASE

**(d)** $C_5H_8$ flux (SOCX - BASE) / |BASE|

**Figure 4.17:** 5-year averages of ocean-to-atmosphere gas fluxes for $C_5H_8$ (a) in BASE and (b) in SOCX. Units are $10^{-12}$ mol(C) $m^{-2}$ $s^{-1}$, positive values are fluxes from the ocean into the atmosphere, negative values denote ocean uptake. Annual total global ocean-to-atmosphere gas fluxes are given in g(C). (c) absolute and (d) relative differences in 5-year averaged ocean-to-atmosphere gas flux of $C_5H_8$ between SOCX and BASE. Units are $10^{-12}$ mol(C) $m^{-2}$ $s^{-1}$ and %, respectively. The differences in the annual total global ocean-to-atmosphere gas flux between SOCX and BASE are given in g(C). Contours denote the relative difference in %, the interval between contour lines is 100 %. Differences in ocean-to-atmosphere gas fluxes in gray shaded areas are not significant on a 99 % level according to a two-sided Student's t-test.

larger than in BASE between 40 °N and 40 °S, in some regions up to a factor of three. The band of higher emissions in SOCX is in an area with minimum $C_5H_8$ outgassing in the tropics and subtropics in the baseline experiment. In BASE, the maximum fluxes from the ocean into the atmosphere for $C_5H_8$ are reached at higher

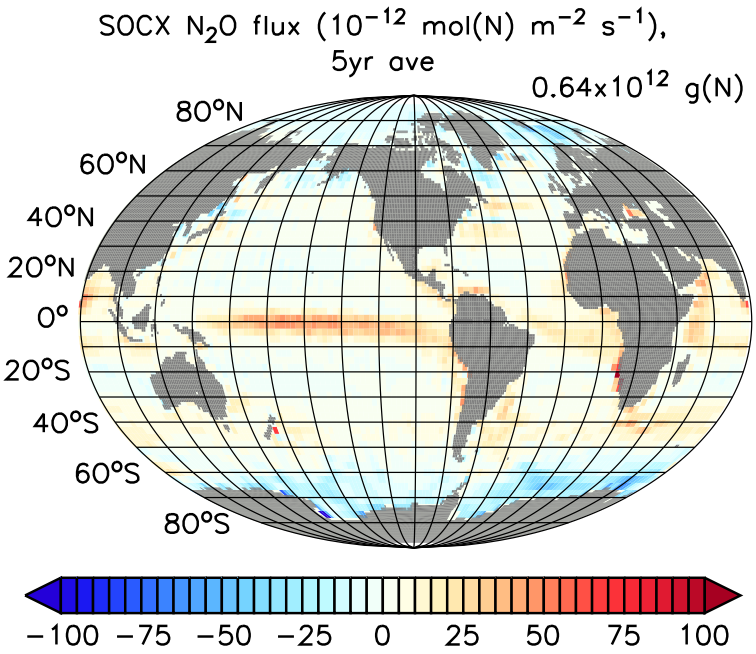


**Figure 4.18:** 5-year average of ocean-to-atmosphere gas fluxes for $N_2O$ in SOCX. Units are $10^{-12}$ mol(N) $m^{-2}$ $s^{-1}$, positive values are fluxes from the ocean into the atmosphere, negative values denote ocean uptake. The annual total global ocean-to-atmosphere gas flux is given in g(N).

latitudes, north of 40 °N in the Atlantic and Pacific, and between 40 °S and 60 °S. This is in line with the surface water $C_5H_8$ concentrations in the baseline simulation (Fig. 4.10). With online calculated surface water $C_5H_8$ concentrations, the maximum outgassing is located in the tropics and subtropics. This is a consequence of the parameterisation of $C_5H_8$ based on chlorophyll concentrations (Eq. 3.10).

The total global annual ocean-to-atmosphere flux of $C_5H_8$ is lower (in both simulations) than the estimates found in literature (Table 4.2). It reaches 0.1 Tg(C) $a^{-1}$ in SOCX, which is at the low end of literature values ranging from 0.1 Tg(C) $a^{-1}$ to 1.2 Tg(C) $a^{-1}$ (Palmer and Shaw, 2005, and references therein), whereas the value of 0.07 Tg(C) $a^{-1}$ in BASE is below these estimates.

### Nitrous oxide ($N_2O$)

The annual averages of the ocean-to-atmosphere $N_2O$ flux in SOCX (Fig. 4.18) show maxima in the equatorial Pacific and south of the Equator in the Atlantic. These maxima are persistent throughout the year (Fig. 4.19) varying, however, in strength, with largest values in August (Fig. 4.19 (h)). The largest variability in the atmosphere-to-ocean flux of $N_2O$ can be seen in the polar regions, with changes from

ocean outgassing of $N_2O$ in the winter months of the particular hemisphere, and ocean uptake during the rest of the year (Fig. 4.19). This reflects the solubility pump for $N_2O$ air-sea gas exchange. For the almost constant oceanic and atmospheric concentrations of $N_2O$, ocean-to-atmosphere flux is controlled by the solubility of $N_2O$ in seawater, which depends on the sea surface temperature.

The total annual global ocean-to-atmosphere flux of $N_2O$ in the sensitivity experiments, for which air-sea gas exchange is calculated from surface ocean chemical concentrations interactively calculated via the oceanic biogeochemical submodel, is $0.64\,\mathrm{Tg(N)\,a^{-1}}$. This value is only about half the lowest ocean-to-atmosphere flux of $N_2O$ estimated in literature (Table 4.2), where the $N_2O$ ocean-to-atmosphere flux is suggested to be in the range of $1.2\,\mathrm{Tg(N)\,a^{-1}}$ to $6.8\,\mathrm{Tg(N)\,a^{-1}}$ (Nevison et al., 1995). As $N_2O$ has no direct impact on the tropospheric chemistry on the time-scale of some years as focused on in this study, atmospheric $N_2O$ mixing ratios were prescribed via the submodel TNUDGE in the atmosphere. The ocean-to-atmosphere $N_2O$ flux in the sensitivity experiment is therefore a purely diagnostic quantity. The too low ocean-to atmosphere flux of $N_2O$ compared to estimates in literature hints to underestimations of surface ocean $N_2O$ concentrations in the sensitivity experiment.

As noted before, the ocean surface $N_2O$ distribution lacks maxima in the tropical high productivity zones (Fig. 4.11 (a)). This deficiency in the model system is also related to the underestimation of NPP in the simulations, as the $N_2O$ ocean concentrations depend on oceanic biogeochemistry—more specifically on aerobic remineralisation of detritus and dissolved organic matter.

### Carbon monoxide (CO)

In BASE, ocean-to-atmosphere fluxes of CO (Fig. 4.20 (a)) exhibit almost no annual cycle, as constant surface concentrations are prescribed throughout the year. Variations in air-sea gas exchange are induced by the meteorological situation only, determining the thermodynamic driving potential as atmospheric CO concentrations change. As CO concentrations in sensitivity studies are determined from photochemical production (Eq. 3.11), maxima in surface ocean CO concentrations and, consequently, maxima in ocean-to-atmosphere fluxes of CO move with sun's zenith. In the annually averaged air-sea gas exchange of CO for the SOCX experiment, maxima in the ocean-to-atmosphere CO flux are apparent in the tropics and subtropics. Compared to the baseline experiment with prescribed CO fluxes from the ocean, SOCX simulates larger annual mean ocean-to-atmosphere fluxes in a latitudinal band

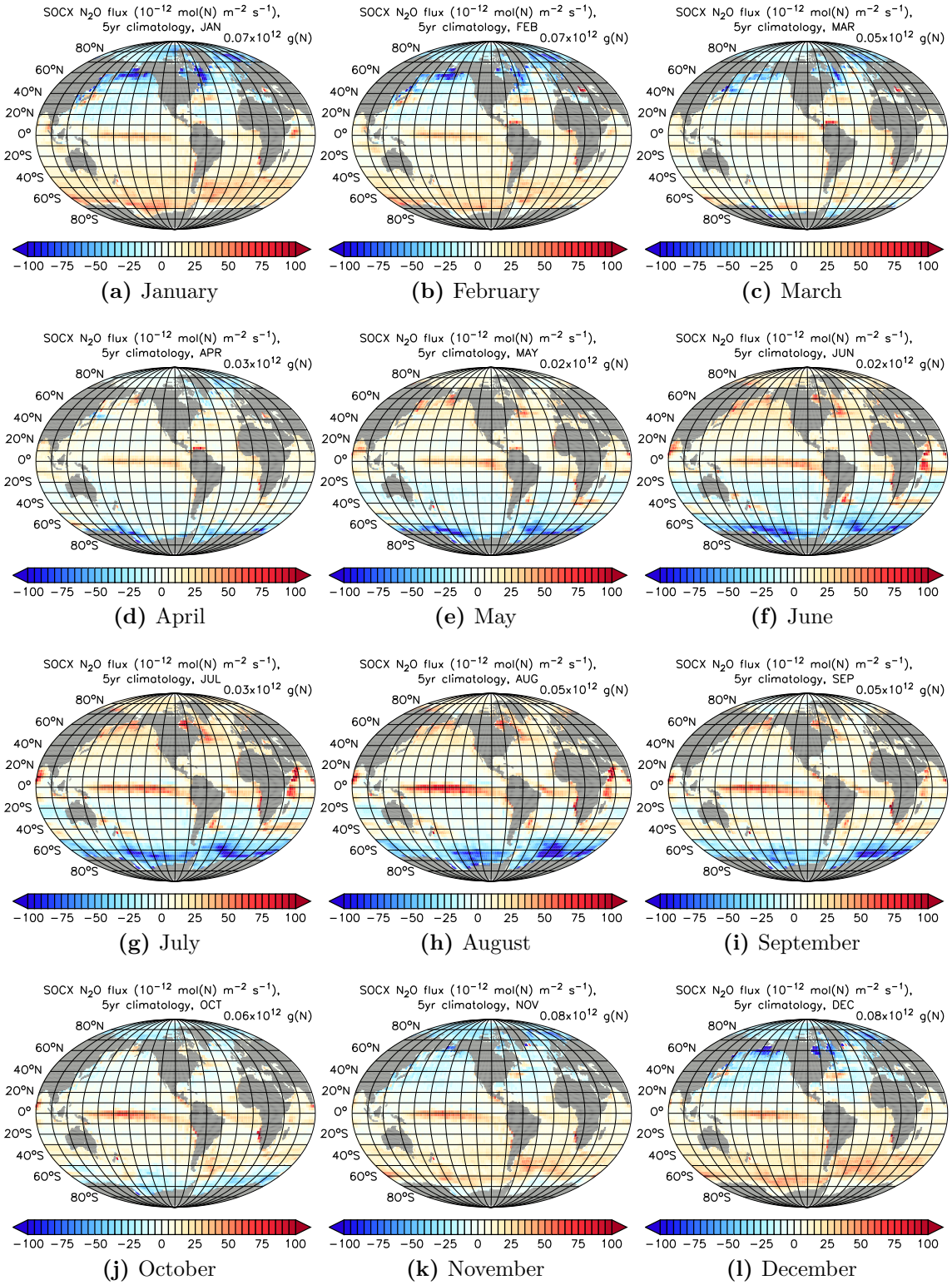


**Figure 4.19:** 5-year monthly climatology of $N_2O$ ocean-to-atmosphere gas fluxes in $10^{-12}\,\mathrm{mol(N)\,m^{-2}\,s^{-1}}$ over five years of SOCX. 5-year averages of the monthly total global ocean-to-atmosphere gas flux are listed in g(N).

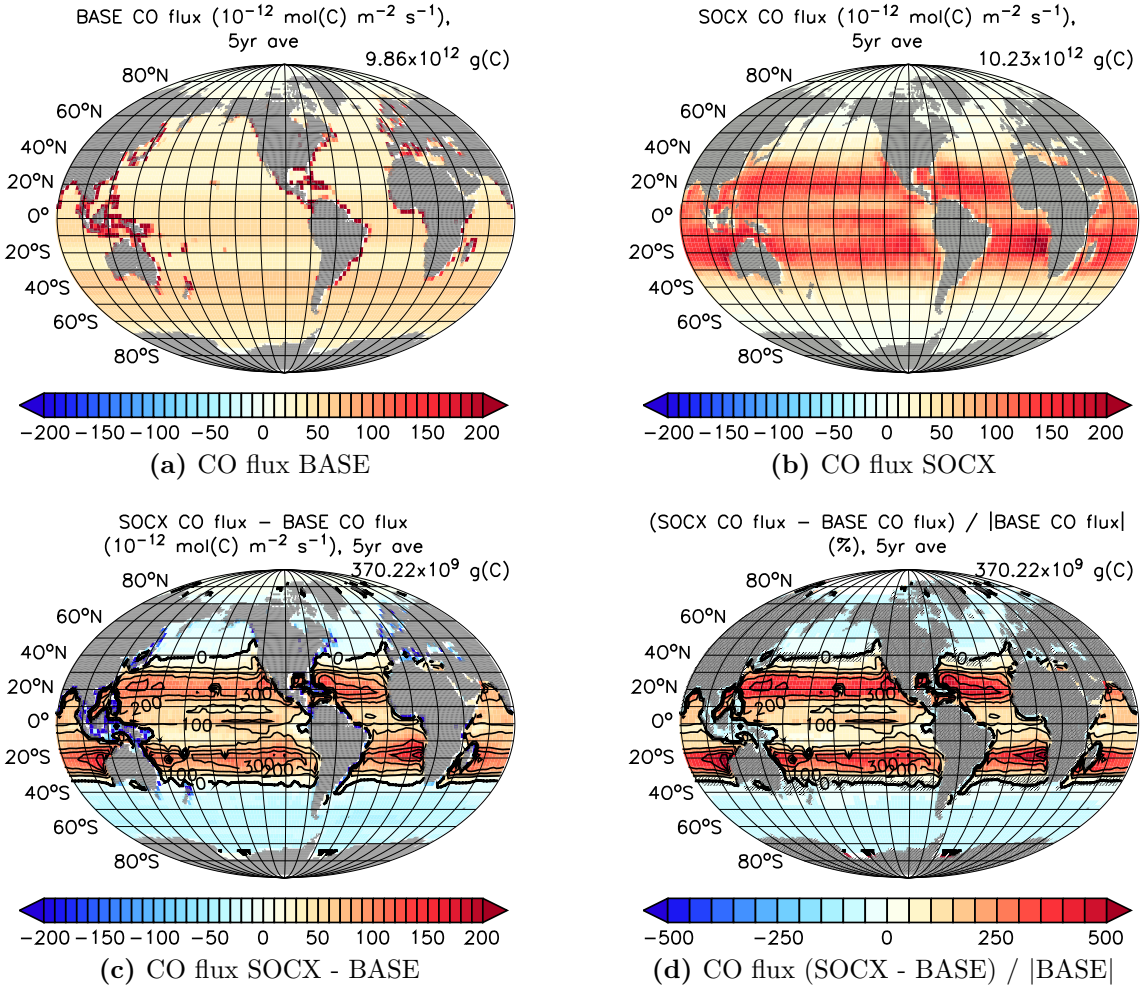


**(a)** CO flux BASE **(b)** CO flux SOCX

**(c)** CO flux SOCX - BASE **(d)** CO flux (SOCX - BASE) / |BASE|

**Figure 4.20:** 5-year averages of ocean-to-atmosphere gas fluxes of CO (a) in BASE and (b) in SOCX. Units are $10^{-12}$ mol(C) $m^{-2}$ $s^{-1}$, positive values are fluxes from the ocean into the atmosphere, negative values denote ocean uptake. Annual total global ocean-to-atmosphere gas fluxes are given in g(C). (c) absolute and (d) relative differences in 5-year averaged ocean-to-atmosphere gas flux of CO between SOCX and BASE. Units are $10^{-12}$ mol(C) $m^{-2}$ $s^{-1}$ and %, respectively. The differences in the annual total global ocean-to-atmosphere gas flux between SOCX and BASE are given in g(C). Contours denote relative differences in %, the interval between contour lines is 100 %. Differences in ocean-to-atmosphere gas fluxes in gray shaded areas are not significant on a 99 % level according to a two-sided Student's t-test.

from 40 °N to 40 °S (Figs. 4.20 (c), 4.20 (c)). Between 20 °N and 20 °S this excess reaches a factor of more than three. In subpolar and polar regions, the annually averaged CO ocean-to-atmosphere fluxes in SOCX are lower by 50 % compared to the fluxes prescribed in BASE.

Total Annual global ocean-to-atmosphere fluxes of CO in BASE and SOCX reach $9.8\,\mathrm{Tg(C)\,a^{-1}}$ and $10.25\,\mathrm{Tg(C)\,a^{-1}}$, respectively. Both results are in accordance with literature values ranging from $8.5\,\mathrm{Tg(C)\,a^{-1}}$ to $86\,\mathrm{Tg(C)\,a^{-1}}$ (Bergamaschi et al., 2000; Ehhalt et al., 2001), however, they are larger than a more recent estimate derived from measurements of $(3.7 \pm 2.6)\,\mathrm{Tg(C)\,a^{-1}}$ by Stubbins et al. (2006).

As the surface concentrations of CO are simulated reasonably well in the model system (cf. Fig. 4.11 (b)), the simulated air-sea fluxes are also expected to be represented well. Compared to the air-sea fluxes of CO in the baseline simulation with constant surface ocean CO concentrations, CO fluxes in SOCX with online calculated surface concentrations show a larger spatial variability, with highest fluxes in the tropical region. This result is in line with the simulated surface ocean CO concentrations (cf. Fig. 4.11 (b)).

### Methanol ($CH_3OH$)

The ocean-to-atmosphere flux of $CH_3OH$ is calculated with an approach using a constant under-saturation of oceanic surface water $CH_3OH$ concentration compared to the atmospheric $CH_3OH$ concentration at the ocean's surface (Singh et al., 2003; Pozzer, 2007). The saturation coefficient for surface ocean water is 0.94 in all simulations conducted in this study. Between the sensitivity studies only differences in air-sea gas exchange of $CH_3OH$ in regions with different atmospheric $CH_3OH$ surface concentrations are expected, as the "virtual" oceanic surface concentration is determined by the saturation coefficient.

In Figure 4.21 the annually averaged net $CH_3OH$ fluxes for BASE and SOCX, as well as differences in the annually averaged ocean-to-atmosphere $CH_3OH$ fluxes between the two experiments are presented. Due to the approach using a saturation coefficient for surface ocean water concentrations of $CH_3OH$ smaller than 1, an under-saturation with respect to the atmospheric concentration of $CH_3OH$ is prescribed over the whole ocean domain. Consequently, ocean-to-atmosphere fluxes for $CH_3OH$ are negative over the ocean (Figs. 4.21 (a), 4.21 (b)).

Relative differences in the annually averaged $CH_3OH$ air-sea gas exchange between SOCX and BASE are in the range of $-4\,\%$ to $20\,\%$ and reach significant levels only regionally in the Pacific east of New Zealand and west of the South American coast (Figs. 4.21 (c), 4.21 (d)). Warm colours (and positive values) in Figures 4.21 (c) and 4.21 (d) denote lower $CH_3OH$ ocean uptake in SOCX, thus lower atmospheric mixing

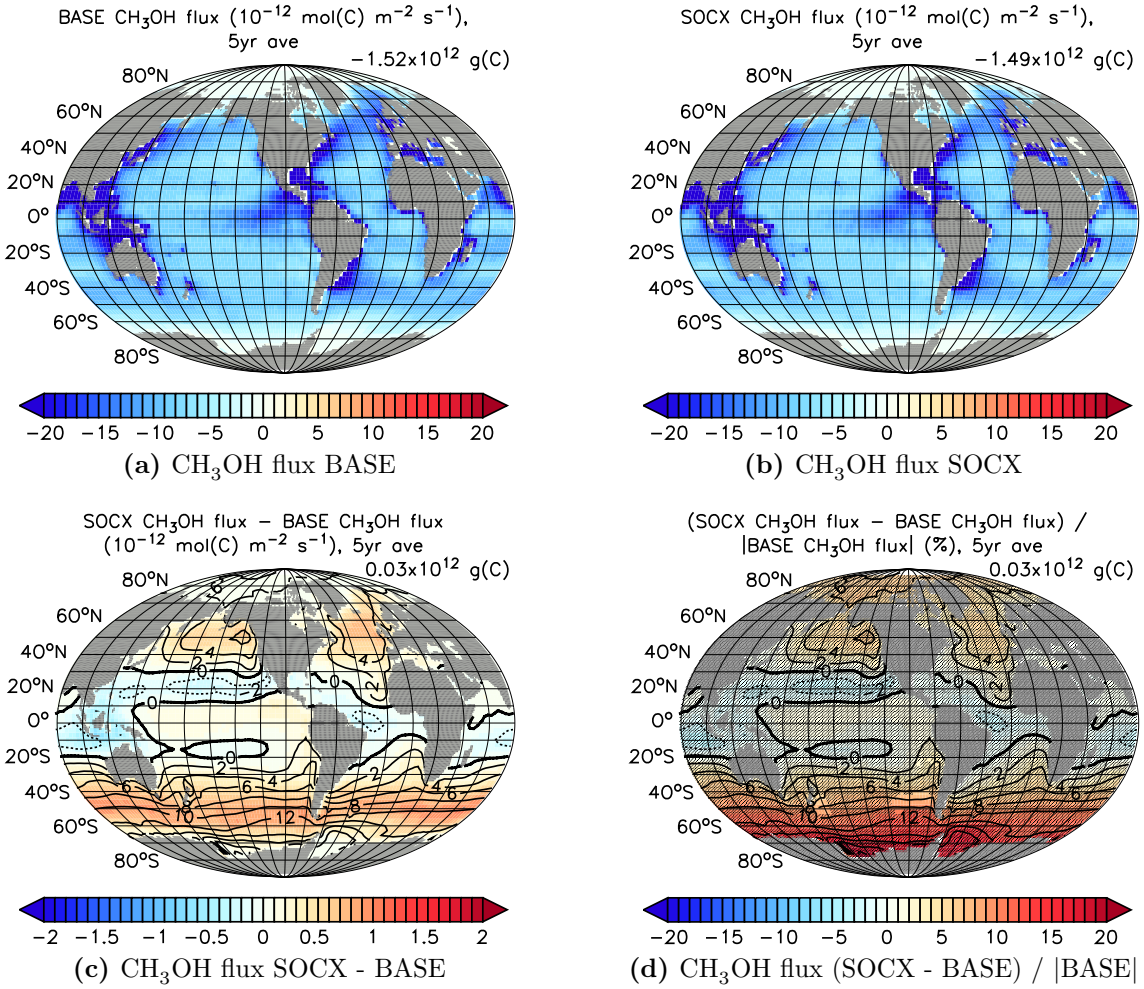


**(a)** $CH_3OH$ flux BASE **(b)** $CH_3OH$ flux SOCX

**(c)** $CH_3OH$ flux SOCX - BASE **(d)** $CH_3OH$ flux (SOCX - BASE) / |BASE|

**Figure 4.21:** Averages of ocean-to-atmosphere gas fluxes for $CH_3OH$ (a) in BASE and (b) in SOCX over five years. Units are $10^{-12}$ mol(C) $m^{-2}$ $s^{-1}$, positive values are fluxes from the ocean into the atmosphere, negative values denote ocean uptake. The total annual global ocean-to-atmosphere gas flux is given in g(C). (c) absolute and (d) relative differences in 5-year averaged ocean-to-atmosphere gas flux of $CH_3OH$ between SOCX and BASE. Units are $10^{-12}$ mol(C) $m^{-2}$ $s^{-1}$ and %, respectively. The difference in the annual total global ocean-to-atmosphere gas flux between SOCX and BASE is given in g(C). Contours denote the relative difference, the interval between contour lines is 2 %. Differences in ocean-to-atmosphere gas fluxes in gray shaded areas are not significant on a 99 % level according to a two-sided Student's t-test.

ratios of $CH_3OH$ are expected in the polar regions in SOCX compared to BASE. In the regions of larger $CH_3OH$ uptake in SOCX (cold colours; negative values) higher atmospheric mixing ratios of $CH_3OH$ than in BASE are expected in SOCX.

#### Relation between ocean-to-atmosphere flux and surface water concentration

Investigation of the relation between oceanic surface water concentrations and the ocean-to-atmosphere fluxes results in scatter diagrams as shown in Fig. 4.22 for DMS, $C_5H_8$, CO, $CO_2$, and $N_2O$. For the trace gases relevant for tropospheric chemistry, whose atmospheric concentrations are determined interactively by the atmospheric chemistry submodel (DMS, $C_5H_8$, and CO), a compact, in first approximation linear relation of their ocean-to-atmosphere flux with the corresponding surface water concentration are found. The linear response of the ocean-to-atmosphere flux of these gases to their oceanic surface water concentration gives confidence in the model system's ability to respond reasonably to sufficiently moderate changes in the oceanic concentration and, hence, corresponding changes in oceanic biogeochemistry.

### 4.2.3 Impact on atmospheric composition

The atmospheric chemical composition in the marine boundary layer and—depending on the atmospheric residence times of the species and its chemical products in focus—the free troposphere is impacted by gas exchange at the ocean's interface. This is analysed next.

#### Dimethyl sulphide (DMS), sulphur dioxide ($SO_2$), and sulphuric acid ($H_2SO_4$)

The atmospheric burden of DMS integrated between the surface and 850 hPa in the baseline simulation (BASE) and in the sensitivity simulation with air-sea gas exchange determined from surface ocean concentrations interactively simulated by the HAMOCC submodel (SOCX) is presented in Figure 4.23. A significant decrease of DMS is apparent over the Southern Ocean in SOCX compared to BASE (Figs. 4.23 (c), 4.23 (d)). This reduction is directly linked to the smaller ocean-to-atmosphere fluxes of DMS in SOCX (Fig. 4.12), related to lower ocean surface concentrations of DMS compared to BASE in this region (Fig. 4.8). A lower atmospheric DMS burden near the surface in SOCX is also simulated in the northern Atlantic, the equatorial and the northern Pacific. The atmospheric DMS burden is larger in the sensitivity simulation over the Indic, the subtropical and tropical Atlantic, and the subtropical Pacific, where locally more than three times the values of the BASE simulation are reached. The pattern of differences in the atmospheric DMS burden

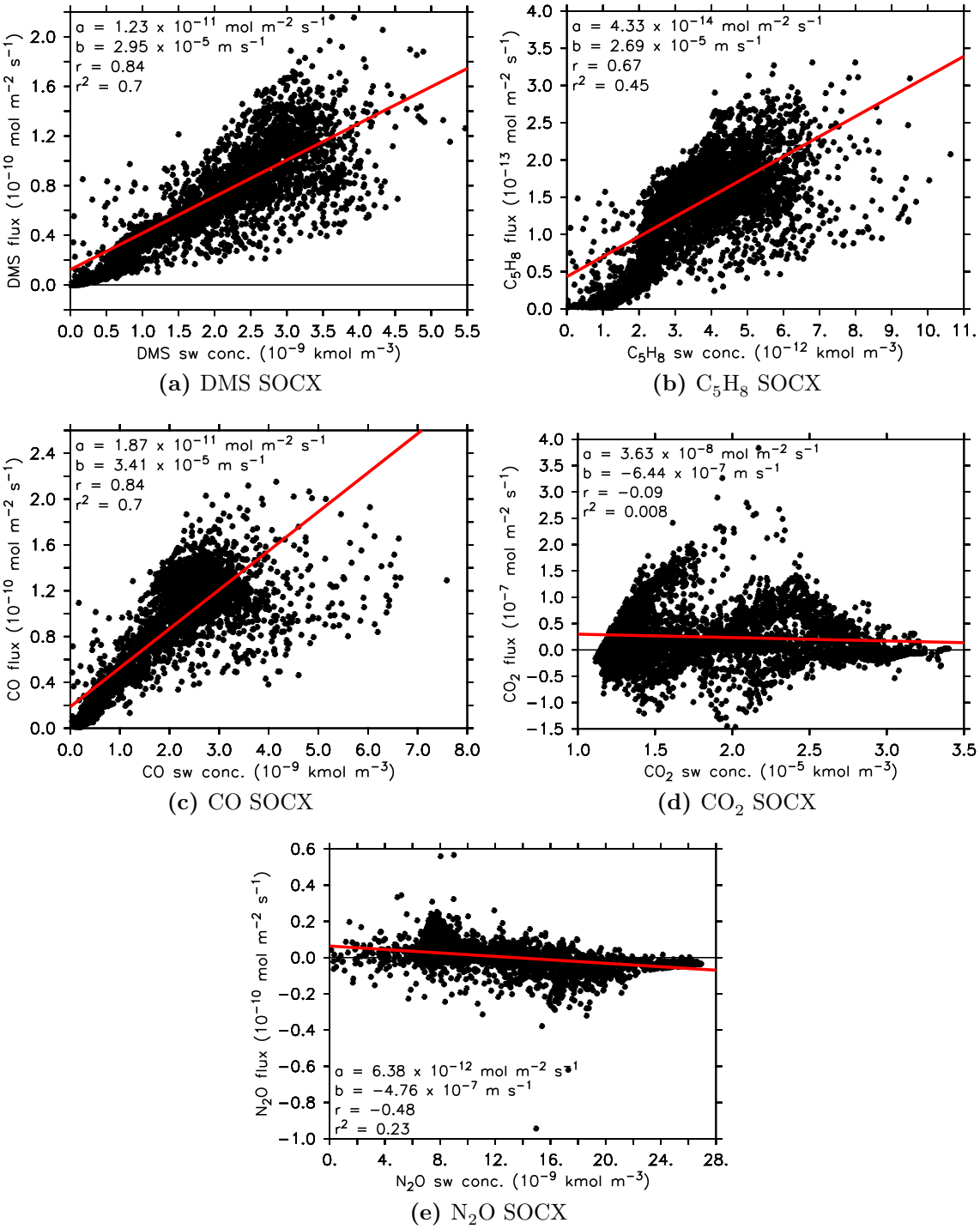


**(a)** DMS SOCX **(b)** $C_5H_8$ SOCX

**(c)** CO SOCX **(d)** $CO_2$ SOCX

**(e)** $N_2O$ SOCX

**Figure 4.22:** Scatter diagrams of ocean-to-atmosphere fluxes versus surface water concentration at each model grid-point for (a) DMS, (b) $C_5H_8$, (c) CO, (d) $CO_2$, and (e) $N_2O$. In red linear regression lines, calculated using the method of least squares, are shown. The regression coefficients $a$ and $b$, the sample correlation coefficient $r$, and the squared correlation coefficient $r^2$ are listed for the individual gases.

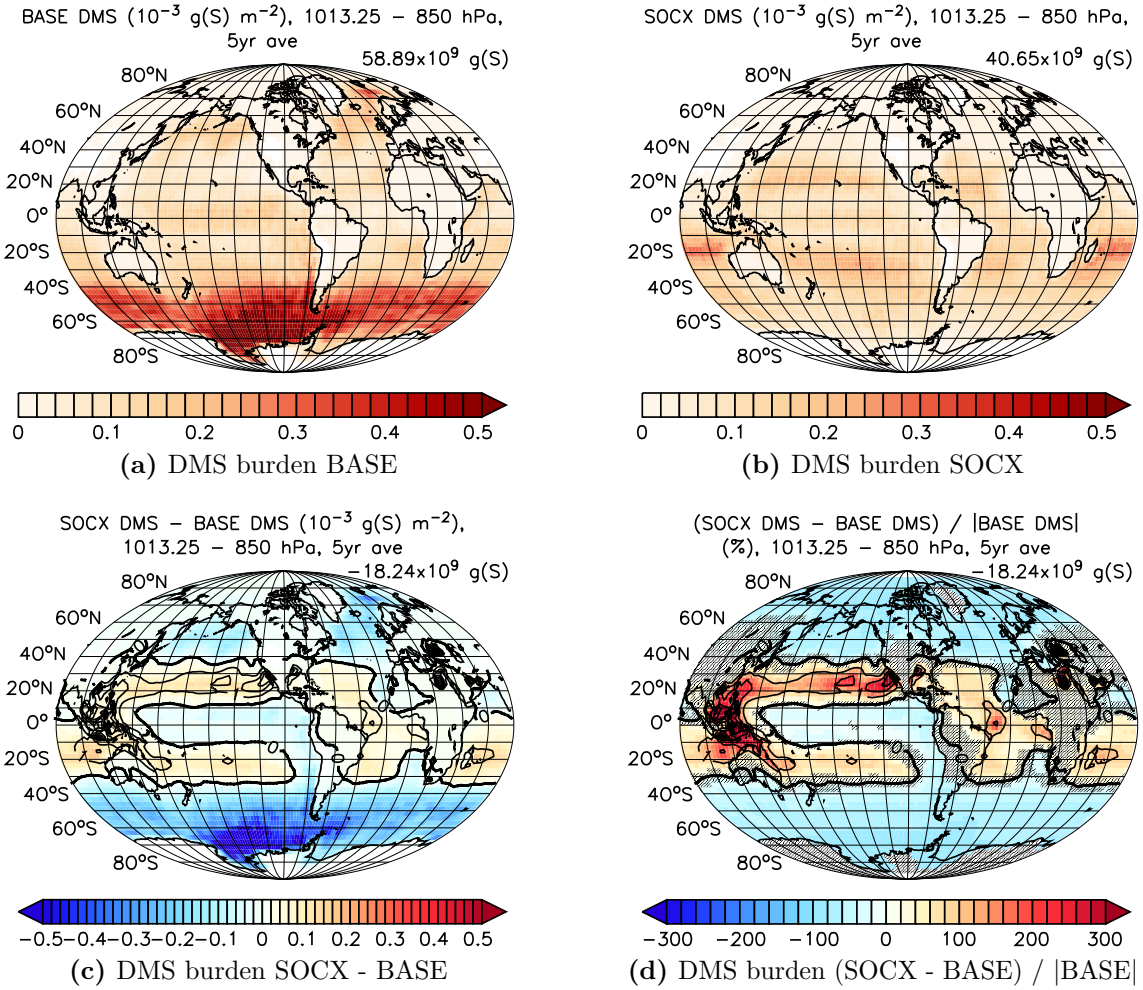


**(a)** DMS burden BASE **(b)** DMS burden SOCX

**(c)** DMS burden SOCX - BASE **(d)** DMS burden (SOCX - BASE) / |BASE|

**Figure 4.23:** 5-year averages of atmospheric DMS burden integrated from the surface to 850 hPa (a) in BASE and (b) in SOCX. Units are $10^{-3}$ g(S) $m^{-2}$. The annual average global burden between the surface and 850 hPa is listed in g(S). (c) absolute and (d) relative differences in 5-year averaged atmospheric DMS burden between SOCX and BASE. Units are $10^{-3}$ g(S) $m^{-2}$ and %, respectively. The difference in the yearly averaged global atmospheric DMS burden integrated from the surface to 850 hPa between SOCX and BASE is given in g(S). Contours denote relative differences in %, the interval between contour lines is 100 %. Differences in atmospheric burdens in gray shaded areas are not significant on a 99 % level according to a two-sided Student's t-test.

between the surface and 850 hPa (Figs. 4.23 (c), 4.23 (d)) is directly correlated with the difference pattern of DMS ocean-to-atmosphere fluxes between BASE and SOCX (Figs. 4.12 (c), 4.12 (d)). This shows the direct impact of elevated and suppressed ocean-to-atmosphere fluxes on the near surface atmospheric DMS mixing ratios.

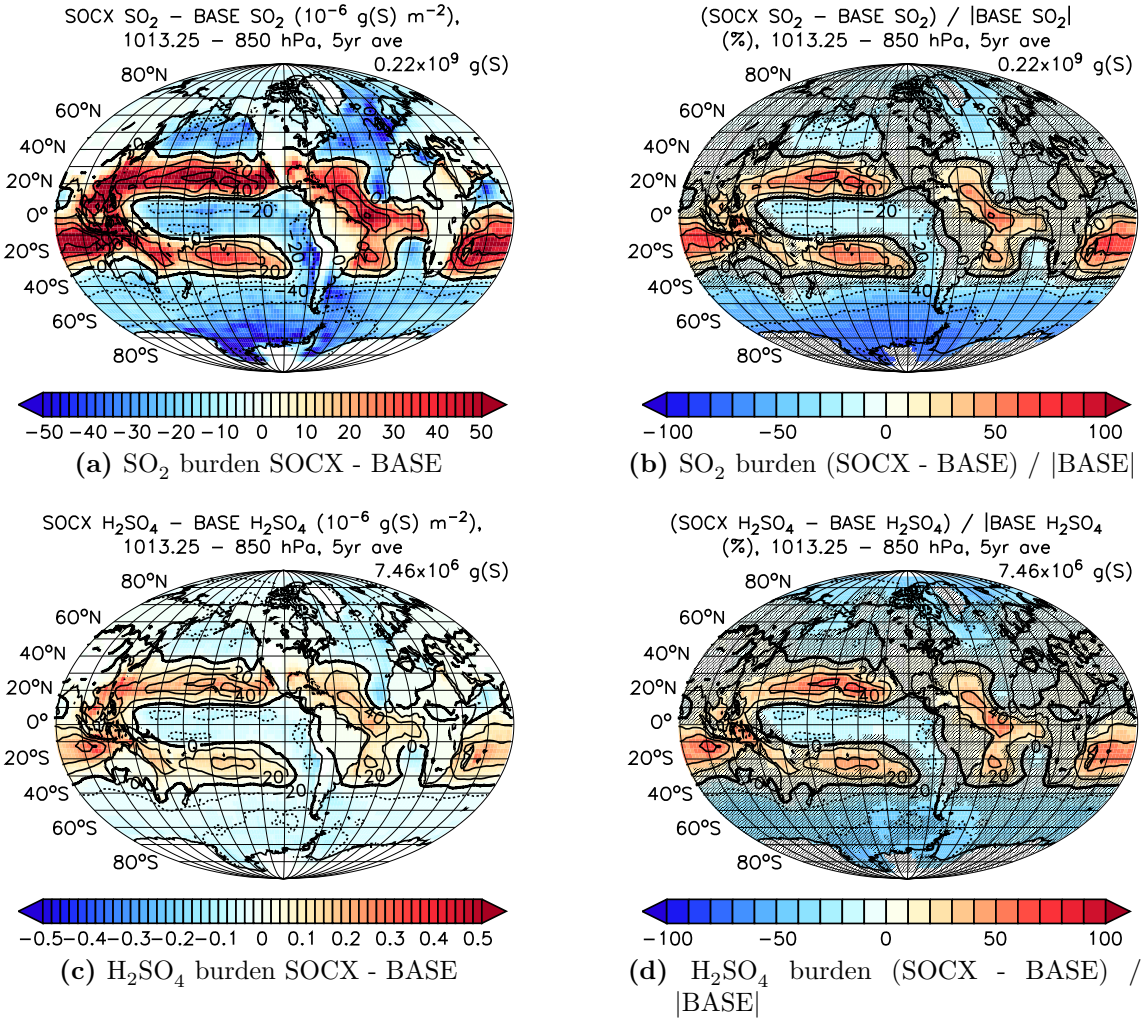


**(a)** $SO_2$ burden SOCX - BASE

**(b)** $SO_2$ burden (SOCX - BASE) / |BASE|

**(c)** $H_2SO_4$ burden SOCX - BASE

**(d)** $H_2SO_4$ burden (SOCX - BASE) / |BASE|

**Figure 4.24:** Absolute (left column) and relative (right column) differences in atmospheric (a), (b) $SO_2$ and (c), (d) $H_2SO_4$ burden integrated from the surface up to 850 hPa between SOCX and BASE. Units are $10^{-6}$ g(S) $m^{-2}$ for (a), (c) and % for (b), (d). Differences in the annual averaged global atmospheric burden integrated from the surface to 850 hPa between SOCX and BASE are listed in g(S). Contours denote relative differences in %, the interval between contour lines is 20 %. Differences in atmospheric burdens in gray shaded areas are not significant on a 99 % level according to a two-sided Student's t-test.

Sulphur dioxide ($SO_2$) is a product of DMS oxidation with the hydroxyl radical (OH) and the nitrate radical ($NO_3$) in the atmosphere (Section 2.2.1). The differences between SOCX and BASE of the atmospheric burden of $SO_2$ (Figs. 4.24 (a), 4.24 (b)) in the lower atmosphere up to 850 hPa exhibit the same difference patterns as DMS (Figs. 4.23 (c), 4.23 (d)). The near surface atmospheric burden of $SO_2$ is significantly higher in SOCX, with values exceeding the BASE simulation by more than 60 %,

in the subtropical Pacific and throughout the tropical and subtropical Atlantic and Indic (Fig. 4.24 (b)). Lower values in SOCX are found in the equatorial Pacific and at the western coast of South America, as well as in the polar oceans. In the Antarctic Ocean, the atmospheric $SO_2$ burden up to 850 hPa reaches only 30 % of the value in BASE. This is associated with the strong DMS source in Antarctic waters in BASE, which are not reproduced in the SOCX experiment (Fig. 4.12).

A further secondary product of atmospheric DMS oxidation, forming via the reaction of $SO_2$ with OH is $H_2SO_4$. In Figures 4.24 (c) and 4.24 (d) absolute and relative differences in the annually averaged atmospheric $H_2SO_4$ burden between the surface and 850 hPa are presented, respectively. The differences in the distribution of $H_2SO_4$ are similar to those of $SO_2$ and DMS. Significant changes of $H_2SO_4$ between BASE and SOCX are simulated in areas of correspondingly significant changes in $SO_2$ burdens. However, the effect is weaker for $H_2SO_4$, as it is scavenged efficiently from the gas-phase. Over the Southern Ocean, a significant decrease of the atmospheric $H_2SO_4$ burden in the layer up to 850 hPa can only be found between 30 °W to 180 °W with respect to BASE. This is the area with the largest decrease in ocean-to-atmosphere fluxes of DMS (Fig. 4.12 (c)) and surface water DMS concentrations (Fig. 4.8 (f)) in SOCX compared to BASE.

Differences in the zonally averaged mixing ratios of DMS, $SO_2$, and $H_2SO_4$ between SOCX and BASE averaged over five years of simulation are presented in Figure 4.25 for the whole troposphere. Common features of all three tracer distributions are the lower mixing ratios in SOCX compared to BASE in the subpolar and polar regions and higher mixing ratios in the subtropics and tropics. Significantly lower atmospheric DMS mixing ratios are simulated also at high latitudes up to 200 hPa in SOCX, reaching less than 20 % of the mixing ratios in BASE (Fig. 4.25 (a)). Two maxima of significantly higher DMS mixing ratios compared to BASE are apparent between 0° and 30 °S and between 10 °N and 30 °N, reaching a local maximum of more than two times the DMS mixing ratio of BASE at about 800 hPa between 20 °N and 30 °N.

The differences between the zonally averaged $SO_2$ mixing ratios in SOCX and BASE (Fig. 4.25 (b)) resemble the corresponding differences of DMS mixing ratios. Over the Southern Ocean, simulated $SO_2$ mixing ratios in SOCX are significantly lower than in the BASE simulation, reaching only 20 % of the value in BASE at 75 °S near the surface. In the southern tropics $SO_2$ mixing ratios are higher in SOCX compared to BASE throughout the atmosphere. In the northern hemisphere,

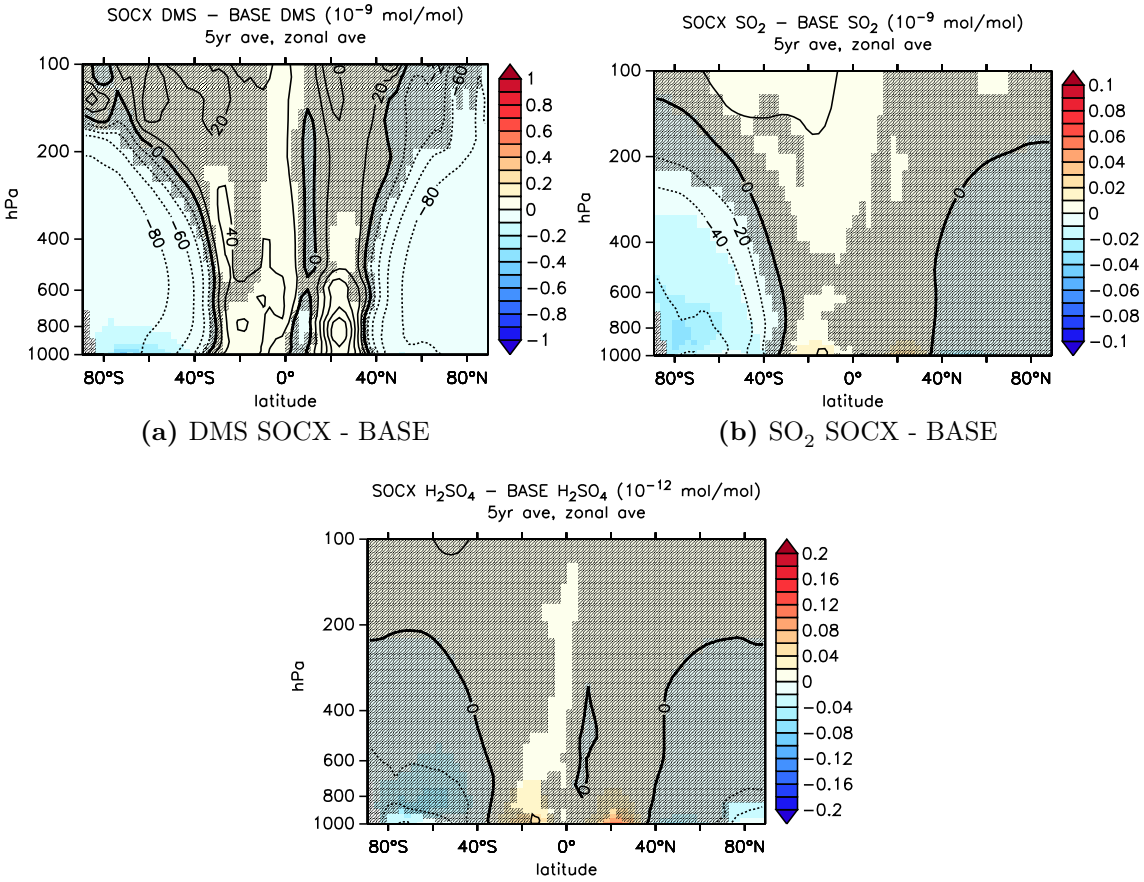


**(a)** DMS SOCX - BASE

**(b)** $SO_2$ SOCX - BASE

**(c)** $H_2SO_4$ SOCX - BASE

**Figure 4.25:** Differences of zonally averaged atmospheric mixing ratios of DMS (in $10^{-9}$ mol mol$^{-1}$), $SO_2$ (in $10^{-9}$ mol mol$^{-1}$), and $H_2SO_4$ (in $10^{-12}$ mol mol$^{-1}$) between SOCX and BASE averaged over five years. Contour lines denote relative differences in mixing ratios between SOCX and BASE in %, the interval between contour lines is 20 %. Differences in mixing ratios in gray shaded areas are not significant on a 99 % level according to a two-sided Student's t-test.

the meridional gradient of DMS is similar as in the southern hemisphere, but no significant changes are detected in the zonally averaged atmospheric $SO_2$ mixing ratios.

The differences in zonally averaged $H_2SO_4$ mixing ratios (Fig. 4.25 (c)) are similar to the difference patterns in DMS and $SO_2$ mixing ratios between SOCX and BASE. The absolute differences in the $H_2SO_4$ mixing ratios are smaller than in the $SO_2$ mixing ratios, as $H_2SO_4$ is a product of $SO_2$ oxidation and it is efficiently removed from the gas-phase by scavenging and wet deposition due to its high solubility. The main features are the significantly lower atmospheric $H_2SO_4$ mixing ratios near the surface in SOCX compared to BASE between 60 °S and 80 °S and poleward of 70 °N,

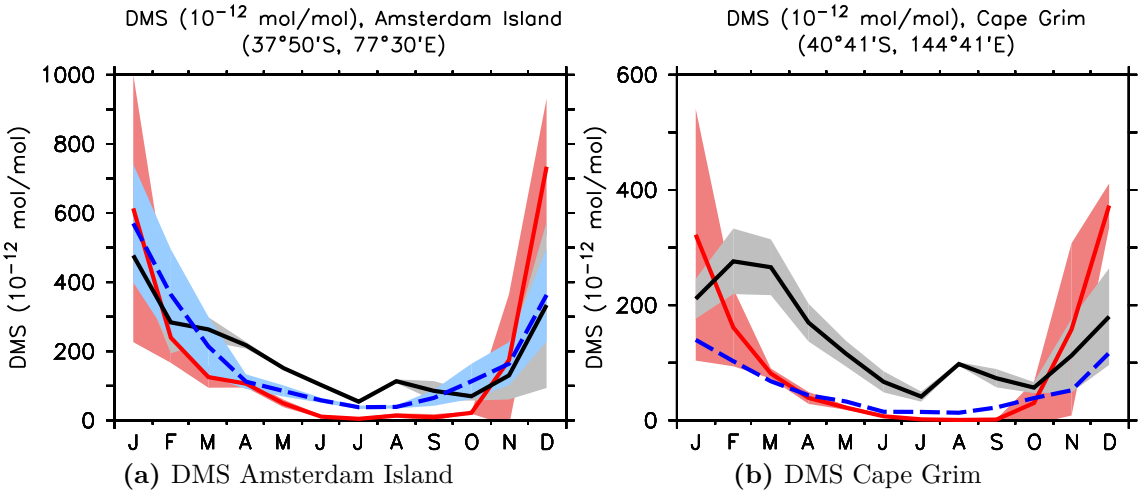


**(a)** DMS Amsterdam Island **(b)** DMS Cape Grim

**Figure 4.26:** Monthly atmospheric DMS mixing ratios in $10^{-12}$ mol mol$^{-1}$ at (a) Amsterdam Island and (b) Cape Grim. Blue broken lines denote measurements from Sciare et al. (2000) for the period 1990 to 1999 at Amsterdam Island and from Ayers et al. (1995) for the period 1988 to 1993 at Cape Grim, black lines are 5-year monthly climatologies from the BASE simulation, red lines are 5-year monthly climatologies from the SOCX simulation. Shaded areas denote inter-annual monthly standard deviations, for Cape Grim no standard deviations have been reported for the observations.

and the significantly larger $H_2SO_4$ mixing ratios in the subtropics near the surface at 30 °N and between 0° and 20 °S, reaching higher up into the atmosphere in the convection zones.

A comparison of the BASE and the SOCX results with measurements over more than ten years at Amsterdam Island in the South Pacific (Sciare et al., 2000) and over four and a half years at Cape Grim in Tasmania (Ayers et al., 1995) are shown in Figure 4.26. Both simulations reasonably capture the annual cycle of atmospheric DMS mixing ratios at these measurement stations. However, in SOCX the maximum of DMS mixing ratios at Amsterdam Island is simulated one month too early (December) with too large value and with a larger inter-annual variability. From April to June and in August, atmospheric DMS mixing ratios are overestimated in the baseline simulation, while in SOCX they are underestimated from May to October.

At Cape Grim, the SOCX simulation is more in line with the measurements than BASE. In BASE, the atmospheric DMS mixing ratios at the measurement station are overestimated throughout the year. The annual maximum is shifted by one month, from January (in the measurements) to February (in the simulation). In the SOCX

simulation, DMS mixing ratios are overestimated from October to February, with the maximum simulated one month too early, in December. A small underestimation can be seen in SOCX also during the period July to September. Overall, both simulations reproduce the measurements at the two stations reasonably well, given the issue that comparisons of point measurements with model simulations on a coarse grid have to be treated with caution.

In summary, the differences in atmospheric mixing ratios of DMS resemble the spatial pattern of the differences in the ocean-to-atmosphere DMS flux. This pattern is reproduced in the atmospheric burden near the surface (Fig. 4.23) and in the zonal DMS distribution (Fig. 4.25 (a)). The products of atmospheric DMS oxidation, $SO_2$ and $H_2SO_4$, show differences similar to those in atmospheric DMS mixing ratios (Figs. 4.24, 4.25 (b), 4.25 (c)). This indicates a reasonable simulation of the response of atmospheric mixing ratios of the sulphur containing species to a modified air-sea gas exchange of DMS, which can be considered as forcing for the atmospheric composition at the lower boundary of the domain.

### Isoprene ($C_5H_8$), formaldehyde (HCHO), hydroxyl radical (OH), ozone ($O_3$), carbon monoxide (CO), and methanol ($CH_3OH$)

Relative differences in the atmospheric burden of $C_5H_8$ up to 850 hPa between SOCX and BASE, shown in Figure 4.27 (a), are directly related to changes in the $C_5H_8$ air-sea gas exchange between SOCX and BASE (Fig. 4.17 (d)), as all the other sources of $C_5H_8$ are identical in both simulations. Atmospheric $C_5H_8$ mixing ratios in the lower atmosphere over the ocean are significantly larger in the tropics and subtropics, whereas over the polar oceans significantly lower mixing ratios are found in SOCX compared to the baseline simulation. This effect is limited to the atmosphere above the ocean, thus only slightly elevated $C_5H_8$ mixing ratios are seen near the Equator after averaging zonally in Figure 4.28 (a). The relative differences in the zonally averaged atmospheric mixing ratios between SOCX and BASE in the tropical and subtropical atmosphere are below 20 %, as the small differences over land are also taken into account in the zonal average. Additionally, $C_5H_8$ emissions over land are much higher than over the ocean.

The effect of lower $C_5H_8$ emissions from the polar and subpolar ocean in SOCX is apparent in the atmospheric $C_5H_8$ mixing ratios in the lower atmosphere. The relative differences between SOCX and BASE in zonally averaged $C_5H_8$ mixing ratios at latitudes between 50 °S and 90 °S is more than −60 % (Fig. 4.28 (a)) because

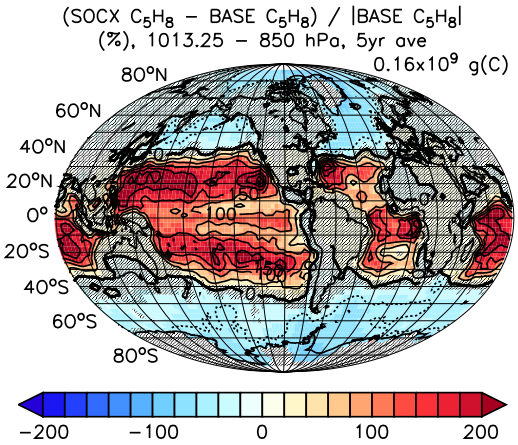


**(a)** $C_5H_8$ burden (SOCX - BASE) / |BASE|

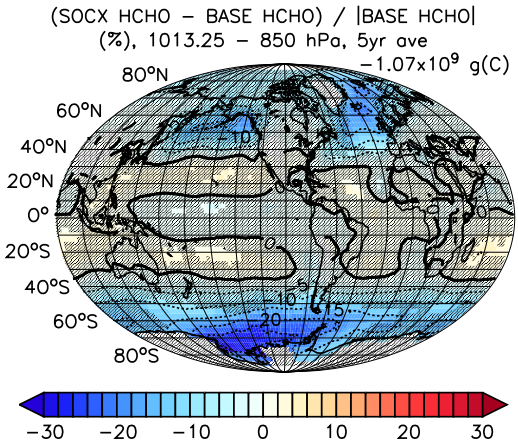


**(b)** HCHO burden (SOCX - BASE) / |BASE|

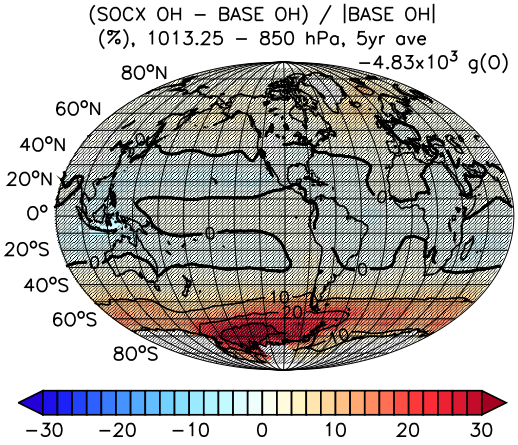


**(c)** OH burden (SOCX - BASE) / |BASE|

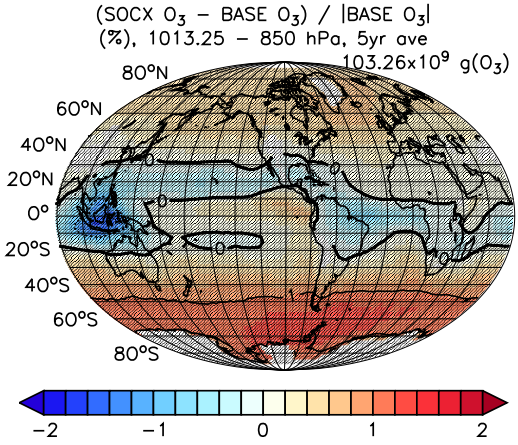


**(d)** $O_3$ burden (SOCX - BASE) / |BASE|

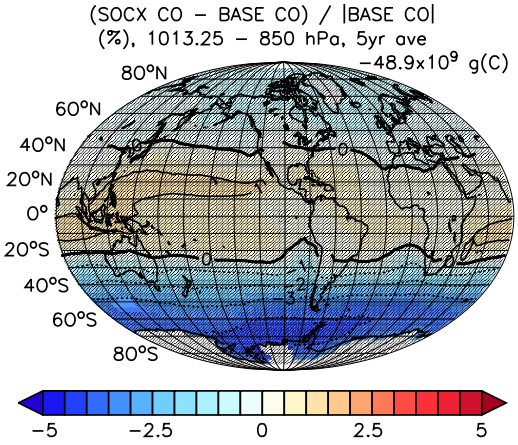


**(e)** CO burden (SOCX - BASE) / |BASE|

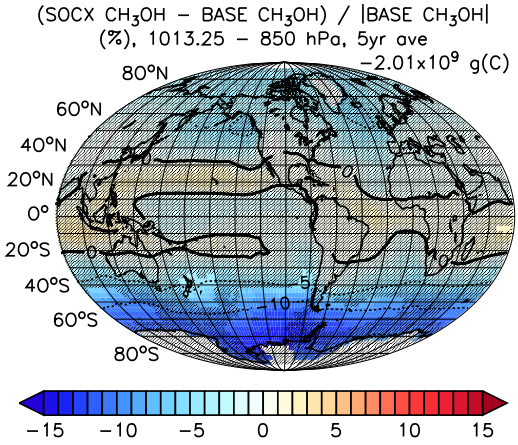


**(f)** $CH_3OH$ burden (SOCX - BASE) / |BASE|

**Figure 4.27:** Relative differences in atmospheric burden integrated from the surface up to 850 hPa of $C_5H_8$, HCHO, OH, $O_3$, CO, and $CH_3OH$ between SOCX and BASE averaged over five years of simulation. Units are %. The interval between contour lines is for (a) 50 %, for (b) 5 %, for (c) 10 %, for (d) and (e) 1 %, and for (f) 5 %. Differences in gray shaded areas are not significant on a 99 % level according to a two-sided Student's t-test.

of the large ocean coverage. At high northern latitudes between 70 °N and 90 °N changes in atmospheric $C_5H_8$ mixing ratios are significant, with the lowest values reaching less than 20 % of the original $C_5H_8$ mixing ratio in BASE.

The modified atmospheric $C_5H_8$ mixing ratios in SOCX have a direct impact on atmospheric mixing ratios of HCHO, OH, and $O_3$. This can be seen in the relative differences of atmospheric burdens integrated between the surface and 850 hPa (Figs. 4.27 (b)–(d)) and the zonally averaged atmospheric mixing ratios (Figs. 4.28 (b)–(d)) of these species. The differences in atmospheric burdens of OH, $O_3$, and CO are, however, statistically not significant on a 99 % confidence level over the five years of simulation. This could be related to the short time-span used for the analysis, and needs to be analysed with longer simulations. Alternatively, inherently stabilising effects could be responsible as well. It is known, for instance, that the $HO_x$ cycle in the atmosphere is well buffered (Lelieveld et al., 2002, 2008; Montzka et al., 2011).

Nonetheless, also the insignificant difference patterns in atmospheric burdens of OH, $O_3$, and CO are consistent and can be explained by the simulated atmospheric chemistry. In the atmosphere $C_5H_8$ reacts with OH and $O_3$ forming HCHO (see Section 2.2.1). In regions with lower $C_5H_8$ mixing ratios less HCHO is formed and OH and $O_3$ mixing ratios are higher in SOCX than in the baseline experiment. Therefore, reduced atmospheric HCHO mixing ratios in SOCX in the equatorial Pacific (Fig. 4.27 (b)) coincide with larger atmospheric OH and $O_3$ mixing ratios in this region (Figs. 4.27 (c), 4.27 (d)).

Changes in the atmospheric distribution of CO between SOCX and BASE (Figs. 4.27 (e), 4.28 (e)) are caused by different oceanic CO emissions (Fig. 4.20), the changed atmospheric mixing ratios of HCHO as precursor of CO, and the modified atmospheric mixing ratios of OH, acting as CO sink (see Section 2.2.1).

Differences in the atmospheric distribution of $CH_3OH$ (Figs. 4.27 (f), 4.28 (f)) can be explained by the changes in OH. In polar regions, where more OH is present in SOCX, more $CH_3OH$ is oxidised to HCHO. In regions with lower atmospheric OH mixing ratios, over the subtropical Pacific, the subtropical and tropical Atlantic, and the Indic, less $CH_3OH$ is oxidised compared to BASE.

The patterns of near surface differences of atmospheric $CH_3OH$ mixing ratios explain the changes in the ocean-to-atmosphere flux in $CH_3OH$ between SOCX and BASE (Fig. 4.21). As a constant under-saturation of $CH_3OH$ in oceanic surface water with respect to the atmosphere is assumed (Singh et al., 2003; Pozzer, 2007), increased (decreased) ocean uptake in form of smaller (larger) ocean-to-atmosphere

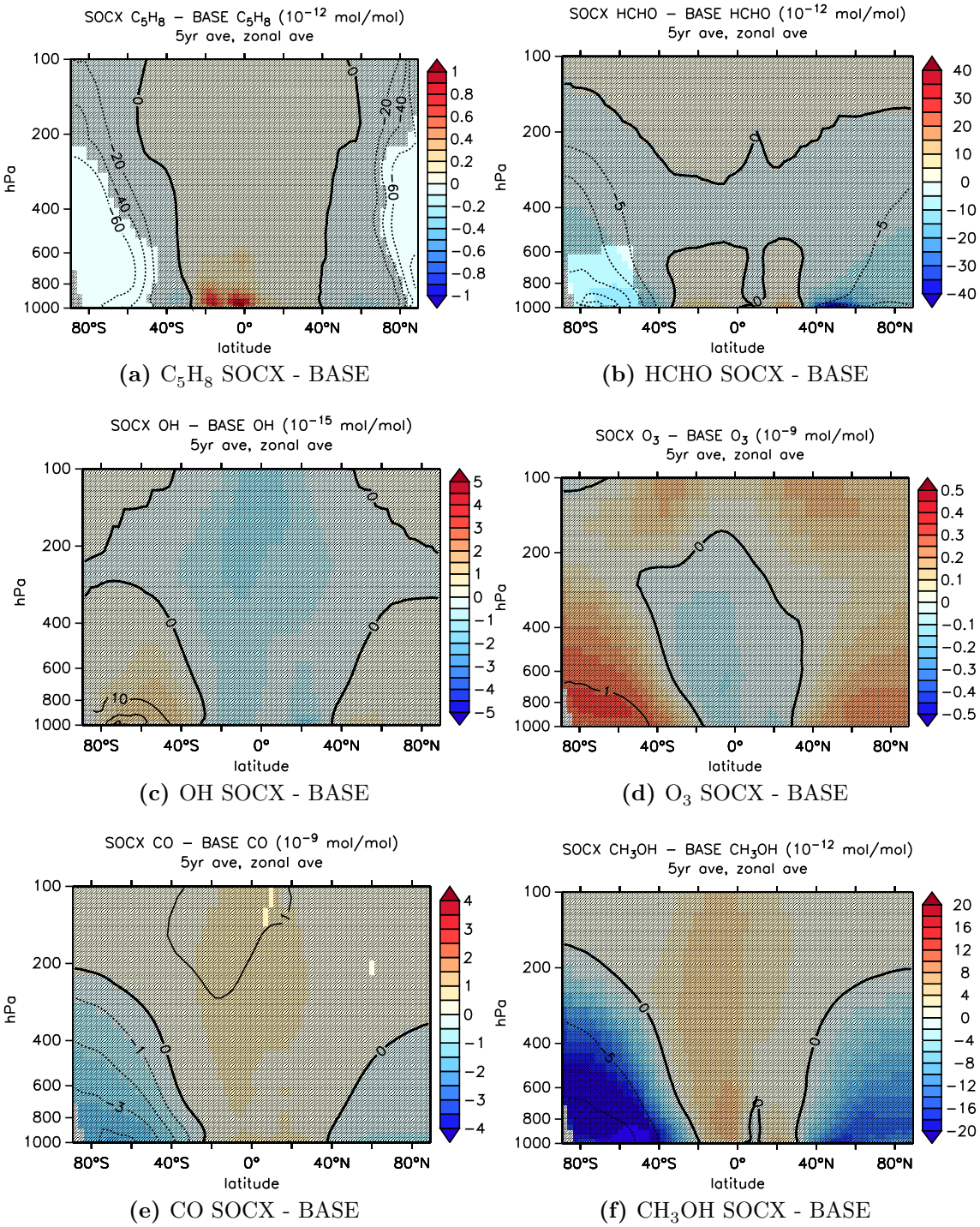


**(a)** $C_5H_8$ SOCX - BASE **(b)** HCHO SOCX - BASE

**(c)** OH SOCX - BASE **(d)** $O_3$ SOCX - BASE

**(e)** CO SOCX - BASE **(f)** $CH_3OH$ SOCX - BASE

**Figure 4.28:** Differences of zonally averaged atmospheric mixing ratios of $C_5H_8$ (in $10^{-12}$ mol mol$^{-1}$), HCHO (in $10^{-12}$ mol mol$^{-1}$), $O_3$ (in $10^{-9}$ mol mol$^{-1}$), OH (in $10^{-15}$ mol mol$^{-1}$), CO (in $10^{-9}$ mol mol$^{-1}$), and $CH_3OH$ (in $10^{-12}$ mol mol$^{-1}$) between SOCX and BASE averaged over five years. Contour lines denote relative differences in mixing ratios between SOCX and BASE in %, the interval between contour lines is for (a), (a) 20 %, for (d) 1 %, for (c) 10 %, for (e) 1 %, and for (f) 5 %. Differences in mixing ratios in gray shaded areas are not significant on a 99 % level according to a two-sided Student's t-test.

fluxes (Figs. 4.21 (c), 4.21 (d)) are simulated in regions with larger (smaller) near surface atmospheric $CH_3OH$ burdens (Fig. 4.27 (f)) and $CH_3OH$ mixing ratios (Fig. 4.28 (f)).

**Nitrogen species**

For the atmospheric nitrogen species, significant changes between SOCX and BASE are detected in the southern polar atmosphere for $NO_2$, $NO_3$, $N_2O_5$ (all Fig. 4.29), $HNO_3$, and nitrous acid (HONO; both Fig. 4.30). These changes are associated with the changed atmospheric $C_5H_8$, HCHO, and OH mixing ratios in this area in SOCX compared to BASE, which in turn are related to the changed air-sea gas exchange of $C_5H_8$ in the simulation (Fig. 4.17).

The largest (and only significant) changes in atmospheric composition of the nitrogen species in SOCX are detected over the Southern Ocean. The lower atmospheric mixing ratios of HCHO over the Southern Ocean (Figs. 4.27 (b), 4.28 (b)), related to the decreased ocean-to-atmosphere flux of $C_5H_8$ in this region (Fig. 4.17 (c)) causes a decrease in CO and an increase in OH (Fig. 4.27). The decreased $C_5H_8$ ocean-to-atmosphere flux in this region is associated with an increase of tropospheric $NO_x$, $NO_3$, $N_2O_5$ (Figs. 4.29, 4.31), $HNO_4$, PAN, and HONO (Figs. 4.30, 4.32), and a decrease of atmospheric $HNO_3$ (Figs. 4.30 (a), 4.32 (a)).

As larger atmospheric mixing ratios of HCHO are simulated over the Southern Ocean (Figs. 4.27 (b), 4.28 (b)), less $NO_3$ is oxidised to $HNO_3$, resulting in increased mixing ratios of $NO_3$ (Figs. 4.29 (d), 4.31 (d)) and decreased mixing ratios of $HNO_3$(Figs. 4.30 (a), 4.32 (a)) . As less $C_5H_8$ is available to react with $NO_3$, lower $C_5H_8$ mixing ratio in this area also contribute to larger $NO_3$ mixing ratios.

Larger atmospheric $NO_x$ mixing ratios are related to increased mixing ratios of $O_3$ (Figs. 4.27 (d), 4.28 (d)) and $NO_3$ (Figs. 4.29 (d), 4.31 (d)) over the Southern Ocean. Increases in HONO mixing ratios (Figs. 4.30 (d), 4.32 (d)) are a consequence of larger NO mixing ratios (Figs. 4.29 (b), 4.31 (b)). Larger atmospheric mixing ratios of $HNO_4$ (Figs. 4.30 (b), 4.32 (b)) are simulated due to the increase of NO (Figs. 4.29 (b), 4.31 (b)) and OH (Figs. 4.27 (c), 4.28 (d)). These results are internally consistent and show a reasonable representation of the atmospheric chemistry and a coupling between atmospheric composition and air-sea fluxes as expected.

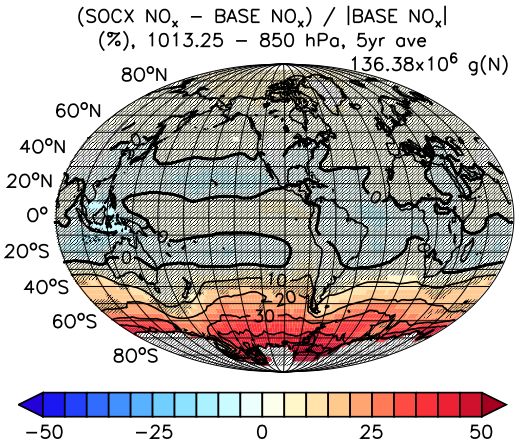


**(a)** $NO_x$ burden (SOCX - BASE) / |BASE|

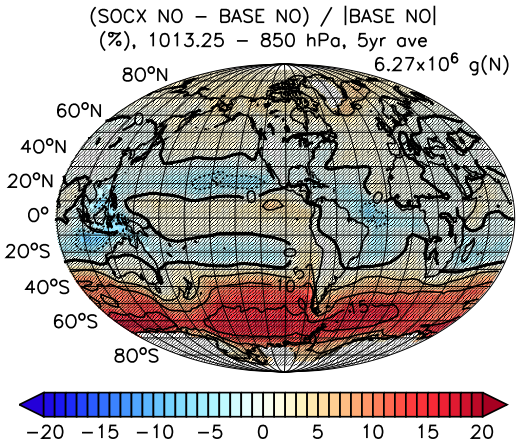


**(b)** NO burden (SOCX - BASE) / |BASE|

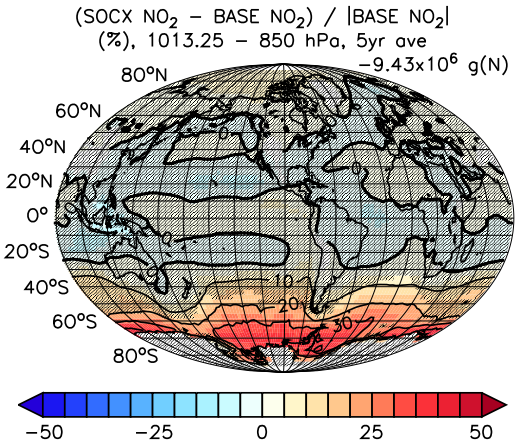


**(c)** $NO_2$ burden (SOCX - BASE) / |BASE|

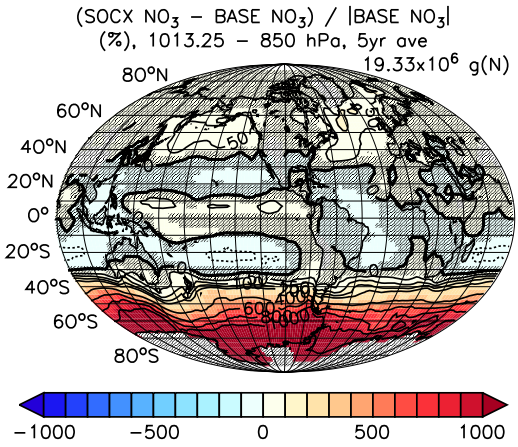


**(d)** $NO_3$ burden (SOCX - BASE) / |BASE|

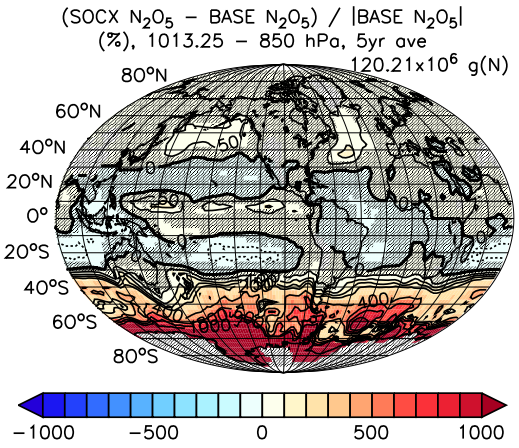


**(e)** $N_2O_5$ burden (SOCX - BASE) / |BASE|

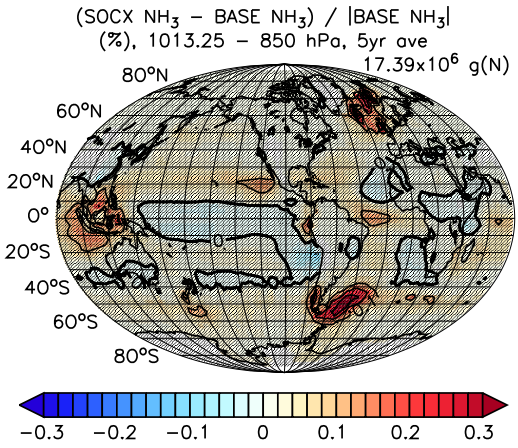


**(f)** $NH_3$ burden (SOCX - BASE) / |BASE|

**Figure 4.29:** Relative differences of atmospheric burdens integrated from the surface up to 850 hPa of $NO_x$, NO, $NO_2$, $NO_3$, $N_2O_5$, and $NH_3$ between SOCX and BASE averaged over five years of simulation. Units are %. The interval between contour lines is for (a) 10 %, for (b) 5 %, for (c) 10 %, for (f) 0.02 %. Contour lines for (d) and (e) are at −50 %, 0 %, 50 %, 100 %, 150 %, 200 %, 400 %, 600 %, 800 % and 1000 %. Differences in atmospheric burdens in gray shaded areas are not significant on a 99 % level according to a two-sided Student's t-test.

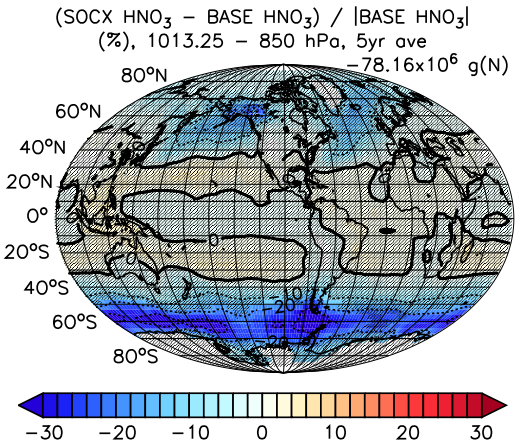


**(a)** $HNO_3$ burden (SOCX - BASE) / |BASE|

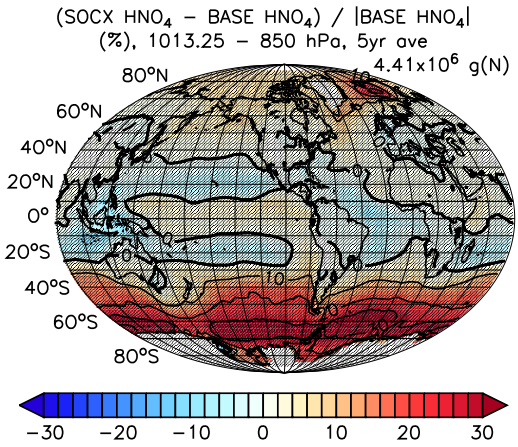


**(b)** $HNO_4$ burden (SOCX - BASE) / |BASE|

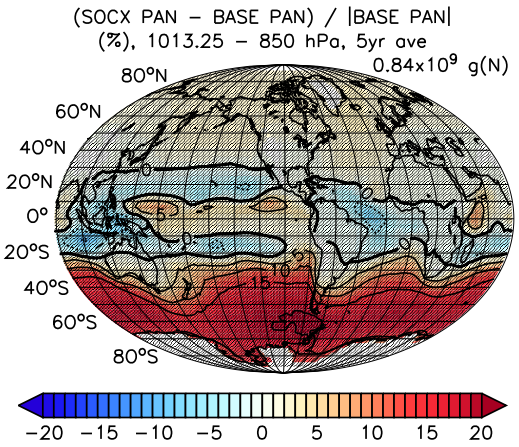


**(c)** PAN burden (SOCX - BASE) / |BASE|

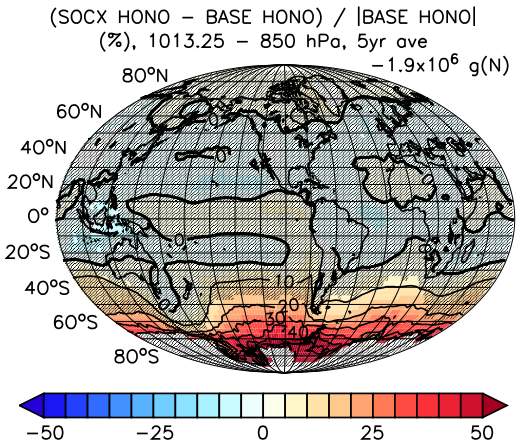


**(d)** HONO burden (SOCX - BASE) / |BASE|

**Figure 4.30:** Relative differences in atmospheric burdens integrated from the surface up to 850 hPa of $HNO_3$, $HNO_4$, PAN, and HONO between SOCX and BASE averaged over five years of simulation. Units are %. The interval between contour lines is for (a) 10 %, for (b) 5 %, for (c) 10 %, and for (e) 10 %. Differences in atmospheric burdens in gray shaded areas are not significant on a 99 % level according to a two-sided Student's t-test.

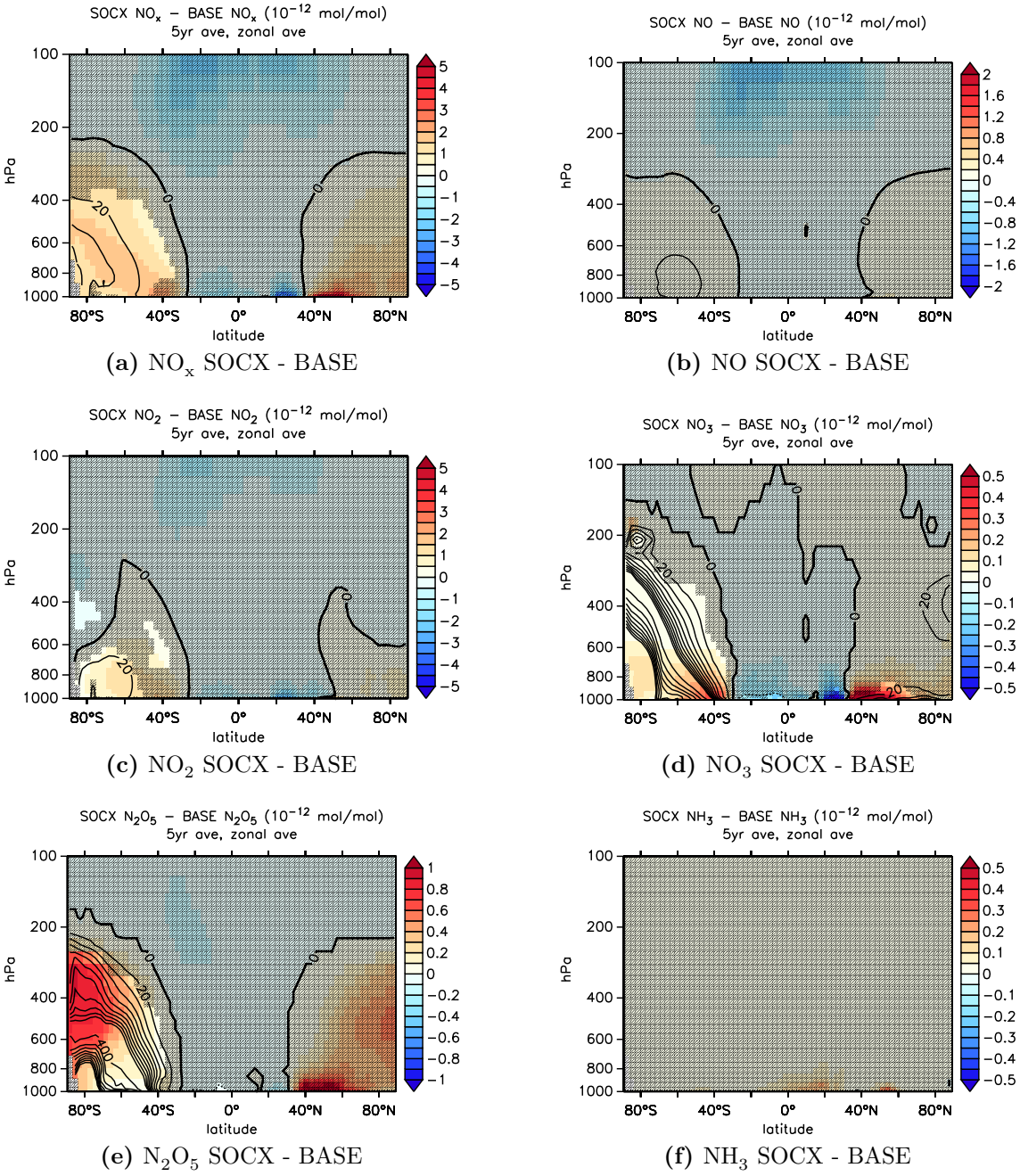


**(a)** $NO_x$ SOCX - BASE

**(b)** NO SOCX - BASE

**(c)** $NO_2$ SOCX - BASE

**(d)** $NO_3$ SOCX - BASE

**(e)** $N_2O_5$ SOCX - BASE

**(f)** $NH_3$ SOCX - BASE

**Figure 4.31:** Differences of zonally averaged atmospheric mixing ratios of $NO_x$, NO, $NO_2$, $NO_3$, $N_2O_5$, and $NH_3$ (in $10^{-12}$ mol mol$^{-1}$) between SOCX and BASE averaged over five years. Contour lines denote relative differences in mixing ratios between SOCX and BASE in %, the interval between contour lines is for (a), (c) 20 %, (b) 10 %, for (d), (e) 20 % up to 200 %, then 200 %. Differences in mixing ratios in gray shaded areas are not significant on a 99 % level according to a two-sided Student's t-test.

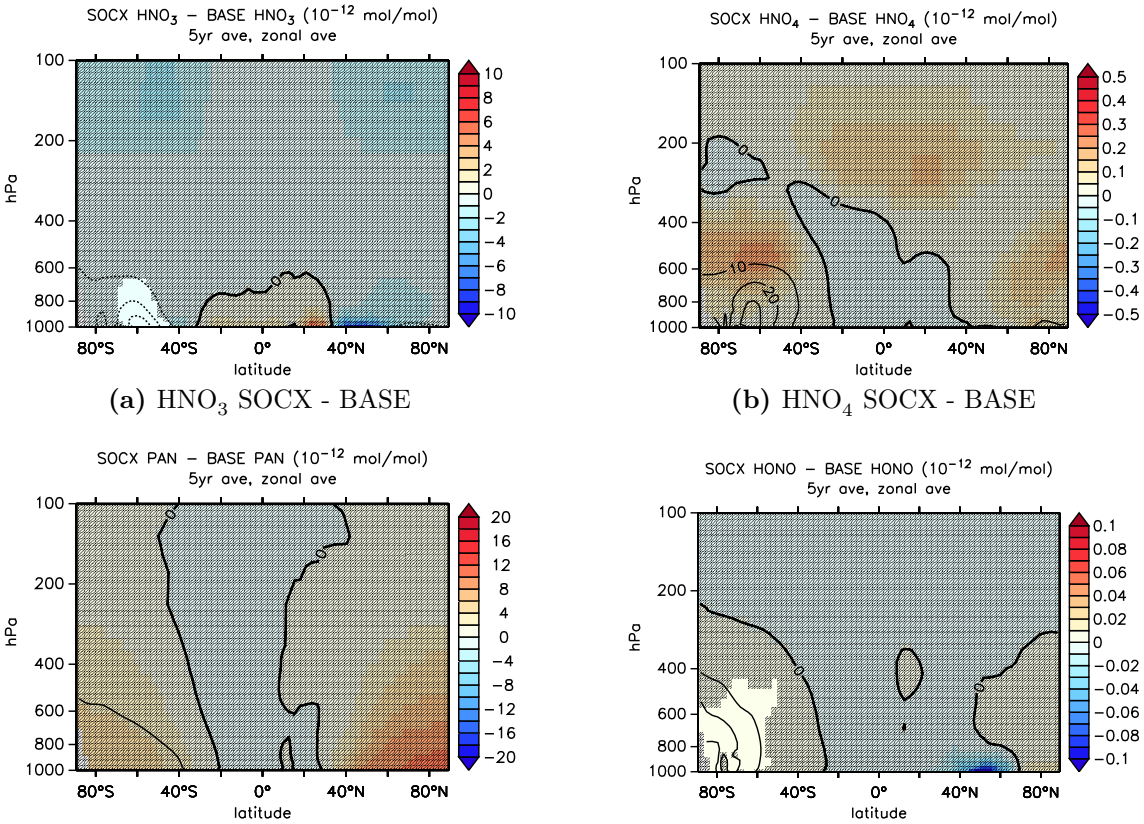


**(a)** $HNO_3$ SOCX - BASE

**(b)** $HNO_4$ SOCX - BASE

**(c)** PAN SOCX - BASE

**(d)** HONO SOCX - BASE

**Figure 4.32:** Differences of zonally averaged atmospheric mixing ratios of $HNO_3$, $HNO_4$, PAN, and HONO (in $10^{-12}$ mol mol$^{-1}$) between SOCX and BASE averaged over five years. Contour lines denote relative differences in mixing ratios between SOCX and BASE in %, the interval between contour lines is for (a), (b), (c) 10 %, for (d) 20 %. Differences in mixing ratios in gray shaded areas are not significant on a 99 % level according to a two-sided Student's t-test.

### Relation between atmospheric burden and ocean-to-atmosphere flux

The relation of atmospheric burden integrated from 1013.25 hPa to 850 hPa to the corresponding ocean-to-atmosphere flux at each model grid-point for DMS, $C_5H_8$, and CO (Fig. 4.33) is not linear as is the relation between ocean-to-atmosphere flux and surface water concentration (see Section 4.2.2). This points to the importance of additional atmospheric processes determining atmospheric composition, like advection, wet and dry deposition, and chemical processing. The model systems response to modified oceanic surface concentrations reflects the expectations and shows the model system's ability to reproduce realistic air-sea gas exchange and atmospheric composition.

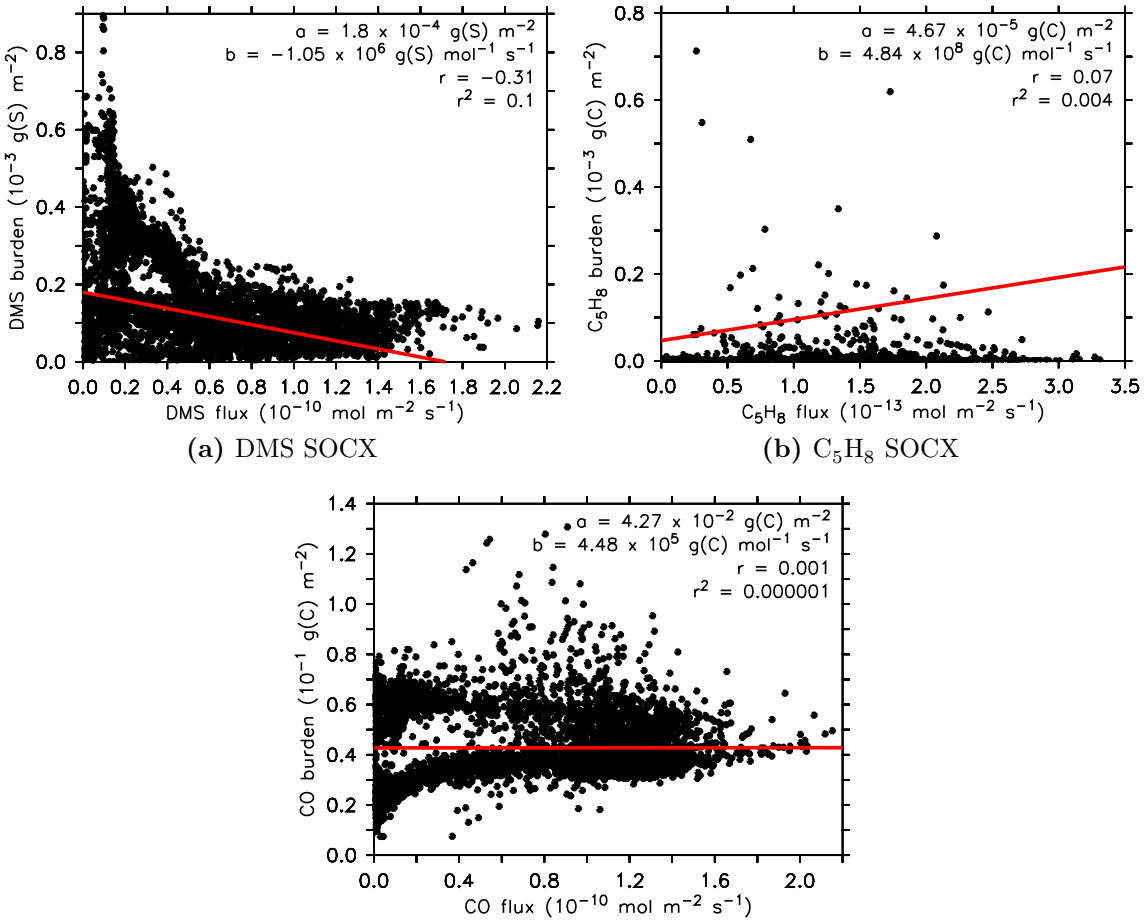


**(a)** DMS SOCX **(b)** $C_5H_8$ SOCX

**(c)** CO SOCX

**Figure 4.33:** Scatter diagrams of ocean-to-atmosphere fluxes versus atmospheric burden integrated from 1013.25 hPa to 850 hPa at each model grid-point for (a) DMS, (b) $C_5H_8$, and (c) CO. In red linear regression lines, calculated using the method of least squares, are shown. The regression coefficients $a$ and $b$, the sample correlation coefficient $r$, and the squared correlation coefficient $r^2$ are listed for the individual gases.

### 4.2.4 Discussion

In summary, differences in atmospheric composition resulting from changed ocean-to-atmosphere fluxes, as simulated in SOCX versus BASE, are mostly insignificant. This shows the ability of the chemically coupled model system with interactive oceanic biogeochemistry to represent reasonable atmospheric composition compared to a model setup using climatological oceanic concentrations. However, whether a simulation period of five years is sufficient to achieve statistically robust results has to be tested in future over a longer simulation time. Systematic, though

insignificant, deviations in the atmospheric composition induced by the changed ocean-to-atmosphere fluxes are nevertheless consistent and as expected. The interaction between oceanic biogeochemistry, surface water concentrations, ocean-to-atmosphere fluxes, and atmospheric concentrations are therefore represented consistently in the model system. The relation between oceanic surface water concentrations and ocean-to-atmosphere fluxes of DMS, $C_5H_8$, and CO are in first order linear (Fig. 4.22), however, the relation of the near surface atmospheric burden to ocean-to-atmosphere fluxes for these gases is not (Fig. 4.33). This reflects the non linear interaction of atmospheric gas and aqueous-phase (in-cloud and scavenging) chemistry with large-scale (advection) and small-scale (convection) transport processes. This is also reflected in mostly insignificant changes of the atmospheric composition as response to the different ocean-to-atmosphere fluxes. The simulated patterns in differences in atmospheric composition are nonetheless consistent with the changed ocean-to-atmosphere fluxes, supporting the models ability to produce reliable responses under transient forcings (e.g. climate change).

## 4.3 Riverine nutrient input into the ocean

In the SRFIX sensitivity experiment additional fluxes of dissolved Fe, Si, $CO_2$, and $N_2$ to the ocean from rivers are considered (Table 4.1). The molar concentrations of these tracers in freshwater runoff from land are prescribed as constant throughout the year and have no spatial variability. Values for the molar concentrations are based on the study by Cotrim da Cunha et al. (2007) and a global annual freshwater discharge of $45 \times 10^{12}\,\mathrm{m^3\,a^{-1}}$. In this study, molar freshwater concentrations of $[\mathrm{Fe}] = 1.022 \times 10^{-8}\,\mathrm{kmol(Fe)\,m^{-3}}$, $[\mathrm{Si}] = 1.488 \times 10^{-4}\,\mathrm{kmol(Si)\,m^{-3}}$, $[\mathrm{CO_2}] = 7.133 \times 10^{-4}\,\mathrm{kmol(C)\,m^{-3}}$, and $[\mathrm{N_2}] = 1.088 \times 10^{-4}\,\mathrm{kmol(N)\,m^{-3}}$ have been used.

### 4.3.1 Impact on oceanic biogeochemistry

Significant changes compared to SOCX are apparent in the surface ocean Fe concentrations in coastal areas in Figure 4.34 (a) for SRFIX. The largest relative differences in Fe concentrations between SRFIX and SOCX with more than 200 % are reached in the Hudson Bay, the Lena delta at the northern Siberian coast, and the Sea of Okhotsk at the Russian east coast. At the North American west coast near Newfoundland the relative differences in surface ocean Fe concentrations are up to 140 %.

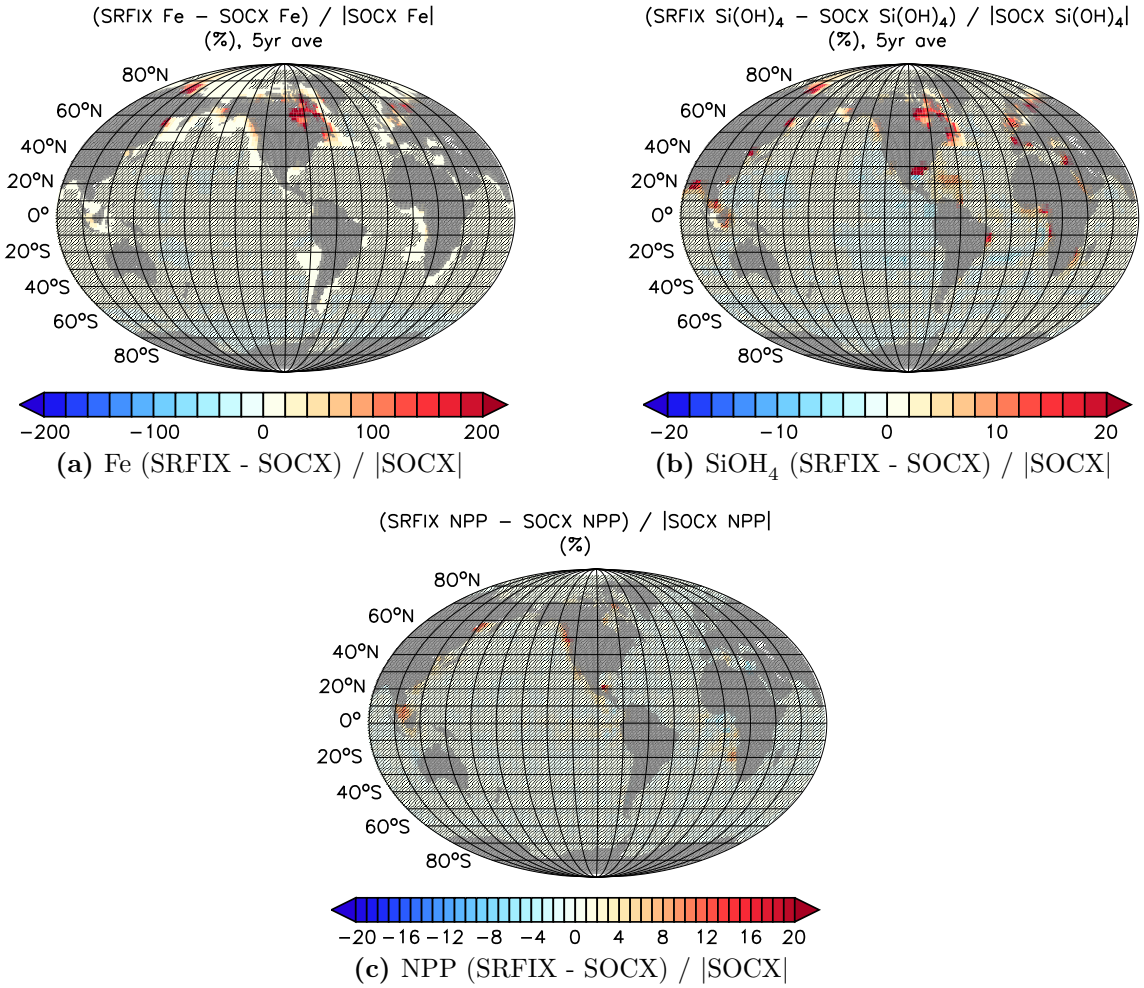


**(a)** Fe (SRFIX - SOCX) / |SOCX|

**(b)** $SiOH_4$ (SRFIX - SOCX) / |SOCX|

**(c)** NPP (SRFIX - SOCX) / |SOCX|

**Figure 4.34:** Relative differences in averaged surface water concentrations of (a) Fe, (b) $Si(OH)_4$, and (c) NPP between SRFIX and SOCX over five years of simulation. Units are %. Differences in concentrations in gray shaded areas are not significant on a 99 % level according to a two-sided Student's t-test.

Furthermore, large differences with more than twice the value in Fe concentration than in the SOCX experiment are seen at the Bering Sea, the Barents Sea, and the Baltic Sea. Relative differences at the Malay Archipelago, the Huang He (Yellow River), and the Congo delta are about 50 %. These results are reasonable, as the main impact of nutrient import by rivers is expected to affect the coastal zones.

For $Si(OH)_4$ surface water concentrations, significantly larger values can be seen in the SRFIX experiment in coastal regions in Figure 4.34 (b) compared to SOCX. The maximum relative difference of $Si(OH)_4$ surface water concentrations is more than 30 % in the Mississippi delta, in the Labrador Sea, the Bay of Biscay, the Yellow River delta, and the Sea of Okhotsk. In the relative differences of surface ocean

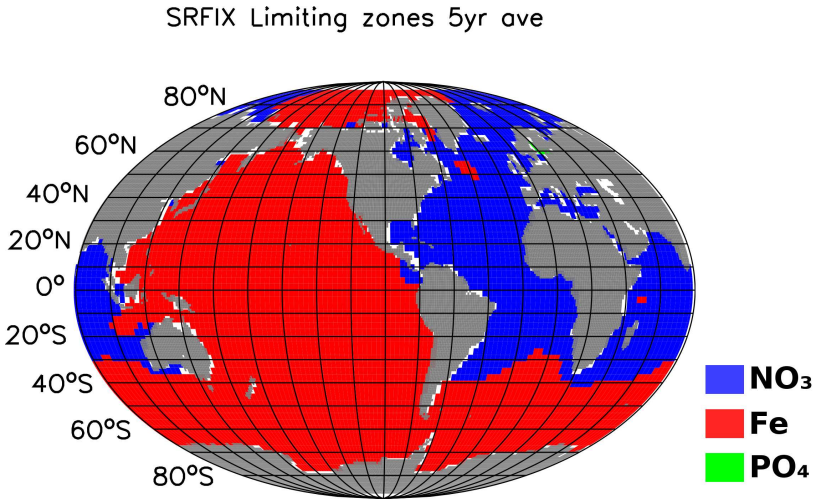


**Figure 4.35:** Limiting nutrients for phytoplankton growth in SRFIX. Colours indicate the limiting nutrient in this region: red is Fe, blue is $NO_3^-$, green is $PO_4^{3-}$.

$Si(OH)_4$ concentrations between SRFIX and SOCX, the impact of the World's largest rivers is apparent, influencing the $Si(OH)_4$ concentrations even in open ocean waters (e.g. for the Amazon River). Surface ocean $Si(OH)_4$ concentrations in SRFIX are comparable to the results obtained by Bernard et al. (2011), using riverine Si input based on data from Dürr et al. (2011).

Major changes in NPP can be seen in coastal areas, directly impacted by additional nutrient import to the ocean from rivers. NPP is increased in SRFIX compared to SOCX by about 10 % in these areas, locally reaching more than 15 %. However, differences in NPP between simulations with additional import of chemical compounds from rivers are statistically not significant at the 99 % level according to a Student's t-test.

Higher, though insignificant, increases in NPP are simulated in the Pacific compared to the Atlantic, which can be attributed to the limiting nutrient for phytoplankton growth in each ocean basin. The limiting nutrient for phytoplankton growth simulated by HAMOCC (Fig. 4.35) in the Pacific is Fe, whereas in the Atlantic it is nitrate in aqueous phase ($NO_3^-$).

The pattern in relative differences of surface ocean DMS concentrations between SRFIX and SOCX (Fig. 4.36 (a)) depict the same distribution as the relative differences in NPP (Fig. 4.34 (c)). These changes in DMS concentrations are also not significant on the 99 % level according to a Student's t-test.

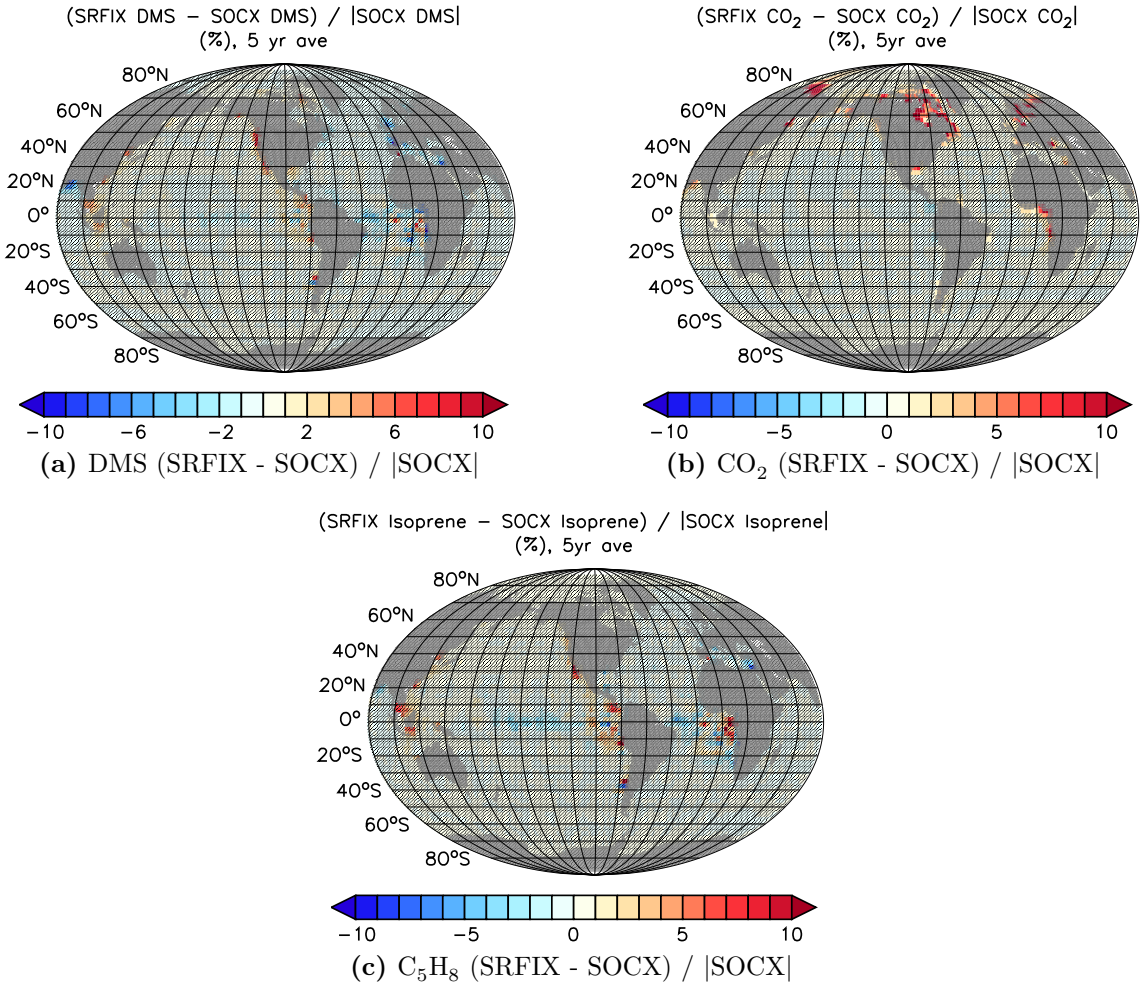


**(a)** DMS (SRFIX - SOCX) / |SOCX|

**(b)** $CO_2$ (SRFIX - SOCX) / |SOCX|

**(c)** $C_5H_8$ (SRFIX - SOCX) / |SOCX|

**Figure 4.36:** Relative differences of surface water concentrations of (a) DMS, (b) $CO_2$, and (c) $C_5H_8$ between SRFIX and SOCX averaged over five years. Units are %. Differences in concentrations in gray shaded areas are not significant on a 99 % level according to a two-sided Student's t-test.

Significant changes in $CO_2$ concentration at the ocean's surface are constrained to the coastal areas (Fig. 4.36 (b)). In these areas, regionally more than 10 % larger values are simulated in the sensitivity study with riverine nutrient import than in the simulation without. Larger $CO_2$ concentrations can be seen in Figure 4.36 (b) for SRFIX at the Bay of Bengal, the Lena Delta, the Bering Sea, the Hudson Bay, the Labrador Sea, the Mississipi Delta, the Bay of Biscay, the Baltic Sea, the Gulf of Guinea, and the Barents Sea. In the Orinoco Delta and the Brazil Basin the relative differences from SRFIX to SOCX are only a few percent, but are significant on a 99 % level. This increase in coastal $CO_2$ concentrations is a direct consequence of additional $CO_2$ import from rivers into the coastal area.

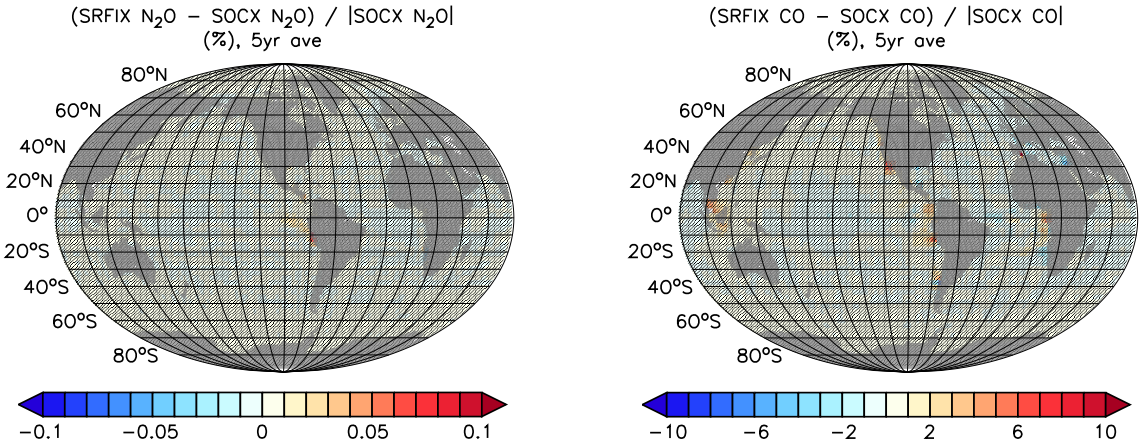


**(a)** $N_2O$ (SRFIX - SOCX) / |SOCX| **(b)** CO (SRFIX - SOCX) / |SOCX|

**Figure 4.37:** Relative differences in averaged surface water concentrations of (a) $N_2O$ and (b) CO between SRFIX and SOCX over five years of simulation. Units are %. Differences in concentrations in gray shaded areas are not significant on a 99 % level according to a two-sided Student's t-test.

As oceanic $C_5H_8$ concentrations are parameterised via chlorophyll concentrations (Eq. 3.10), relative differences in SRFIX for $C_5H_8$ (Fig. 4.36 (c)) resemble the relative differences in NPP. The changes in $C_5H_8$ reach up to 10 % locally, but are statistically not significant on the 5-year time basis analysed here.

Further, no significant changes are found in surface water $N_2O$ concentrations (Fig. 4.37 (a)). Relative differences between the sensitivity experiments with and without riverine nutrient input are below 0.1 %.

Relative differences of oceanic CO surface concentrations (Fig. 4.37 (b)) show a similar pattern as the relative differences of NPP. Oceanic CO concentrations in the model system are determined by photochemical CO production from dissolved organic matter (DOM; Eqs. 3.11 and 3.12). DOM concentrations change according to chlorophyll concentrations, and hence NPP. The changes in the surface water CO concentrations in SRFIX are also statistically not significant on a 5-year time basis.

In summary, the simulation with riverine nutrient import show reasonable results in oceanic chemical composition and biogeochemistry. The effect is—as expected—mainly confined to coastal areas, which act as an interface between land and open ocean. In major river outflows and via advection, changes in coastal chemical composition also contribute to changes in the open ocean.

The impact of riverine nutrient import in coastal areas, simulated with the coarse-grained global model system, are mostly insignificant for oceanic surface water concentrations of gases taking part in air-sea gas exchange, resulting in weak changes in ocean-to-atmosphere fluxes. However, regionally small impacts could gain high importance, especially in coastal areas with high population densities, where atmospheric pollution interacts with biogenic ocean emissions, also influenced by further nutrient import from sewage and fertiliser usage through rivers. To gain deeper insights in these interactions, a higher resolution of the model system leading to better resolved coastal shelf areas and a better representation of biogeochemical processes in the coastal oceans in the model system are necessary.

### 4.3.2 Impact on ocean-to-atmosphere fluxes and atmospheric chemical composition

Differences in 5-year averages of ocean-to-atmosphere fluxes for DMS, $CO_2$, and $C_5H_8$ between SRFIX and SOCX are presented in Figure 4.38. The pattern in differences correspond to the pattern of differences of surface water concentrations for the different species (Fig. 4.36). Although the changes in air-sea gas exchange of DMS and $C_5H_8$ reach relative differences over 5 % locally in coastal regions with higher surface ocean concentrations in SRFIX compared to SOCX, these changes are not significant over the analysed time interval of five years. Significant increases in ocean-to-atmosphere fluxes of $CO_2$ between SRFIX and SOCX can be seen in Figure 4.38 (b). In the coastal regions of Siberia, the Hudson Bay, the Labrador Sea, the Mississippi Delta, the Sea of Okhotsk, the South American and African Atlantic additional ocean-to-atmosphere $CO_2$ fluxes of more than 50 % are simulated in the sensitivity study including nutrient input by rivers compared to the simulation without additional riverine import. These changes are reasonable, as additional $CO_2$ is imported to the coastal zone via riverine nutrient import.

For $N_2O$ and CO air-sea gas exchange (Fig. 4.39) no significant changes on the 99 % level are simulated in SRFIX compared to SOCX. Changes in fluxes are predominantly in coastal areas and locally exceed the fluxes in SOCX by more than 5 %. The pattern of differences in ocean-to atmosphere fluxes of $N_2O$ and CO resemble the distribution of differences in surface ocean concentrations (Fig. 4.37).

Because of the small, insignificant changes in the ocean-to-atmosphere fluxes in all species under consideration except $CO_2$, there are no significant changes simulated in atmospheric chemical composition for the species investigated in Section

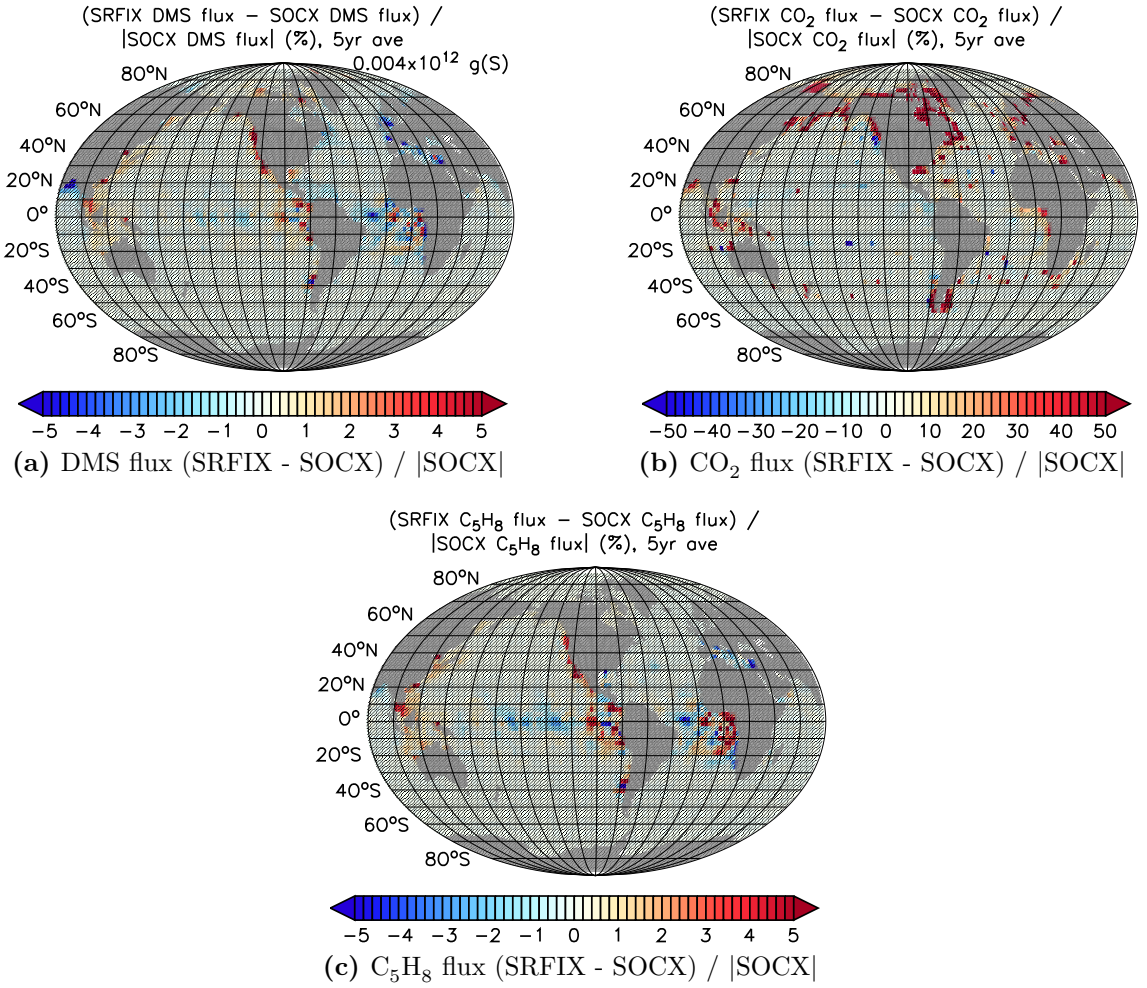


**(a)** DMS flux (SRFIX - SOCX) / |SOCX|

**(b)** $CO_2$ flux (SRFIX - SOCX) / |SOCX|

**(c)** $C_5H_8$ flux (SRFIX - SOCX) / |SOCX|

**Figure 4.38:** Relative differences in averaged ocean-to-atmosphere fluxes of (a) DMS, (b) $CO_2$, and (c) $C_5H_8$ between SRFIX and SOCX over five years of simulation. Units are %. Differences in ocean-to-atmosphere fluxes in gray shaded areas are not significant on a 99 % level according to a two-sided Student's t-test.

4.2.3. This holds true for lower tropospheric burdens up to 850 hPa and for zonal averages, averaged over the five years of simulation. Atmospheric mixing ratios of the greenhouse gases $CO_2$ and $N_2O$ have been, however, prescribed using TNUDGE and are not directly relevant for tropospheric chemistry. The impact of significant changes of $CO_2$ ocean-to-atmosphere fluxes in coastal areas has to be determined in additional experiments, which do not prescribe atmospheric $CO_2$ mixing ratios. Such additional transient simulations under changing anthropogenic emissions come with higher computational demands for preparation and performance, and thus lie beyond the scope of this study.

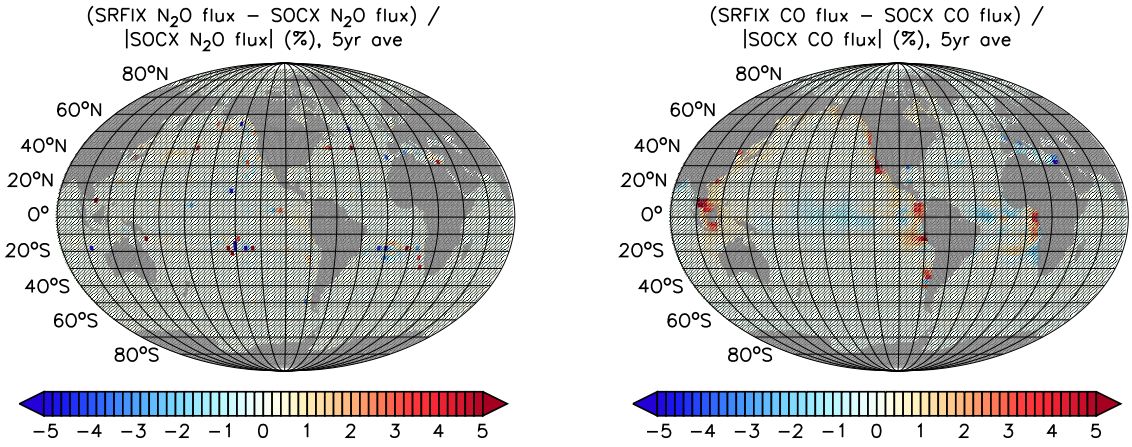


**(a)** $N_2O$ flux (SRFIX - SOCX) / |SOCX| **(b)** CO flux (SRFIX - SOCX) / |SOCX|

**Figure 4.39:** Relative differences in averaged ocean-to-atmosphere fluxes of (a) $N_2O$ and (b) CO between SRFIX and SOCX over five years of simulation. Units are %. Differences in ocean-to-atmosphere fluxes in gray shaded areas are not significant on a 99 % level according to a two-sided Student's t-test.

## 4.4 Consistent modelling of nutrient import of the ocean by aeolian dust

Deposition of mineral aerosol is the main iron source in open ocean waters (e.g. Martin et al. (1991); Sections 2.4, 3.7). In this Section the differences between the sensitivity study using an "online" coupled dust deposition from the atmospheric model domain (SDUST) and the sensitivity study with a prescribed dust deposition climatology (SOCX) are discussed.

### 4.4.1 Differences in dust deposition between climatological and online dust input

Dust deposition is considered as source of Fe and Si to the ocean biogeochemistry in this study. In the model system, two possibilities exist to provide dust input from the atmosphere at the top of the oceanic domain. Dust deposition can be provided as prescribed dust deposition climatology, or from an "online" calculated dust deposition. In the remainder of this chapter differences between the SOCX and SDUST sensitivity experiment are shown. The only difference in the model setups between these two sensitivity experiments is the handling of dust deposition and import to the biogeochemistry submodel.

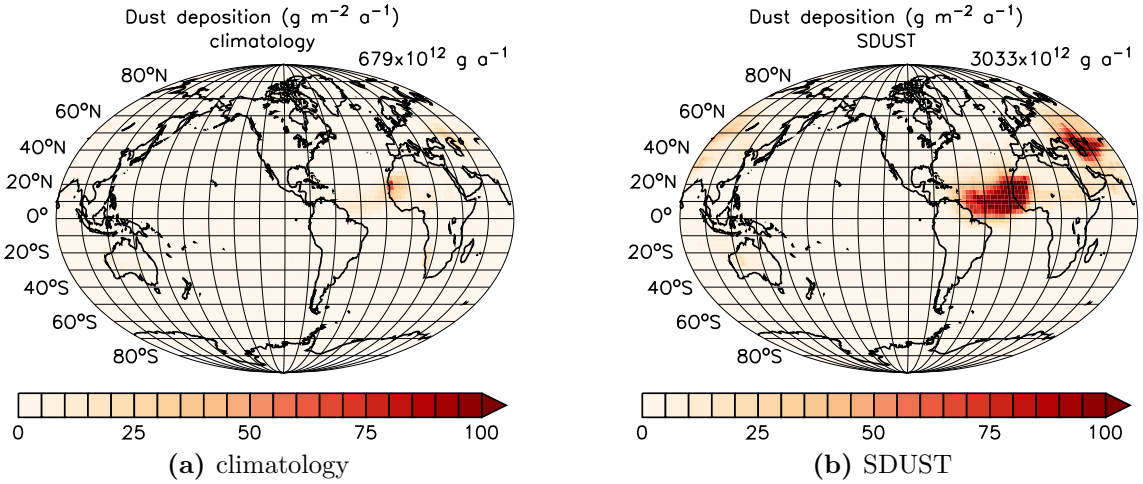


**Figure 4.40:** Averaged dust deposition flux in $\mathrm{g\,m^{-2}\,a^{-1}}$: (a) average of prescribed climatological dust deposition, (b) 5-year average of online calculated dust deposition in SDUST. Averaged annual global integrated dust deposition is given in $\mathrm{Tg\,a^{-1}}$.

In the SOCX experiment the dust deposition is prescribed from a monthly climatology (Timmreck and Schulz, 2004), whereas in the SDUST experiment the dust deposition is calculated from atmospheric deposition fields using the SCALC submodel (see Sections 3.7, 3.8, Appendix C). This results in a more consistent modelling of feedbacks between the atmosphere and the ocean. Because of an increased coupling frequency between the oceanic and atmospheric model domain of 2 h an additional variability compared to the monthly climatology is introduced in the simulations.

The dust deposition fluxes used in the sensitivity experiments with climatological dust deposition from the atmospheric domain (SOCX) is presented in Figure 4.40 (a). A high dust deposition flux can be seen near the source regions, like the plume reaching out to the Atlantic from the Sahara. The integrated global dust deposition of the simulations with climatologically prescribed dust deposition is $679\,\mathrm{Tg\,a^{-1}}$, $282\,\mathrm{Tg\,a^{-1}}$ of which are deposited over the ocean.

The total dust deposition calculated online from the partial atmospheric fluxes of the different submodels for dry and wet deposition are presented in Figure 4.40 (b). Compared to the climatological dust deposition, the online calculated dust deposition generally exhibit higher dust deposition fluxes, whereas the pattern in dust deposition is comparable between the two simulations.

The integrated global dust deposition is 3033 Tg a$^{-1}$ in the SDUST experiment, which is at the high end of dust deposition estimates from model simulations reported in literature (Huneeus et al., 2011; Gläser et al., 2012). The input of mineral aerosol to the ocean from "online" calculated dust deposition is 1508 Tg a$^{-1}$.

The calculated mineral aerosol input to the ocean in SDUST is 66 % higher than the measurement based estimate of 910 Tg a$^{-1}$ by Duce et al. (1991). The climatological dust deposition in SOCX over the ocean is 69 % lower than this estimate. Assuming that 3.5 % of the deposited dust mass is iron, the iron import to the ocean is 52.8 Tg a$^{-1}$ in SDUST and 9.9 Tg a$^{-1}$ in the case of climatological prescribed dust deposition, compared to 32 Tg a$^{-1}$ as estimated by Duce et al. (1991).

The pattern in dust deposition fluxes from the climatology and the online calculated dust source (Fig. 4.40 (a)) are reflected in the surface water dust mass concentrations (Fig. 4.41), showing maxima in the region of high deposition fluxes in the Atlantic. In this region, surface water dust concentration offshore the African west coast in SDUST reaches more than ten times the value simulated with the climatological dust deposition in SOCX. Further, significantly larger surface water dust mass concentrations are simulated throughout the global ocean, with exception of the South American and South African west coasts, where significantly lower dust concentrations are simulated in SDUST compared to SOCX (Fig. 4.41 (c), off-scale in Fig. 4.41 (d)).

### 4.4.2 Impact on oceanic surface concentrations, air-sea gas exchange, and atmospheric composition

Changes in surface water concentration of Fe and $Si(OH)_4$ by the additional source from aeolian import of dust is presented in Figure 4.42. The major impact of the interactive dust deposition on surface ocean Fe concentrations in SDUST is the increase in the tropical and subtropical Atlantic, reaching more than six times the concentrations simulated in SOCX near the source region at the African coast (Figs. 4.42 (a), 4.42 (b)). Furthermore, increased Fe concentrations are simulated in SDUST compared to SOCX in the Indian Ocean and at the Australian west coast. Slight decreases are apparent at the west coasts of South America and southern Africa. These results are reasonable and directly related to the changed dust deposition (Figs. 4.40 (b)) and the changes in surface ocean dust concentrations (Fig. 4.41 (d)).

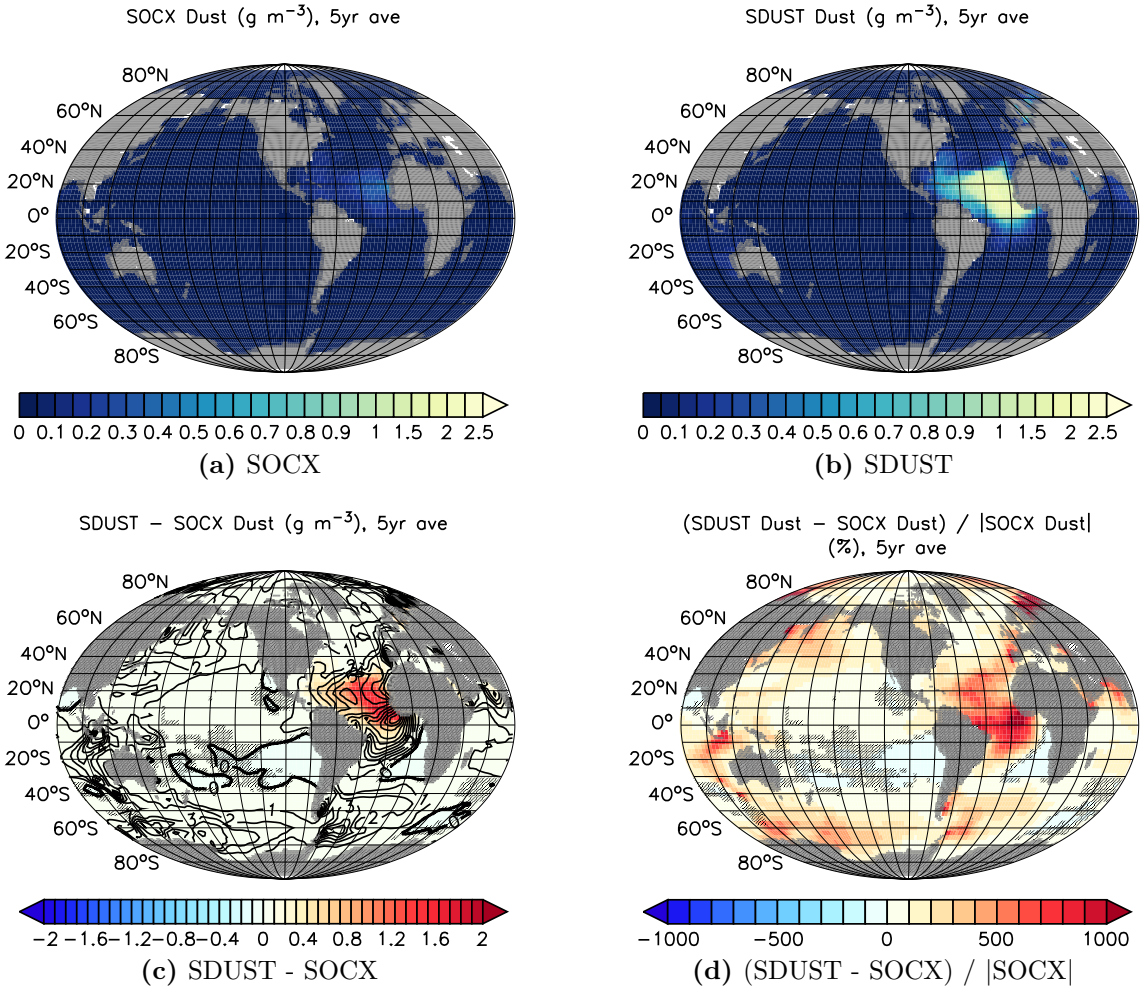


**Figure 4.41:** Surface water dust mass concentrations (a) in SOCX and (b) in SDUST. Units are g m$^{-3}$. (c) differences in surface water dust mass concentrations between SDUST and SOCX in g m$^{-3}$. Contours denote relative difference, the interval between contour lines is 100 %. (d) relative differences in surface water dust mass concentrations between SDUST and SOCX in %. Differences in concentrations in gray shaded areas are not significant on a 99 % level according to a two-sided Student's t-test.

For $Si(OH)_4$, the impact of the changed dust deposition on the difference pattern in surface ocean concentration between SDUST and SOCX (Figs. 4.42 (c), 4.42 (d)) is not as obvious as for Fe. As there are a-priori high $Si(OH)_4$ concentration in the surface ocean, resulting from the deficiencies in the representation of NPP in the model (cf. Section 4.2.1), the relative impact of additional $Si(OH)_4$ from dust deposition is small. Si is not treated as limiting nutrient in the oceanic biogeochemistry model, however, $Si(OH)_4$ concentrations influence the partitioning

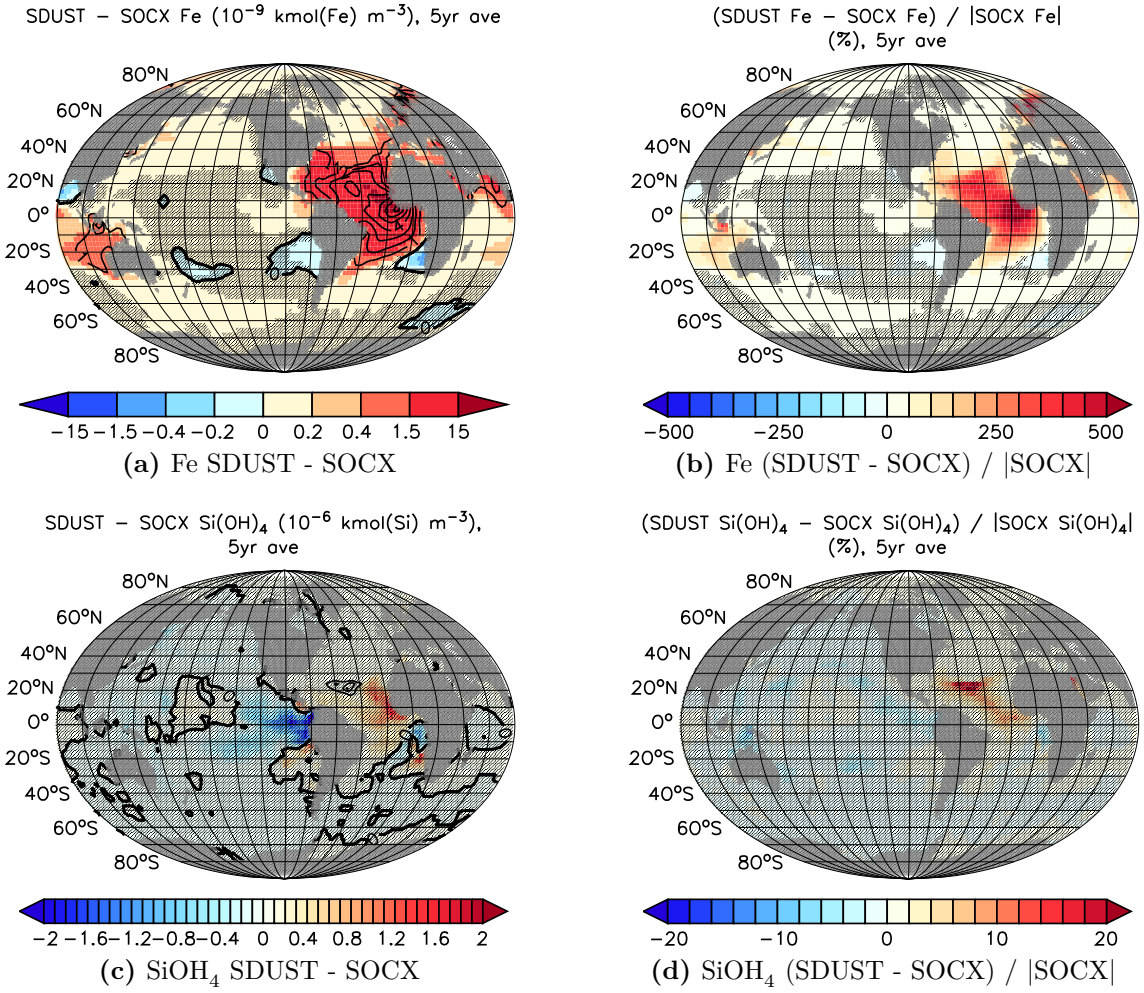


**(a)** Fe SDUST - SOCX **(b)** Fe (SDUST - SOCX) / |SOCX|

**(c)** $SiOH_4$ SDUST - SOCX **(d)** $SiOH_4$ (SDUST - SOCX) / |SOCX|

**Figure 4.42:** Absolute differences in surface water mass concentrations of (a) Fe and (c) $Si(OH)_4$ between SOCX and SDUST. Units are $g\,m^{-3}$. Contours denote relative differences, the interval between contour lines is for (a) 100 % and for (c) 10 %. Relative differences in surface water dust mass concentrations of (b) Fe and (d) $Si(OH)_4$ between SDUST and SOCX in %. Differences in concentrations in gray shaded areas are not significant on a 99 % level according to a two-sided Student's t-test.

between the two phytoplankton classes of HAMOCC (cf. Section 3.3). To asses the impact of aeolian Si input to the ocean, further simulations with an updated parameterisation of NPP in the model are necessary.

The increase of $Si(OH)_4$ in the Atlantic correlates with the higher dust deposition in this region, whereas the changes at the west coast of South America and southern Africa have the opposite sign. This is caused by changes in the ocean biogeochemistry—apparent in differences in NPP—in these regions (Fig. 4.43). In SDUST the

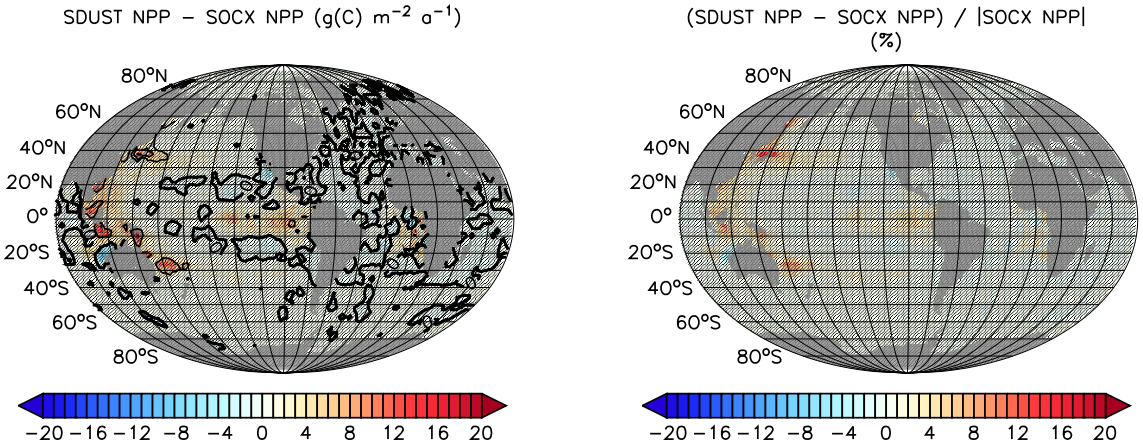


**(a)** NPP SDUST - SOCX **(b)** NPP (SDUST - SOCX) / |SOCX|

**Figure 4.43:** (c) absolute difference and (d) relative difference in water column NPP between SDUST and SOCX in g(C) $m^{-2}$ $a^{-1}$ and %, respectively. Contours denote relative differences. The interval between contour lines is 5 %.

HAMOCC simulated limiting nutrient for phytoplankton growth is Fe (Fig. 4.44). Decreased Fe input to the ocean at the west coasts of South America and southern Africa in SDUST (Figs. 4.42 (a), 4.42 (b)) is accompanied by higher iron stress and, hence, a reduced phytoplankton growth, depleting lower amounts of $Si(OH)_4$. However, changes in the surface ocean $Si(OH)_4$ concentration between SDUST and SOCX are not significant for the analysed time-span of five years.

Changes in surface concentrations of DMS, $C_5H_8$, and CO (Fig. 4.45) show the same pattern as differences in NPP between SDUST and SOCX. All differences in surface concentrations of these compounds are not significant based on the analysed five years of simulation, reaching at most relative changes of 10 %, which is lower than the local inter-annual variation. Differences in the surface ocean concentrations of $CO_2$ and $N_2O$ between the sensitivity study with online calculated dust deposition and with the climatological deposition field are even lower (Figs. 4.45 (d), 4.45 (e)).

The small differences in surface ocean concentrations between SDUST and SOCX, are reflected in the changed ocean-to-atmosphere fluxes of the species (Fig. 4.46). All differences are directly related to the changes in surface ocean concentrations and are not significant, reaching relative differences between the two sensitivity simulations of up to 5 %. Relative differences in $CO_2$ air-sea fluxes reach locally up to 50 % (Fig. 4.46 (d)), but these high relative changes are confined to regions with a very low $CO_2$ gas exchange (Fig. 4.9 (b)). However, the small changes in the ocean-to-atmosphere

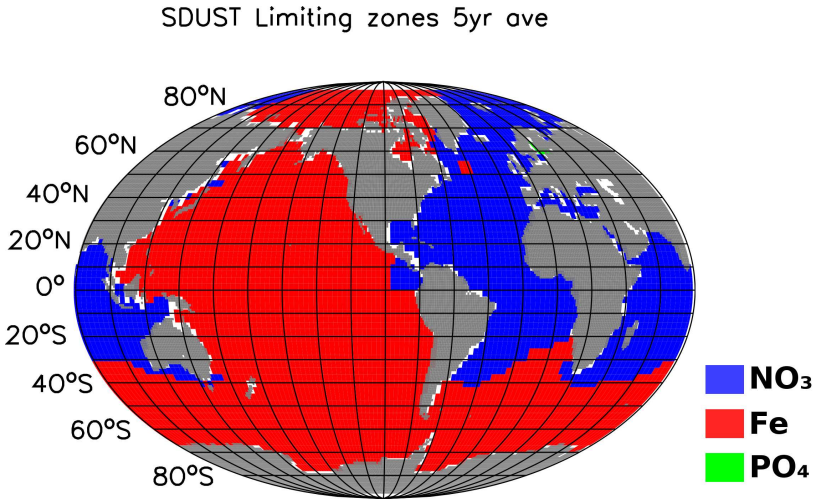


**Figure 4.44:** Limiting nutrients for phytoplankton growth in SDUST. Colours indicate the limiting nutrient in this region: red is Fe, blue is $NO_3^-$, green is $PO_4^{3-}$.

flux between SDUST and SOCX are statistically not significant over the analysed five years and have no significant impact on atmospheric mixing ratios of the specific gas (not shown).

### 4.4.3 Discussion

In summary, the results of the SDUST sensitivity study with a changed atmospheric dust deposition are reasonable. Differences between SDUST and SOCX and responses of the oceanic biogeochemistry and chemical composition to the changed atmospheric forcing are as expected. Impacts of the changed atmospheric dust deposition via changes in oceanic chemical composition on atmospheric composition are not significant on the analysed time-scale of five years, as there are only small impacts of the higher dust deposition—and hence Fe source—on the oceanic NPP in the Atlantic because of the $NO_3^-$ limitation for phytoplankton growth.

In conclusion, the inclusion of an online calculated atmospheric source for dust deposition has only small impacts on oceanic NPP and oceanic concentrations compared to a climatological dust source. This results in small, statistically not significant changes in ocean-to-atmosphere fluxes and no significant impact on atmospheric composition under present day conditions. But the inclusion of online calculated dust deposition provides a more consistent model system, which can be used to assess feedback trends under changed forcings (e.g. pre-industrial, industrial, climate change conditions).

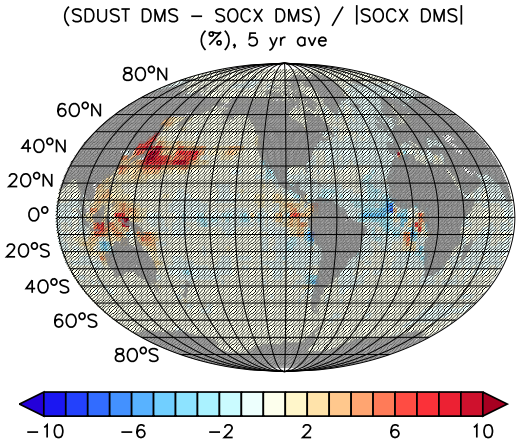


**(a)** DMS (SDUST - SOCX) / |SOCX|

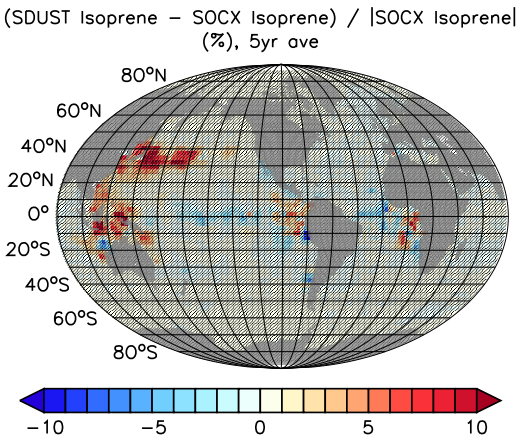


**(b)** $C_5H_8$ (SDUST - SOCX) / |SOCX|

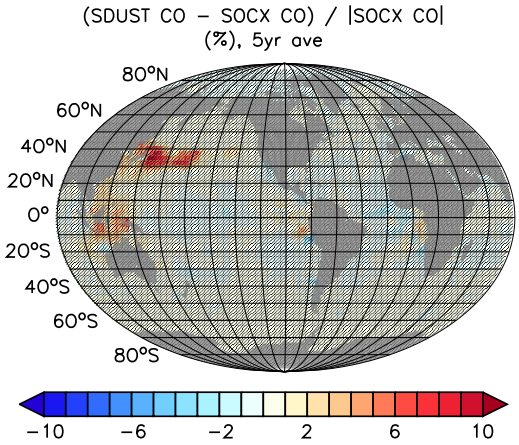


**(c)** CO (SDUST - SOCX) / |SOCX|

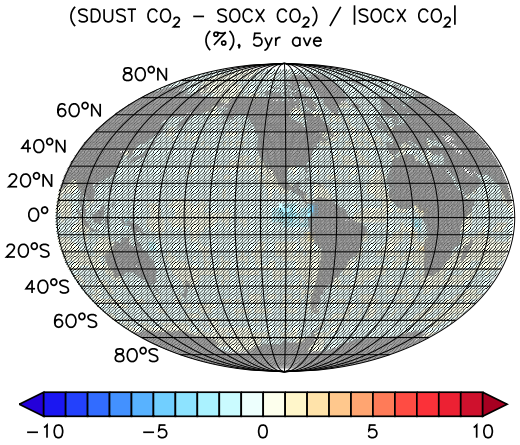


**(d)** $CO_2$ (SDUST - SOCX) / |SOCX|

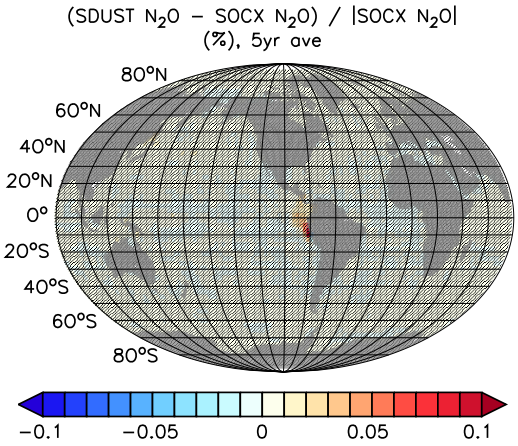


**(e)** $N_2O$ (SDUST - SOCX) / |SOCX|

**Figure 4.45:** Relative differences of surface water concentrations of (a) DMS, (b) $C_5H_8$, (c) CO, (d) $CO_2$, and (e) $N_2O$ between SDUST and SOCX averaged over five years of simulation. Units are %. Differences in concentrations in gray shaded areas are not significant on a 99 % level according to a two-sided Student's t-test.

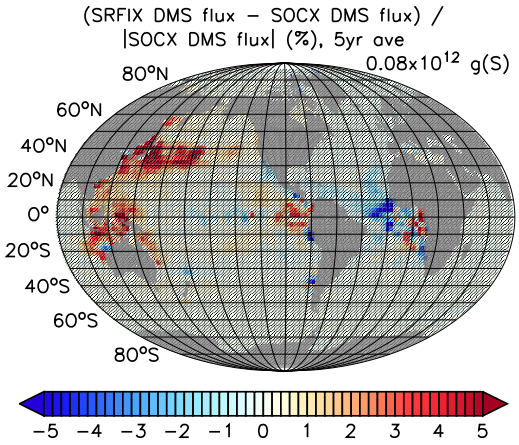


**(a)** DMS flux (SDUST - SOCX) / |SOCX|

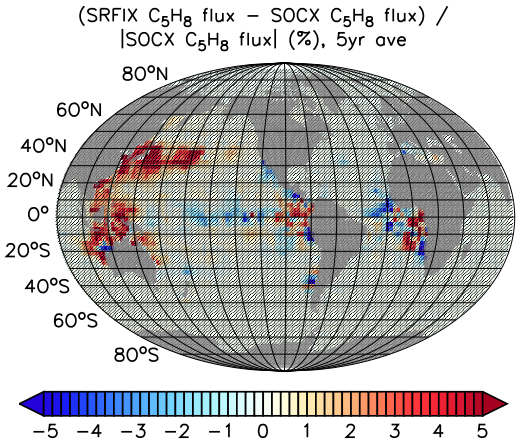


**(b)** $C_5H_8$ flux (SDUST - SOCX) / |SOCX|

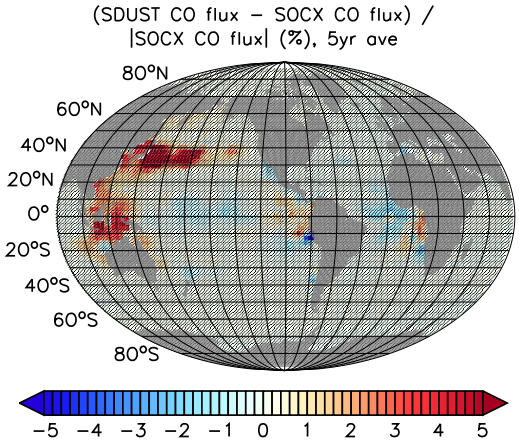


**(c)** CO flux (SDUST - SOCX) / |SOCX|

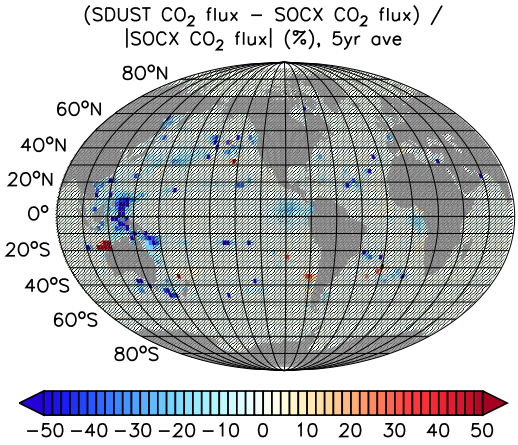


**(d)** $CO_2$ flux (SDUST - SOCX) / |SOCX|

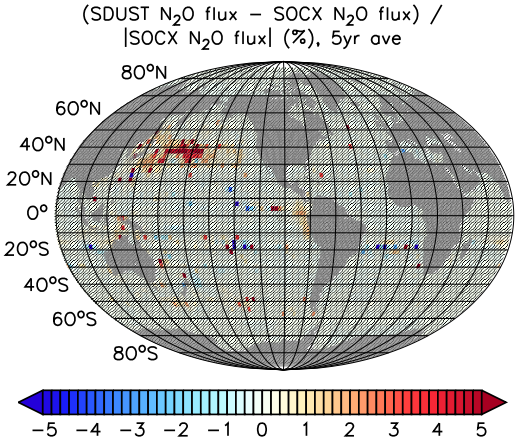


**(e)** $N_2O$ flux (SDUST - SOCX) / |SOCX|

**Figure 4.46:** Relative differences in averaged ocean-to-atmosphere fluxes of (a) DMS, (b) $C_5H_8$, (c) CO, (d) $CO_2$, and (e) $N_2O$ between SDUST and SOCX over five years of simulation. Units are %. Differences in ocean-to-atmosphere fluxes in gray shaded areas are not significant on a 99 % level according to a two-sided Student's t-test.

## 4.5 Summary

Several sensitivity studies with the model system were performed using year-2000 conditions. One sensitivity study was performed to asses the impact of interactive oceanic biogeochemistry via air-sea gas exchange on atmospheric composition. Further sensitivity studies were performed, to assess the impact of riverine nutrient import into the ocean and of nutrient import from online calculated aeolian dust deposition on oceanic biogeochemistry and—via air-sea gas exchange—on atmospheric composition.

For simulating realistic surface ocean tracer concentrations, a reasonable representation of upper ocean dynamics and biogeochemistry is necessary. The model system shows only small deviations in SST and SSS after a spin-up phase of the dynamically coupled model system of 100 years and an additional chemically coupled spin-up phase of 30 years. The biogeochemistry submodel shows deviations in NPP and EP, resulting from a higher coupling frequency of 2 h for surface ocean irradiation, compared to the original code, which uses a daily-mean value. These deviations in NPP impacts surface ocean concentrations of DMS, $C_5H_8$, $CO_2$, and $N_2O$, resulting in deviations in ocean-to-atmosphere fluxes of these compounds compared to a baseline simulation with prescribed, measurement based oceanic concentrations.

Ocean-to-atmosphere fluxes of DMS, $C_5H_8$, and CO are in first order approximation linearly related to the corresponding surface ocean concentration in the model system's grid boxes. The response of atmospheric mixing ratios, however, cannot be approximated linearly, due to non-linear atmospheric chemistry and transport processes.

Despite the systematic deviations resulting from deficiencies in the representation of the NPP in the oceanic biogeochemistry submodel, relative differences between sensitivity studies could be assessed. The linear dependence of the air-sea gas exchange with surface ocean concentrations gives further confidence for the results to be valid over a wide range of oceanic concentrations. For atmospheric concentrations, however, additional processes like advection, dry and wet deposition, and chemical processing are important and weaken the oceanic signal.

The impact of additional nutrients in the surface ocean on oceanic biogeochemistry via riverine import is small, depending on the limiting nutrient for phytoplankton growth in the specific ocean basin. Changes, however are in line with expectation, yielding impacts mainly in coastal areas. The impact on ocean-to-atmosphere fluxes are, however, insignificant over the analysed five years, with the exception for $CO_2$

in coastal areas. This is in line with the expected higher import of riverine $CO_2$ to the coastal ocean. The impact of changes in the coastal surface ocean concentrations of DMS, $C_5H_8$, and CO on the global air-sea gas exchange is insignificant, but could be important on the regional scale, especially in coastal areas, where anthropogenic pollution may react with oceanic biogenic emissions. To investigate this impact, a higher model resolution and a better representation of coastal oceanic biogeochemical processes in the model system are necessary.

The implementation of deposition of Fe and Si from an online calculated dust deposition instead of using prescribed climatological deposition fluxes, introduces additional variation with the meteorological situation and consistent simulations under modified climate conditions become possible. The impact on oceanic biogeochemistry by the modified source is reasonable, changing surface ocean concentrations of dissolved dust, Fe, and $Si(OH)_4$, especially in areas with larger deposition fluxes in the Atlantic. The response in NPP, however, is small, depending on the simulated limiting nutrient for phytoplankton growth in the specific ocean basin. To asses the impact of nutrient import by the online calculated dust deposition under changed climate conditions, which may impact the simulated patterns of the limiting nutrient, further simulations have to be performed. Furthermore, investigation of the impact of nitrogen (N) deposition from the atmosphere (Spokes et al., 2000; Tost et al., 2007a) on the biogeochemistry in the $NO_3^-$ limited Atlantic basin may be interesting.

# Chapter 5

# Preparation for long term simulations with chemistry

Long-term simulations with the fully coupled model system, focusing on tropospheric chemistry require a reasonable forcing from the stratosphere, and hence the inclusion of stratospheric chemistry. After reproducing the interaction of oceanic and tropospheric chemistry on shorter time-scales withe the chemically coupled model system, the next step is to implement a model system with stratospheric chemistry coupled to an interactive ocean model. Long-term simulations with tropospheric chemistry with the fully coupled atmosphere-ocean model for analysing trends in the troposphere over decades requires the reproduction of the current tropospheric state and stratospheric forcings as upper boundary to tropospheric dynamics and chemistry. The application of the model system over longer time-scale also requires additional optimisation of parameters used for closure in subgrid-scale parameterisations, to obtain a stable climate in the model system under unaltered forcings (minimising model system drift).

To use the model system for long term simulations (centuries), several prerequisites must be fulfilled, first of all the computational costs of such a complex simulation must be reduced. The inclusion of the computationally efficient atmospheric chemistry submodel E4CHEM (Baumgaertner et al., 2010) for stratospheric chemistry was tested in the ECHAM/MESSy Atmospheric Chemistry (EMAC; Jöckel et al., 2005, 2006, 2010) model system. Until now, no long term simulation with air-sea gas exchange and simplified stratospheric chemistry has been performed with this model

system. This chapter describes the preparatory work to enable the model to simulate air-sea gas exchange in combination with simplified stratospheric chemistry on climatological time scales.

To be able to perform long term simulations on current computer systems in reasonable time, the model was used in a setup with a coarser vertical resolution compared to Jöckel et al. (2010). Instead of 90 vertical model levels, a setup with 47 hybrid pressure levels, ranging from Earth's surface up to a pressure of 0.01 hPa resolving the middle atmosphere (L47MA), was used in this study.

The determination of a set of values for free parameters to close subgrid-scale parameterisations for the specific vertical and horizontal model resolution is described in Section 5.1. The final set of parameters determined from this process of model "tuning" is presented in Section 5.2.

## 5.1 Parameter optimisation

For a numerical solution of the underlying partial differential equations of the model system, these equations have to be discretised in the spatial and temporal domain. Processes on smaller scales than explicitly resolved in the discretised model system acting as forcing terms in the system of partial differential equations have to be parameterised. With parameterisations, the impact of the unresolved process on the larger scale model state is calculated using available information of the coarser model state itself (Schirber et al., 2013). As such, parameterisations imply some degree of freedom, i.e. they usually contain parameters whose values can be chosen in a certain range to achieve a physically meaningful representation of the unresolved process. These free parameters have to be determined to close the parameterisations, but they are not necessarily directly measurable. In the process of model development, these parameters are optimised to achieve a model system capable of reproducing the present day climate state. Whereas this parameter optimisation is—to a certain degree—arbitrary, the set of parameters are chosen within their uncertainty range to achieve physically meaningful results.

To obtain a simulation of a stable climate state, while all external forcing parameters a kept constant, parameter optimisation aims to balance Earth's energy budget in the model system (Mauritsen et al., 2012). In the coupled model system of the European Centre HAMburg general circulation model (ECHAM) and Max Planck Institute Ocean Model (MPIOM; Marsland et al., 2003; Jungclaus et al., 2006), the method of parameter optimisation means finding a set of parameters

to close the parameterisation of clouds and convective processes, not resolved on the model's resolution (Mauritsen et al., 2012). This method is also used here to close the subgrid parameterisation of cloud processes, which influences the model's radiation balance. Thus, parameter optimisation is used to compensate uncertainties in the representation of clouds and their related processes. The goal is to reach a balance in radiative fluxes at the top of the atmosphere (TOA) and in this way to minimise model drift. The choice of the final parameter set for the model system depends on the model's horizontal and vertical resolution.

As there were no parameters present for the chosen vertical resolution in the original model code, several model simulations—each spanning one century—for year-2000 conditions were performed to find a suitable parameter set. The model setup comprises the atmospheric dynamics coupled to the dynamical ocean general circulation model. The main focus is on the radiation balance at the TOA. However, because of shortcomings in the model system's energy conservation (Stevens et al., 2013), an interval of $0\,\mathrm{W\,m^{-2}}$ to $2\,\mathrm{W\,m^{-2}}$ (incoming) for the net radiation balance of incoming and outgoing radiation at TOA is considered acceptable. The targeted global mean surface temperature is about 14 °C. Under these constraints, several model variables are checked, to assure that the simulation is comparable to present day conditions. These diagnostic model variables—besides the net longwave and shortwave radiation at TOA—are cloud cover, liquid water path, and water vapour path (cf. Mauritsen et al., 2012).

All parameters, which are used for optimisation of the model system to reach a balance in the simulated net radiation at TOA together with a realistic surface temperature, are cloud-related. Subgrid-scale parameterisation of clouds is the most uncertain aspect in general circulation models (GCMs), and at the same time cloud and convective processes exert a large impact on radiation balance (Mauritsen et al., 2012). In general, there are several parameters influencing the parameterisation of clouds and convection, and thus radiative transfer, but not all are used in the process of parameter optimisation. An optimised model w.r.t. its climate state and radiation balance is achieved using five of these parameters, whereas the values of other parameters are chosen as in the original model code and in accordance with model setups at comparable horizontal or vertical resolution.

In the process of parameter optimisation, the goal is to keep all free model parameters close to the original, physically meaningful values of "neighbouring" model resolutions. Whenever possible, values derived from measurements are used. Here, the five model parameters *zasic*, *zinhoml*, *zinhomi*, *cmfctop* and *cprcon*, which

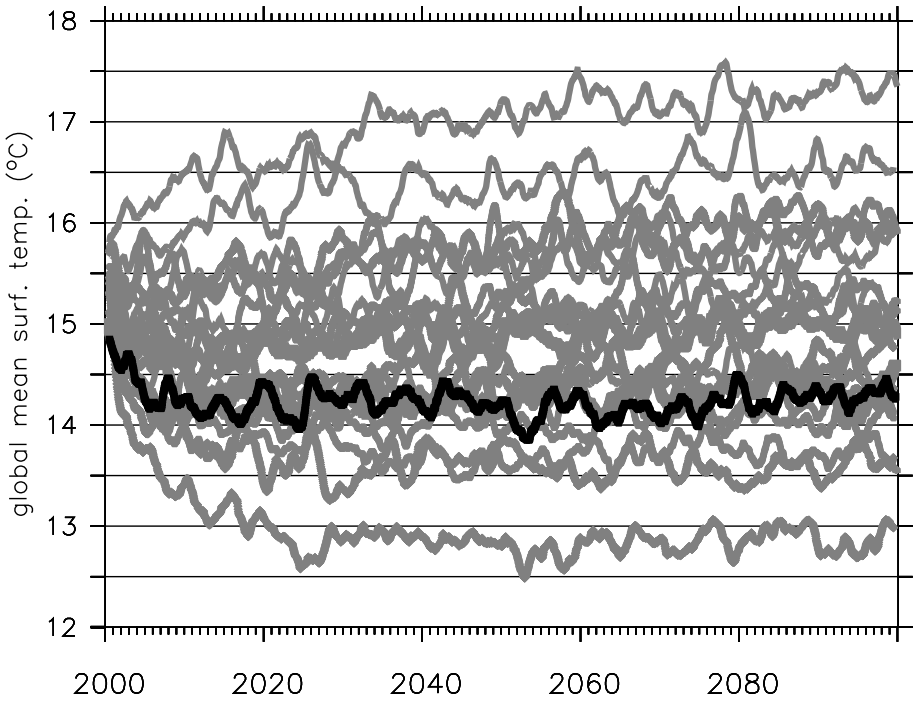


**Figure 5.1:** Running annual global mean surface temperature of the parameter optimisation simulations. The black line represents simulation number *31* using a set of optimised parameters, gray lines the other simulations.

are further described below, are used for parameter optimisation of the model system in a setup using a horizontal resolution of T42 and 47 vertical levels resolving the middle atmosphere (L47MA). Values of the parameters controlling the accretion of cloud droplets (*cauloc*) and the entrainment rate for shallow convection (*entrscv*) are chosen as in "neighbouring" model resolutions. A complete overview of parameters used in the model system depending on horizontal and vertical resolution in the model configurations with and without coupling to an interactive ocean model are listed in Appendix D.

To determine the set of optimised parameter values for the model setup, the values of the different parameters were varied in several model simulations. Table 5.1 lists the model simulations with corresponding values of the parameters. These simulations were performed for 100 years, each. The initial 50 years of the simulations as spin-up phase are neglected, and the mean values of the final 50 years in surface temperature, radiation fluxes and balance at TOA, cloud cover, and water paths were analysed. The combination of parameter values resulting in a minimal net radiation

| simulation number | zasic | zinhomi | zinhoml | cmfctop | cprcon ($10^{-4}\,s^{-1}$) |
|---|---|---|---|---|---|
| 0 | 0.89 | 0.85 | 0.70 | 0.30 | 1.50 |
| 1 | 0.85 | 0.85 | 0.70 | 0.30 | 1.50 |
| 2 | 0.80 | 0.85 | 0.70 | 0.30 | 1.50 |
| 3 | 0.80 | 0.85 | 0.70 | 0.22 | 1.50 |
| 4 | 0.89 | 0.80 | 0.70 | 0.22 | 1.50 |
| 5 | 0.85 | 0.80 | 0.70 | 0.22 | 1.50 |
| 6 | 0.80 | 0.80 | 0.70 | 0.22 | 1.50 |
| 7 | 0.80 | 0.80 | 0.70 | 0.26 | 1.50 |
| 8[a] | 0.80 | 0.80 | 0.70 | 0.22 | 1.50 |
| 10 | 0.91 | 0.97 | 0.92 | 0.22 | 1.50 |
| 11 | 0.80 | 0.97 | 0.92 | 0.22 | 1.50 |
| 12 | 0.85 | 0.97 | 0.92 | 0.22 | 1.50 |
| 14 | 0.91 | 0.97 | 0.92 | 0.20 | 1.50 |
| 16 | 0.91 | 0.97 | 0.92 | 0.22 | 1.00 |
| 23[b] | 0.89 | 0.80 | 0.70 | 0.22 | 1.50 |
| 25 | 0.89 | 1.00 | 0.70 | 0.22 | 1.50 |
| 26 | 0.89 | 1.00 | 0.90 | 0.22 | 1.50 |
| 28 | 0.89 | 0.80 | 0.77 | 0.21 | 3.00 |
| 29 | 0.89 | 0.85 | 0.80 | 0.21 | 3.00 |
| 30 | 0.89 | 0.85 | 0.90 | 0.21 | 3.00 |
| 31 | 0.89 | 0.80 | 0.90 | 0.21 | 3.00 |

[a] in simulation 8 *cauloc*=3.0, in all other simulations *cauloc*=0.0

[b] in simulation 23 the ocean model is operated on the horizontal grid GR15, in all other simulations on GR30

**Table 5.1:** Values of the free parameters used in the simulations for parameter optimisation. For a description of the parameters, see text.

flux at the top of the atmosphere and a realistic global surface temperature, and simultaneously resulting in reasonable values for the other model variables diagnosed, are chosen as optimal parameter set.

Figure 5.1 shows the evolution of the global mean surface temperature in the parameter optimisation simulations. The highlighted curve corresponds to simulation number *31*. In this simulation the global mean surface temperature averaged over the last 50 years of the simulation reaches a value of 14.2 °C. Furthermore, the global mean surface temperature of this simulation is subject to only a minimal drift after a decrease during the first ten years of the simulation period. In that way simulation number *31* meets the constraint of a realistic and stable climate state. The fulfilment of the further prerequisites in this model simulation, the meaning of the free parameters and the impact of their variation on the model system's climate state are discussed in the following sub-sections.

### 5.1.1 Correction factor for asymmetric radiation scattering (*zasic*)

Radiative properties of ice clouds are parameterised using the ice water path. Scattering properties of clouds in the solar spectrum—mass extinction coefficient, single scattering albedo, and asymmetry factor—are determined using idealised Mie calculations (Roeckner et al., 1996). For application in GCMs, the results are averaged and expressed as functions of the effective particle radius.

The degree of anisotropic scattering in ice clouds is described by the asymmetry factor $\gamma_i$ (Stephens et al., 1990). A value of $\gamma_i = 1$ indicates complete forward scattering, whereas a value of $\gamma_i = -1$ is for total backscattering, a value of $\gamma_i = 0$ characterises isotropic scattering. Over a large range of wavelengths, the asymmetry factor for clouds is $\gamma_i = 0.7$–$0.9$ (Stephens et al., 1990). Measurements suggest, that an asymmetry factor of $\gamma_i = 0.8$ should be used to model scattering in clouds (Francis et al., 1994). Mie theory overestimates the asymmetry factor for ice clouds, yielding a value of $\gamma_i = 0.87$ (Roeckner et al., 1996, 2003; Stephens et al., 1990). The model parameter *zasic* accounts for correction of asymmetric radiation scattering in ice clouds. The value of the correction factor *zasic* used in the model should be 0.91 to achieve an asymmetry factor of $\gamma_i \approx 0.8$ (Roeckner et al., 1996, 2003), whereas in ECHAM5 simulations without coupled ocean, a correction factor for the asymmetry factor of 0.85 is used (see Appendix D for an overview of model parameters values in different model setups).

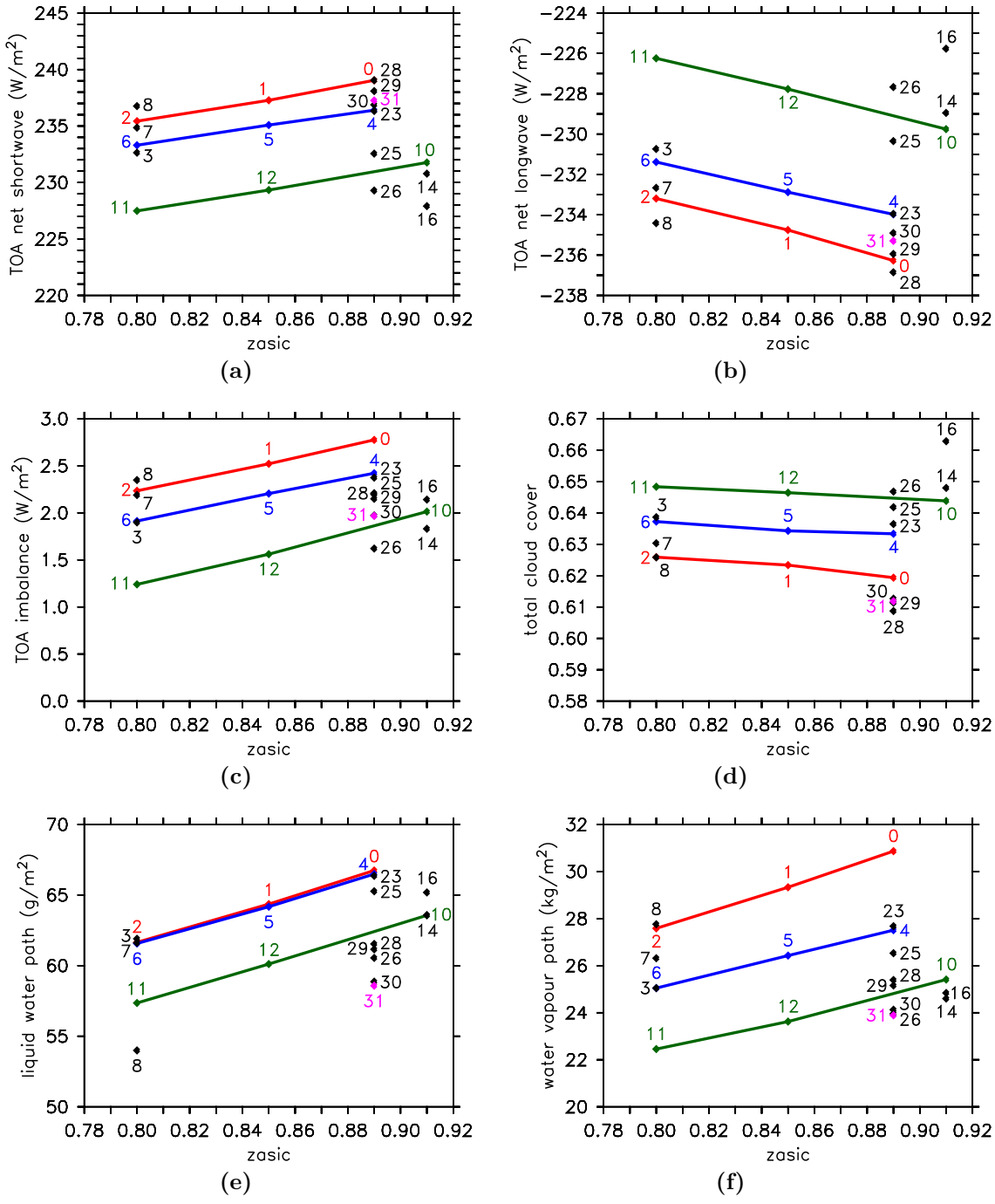


**Figure 5.2:** Variation of the simulated atmospheric state with the value of the asymmetric radiation scattering correction factor for ice clouds (*zasic*). The numbers indicate the corresponding simulation as listed in Table 5.1. Parameter optimisation simulations only differing in the chosen value of *zasic* are connected using coloured lines. The final parameter set number *31* is marked in purple.

Variations in the atmospheric state of the model system with a modified value of *zasic* are shown in Fig. 5.2. In these diagrams, simulations linked with a coloured line can be compared directly, as only the value of the parameter indicated on the ordinate is changed, whereas other parameters are kept constant.

The correction of the asymmetry factor has a direct impact on radiative transfer, and hence on the radiation balance at the top of the atmosphere (Fig. 5.2 (a)–(c)). The net shortwave radiation flux at TOA increases with an increasing *zasic* (Fig. 5.2 (a)). Positive values of the radiation flux indicates larger incoming radiation. The TOA net longwave radiation flux decreases as the outgoing longwave radiative flux increases (the negative sign indicates upward radiative flux) with an increasing correction factor for asymmetric radiation scattering. This behaviour is expected, as an increased correction factor results in more forward scattering and less backward scattering in the shortwave radiation in ice clouds. As the TOA shortwave downward flux is constant ($341.3\,\mathrm{W\,m^{-2}}$), changes in the net shortwave radiative flux at TOA has to be caused by a changed upward flux. In the case of higher (lower) values of *zasic*, the asymmetry factor is higher (lower) and a reduced (an enhanced) backscattering of shortwave radiation decreases (increases) the shortwave upward flux resulting in a larger (smaller) net shortwave radiation flux at TOA.

The behaviour of the outgoing longwave radiation (Fig. 5.2 (b)) is straightforward. As more shortwave radiation reaches the surface in case of a higher asymmetry factor, there is more heating resulting in enhanced upward longwave radiation. The imbalance of the net TOA radiation fluxes is slightly enhanced with higher values of *zasic* (Fig. 5.2 (c)).

There is little change in the total cloud cover as *zasic* varies (Fig. 5.2 (d)). Generally all parameter optimisation experiments simulate more than 60 % cloud cover, which is acceptable (Mauritsen et al., 2012). Satellite derived cloud cover estimates are generally higher, but difficult to compare to the model output (see, e.g Bodas-Salcedo et al., 2011).

Liquid water path and water vapour path rise with increased values of *zasic* (Fig. 5.2 (e) and (f)). While all parameter optimisation simulations are within the accepted range of $50\,\mathrm{g\,m^{-2}}$ to $80\,\mathrm{g\,m^{-2}}$ for the liquid water path (Mauritsen et al., 2012), some model simulations overestimate the water vapour path, which should be about $24\,\mathrm{kg\,m^{-2}}$ to $25\,\mathrm{kg\,m^{-2}}$.

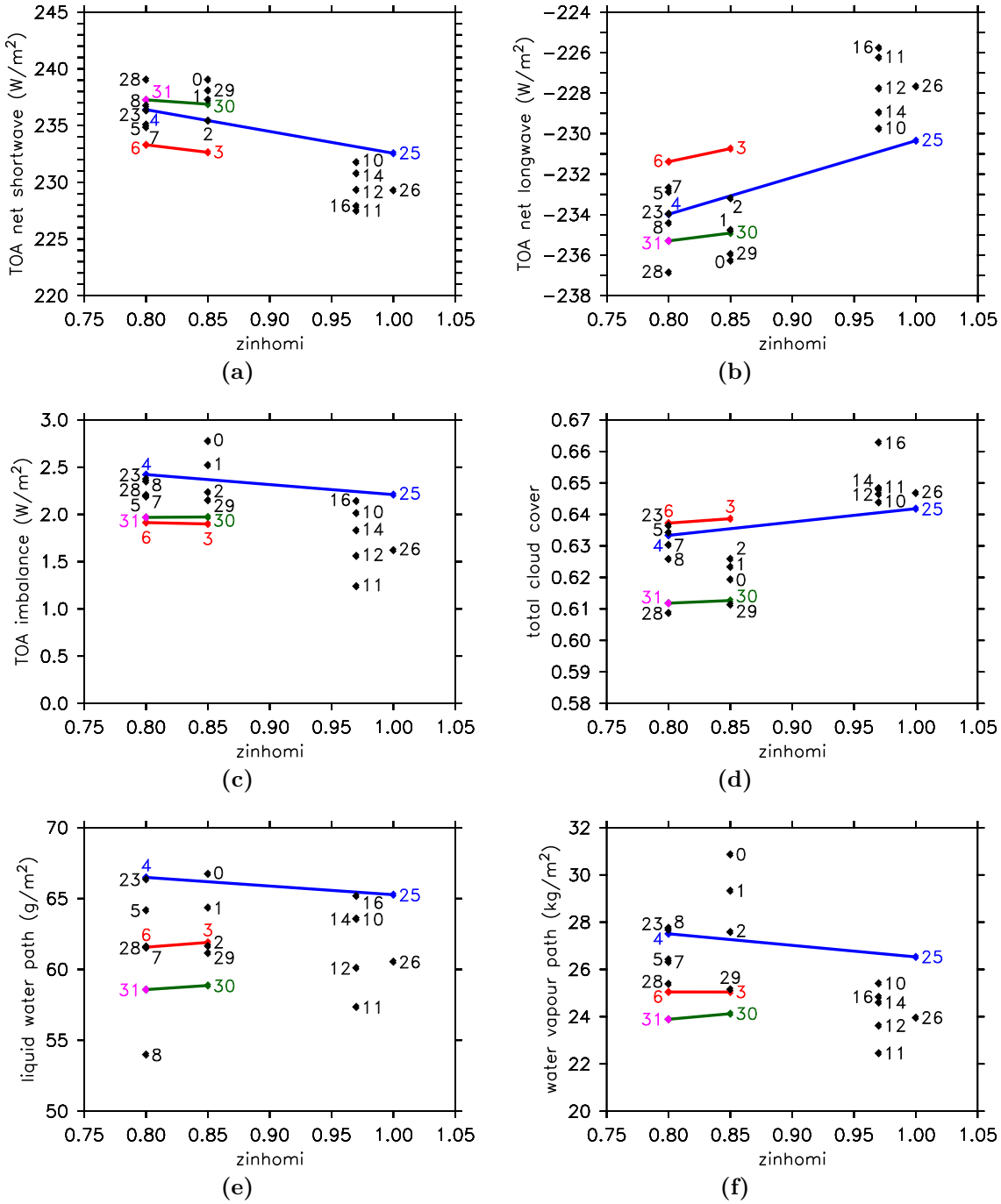


**Figure 5.3:** As Fig. 5.2, showing variation of the simulated atmospheric state with the homogeneity factor of ice clouds *zinhomi*.

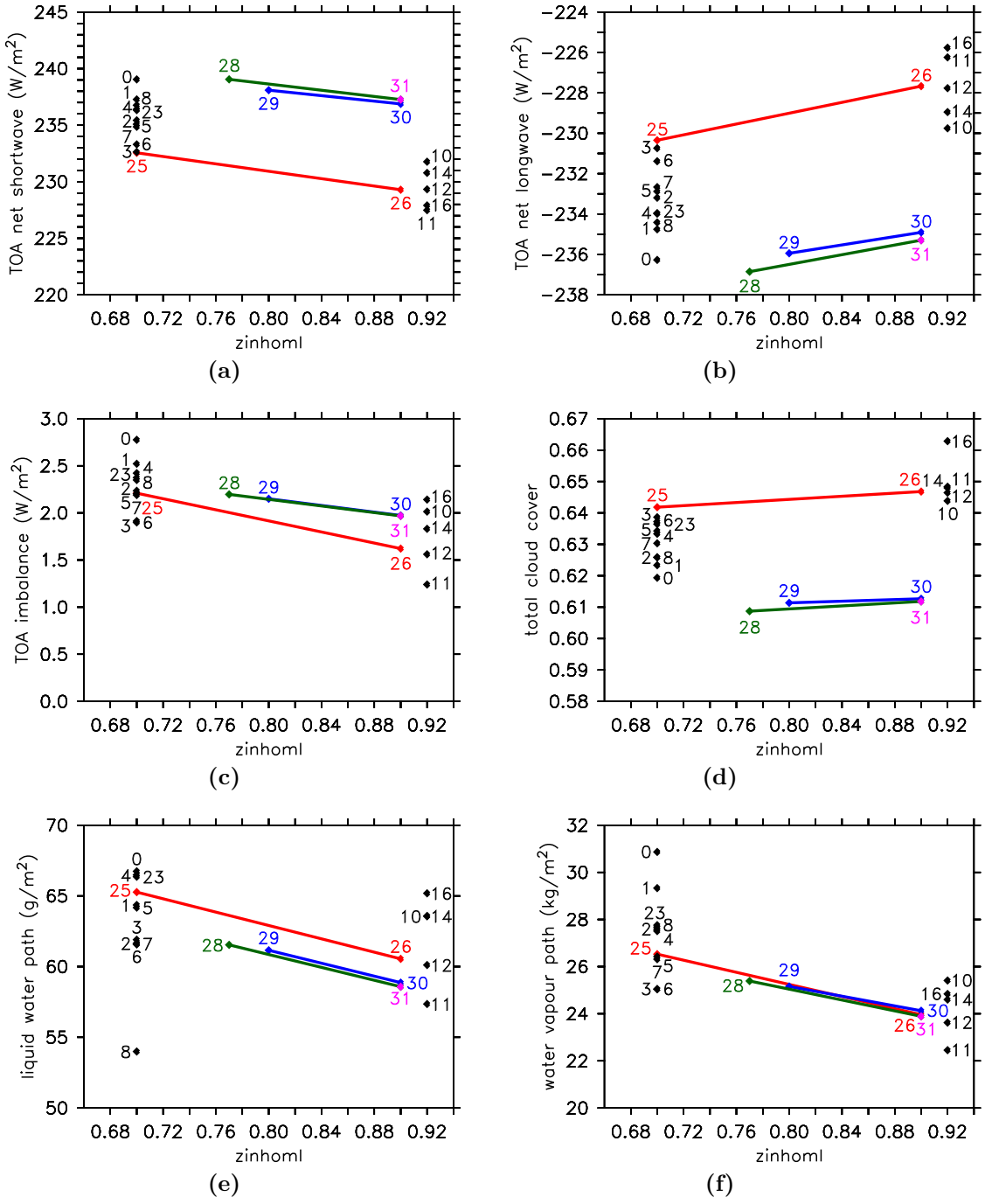


**Figure 5.4:** As Fig. 5.2, showing variation of the simulated atmospheric state with the homogeneity factor of liquid clouds (*zinhoml*).

### 5.1.2 Cloud homogeneity factors (*zinhomi* and *zinhoml*)

The parameters called homogeneity factors account for inhomogeneities in cloud thickness, which can not be represented at the typically used horizontal resolutions of climate models. There are two homogeneity factors in the model's radiation code, one for liquid clouds (*zinhoml*) and one for ice clouds (*zinhomi*). As Mauritsen et al. (2012) show, for the Max Planck Institute Earth System Model (MPI-ESM) any change in the homogeneity factor for liquid clouds corresponds to a change in the net short-wave radiation at TOA, whereas the other global quantities show almost no reaction. The homogeneity factor for liquid clouds was therefore identified as possibility to close the radiation balance.

Changes in the atmospheric state induced by variation of the homogeneity factor for ice clouds (*zinhomi*), are shown in Fig. 5.3. An increase in *zinhomi* causes a decrease of the net longwave flux at TOA (Fig. 5.3 (a)) and a decrease in the outgoing shortwave flux (Fig. 5.3 (b)). This behaviour is understandable, as a more homogeneous cloud cover tends to reflect more shortwave radiation—manifesting in a lower net shortwave radiative flux at TOA—and to shield more upward longwave radiation from Earth's surface, thus lowering the outgoing longwave radiative flux at TOA. A slight decrease in the radiation imbalance at TOA can be seen in Fig. 5.3 (c). There is a minor increase in cloud cover with higher values of *zinhomi* (Fig. 5.3 (d)). A decrease of liquid water path (Fig. 5.3 (e)) and water vapour path (Fig. 5.3 (f)) is found after a slightly initial increase with larger values of the homogeneity factor for ice clouds.

The influence of the homogeneity factor for liquid clouds (*zinhoml*) on atmospheric variables is presented in Fig. 5.4. As for *zinhomi*, net shortwave radiative flux (Fig. 5.4 (a)) and outgoing net longwave radiative flux (Fig. 5.4 (b)) at TOA are decreasing as the value of *zinhoml* increases. This results in a lower radiation imbalance at TOA with larger values of *zinhoml* (Fig. 5.4 (c)). The impact on cloud cover is a marginal increase over the tested range with increasing values of *zinhoml*. Both, liquid water path and water vapour path are reduced with enhanced values of *zinhoml*.

From these results, in the model system used in this study it is more challenging to only use *zinhoml* for closing the radiation balance, as suggested for MPI-ESM (Mauritsen et al., 2012). Because of changes in the parameterisation of cloud related processes in the development of ECHAM6 (Stevens et al., 2013), the decoupling of *zinhoml* from liquid water path and water vapour path are not reproduced here. Nevertheless, *zinhomi* and *zinhoml* are important parameters for closing the TOA

radiative imbalance in this study, as the sensitivity of cloud cover, liquid water path, and water vapour path on changed homogeneity factors are small enough to keep the model system in the accepted range for these atmospheric variables.

### 5.1.3 Fraction of convective mass flux above the level of non-buoyancy (*cmfctop*)

The convective mass flux at the level of non-buoyancy influences the atmospheric radiative transfer. The parameter used in the convection parameterisation (Tiedtke, 1989; Nordeng, 1994) is named *cmfctop* in the model system. This parameter determines the fraction of mass overshooting the level of non-buoyancy in convective clouds.

The increase of this parameter directly decreases the cloud cover (Fig. 5.5 (d)). A reduced cloud cover goes along with less reflection of incoming shortwave radiation, thus leading to an increase of the net shortwave radiative flux at TOA (Fig. 5.5 (a)). As more solar radiation reaches Earth's surface, a higher global mean surface temperature is reached (Mauritsen et al., 2012). More absorption of solar radiation at the surface results in an elevated upward longwave radiative flux, visible in the net longwave radiative flux at TOA as an increase in outgoing (negative) longwave radiation (Fig. 5.5 (b)). Disturbing the cloud cover and radiative fluxes in the system leads to an enhanced radiative imbalance at TOA with higher values of *cmfctop* (Fig. 5.5 (c)).

The liquid water path is not influenced by the choice of the value of *cmfctop* (Fig. 5.5 (e)), whereas the water vapour path increases with an increased value of *cmfctop* (Fig. 5.5 (f)), because of a higher global mean surface temperature. As *cmfctop* influences the hydrological cycle by impacting the distribution of water mass in the atmosphere, it has a big impact on radiative transfer in the atmosphere, and thus on the radiative imbalance at TOA. When changing *cmfctop* during the procedure of parameter optimisation, special care has to be taken, as changes have also big impacts on cloud cover and water vapour path, as well as on global mean surface temperature.

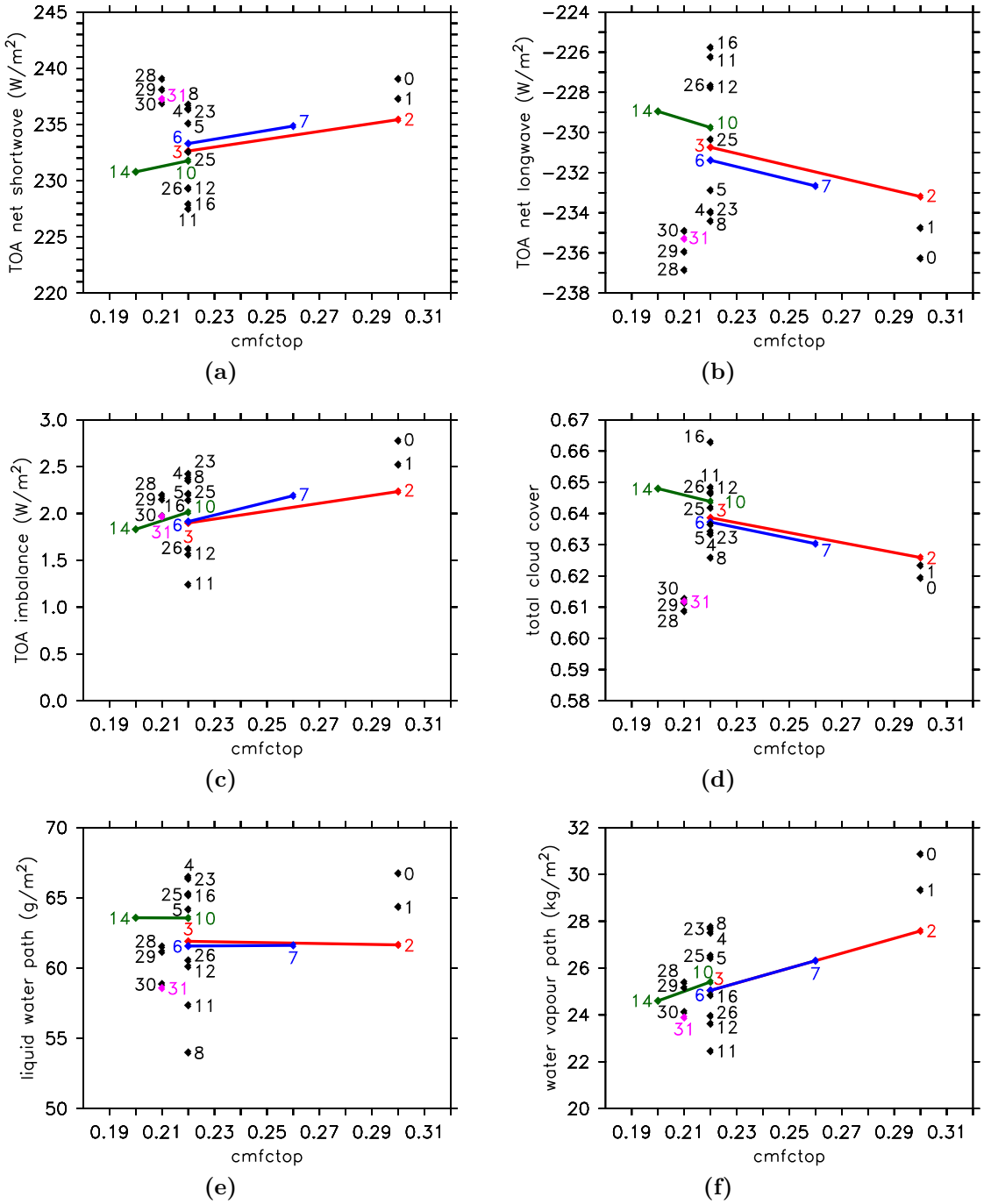


**Figure 5.5:** As Fig. 5.2, showing variation of the simulated atmospheric state with the fraction of convective mass flux above the level of non-buoyancy *cmfctop*.

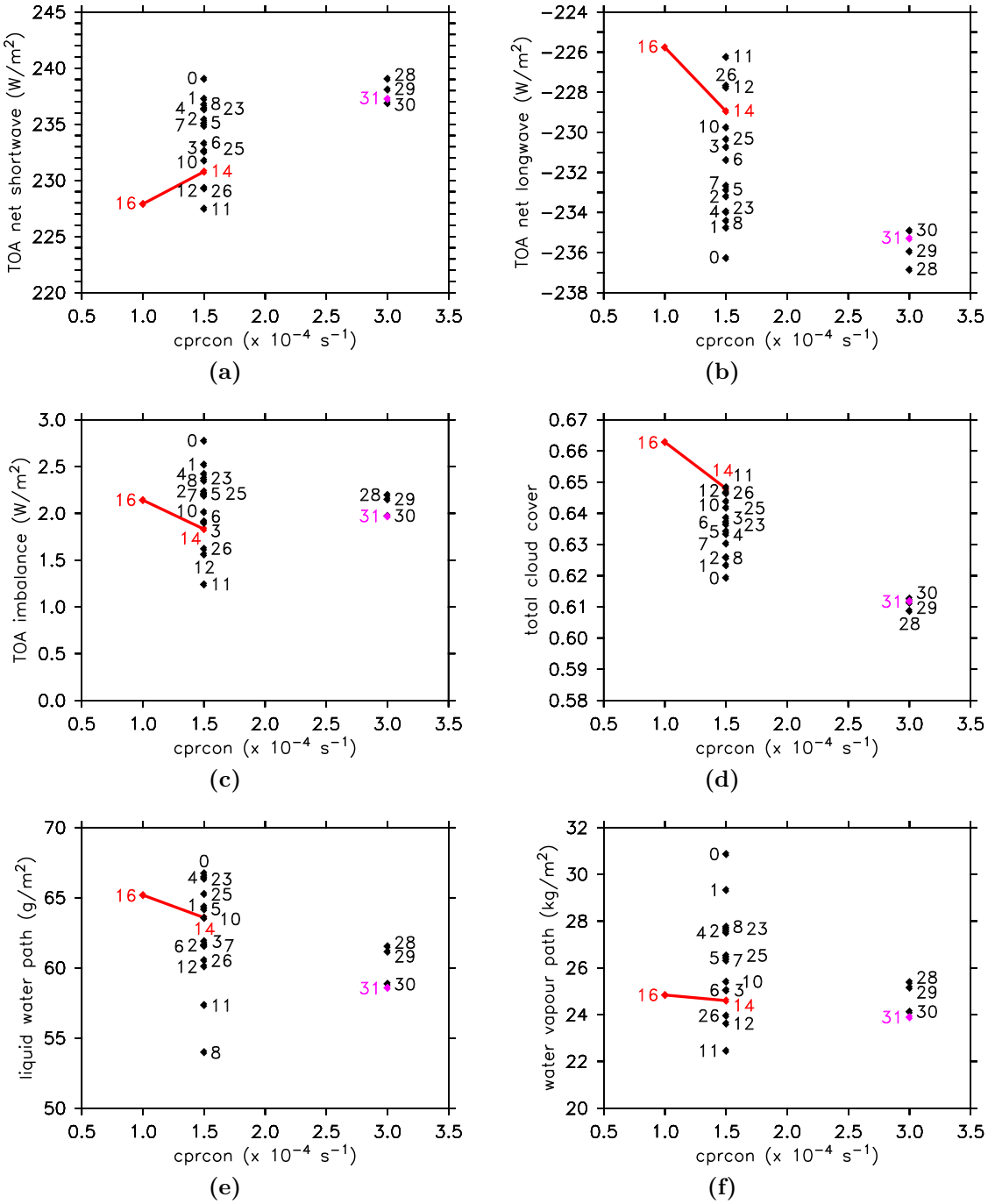


**Figure 5.6:** As Fig. 5.2, showing variation of the simulated atmospheric state with the conversion rate from cloud water to rain (*cprcon*).

### 5.1.4 Conversion rate from cloud water to rain (*cprcon*)

The conversion rate from cloud water to rain in convective clouds (*cprcon*) is also a parameter, which impacts radiative transfer, cloud cover, liquid water path, and water vapour path. Larger values of this parameter generally lead to a reduced cloud cover and reduced water vapour, as larger parts of cloud water are precipitated (Mauritsen et al., 2012).

The impact of changes in *cprcon* on the average state of the atmosphere is shown in Fig. 5.6. Rising the value of *cprcon* leads, as expected, to a reduced cloud cover (Fig. 5.6 (d)). Reductions of liquid water path (Fig. 5.6 (e)) and water vapour path (Fig. 5.6 (f)) with an increasing value of *cprcon* are visible. This effect is caused by enhanced conversion from cloud water to precipitation. Linked to this process, removal of water from the atmosphere is enhanced as the value of *cprcon* is increased.

This interference with the model's hydrological cycle is clearly visible in the radiative imbalance at TOA (Fig. 5.6 (c)). As the value of *cprcon* increases, the radiative imbalance at TOA decreases. This is caused by less reflection of shortwave radiation in the model's atmosphere, due to the reduced cloud cover. Less shortwave reflection can be seen in the net shortwave radiative fluxes at TOA (Fig. 5.6 (a)), which increases with larger values of *cprcon*, as less reflected shortwave radiation reaches the top of the atmosphere as upward shortwave radiation. Less shortwave radiation, in turn, implies a higher global mean surface temperature and an increased upward longwave radiative flux, which is visible at TOA in the longwave radiation budget (Fig. 5.6 (b)).

### 5.1.5 Entrainment rate for shallow convection (*entrscv*) and accretion of cloud droplets by precipitation (*cauloc*)

Parameters controlling the entrainment rate for shallow convection (*entrscv*) and the accretion of cloud droplets by precipitation (*cauloc*) in the parameterisation of cloud processes are not varied during this parameter optimisation.

Increasing the entrainment rate for shallow convection (*entrscv*) leads to effects opposite to the effects due to increased convective mass flux at the level of non-buoyancy (*cmfctop*). As *entrscv* does not change with different vertical and horizontal resolutions in the original model code, its value of $3.00 \times 10^{-4}\,\mathrm{m}^{-1}$ is kept constant during the parameter optimisation process. The chosen value is consistent with the value of the standard ECHAM6 setup reported by Mauritsen et al. (2012).

One test simulation was performed, however, using a value of *cauloc* = 3.0 instead of the standard value *cauloc* = 0.0, to test the impact of changes in this parameter. Comparison of this simulation (*23*) with the corresponding standard simulation (*4*), where all parameters except for *cauloc* are set to the same values, reveals only minimal differences in the atmospheric state (cf. Figs. 5.2–5.6, simulations *4* and *23*). Using *cauloc* as parameter for parameter optimisation is hence not further considered. The value of the parameter is set to zero, consistent with the value chosen for coupled model configurations in the original model code.

## 5.2 Results from parameter optimisation simulations

Model simulations with varied values for the parameters described above, reveal a set of parameters, for which the constraints of a reasonable atmospheric climate state are met. In simulation number *31* a global mean temperature averaged over the last 50 years of the simulation of 14.2 °C is achieved. Furthermore, this global mean surface temperature is subject to only a minimal drift after an initial decrease during the first ten years of the simulation period (Fig. 5.1). The radiative imbalance at TOA averaged over the last 50 years of the simulation is 1.97 $\mathrm{W\,m^{-2}}$, thus well within the accepted range of 0 $\mathrm{W\,m^{-2}}$ to 2 $\mathrm{W\,m^{-2}}$. All atmospheric variables analysed in Section 5.1 are in the appropriate range of values (cf. Figs. 5.2–5.6). The set of parameters determined from the parameter optimisation simulations are listed in Table 5.2. The choice of this specific set of parameters, however, remains somehow subjective, as other parameter sets may also satisfy the constraints. Here, the parameters for the 47 levels middle atmosphere (L47MA) setup are chosen in a way, that the values are close to values of "neighbouring" model resolutions in the original model code.

| zasic | zinhomi | zinhoml | cmfctop | cprcon ($10^{-4}\,\mathrm{s^{-1}}$) | cauloc | entrscv ($10^{-4}\,\mathrm{m^{-1}}$) |
|---|---|---|---|---|---|---|
| 0.89 | 0.80 | 0.90 | 0.21 | 3.00 | 0.0 | 3.0 |

**Table 5.2:** Set of parameter values used for the coupled model setup with atmospheric resolution of T42L47MA and oceanic resolution GR30 from simulation number *31*. For a description of the parameters, see Section 5.1.

| zasic | zinhomi | zinhoml | cmfctop | cprcon ($10^{-4}\,s^{-1}$) | cauloc | entrscv ($10^{-4}\,m^{-1}$) |
|---|---|---|---|---|---|---|
| 0.91 | 0.80 | 0.70 | 0.21 | 2.00 | 0.0 | 3.0 |

**Table 5.3:** Final set of parameters used for the coupled model setup with an atmospheric resolution of T42L47MA, oceanic resolution GR30, and the updated HD submodel. For a description of the parameters, see Section 5.1.

An additional fine tuning of the parameter set had to be performed after updating the Hydrological Discharge (HD) submodel to a version of HD (Hagemann and Dümenil, 1998) similar to the implementation in ECHAM6 (Stevens et al., 2013). This update was introduced to achieve a better computational performance of the model system. Introducing a modified HD submodel affects—within the range of uncertainty—the hydrological cycle of the model system. Even small changes in the hydrological cycle impact the atmospheric radiative transfer and surface temperature distribution.

Therefore, the final set of parameters is determined from an additional 30 year simulation. This model setup, including the final set of parameters and the updated implementation of the HD submodel, has been used for all sensitivity simulations in this study. The final set of parameters for the coupled model system with an atmospheric resolution of T42L47MA and an oceanic resolution of GR30 is listed in Table 5.3.

# Chapter 6

# Conclusions and outlook

The oceanic biogeochemistry model HAMburg Ocean Carbon Cycle model (HAMOCC; Six and Maier-Reimer, 1996; Maier-Reimer et al., 2005; Wetzel et al., 2005) has been implemented successfully as a Modular Earth Submodel System (MESSy; Jöckel et al., 2010) submodel and tested in the coupled ECHAM/MESSy Atmospheric Chemistry (EMAC; Jöckel et al., 2005, 2006, 2010)-Max Planck Institute Ocean Model (MPIOM; Marsland et al., 2003; Jungclaus et al., 2006) model system. The inclusion of air-sea gas exchange and the online calculation of oceanic chemical composition introduces additional feedback mechanisms into the model system. These feedback mechanisms work, for instance, via the link between air-sea gas exchange, atmospheric composition and chemistry, and atmospheric radiative transfer. A modified atmospheric composition directly affects surface irradiance and has an impact on oceanic biogeochemistry, which, in turn, alters oceanic concentrations, closing the feedback loop via a modified air-sea gas exchange.

Further influence on oceanic biogeochemistry is expected from external import of nutrients to the ocean by riverine input, mainly impacting coastal areas. In open ocean areas, additional impact on oceanic biogeochemistry is exerted by nutrient import from dust, which might also vary with climate. These feedback mechanisms can also be perturbed by anthropogenic influence. For instance, sewage, fertiliser use, water management, damming of rivers, and changes in land use influence nutrient concentrations and discharge of rivers. Further, desertification by human influence on land use and water management influences dust mobilisation and, hence, dust deposition after transport.

With the extended model system, provided as a result of the present study, it became possible to assess contributions of individual processes in these feedback chains. In a set of simulations, it could be shown, that the fully coupled model system, including interactive oceanic biogeochemistry and air-sea gas exchange produces internally consistent results, comparable to a model setup with prescribed oceanic concentrations for year 2000 conditions.

The main goals reached in this study are:

- The required model extensions to achieve a fully coupled ocean-atmosphere model system, including oceanic biogeochemistry and feedbacks between oceanic biogeochemistry and atmospheric chemistry by air-sea gas exchange, dust deposition, and riverine nutrient import, have been successfully implemented.

- Different sensitivity simulations with the model system over 5 years of simulation time for a year-2000 time-slice setup focusing on tropospheric chemistry (mainly DMS, $C_5H_8$, CO, $CH_3OH$, and their products) have been conducted and evaluated.

- The oceanic concentrations and ocean-to-atmosphere fluxes of $CO_2$ and $N_2O$ in preparation for long-term simulations with interactive stratospheric chemistry have been evaluated.

- The model parameters for the closure of the subgrid-scale cloud parameterisation have been optimised to minimise the model systems climate drift. This provides a model system applicable for simulations on longer time-scales.

Treating the physical ocean model as "black box", driving the oceanic circulation and oceanic tracer advection, no changes have been applied to the implementation by Pozzer et al. (2011) in the present study. The evaluation of simulated ocean dynamics show reasonable results. Oceanic sea surface temperature (SST) and sea surface salinity (SSS) have been simulated realistically in the model system. Deviations in simulated SST and SSS from observation based estimates from the World Ocean Atlas (WOA) are comparable to differences in previous studies with different model systems (Marsland et al., 2003; Jungclaus et al., 2006; Assmann et al., 2010; Pozzer et al., 2011; Tjiputra et al., 2013). In these studies, deficiencies in SST have been related to discrepancies in surface ocean circulation paths (Marsland et al., 2003; Jungclaus et al., 2006; Assmann et al., 2010), and to an underestimation of stratocumulus clouds and too weak coastal upwelling at the western coasts of

America and Africa (Jungclaus et al., 2006; Assmann et al., 2010; Pozzer et al., 2011). Deficiencies in SSS have been related to discrepancies in the simulated atmospheric hydrological cycle (Schneider et al., 2007, 2008) and deficiencies in the representation of the Arctic large scale freshwater cycle (Serreze et al., 2006), mostly due to the model's coarse resolution.

The novel model system, including the biogeochemistry submodel, has been evaluated thoroughly. As the coupling frequency between ocean and atmosphere has been increased to a coupling time step of 2 h, in order to resolve diurnal cycles, the biogeochemical submodel receives a different solar irradiance compared to the original model code working with daily averaged values. This significantly impacts the oceanic net primary production (NPP) from phytoplankton photosynthesis. In the parameterisation of phytoplankton growth the slope of the P-I-curve (production versus light intensity) has therefore been changed to adapt the NPP to this changed boundary condition. The resulting model setup, however, produces still a too low NPP of 36.3 $\mathrm{Pg(C)\,a^{-1}}$ and, related to this, a too low export production (EP) of 7.3 $\mathrm{Pg(C)\,a^{-1}}$. The prerequisite for future experiments with this model system is thus the adaption of the phytoplankton growth parameterisation to the increased coupling frequency of the model system, to achieve NPP and EP closer to observation based estimates.

Because of the deficiencies in reproducing NPP from observations, the model system experiences deficiencies in oceanic surface concentrations of orthophosphate ($PO_4^{3-}$), silicic acid ($Si(OH)_4$), dimethyl sulphide ($(CH_3)_2S$, DMS), isoprene ($C_5H_8$), nitrous oxide ($N_2O$), and carbon dioxide ($CO_2$). This implies different air-sea gas exchange fluxes in the model system compared to simulations with prescribed oceanic concentrations based on observations. However, treating these deficiencies in oceanic surface concentrations as modified forcings (compared to prescribed), the model system simulates a reasonable air-sea gas exchange, as well as a consistent response of the atmospheric composition.

Large discrepancies in $CO_2$ air-sea flux are simulated related to deficiencies in the representation of NPP and a too short spin-up time. As the present study focuses on tropospheric chemistry on time scales of years, atmospheric concentrations of $CO_2$ and $N_2O$ have been prescribed, ocean-to-atmosphere fluxes of these species could only be analysed as diagnostic quantities. For deeper investigation of $CO_2$ air-sea gas exchange, further model simulations with better represented NPP are needed. Furthermore, a model simulation with transient forcings from pre-industrial to present-day conditions with interactive atmospheric concentrations of $CO_2$ is required to

test the representation of $CO_2$ gas exchange and its trend. For simulations on longer time-scales (centuries) $N_2O$ emissions become important as source of stratospheric nitrogen oxides ($NO_x$). To asses the impact of ocean-to-atmosphere fluxes of $N_2O$ on stratospheric chemistry, model simulations on longer time-scales with interactive atmospheric $N_2O$ concentrations are necessary.

Despite these issues, a number of sensitivity simulations focusing on the role of specific feedbacks (relative changes) could be performed. The analysis of differences between sensitivity studies has been possible, as only relative differences have been analysed. For instance, the impact of riverine nutrient import to the ocean has been tested in the model system.

The cause-effect chain in the model system between surface water composition, air-sea gas exchange, and atmospheric composition is mostly as expected. Simulated air-sea gas exchange is in first order approximation related linearly to the corresponding simulated oceanic surface water concentrations for DMS, $C_5H_8$, and carbon monoxide (CO), whereas no linear relationship between near surface atmospheric burden and air-sea gas exchange is simulated. Here additional non linear interactions between atmospheric chemistry with large-scale and small-scale transport processes play an important role in determining atmospheric composition.

Overall, the simulated global budgets of ocean-to-atmosphere fluxes are comparable to values simulated with prescribed oceanic concentrations, and to values published in literature. However, regionally large impacts on atmospheric concentrations, especially in atmospheric compounds linked to DMS and $C_5H_8$ chemistry are simulated. These differences are, as expected, related to the different patterns in air-sea gas exchange, resulting from different surface water concentrations between simulations with online calculated oceanic biogeochemistry and a prescribed oceanic composition.

The impact of additional riverine nutrient import on oceanic biogeochemistry is mostly insignificant. Nevertheless, the resulting patterns are reasonable, showing changes in the ocean surface concentrations of iron (Fe), $Si(OH)_4$, and $CO_2$ mainly in coastal areas. Enhanced Fe and $Si(OH)_4$ concentrations are simulated in these areas, partly affecting the open ocean. Additional $CO_2$ import from rivers results in higher $CO_2$ surface water concentrations in coastal areas and, hence, higher $CO_2$ outgassing in these regions. As atmospheric $CO_2$ concentrations have been fixed in the atmospheric chemistry submodel during all sensitivity simulations in this study, an impact on atmospheric composition or dynamics could not be assessed. The impact on atmospheric concentrations from other chemical species is also insignificant on the

analysed time-scale of 5 years. Impacts on oceanic biogeochemistry in coastal areas, however, could be important on regional scales, especially in high polluted coastal areas. To investigate theses feedbacks in more detail, a higher model resolution and the inclusion of additional processes important to coastal biogeochemistry into the model system are necessary. Moreover, additional import of the least available organic element from rivers needs to be implemented in the model system by the method of Bernard et al. (2010), to couple dissolved organic matter (DOM) from rivers to the oceanic biogeochemistry. The novel model system is already prepared to use also spatial and temporal variable riverine nutrient import into the ocean utilising the OTPHYSC (Ocean Tracer PHYsiCs) submodel. To apply high resolution nutrient data in the coarse model system, additional processing of the data may be necessary, for instance using the approach of coastal catchments (COSCATs) by Meybeck et al. (2006).

Another potentially important feedback, which might be influenced by climate change is nutrient import to the ocean by dust deposition. Interactive dust deposition providing Fe and silica ($SiO_2$) to the surface ocean has been implemented in the model system. For this study a novel submodel has been developed, calculating the total dust deposition flux from partial dust fluxes from dry deposition, sedimentation, and scavenging. The results of the sensitivity study with consistent dust deposition from the atmosphere to the ocean are comparable to the results with a prescribed dust deposition source (both for the year-2000 conditions). With the extended model system, the present study provides a tool to assess contributions of individual processes in these highly non-linear feedback chains. Yet, higher surface ocean Fe and $Si(OH)_4$ concentrations are simulated in the high deposition zones of Saharan dust in the Atlantic. Changes in NPP resulting from the modified atmospheric dust source are, however, small, hence no significant impact on the secondary (i.e., other than Fe and $Si(OH)_4$) surface ocean tracer concentrations are simulated. This is a consequence of the simulated limiting nutrient for phytoplankton growth, which is nitrate in aqueous phase ($NO_3^-$) in the major dust deposition zones in the Atlantic. As a consequence no significant changes in air-sea gas exchange and in atmospheric composition on a 5-year time-scale have been simulated. Nevertheless, the inclusion of interactively calculated dust deposition provides a more consistent simulation of nutrient supply to the surface ocean and extends the model system for further studies under different climatic conditions.

As outlined above, changes in NPP from additional and modified nutrient sources strongly depend on the limiting nutrient for phytoplankton growth in the specific region. The simulation of the limiting nutrient for phytoplankton growth in the model system is in line with results by Assmann et al. (2010). As the Atlantic is $NO_3^-$ limited in the model simulations, the impact of larger Fe sources from an increased atmospheric deposition compared to the climatological dust deposition fluxes is low. In this region sources of nitrogen (N) become more important. It is thus recommended to test the model system's response to additional N deposition from the atmosphere (Spokes et al., 2000; Tost et al., 2007a), which is not included at the moment.

Ultimately, the novel model system is to be applied for applications with detailed chemistry on longer time scales (centuries). In long term simulations, used for example for trend analyses, the stratosphere plays an important role for tropospheric dynamics and chemistry. For practical reasons of reducing the computational time to about one half of the full T42L90MA setup with 90 levels in the atmosphere, a T42L47MA model setup with 47 atmospheric levels has been used in the present study. For the coupling with the ocean model, the required parameter optimisation has been performed to find a set of parameters for subgrid-scale, mostly cloud-related processes to provide a stable climate under constant forcings. A suitable parameter set for this model setup could be derived and the response of several atmospheric properties to changes in the parameters have been analysed. This may also be useful as a guide for future parameter optimisations for model setups with different resolutions.

Conclusively, a dynamically and chemically coupled atmosphere-ocean simulation system has been developed and evaluated for present-day conditions. It is now ready for investigations of long-term changes in atmospheric chemistry and oceanic biogeochemistry.

# Appendix A

# The MESSy submodel HAMOCC

This chapter presents an overview of the model parameters for the MESSy submodel HAMOCC available for modification via the user interface namelist. Table A.1 lists all parameters, short descriptions, their default values, and the values used in this study. A commented example of the user interface namelist is provided in Listing A.1.

| variable | description | default value | value used |
|---|---|---|---|
| 1) Redfield ratios and constants | | | |
| ro2ut | -$O_2$:P ratio in mol($O_2$) mol(P)$^{-1}$ | 172. | default |
| rcar | C:P ratio in mol(C) mol(P)$^{-1}$ | 122. | default |
| rnit | N:P ratio in mol(N) mol(P)$^{-1}$ | 16. | default |
| nitdem | nitrate consumption during remineralisation of detritus in suboxic water in mol(N) mol(P)$^{-1}$ | 121.6 | default |
| n2prod | production of $N_2$ during remineralisation in suboxic water in mol(N) mol(P)$^{-1}$ | 68.8 | default |
| rcalc | calcium carbonate to organic P production ratio in mol(C) mol(P)$^{-1}$ | 35. | default |
| ropal | ratio of opal to organic phosphorous production in mol(Si) mol(P)$^{-1}$ | 25. | default |
| n2_fixation | nitrogen fixation by blue algae rate in d$^{-1}$ | 0.005 | default |
| rno3 | N:P ratio in sediment pore water in mol(N) mol(P)$^{-1}$ | 16. | default |
| perc_diron | molar fraction of soluble Fe in dust in mol(Fe) g(Dust)$^{-1}$ | 5.372e-6 | default |
| riron | Fe:P stoichiometric ratio in mol(Fe) mol(P)$^{-1}$ | 3.66e-4 | default |
| fesoly | dissolved molar iron concentration in deep water in kmol(Fe) m$^{-3}$ | 6.e-10 | default |
| relaxfe | relaxation rate to fesoly for Fe in deep water in d$^{-1}$ | 1.36986e-4 | default |

**Table A.1:** Parameters available via user namelist in the implementation of HAMOCC as MESSy submodel and parameter values used in this study.

| variable | description | default value | value used |
|---|---|---|---|
| 2) Radiation and Photosynthesis | | | |
| pi_alpha | initial slope of production vs irradiance in $d^{-1}(W\,m^{-2})^{-1}$ | 0.02 | 0.008 |
| fPAR | fraction of photosynthetic available radiation | 0.4 | default |
| ctochl[a] | C to Chlorophyll ratio in $g(C)\,g(Chl)^{-1}$ | 60. | default |
| atten_w[a] | Gelbstoff attenuation in $m^{-1}$ | 0.04 | default |
| atten_f[a,b] | fraction of shortwave radiation absorbed at ocean surface | 0.4 | default |
| 3) Phytoplankton | | | |
| phytomi | minimum concentration of phytoplankton in $kmol(P)\,m^{-3}$ | 1.e-11 | default |
| bkphy | half saturation constant for phytoplankton in $kmol(P)\,m^{-3}$ | 1.e-8 | default |
| bkopal | half saturation constant for $SiOH_4$ in $kmol(Si)\,m^{-3}$ | 1.e-6 | default |
| remido | remineralisation rate of DOM in $d^{-1}$ | 0.008 | default |
| dyphy | mortality rate of phytoplankton in $d^{-1}$ | 0.008 | default |
| gammap | phytoplankton exudation rate in $d^{-1}$ | 0.03 | default |
| 4) Zooplankton | | | |
| bkzoo | half saturation constant for grazing in $kmol(P)\,m^{-3}$ | 4.e-8 | default |
| grami | minimum concentration of zooplankton in $kmol(P)\,m^{-3}$ | 1.e-11 | default |
| zinges | assimilation efficiency of zooplankton | 0.6 | default |
| epsher | (1-epsher) = fraction of grazing egested | 0.8 | default |
| grazra | grazing rate in $d^{-1}$ | 1.0 | default |
| spemor | mortality rate of zooplankton in $d^{-1}$ | 3.e6 | default |
| gammaz | zooplankton excretion rate in $d^{-1}$ | 0.06 | default |
| ecan | fraction of mortality as $PO_4$ | 0.95 | default |

[a] only in MPIOM version 1.3, not available in MPIOM version 1.5
[b] only used, if L_HAMOCC_COUPLING=T in mpiom.nml (feedback of oceanic biogeochemistry on ocean dynamics)

**Table A.1:** Continued.

| variable | description | default value | value used |
|---|---|---|---|
| 5) Deep Ocean Remineralisation, Dissolution, Mortality, Sinking | | | |
| sinkspeed_poc[c] | sinking velocity of detritus in $m\,d^{-1}$ | 5.0 | –[c] |
| sinkspeed_opal[c] | sinking velocity of opal in $m\,d^{-1}$ | 30.0 | –[c] |
| sinkspeed_cal[c] | sinking velocity of calcium carbonate in $m\,d^{-1}$ | 30.0 | –[c] |
| drempoc | detritus remineralisation rate in $d^{-1}$ | 0.025 | 0.1[d] |
| dremdoc | DOC remineralisation rate in $d^{-1}$ | 0.004 | default |
| dremn2o | remineralisation using N2O in $d^{-1}$ | 0.01 | default |
| denitrification | fraction of remineralisation from denitrification in oxygen low waters | 0.05 | default |
| sulfate_reduction | remineralisation from sulfate reduction in oxygen low waters in $d^{-1}$ | 0.005 | default |
| dremopal | opal dissolution rate in $d^{-1}$ | 0.01 | 3.3e-3[d] |
| dremcalc | calcium carbonate dissolution rate in $d^{-1}$ | 0.075 | default |
| dphymor | phytoplankton mortality rate in $d^{-1}$ | 0.1 | 0.2[d] |
| dzoomor | zooplankton mortality rate in $d^{-1}$ | 0.02 | default |
| 6) DMS | | | |
| dmspar(1) | parameter for temperature dependence of DMS release by phytoplankton in °C | 10. | default |
| dmspar(2) | DMS photolysis by UV-radiation in $(W\,m^{-2})^{-1}\,d^{-1}$ | 0.0075 | default |
| dmspar(3) | microbial DMS consumption in $°C^{-1}\,d^{-1}$ | 0.0096 | default |
| dmspar(4) | production with delcar in $mol(S)\,mol(C)^{-1}\,d^{-1}$ | 0.053819251 | default |
| dmspar(5) | production with delsil (diatoms) $mol(S)\,mol(Si)^{-1}\,d^{-1}$ | 0.054892261e-01 | default |
| dmspar(6) | half saturation constant for microbial production in $kmol(S)\,m^{-3}$ | 0.1e-07 | default |
| 7) AGG (Aggregation sinking) | | | |
| calmax | maximum fraction of $CaCO_3$ production (max. rain ratio) (AGG) | 0.20 | default |

[c] no effect if L_AGG=T in hamocc.nml (aggregation sinking)
[d] value used because of aggregation sinking

**Table A.1:** Continued.

**Listing A.1:** hamocc.nml

```
! -*- f90 -*-
&CPL
 L_DUST =  T                    ! T =  dust input from climatology,
                                ! F  = input from on-line module
 dust_input = 'a2o','dust_in' ! if L_DUST=T => channel and  ↩
    channel object for
                                ! dust input into the ocean
 L_SKIP_INT = F
/
&CTRL
 L_CHECK = F                    ! output of checks
 L_AGG   = T                    ! explicit calculation of marine  ↩
    snow :
 !                              ! particle size distributions  ↩
    explicit calculated
 ! WHEN using AGG, set parameters of drempoc, dremopal and  ↩
    dphymor !!
 L_BGC_DIAG = T                 ! hamocc diagnostics
 isac   =  1                    !sediment acceleration factor
 rmasks =  0                    ! mask value for tracer on land
 hamocc_ini_files_path =  ↩
    "$INPUTDIR_MPIOM/${MPIOM_HRES}/hamocc/init_files"
 !
 ! 1) Redfield ratios and constants
 ! extended redfield ratio declaration
 ro2ut     = 172.         ! -O2:P ratio
 rcar      = 122.         ! C:P ratio
 rnit      = 16.          ! N:P ratio
 nitdem    = 121.6        ! nitrate demand to remin. 1 mol P in  ↩
    suboxic water
 n2prod    = 68.8         ! N2 production for 1 mol P  ↩
    remineralized in subox. wat.
 rcalc     = 35.          ! calcium carbonate to organic P prod.  ↩
    ratio
 ropal     = 25.          ! opal to organic phosphorous prod. ratio
 n2_fixation = 0.005      ! nitrogen fixation by blue algae rate  ↩
    in 1/d
 rno3      =  16.         ! N:P ratio in pore water in sediment
 perc_diron = 5.372e-6  ! weight percent iron in dust
 !             ! deposition (0.035) times Fe solubility (0.01) / ↩
     55.85 g--> mol
 riron = 3.66e-4          ! Fe to P stoichiometric ratio * umol->mol)
```

```
fesoly  = 6.e-10        ! dissolved molar iron
!                       ! concentration in deep water (for  ↩
   relaxation) (mol/m3)
relaxfe = 1.36986e-4    ! relaxation time for iron to fesoly
!                       ! in 1/d; corresponds to 20 yrs
!
! 2) Radiation and Pothosythesis
pi_alpha = 0.008        ! initial slope of production vs irradiance
!                       ! curve (alpha) (0.002 for 10 steps per  ↩
   day)
fPAR     = 0.4          ! fraction of Photosynthetic Active  ↩
   Radiation
!
! For use with MPIOM_13B ONLY!!
! parameters for sw-radiation attenuation
ctochl   = 60.          ! C to Chlorophyll ratio
atten_w  = 0.04         ! Gelbstoff attenuation in 1/m
atten_f  = 0.4          ! fraction of sw-radiation dir. absorbed ↩
    in sfc. layer
!         ! (only used if L_HAMOCC_COUPLING in mpiom.nml)  ↩
   [feedback bgc-ocean]
! END: For use with MPIOM_13B ONLY
!
! 3) Phytoplankton
phytomi  = 1.e-11       ! minimum concentration of phytoplankton
!                       ! i.e. 1.e-11 kmol P/m3 = 1e-5 mmol P/m3
bkphy    = 1.e-8        ! half saturation constant for  ↩
   phytoplankton (kmol/m3)
bkopal   = 1.e-6        ! half saturation constant for Si(OH)4
!                       ! i.e. 1.0  mmol Si/m3
remido   = 0.008        ! 1/d -remin. rate (of DOM)
dyphy    = 0.008        ! 1/d -mortality rate of phytoplankton
gammap   = 0.03         ! 1/d -exudation rate
!
! 4) Zooplankton
bkzoo    = 4.e-8        ! half saturation constant for grazing
!                       ! i.e. 0.04 mmol P/m3
grami    = 1.e-11       ! minimum concentration of zooplankton
!                       ! i.e. 1.e-11 kmol P/m3 = 1e-5 mmol P/m3
zinges   = 0.6          ! dimensionless fraction -
!                       ! assimilation efficiency of zooplankton
epsher   = 0.8          ! dimensionless fraction -
!                       ! (1-epsher)=fraction of grazing egested
```

```
 grazra    = 1.0          ! 1/d -grazing rate [emr: 0.6-0.9]
 spemor    = 3.e6         ! 1/d -mortality rate of zooplankton
 gammaz    = 0.06         ! 1/d -excretion rate
 ecan      = 0.95         ! fraction of mortality as PO_4
 !
 ! 5) Deep Ocean Remineralisation, Dissolution, Mortality, Sinking
 ! note: this sinking speeds have no effect in case of L_AGG=.TRUE.
! sinkspeed_poc  = 5.0  ! daily sinking speed of poc
! sinkspeed_opal = 30.0 ! daily sinking speed of opal
! sinkspeed_cal  = 30.0 ! daily sinking speed of cal
 ! water column remineralisation constants
 ! drempoc  = 0.025      ! detritus remineralisation rate in 1/d
 ! !                     ! 0.75/month
 ! AGG: drempoc = 0.1
 drempoc  = 0.1          ! detritus remineralisation rate in 1/d
 dremdoc  = 0.004        ! DOC remineralisation rate in 1/d
 dremn2o  = 0.01         ! remineralisation using N2O in 1/d
 denitrification = 0.05 ! fraction of remineralisation from
 !                       ! denitrification in oxygen low waters
 sulfate_reduction  = 0.005  ! remineralisation from sulfate
 !                           ! reduction in oxygen low waters in ↩
     1/d
 ! dremopal = 0.01       ! Opal dissolution rate in 1/d
 ! AGG: dremopal = 3.3e-3
 dremopal = 3.3e-3       ! Opal dissolution rate in 1/d
 dremcalc = 0.075        ! 1/d
 ! dphymor  = 0.1        ! Phytoplankton mortality rate in 1/d
 ! AGG: dphymor = 0.2
 dphymor  = 0.2          ! Phytoplankton mortality rate in 1/d
 dzoomor  = 0.02         ! Zooplankton mortality rate in 1/d
 !
 ! 7) DMS
 dmspar(1) = 10.             ! temperature dependent release by  ↩
    phytoplankton
 dmspar(2) = 0.0075          ! photolysis (uv-destruction)
 dmspar(3) = 0.0096          ! microbial consumption
 dmspar(4) = 0.053819251     ! production with delcar
 dmspar(5) = 0.054892261e-01 ! production with delsil (diatoms)
 dmspar(6) = 0.100000000e-07 ! half saturation microbial
 !
 ! 8) AGG (Aggregation sinking)
 calmax    = 0.20        ! max fraction of CaCO3 production (AGG)
 !                       ! (max rain ratio)
```

/

# Appendix B

# The MESSy submodel OTPHYSC

OTPHYSC (Ocean Tracer PHYsiCs) couples the oceanic biogeochemical tracers to the oceanic dynamics. It also provides an interface to update oceanic tracers with chemical fluxes provided at the ocean's surface from other submodels (AIRSEA, SCAV).

An extension has been developed to update oceanic tracers at the land-ocean interface with chemical fluxes stemming from rivers. Further, six switches have been implemented to switch off several feedbacks from the ocean dynamics on the oceanic tracers. An example of an user interface namelist is provided in Listing B.1.

Air-sea fluxes are defined via:

```
AOFLUX(<number>) = '<ocean tracer>', '<flux  ↩
   channel>', '<flux object>', '<process>'
```

where `<number>` is an unique identifier for `AOFLUX`. `<ocean tracer>` is the name of the oceanic tracer field. The air-sea flux is provided by the channel object `<flux object>`, which can be found in the channel `<flux channel>`. `<process>` identifies the process, which calculates the air-sea flux, valid choices are `airsea` and `scav`. Depending on `<process>`, the appropriate conversion of units is chosen. For `airsea` a flux in $\mathrm{mol(X)\,m^{-2}\,s^{-1}}$ is assumed, for `scav` a flux in $\mathrm{molecules(X)\,m^{-2}\,s^{-1}}$.

The amount of tracer added to the ocean from rivers is determined from the freshwater flux and the molar tracer concentration in the freshwater. The freshwater input to the ocean is provided in the channel object `RIVER_OBJECT` of the channel `RIVER_CHANNEL`. The molar concentration of tracers can be given as constant via a key-value pair:

```
RINPUT(<number>) = '<ocean tracer>', <value>
```

Alternatively a 2D field of molar concentrations, provided by the channel object `<channel object>` in the channel `<channel>` can be used:

```
RINPUT_TR(<number>) = '<ocean tracer>', '<channel>', ↩
    '<channel object>'
```

**Listing B.1:** otphysc.nml

```
! -*- f90 -*-
&CTRL
MASK_VALUE = 0.0       ! mask value over land
/
&CPL
!############################################################
! AIR-SEA INTERACTIONS / SCAVENGING UPDATE IN THE OCEAN
!############################################################
! 'name ocean tracer', 'flux_channel', 'flux_object', process
!  process = 'scav', 'airsea'
!
AOFLUX(1) = 'O2',   'a2o', 'O2_ao_flux',   'airsea'
AOFLUX(2) = 'N2O',  'a2o', 'N2O_ao_flux',  'airsea'
AOFLUX(3) = 'N2',   'a2o', 'N2_ao_flux',   'airsea'
AOFLUX(4) = 'C12',  'a2o', 'CO2_ao_flux',  'airsea'
AOFLUX(5) = 'DMS',  'a2o', 'DMS_ao_flux',  'airsea'
AOFLUX(6) = 'ISOP', 'a2o', 'C5H8_ao_flux', 'airsea'
AOFLUX(7) = 'CO',   'a2o', 'CO_ao_flux',   'airsea'
!
!############################################################
! INPUT OF RIVER NUTRIENT TO  THE OCEAN
!############################################################
! freshwater input channel and channel object
RIVER_CHANNEL= 'a2o'
RIVER_OBJECT = 'disch_m3s'
!
! constant molar concentrations
! 'name ocean tracer', amount of input (mol/L)
RINPUT(1) = 'Fe',  1.022E-8
RINPUT(2) = 'C12', 7.133E-4
!
! molar concentration fields
! 'name ocean tracer', 'channel', 'channel object'
RINPUT_TR(1) = 'Si', 'a2o', 'Si'
RINPUT_TR(2) = 'N2', 'a2o', 'N2'
!
```

```
!############################################################
! Switches for skipping processes
L_SKIP_ADV = F          ! advection
L_SKIP_MIX = F          ! mixing
L_SKIP_DIF = F          ! diffusion
!############################################################
L_SKIP_DIL = F          ! dillution
L_SKIP_AOE = F          ! atmosphere-ocean exchange
L_SKIP_RIV = F          ! river input
!############################################################
/
```

# Appendix C

# The MESSy submodel SCALC

The novel MESSy submodel SCALC (Simple CALCulations) has been developed to perform simple mathematical operations on CHANNEL objects and provide results of the calculations as new CHANNEL objects.

Each `CALC` object has an unique identifier `<number>`. `<object out>` is the name of the channel object, which contains the result of the calculation in the SCALC channel. The channel object `<object out>` is created by the SCALC submodel during runtime and should have a unique name in the SCALC channel. `<method>` selects the mathematical operation, which is applied to the channel objects specified in `<object list>`. At the moment, the only mathematical method implemented is summation (`SUM`).

The syntax in the user interface namelist is as follows:

```
CALC(<number>) = '<object out>', '<object list>',  ↩
   '<method>'
```

where `<object list>` is build up from `<input object>`s. The `<input object>`s are separated by semicolons:

```
<object list> = <input object>[;<input object>][;...]
```

An `<input object>` comprises one or more `<channel object>`s, which can be grouped with commas, if they belong to the same `<channel>`. An optional `<scaling factor>` is separated from the `<channel object>` with `%`:

```
<input object>=<channel>:<channel object>[%<scaling  ↩
   factor>][,<channel object> [%<scaling  ↩
   factor>]][,...]
```

Below, in Listing C.1, an example of the user interface namelist for SCALC is given.

For the first example `CALC(1)`, a new channel object `ddep_dust` is created in the SCALC channel. The new channel object `ddep_dust` contains the sum of the channel objects `ddepflux_DU_as`, `ddepflux_DU_ai`, `ddepflux_DU_cs`, and `ddepflux_DU_ci`. Each of these channel objects is available from the channel `ddep_gp` and each is scaled with a factor of $2.0 \times 10^{-18}$.

The second example `CALC(2)` results in a channel object `dust`, which is the sum over twelve channel objects in the channels `ddep_gp`, `sedi_gp`, and `scav_gp`.

**Listing C.1:** scalc.nml

```
! -*- f90 -*-
&CPL
! 'name output object', 'channel : object % scaling, object %  ↩
   scaling; channel : object % scaling', 'operation'
!
CALC(1) = 'ddep_dust', 'ddep_gp:ddepflux_DU_as%2.e-18, ↩
   ddepflux_DU_ai%2.e-18,ddepflux_DU_cs%2.e-18,ddepflux_DU_ci%2. ↩
   e-18', 'SUM'
CALC(2) = 'dust', 'ddep_gp:ddepflux_DU_as,ddepflux_DU_ai, ↩
   ddepflux_DU_cs,ddepflux_DU_ci;sedi_gp:sediflux_DU_as, ↩
   sediflux_DU_ai,sediflux_DU_cs,sediflux_DU_ci;scav_gp: ↩
   wetflx_aer_cv_DU_cs,wetflx_aer_cv_DU_ci,wetflx_aer_ls_DU_cs, ↩
   wetflx_aer_ls_DU_ci', 'SUM'
/
```

# Appendix D

# Overview of model parameters to be optimised

| | | zasic | | | | zinhomi | | | | zinhoml | | | | zinpar | |
|---|---|---|---|---|---|---|---|---|---|---|---|---|---|---|---|
| | | correction for asymmetry factor of ice clouds rad_int.f90 messy_rad4all.f90 | | | | inhomogeneity factor for ice clouds rad_int.f90 messy_rad4all_e5.f90 | | | | inhomogeneity factor for for liquid clouds rad_int.f90 messy_rad4all.f90 | | | | rad_int.f90 messy_rad4all.f90 | |
| | | ECHAM5 | | EMAC | | ECHAM5 | | EMAC | | ECHAM5 | | EMAC | | ECHAM5 | EMAC |
| | | | coupled | | coupled | | coupled | | coupled | | coupled | | coupled | | |
| T10 | L11 | 0.85 | 0.91 | 0.85 | 0.89 | – | – | 0.70 | – | var.[a] | 0.70 | var.[a] | 0.70 | – | 0.10[b] |
| | L19 | 0.85 | 0.91 | 0.85 | 0.89 | – | – | 0.80 | – | var.[a] | 0.70 | var.[a] | 0.70 | – | 0.05[b] |
| | L41 | 0.85 | 0.91 | 0.85 | 0.89 | – | – | 0.80 | – | var.[a] | 0.70 | var.[a] | 0.70 | – | 0.05[b] |
| T21 | L11 | 0.85 | 0.91 | 0.85 | 0.89 | 0.70 | – | 0.70 | – | var.[a] | 0.70 | var.[a] | 0.70 | 0.10[b] | 0.10[b] |
| | L19 | 0.85 | 0.91 | 0.85 | 0.89 | 0.80 | – | 0.80 | – | var.[a] | 0.70 | var.[a] | 0.70 | 0.05[b] | 0.05[b] |
| | L41 | 0.85 | 0.91 | 0.85 | 0.89 | – | – | 0.80 | – | var.[a] | 0.70 | var.[a] | 0.70 | – | 0.05[b] |
| T31 | L11 | 0.85 | 0.91 | 0.85 | 0.89 | 0.70 | – | 0.70 | – | var.[a] | 0.70 | var.[a] | 0.70 | 0.10[b] | 0.10[b] |
| | L19 | 0.85 | 0.91 | 0.85 | 0.89 | 0.80 | – | 0.80 | 0.70 | var.[a] | 0.70 | var.[a] | 0.70 | 0.06[b] | 0.06[b] |
| | L31 | 0.85 | 0.91 | 0.85 | 0.89 | 0.85 | – | 0.85 | – | var.[a] | 0.70 | var.[a] | 0.70 | 0.08[b] | 0.08[b] |
| | L41 | 0.85 | 0.91 | 0.85 | 0.89 | – | – | 0.85 | – | var.[a] | 0.70 | var.[a] | 0.70 | – | 0.08[b] |
| | L39MA | 0.85 | 0.91 | 0.85 | 0.89 | 0.85 | – | 0.85 | – | var.[a] | 0.70 | var.[a] | 0.70 | 0.06[b] | 0.06[b] |
| | L47MA | 0.85 | 0.91 | 0.85 | 0.89 | 0.85 | – | 0.85 | – | var.[a] | 0.70 | var.[a] | 0.70 | 0.08[b] | 0.08[b] |
| | L49MA | 0.85 | 0.91 | 0.85 | 0.89 | 0.85 | – | 0.85 | – | var.[a] | 0.70 | var.[a] | 0.70 | 0.08[b] | 0.08[b] |
| | L87MA | 0.85 | 0.91 | 0.85 | 0.89 | 0.85 | – | 0.85 | – | var.[a] | 0.70 | var.[a] | 0.70 | 0.08[b] | 0.08[b] |
| | L90MA | 0.85 | 0.91 | 0.85 | 0.89 | 0.85 | – | 0.85 | – | var.[a] | 0.70 | var.[a] | 0.70 | 0.07[b] | 0.07[b] |
| | L95MA | 0.85 | 0.91 | 0.85 | 0.89 | 0.85 | – | 0.85 | – | var.[a] | 0.70 | var.[a] | 0.70 | 0.08[b] | 0.08[b] |

[a] variable, function of zinpar.

[b] zinpar is used in uncoupled simulations only.

**Table D.1:** Values of the cloud related parameters *zasic*, *zinhomi*, *zinhoml*, *zinpar* used for parameter optimisation in the model system. In case of "–" the value of the uncoupled case is used, parameters for T10 and L41 have been introduced for EMAC and are not available in the original ECHAM5 model.

| | | zasic | | | | zinhomi | | | | zinhoml | | | | zinpar | |
|---|---|---|---|---|---|---|---|---|---|---|---|---|---|---|---|
| | | ECHAM5 | | EMAC | | ECHAM5 | | EMAC | | ECHAM5 | | EMAC | | ECHAM5 | EMAC |
| | | | coupled | | coupled | | coupled | | coupled | | coupled | | coupled | | |
| T42 | L19 | 0.85 | 0.91 | 0.85 | 0.89 | 0.85 | – | 0.85 | – | var.[a] | 0.70 | var.[a] | 0.70 | 0.07[b] | 0.07[b] |
| | L31 | 0.85 | 0.91 | 0.85 | 0.89 | 0.85 | – | 0.85 | – | var.[a] | 0.70 | var.[a] | 0.70 | 0.08[b] | 0.08[b] |
| | L41 | 0.85 | 0.91 | 0.85 | 0.89 | – | – | 0.85 | – | var.[a] | 0.70 | var.[a] | 0.70 | – | 0.08[b] |
| | L39MA | 0.85 | 0.91 | 0.85 | 0.89 | 0.85 | – | 0.85 | – | var.[a] | 0.70 | var.[a] | 0.70 | 0.07[b] | 0.07[b] |
| | L47MA | 0.85 | 0.91 | 0.85 | 0.89 | 0.85 | – | 0.85 | 0.80 | var.[a] | 0.70 | var.[a] | 0.90 | 0.08[b] | 0.08[b] |
| | [c] | | | | 0.91 | | | | 0.80 | | | | 0.70 | | |
| | L49MA | 0.85 | 0.91 | 0.85 | 0.89 | 0.85 | – | 0.85 | – | var.[a] | 0.70 | var.[a] | 0.70 | 0.08[b] | 0.08[b] |
| | L87MA | 0.85 | 0.91 | 0.85 | 0.89 | 0.85 | – | 0.85 | – | var.[a] | 0.70 | var.[a] | 0.70 | 0.08[b] | 0.08[b] |
| | L90MA | 0.85 | 0.91 | 0.85 | 0.89 | 0.85 | – | 0.85 | – | var.[a] | 0.70 | var.[a] | 0.70 | 0.08[b] | 0.08[b] |
| | L95MA | 0.85 | 0.91 | 0.85 | 0.89 | 0.85 | – | 0.85 | – | var.[a] | 0.70 | var.[a] | 0.70 | 0.08[b] | 0.08[b] |
| T63 | L19 | 0.85 | 0.91 | 0.85 | 0.89 | 0.85 | – | 0.85 | – | var.[a] | 0.70 | var.[a] | 0.70 | 0.08[b] | 0.08[b] |
| | L31 | 0.85 | 0.91 | 0.85 | 0.89 | 0.85 | 0.80 | 0.85 | 0.80 | var.[a] | 0.70 | var.[a] | 0.70 | 0.10[b] | 0.10[b] |
| | L41 | 0.85 | 0.91 | 0.85 | 0.89 | – | – | 0.85 | – | var.[a] | 0.70 | var.[a] | 0.70 | – | 0.10[b] |
| | L39MA | 0.85 | 0.91 | 0.85 | 0.89 | 0.85 | – | 0.85 | – | var.[a] | 0.70 | var.[a] | 0.70 | 0.08[b] | 0.08[b] |
| | L47MA | 0.85 | 0.91 | 0.85 | 0.89 | 0.85 | 0.80 | 0.85 | 0.80 | var.[a] | 0.70 | var.[a] | 0.70 | 0.10[b] | 0.10[b] |
| | L49MA | 0.85 | 0.91 | 0.85 | 0.89 | 0.85 | 0.80 | 0.85 | 0.80 | var.[a] | 0.70 | var.[a] | 0.70 | 0.10[b] | 0.10[b] |
| | L87MA | 0.85 | 0.91 | 0.85 | 0.89 | 0.85 | 0.80 | 0.85 | 0.80 | var.[a] | 0.70 | var.[a] | 0.70 | 0.10[b] | 0.10[b] |
| | L90MA | 0.85 | 0.91 | 0.85 | 0.89 | 0.85 | – | 0.85 | – | var.[a] | 0.70 | var.[a] | 0.70 | 0.10[b] | 0.10[b] |
| | L95MA | 0.85 | 0.91 | 0.85 | 0.89 | 0.85 | 0.80 | 0.85 | 0.80 | var.[a] | 0.70 | var.[a] | 0.70 | 0.10[b] | 0.10[b] |

[a] variable, function of zinpar.
[b] zinpar is used in uncoupled simulations only.
[c] values determined for EMAC with updated HD submodel.

**Table D.1:** continued.

| | | zasic | | | | zinhomi | | | | zinhoml | | | | zinpar | |
|---|---|---|---|---|---|---|---|---|---|---|---|---|---|---|---|
| | | ECHAM5 | | EMAC | | ECHAM5 | | EMAC | | ECHAM5 | | EMAC | | ECHAM5 | EMAC |
| | | | coupled | | coupled | | coupled | | coupled | | coupled | | coupled | | |
| T85 | L19 | 0.85 | 0.91 | 0.85 | 0.89 | 0.85 | – | 0.85 | – | var.[a] | 0.70 | var.[a] | 0.70 | 0.08[b] | 0.08[b] |
| | L31 | 0.85 | 0.91 | 0.85 | 0.89 | 0.90 | – | 0.90 | – | var.[a] | 0.70 | var.[a] | 0.70 | 0.10[b] | 0.10[b] |
| | L41 | 0.85 | 0.91 | 0.85 | 0.89 | – | – | 0.90 | – | var.[a] | 0.70 | var.[a] | 0.70 | – | 0.10[b] |
| | L39MA | 0.85 | 0.91 | 0.85 | 0.89 | 0.85 | – | 0.85 | – | var.[a] | 0.70 | var.[a] | 0.70 | 0.08[b] | 0.08[b] |
| | L47MA | 0.85 | 0.91 | 0.85 | 0.89 | 0.90 | – | 0.90 | – | var.[a] | 0.70 | var.[a] | 0.70 | 0.10[b] | 0.10[b] |
| | L49MA | 0.85 | 0.91 | 0.85 | 0.89 | 0.90 | – | 0.90 | – | var.[a] | 0.70 | var.[a] | 0.70 | 0.10[b] | 0.10[b] |
| | L87MA | 0.85 | 0.91 | 0.85 | 0.89 | 0.90 | – | 0.90 | – | var.[a] | 0.70 | var.[a] | 0.70 | 0.10[b] | 0.10[b] |
| | L90MA | 0.85 | 0.91 | 0.85 | 0.89 | 0.90 | – | 0.90 | – | var.[a] | 0.70 | var.[a] | 0.70 | 0.10[b] | 0.10[b] |
| | L95MA | 0.85 | 0.91 | 0.85 | 0.89 | 0.90 | – | 0.90 | – | var.[a] | 0.70 | var.[a] | 0.70 | 0.10[b] | 0.10[b] |
| T106 | L19 | 0.85 | 0.91 | 0.85 | 0.89 | 0.85 | – | 0.85 | – | var.[a] | 0.70 | var.[a] | 0.70 | 0.08[b] | 0.08[b] |
| | L31 | 0.85 | 0.91 | 0.85 | 0.89 | 0.90 | – | 0.90 | – | var.[a] | 0.70 | var.[a] | 0.70 | 0.12[b] | 0.12[b] |
| | L41 | 0.85 | 0.91 | 0.85 | 0.89 | – | – | 0.90 | – | var.[a] | 0.70 | var.[a] | 0.70 | – | 0.12[b] |
| | L60 | 0.85 | 0.91 | 0.85 | 0.89 | 0.90 | – | 0.90 | – | var.[a] | 0.70 | var.[a] | 0.70 | 0.12[b] | 0.12[b] |
| | L39MA | 0.85 | 0.91 | 0.85 | 0.89 | 0.85 | – | 0.85 | – | var.[a] | 0.70 | var.[a] | 0.70 | 0.08[b] | 0.08[b] |
| | L47MA | 0.85 | 0.91 | 0.85 | 0.89 | 0.90 | – | 0.90 | – | var.[a] | 0.70 | var.[a] | 0.70 | 0.12[b] | 0.12[b] |
| | L49MA | 0.85 | 0.91 | 0.85 | 0.89 | 0.90 | – | 0.90 | – | var.[a] | 0.70 | var.[a] | 0.70 | 0.12[b] | 0.12[b] |
| | L87MA | 0.85 | 0.91 | 0.85 | 0.89 | 0.90 | – | 0.90 | – | var.[a] | 0.70 | var.[a] | 0.70 | 0.12[b] | 0.12[b] |
| | L90MA | 0.85 | 0.91 | 0.85 | 0.89 | 0.90 | – | 0.90 | – | var.[a] | 0.70 | var.[a] | 0.70 | 0.12[b] | 0.12[b] |
| | L95MA | 0.85 | 0.91 | 0.85 | 0.89 | 0.90 | – | 0.90 | – | var.[a] | 0.70 | var.[a] | 0.70 | 0.12[b] | 0.12[b] |
| | L191MA | 0.85 | 0.91 | 0.85 | 0.89 | 0.90 | – | 0.90 | – | var.[a] | 0.70 | var.[a] | 0.70 | 0.12[b] | 0.12[b] |

[a] variable, function of zinpar.
[b] zinpar is used in uncoupled simulations only.

**Table D.1:** continued.

| | | zasic | | | | zinhomi | | | | zinhoml | | | | zinpar | |
|---|---|---|---|---|---|---|---|---|---|---|---|---|---|---|---|
| | | ECHAM5 | | EMAC | | ECHAM5 | | EMAC | | ECHAM5 | | EMAC | | ECHAM5 | EMAC |
| | | coupled | | coupled | | coupled | | coupled | | coupled | | coupled | | | |
| T159 | L19 | 0.85 | 0.91 | 0.85 | 0.89 | 0.85 | – | 0.85 | – | var.[a] | 0.70 | var.[a] | 0.70 | 0.08[b] | 0.08[b] |
| | L31 | 0.85 | 0.91 | 0.85 | 0.89 | 0.90 | – | 0.90 | – | var.[a] | 0.70 | var.[a] | 0.70 | 0.12[b] | 0.12[b] |
| | L41 | 0.85 | 0.91 | 0.85 | 0.89 | – | – | 0.90 | – | var.[a] | 0.70 | var.[a] | 0.70 | – | 0.12[b] |
| | L60 | 0.85 | 0.91 | 0.85 | 0.89 | 0.90 | – | 0.90 | – | var.[a] | 0.70 | var.[a] | 0.70 | 0.12[b] | 0.12[b] |
| | L39MA | 0.85 | 0.91 | 0.85 | 0.89 | 0.85 | – | 0.85 | – | var.[a] | 0.70 | var.[a] | 0.70 | 0.08[b] | 0.08[b] |
| | L47MA | 0.85 | 0.91 | 0.85 | 0.89 | 0.90 | – | 0.90 | – | var.[a] | 0.70 | var.[a] | 0.70 | 0.12[b] | 0.12[b] |
| | L49MA | 0.85 | 0.91 | 0.85 | 0.89 | 0.90 | – | 0.90 | – | var.[a] | 0.70 | var.[a] | 0.70 | 0.12[b] | 0.12[b] |
| | L87MA | 0.85 | 0.91 | 0.85 | 0.89 | 0.90 | – | 0.90 | – | var.[a] | 0.70 | var.[a] | 0.70 | 0.12[b] | 0.12[b] |
| | L90MA | 0.85 | 0.91 | 0.85 | 0.89 | 0.90 | – | 0.90 | – | var.[a] | 0.70 | var.[a] | 0.70 | 0.12[b] | 0.12[b] |
| | L95MA | 0.85 | 0.91 | 0.85 | 0.89 | 0.90 | – | 0.90 | – | var.[a] | 0.70 | var.[a] | 0.70 | 0.12[b] | 0.12[b] |
| | L191MA | 0.85 | 0.91 | 0.85 | 0.89 | 0.90 | – | 0.90 | – | var.[a] | 0.70 | var.[a] | 0.70 | 0.12[b] | 0.12[b] |
| T255 | L31 | 0.85 | 0.91 | 0.85 | 0.89 | 0.90 | – | 0.90 | – | var.[a] | 0.70 | var.[a] | 0.70 | 0.12[b] | 0.12[b] |
| | L41 | 0.85 | 0.91 | 0.85 | 0.89 | – | – | 0.90 | – | var.[a] | 0.70 | var.[a] | 0.70 | – | 0.12[b] |
| | L60 | 0.85 | 0.91 | 0.85 | 0.89 | 0.90 | – | 0.90 | – | var.[a] | 0.70 | var.[a] | 0.70 | 0.12[b] | 0.12[b] |
| | L39MA | 0.85 | 0.91 | 0.85 | 0.89 | 0.85 | – | 0.85 | – | var.[a] | 0.70 | var.[a] | 0.70 | 0.08[b] | 0.08[b] |
| | L47MA | 0.85 | 0.91 | 0.85 | 0.89 | 0.90 | – | 0.90 | – | var.[a] | 0.70 | var.[a] | 0.70 | 0.12[b] | 0.12[b] |
| | L49MA | 0.85 | 0.91 | 0.85 | 0.89 | 0.90 | – | 0.90 | – | var.[a] | 0.70 | var.[a] | 0.70 | 0.12[b] | 0.12[b] |
| | L87MA | 0.85 | 0.91 | 0.85 | 0.89 | 0.90 | – | 0.90 | – | var.[a] | 0.70 | var.[a] | 0.70 | 0.12[b] | 0.12[b] |
| | L90MA | 0.85 | 0.91 | 0.85 | 0.89 | 0.90 | – | 0.90 | – | var.[a] | 0.70 | var.[a] | 0.70 | 0.12[b] | 0.12[b] |
| | L95MA | 0.85 | 0.91 | 0.85 | 0.89 | 0.90 | – | 0.90 | – | var.[a] | 0.70 | var.[a] | 0.70 | 0.12[b] | 0.12[b] |

[a] variable, function of zinpar.
[b] zinpar is used in uncoupled simulations only.

**Table D.1:** continued.

| | | zasic | | | | zinhomi | | | | zinhoml | | | | zinpar | |
|---|---|---|---|---|---|---|---|---|---|---|---|---|---|---|---|
| | | ECHAM5 | | EMAC | | ECHAM5 | | EMAC | | ECHAM5 | | EMAC | | ECHAM5 | EMAC |
| | | | coupled | | coupled | | coupled | | coupled | | coupled | | coupled | | |
| T255 | L191MA | 0.85 | 0.91 | 0.85 | 0.89 | 0.90 | – | 0.90 | – | var.[a] | 0.70 | var.[a] | 0.70 | 0.12[b] | 0.12[b] |
| T319 | L31 | 0.91 | 0.91 | 0.85 | 0.89 | 1.00 | – | 1.00 | – | var.[a] | 0.70 | var.[a] | 0.70 | 0.12[b] | 0.12[b] |
| | L60 | 0.91 | 0.91 | 0.85 | 0.89 | 0.90 | – | 0.90 | – | var.[a] | 0.70 | var.[a] | 0.70 | 0.12[b] | 0.12[b] |
| | L39MA | 0.91 | 0.91 | 0.85 | 0.89 | 0.85 | – | 0.85 | – | var.[a] | 0.70 | var.[a] | 0.70 | 0.08[b] | 0.08[b] |
| | L47MA | 0.91 | 0.91 | 0.85 | 0.89 | 1.00 | – | 1.00 | – | var.[a] | 0.70 | var.[a] | 0.70 | 0.12[b] | 0.12[b] |
| | L49MA | 0.91 | 0.91 | 0.85 | 0.89 | 1.00 | – | 1.00 | – | var.[a] | 0.70 | var.[a] | 0.70 | 0.12[b] | 0.12[b] |
| | L87MA | 0.91 | 0.91 | 0.85 | 0.89 | 1.00 | – | 1.00 | – | var.[a] | 0.70 | var.[a] | 0.70 | 0.12[b] | 0.12[b] |
| | L90MA | 0.91 | 0.91 | 0.85 | 0.89 | 0.90 | – | 0.90 | – | var.[a] | 0.70 | var.[a] | 0.70 | 0.12[b] | 0.12[b] |
| | L95MA | 0.91 | 0.91 | 0.85 | 0.89 | 1.00 | – | 1.00 | – | var.[a] | 0.70 | var.[a] | 0.70 | 0.12[b] | 0.12[b] |
| | L191MA | 0.91 | 0.91 | 0.85 | 0.89 | 0.90 | – | 0.90 | – | var.[a] | 0.70 | var.[a] | 0.70 | 0.12[b] | 0.12[b] |

[a] variable, function of zinpar.

[b] zinpar is used in uncoupled simulations only.

**Table D.1:** continued.

| | | cauloc | | | | cmfctop | | | | cprcon | | | | entrscv | | | |
|---|---|---|---|---|---|---|---|---|---|---|---|---|---|---|---|---|---|
| | | accretion of cloud droplets by precipitation mo_cloud.f90 messy_cloud_ori.f90 | | | | convective mass flux at level of neutral buoyancy mo_cumulus_flux.f90 messy_convect_tiedtke _param.f90 | | | | conversion from cloud water to rain mo_cumulus_flux.f90 messy_convect_tiedtke _param.f90 | | | | entrainment rate for shallow convection mo_cumulus_flux.f90 messy_convect_tiedtke _param.f90 | | | |
| | | ECHAM5 | | EMAC | | ECHAM5 | | EMAC | | ECHAM5 | | EMAC | | ECHAM5 | | EMAC | |
| | | | coupled | | coupled | | coupled | | coupled | | coupled | | coupled | | coupled | | coupled |
| T10 | L11 | 5.00 | 0.00 | 5.00 | 0.00 | 0.30 | – | 0.30 | – | 1.0E-3 | – | 1.0E-3 | – | 3.0E-4 | 3.0E-4 | 3.0E-4 | 3.0E-4 |
| | L19 | 1.00 | 0.00 | 1.00 | 0.00 | 0.10 | – | 0.10 | – | 8.0E-4 | – | 8.0E-4 | – | 1.0E-3 | 3.0E-4 | 1.0E-3 | 3.0E-4 |
| | L41 | – | – | – | – | – | – | – | – | – | – | – | – | – | – | – | – |
| T21 | L11 | 5.00 | 0.00 | 5.00 | 0.00 | 0.30 | – | 0.30 | – | 1.0E-3 | – | 1.0E-3 | – | 3.0E-4 | 3.0E-4 | 3.0E-4 | 3.0E-4 |
| | L19 | 1.00 | 0.00 | 1.00 | 0.00 | 0.10 | – | 0.10 | – | 8.0E-4 | – | 8.0E-4 | – | 1.0E-3 | 3.0E-4 | 1.0E-3 | 3.0E-4 |
| | L41 | – | – | – | – | – | – | – | – | – | – | – | – | – | – | – | – |
| T31 | L11 | 5.00 | 0.00 | 5.00 | 0.00 | 0.30 | – | 0.30 | – | 1.0E-3 | – | 1.0E-3 | – | 3.0E-4 | 3.0E-4 | 3.0E-4 | 3.0E-4 |
| | L19 | 1.00 | 0.00 | 1.00 | 0.00 | 0.10 | 0.20 | 0.10 | 0.20 | 4.0E-4 | – | 4.0E-4 | – | 1.0E-3 | 3.0E-4 | 1.0E-3 | 3.0E-4 |
| | L31 | 2.00 | 0.00 | 2.00 | 0.00 | 0.30 | – | 0.30 | – | 1.5E-4 | – | 1.5E-4 | – | 1.0E-3 | 3.0E-4 | 1.0E-3 | 3.0E-4 |
| | L41 | – | – | 2.00 | 0.00 | – | – | – | – | – | – | – | – | 1.0E-3 | 3.0E-4 | 1.0E-3 | 3.0E-4 |
| | L39MA | 3.00 | 0.00 | 3.00 | 0.00 | 0.25 | – | 0.25 | – | 3.0E-4 | – | 3.0E-4 | – | 1.0E-3 | 3.0E-4 | 1.0E-3 | 3.0E-4 |
| | L47MA | 2.00 | 0.00 | 2.00 | 0.00 | 0.30 | – | 0.30 | – | 1.5E-4 | – | 1.5E-4 | – | 1.0E-3 | 3.0E-4 | 1.0E-3 | 3.0E-4 |
| | L49MA | 2.00 | 0.00 | 2.00 | 0.00 | 0.30 | – | 0.30 | – | 1.5E-4 | – | 1.5E-4 | – | 1.0E-3 | 3.0E-4 | 1.0E-3 | 3.0E-4 |
| | L87MA | 2.00 | 0.00 | 2.00 | 0.00 | 0.30 | – | 0.30 | – | 1.5E-4 | – | 1.5E-4 | – | 1.0E-3 | 3.0E-4 | 1.0E-3 | 3.0E-4 |
| | L90MA | 3.00 | 0.00 | 3.00 | 0.00 | 0.30 | – | 0.30 | – | 1.5E-4 | – | 1.5E-4 | – | 1.0E-3 | 3.0E-4 | 1.0E-3 | 3.0E-4 |
| | L95MA | 2.00 | 0.00 | 2.00 | 0.00 | 0.30 | – | 0.30 | – | 1.5E-4 | – | 1.5E-4 | – | 1.0E-3 | 3.0E-4 | 1.0E-3 | 3.0E-4 |

**Table D.2:** Values of the cloud related parameters *cauloc*, *cmfctop*, *cprcon*, *entrscv* used for parameter optimisation in the model system. In case of "–" the value of the uncoupled case is used, parameters for T10 and L41 have been introduced for EMAC and are not available in the original ECHAM5 model.

| | | cauloc | | | | cmfctop | | | | cprcon | | | | entrscv | | | |
|---|---|---|---|---|---|---|---|---|---|---|---|---|---|---|---|---|---|
| | | ECHAM5 | | EMAC | | ECHAM5 | | EMAC | | ECHAM5 | | EMAC | | ECHAM5 | | EMAC | |
| | | | coupled | | coupled | | coupled | | coupled | | coupled | | coupled | | coupled | | coupled |
| T42 | L19 | 2.00 | 0.00 | 2.00 | 0.00 | 0.12 | – | 0.12 | – | 4.0E-4 | – | 4.0E-4 | – | 1.0E-3 | 3.0E-4 | 1.0E-3 | 3.0E-4 |
| | L31 | 2.00 | 0.00 | 2.00 | 0.00 | 0.30 | – | 0.30 | – | 1.5E-4 | – | 1.5E-4 | – | 1.0E-3 | 3.0E-4 | 1.0E-3 | 3.0E-4 |
| | L41 | – | – | 3.00 | 0.00 | – | – | 0.22 | – | – | – | 1.5E-4 | – | 1.0E-3 | 3.0E-4 | 1.0E-3 | 3.0E-4 |
| | L39MA | 3.00 | 0.00 | 3.00 | 0.00 | 0.25 | – | 0.25 | – | 3.0E-4 | – | 3.0E-4 | – | 1.0E-3 | 3.0E-4 | 1.0E-3 | 3.0E-4 |
| | L47MA | 2.00 | 0.00 | 2.00 | 0.00 | 0.30 | – | 0.30 | 0.21 | 1.5E-4 | – | 1.5E-4 | 3.0E-4 | 1.0E-3 | 3.0E-4 | 1.0E-3 | 3.0E-4 |
| | [a] | | | | 0.00 | | | | 0.21 | | | | 2.0E-4 | | | | 3.0E-4 |
| | L49MA | 2.00 | 0.00 | 2.00 | 0.00 | 0.30 | – | 0.30 | – | 1.5E-4 | – | 1.5E-4 | – | 1.0E-3 | 3.0E-4 | 1.0E-3 | 3.0E-4 |
| | L87MA | 2.00 | 0.00 | 2.00 | 0.00 | 0.30 | – | 0.30 | – | 1.5E-4 | – | 1.5E-4 | – | 1.0E-3 | 3.0E-4 | 1.0E-3 | 3.0E-4 |
| | L90MA | 3.00 | 0.00 | 3.00 | 0.00 | 0.30 | – | 0.30 | – | 1.5E-4 | – | 1.5E-4 | – | 1.0E-3 | 3.0E-4 | 1.0E-3 | 3.0E-4 |
| | L95MA | 2.00 | 0.00 | 2.00 | 0.00 | 0.30 | – | 0.30 | – | 1.5E-4 | – | 1.5E-4 | – | 1.0E-3 | 3.0E-4 | 1.0E-3 | 3.0E-4 |
| T63 | L19 | 3.00 | 0.00 | 3.00 | 0.00 | 0.15 | – | 0.15 | – | 3.0E-4 | – | 3.0E-4 | – | 1.0E-3 | 3.0E-4 | 1.0E-3 | 3.0E-4 |
| | L31 | 5.00 | 0.00 | 5.00 | 0.00 | 0.30 | 0.22 | 0.30 | 0.22 | 1.0E-4 | – | 1.0E-4 | – | 1.0E-3 | 3.0E-4 | 1.0E-3 | 3.0E-4 |
| | L41 | – | – | 5.00 | 0.00 | – | – | – | – | – | – | – | – | 1.0E-3 | 3.0E-4 | 1.0E-3 | 3.0E-4 |
| | L39MA | 3.00 | 0.00 | 3.00 | 0.00 | 0.25 | – | 0.25 | – | 3.0E-4 | – | 3.0E-4 | – | 1.0E-3 | 3.0E-4 | 1.0E-3 | 3.0E-4 |
| | L47MA | 5.00 | 0.00 | 5.00 | 0.00 | 0.30 | 0.22 | 0.30 | 0.22 | 1.0E-4 | – | 1.0E-4 | – | 1.0E-3 | 3.0E-4 | 1.0E-3 | 3.0E-4 |
| | L49MA | 5.00 | 0.00 | 5.00 | 0.00 | 0.30 | 0.22 | 0.30 | 0.22 | 1.0E-4 | – | 1.0E-4 | – | 1.0E-3 | 3.0E-4 | 1.0E-3 | 3.0E-4 |
| | L87MA | 5.00 | 0.00 | 5.00 | 0.00 | 0.30 | 0.22 | 0.30 | 0.22 | 1.0E-4 | – | 1.0E-4 | – | 1.0E-3 | 3.0E-4 | 1.0E-3 | 3.0E-4 |
| | L90MA | 5.00 | 0.00 | 5.00 | 0.00 | 0.30 | – | 0.30 | – | 1.0E-4 | – | 1.0E-4 | – | 1.0E-3 | 3.0E-4 | 1.0E-3 | 3.0E-4 |
| | L95MA | 5.00 | 0.00 | 5.00 | 0.00 | 0.30 | 0.22 | 0.30 | 0.22 | 1.0E-4 | – | 1.0E-4 | – | 1.0E-3 | 3.0E-4 | 1.0E-3 | 3.0E-4 |

[a] values determined for EMAC with updated HD submodel.

**Table D.2:** continued.

| | | cauloc | | | | cmfctop | | | | cprcon | | | | entrscv | | | |
|---|---|---|---|---|---|---|---|---|---|---|---|---|---|---|---|---|---|
| | | ECHAM5 | | EMAC | | ECHAM5 | | EMAC | | ECHAM5 | | EMAC | | ECHAM5 | | EMAC | |
| | | | coupled | | coupled | | coupled | | coupled | | coupled | | coupled | | coupled | | coupled |
| T85 | L19 | 3.00 | 0.00 | 3.00 | 0.00 | 0.20 | – | 0.20 | – | 2.5E-4 | – | 2.5E-4 | – | 1.0E-3 | 3.0E-4 | 1.0E-3 | 3.0E-4 |
| | L31 | 5.00 | 0.00 | 5.00 | 0.00 | 0.35 | – | 0.35 | – | 1.0E-4 | – | 1.0E-4 | – | 1.0E-3 | 3.0E-4 | 1.0E-3 | 3.0E-4 |
| | L41 | – | – | 5.00 | 0.00 | – | – | – | – | – | – | – | – | 1.0E-3 | 3.0E-4 | 1.0E-3 | 3.0E-4 |
| | L39MA | 3.00 | 0.00 | 3.00 | 0.00 | 0.25 | – | 0.25 | – | 2.0E-4 | – | 2.0E-4 | – | 1.0E-3 | 3.0E-4 | 1.0E-3 | 3.0E-4 |
| | L47MA | 5.00 | 0.00 | 5.00 | 0.00 | 0.35 | – | 0.35 | – | 1.0E-4 | – | 1.0E-4 | – | 1.0E-3 | 3.0E-4 | 1.0E-3 | 3.0E-4 |
| | L49MA | 5.00 | 0.00 | 5.00 | 0.00 | 0.35 | – | 0.35 | – | 1.0E-4 | – | 1.0E-4 | – | 1.0E-3 | 3.0E-4 | 1.0E-3 | 3.0E-4 |
| | L87MA | 5.00 | 0.00 | 5.00 | 0.00 | 0.35 | – | 0.35 | – | 1.0E-4 | – | 1.0E-4 | – | 1.0E-3 | 3.0E-4 | 1.0E-3 | 3.0E-4 |
| | L90MA | 5.00 | 0.00 | 5.00 | 0.00 | 0.35 | – | 0.35 | – | 1.0E-4 | – | 1.0E-4 | – | 1.0E-3 | 3.0E-4 | 1.0E-3 | 3.0E-4 |
| | L95MA | 5.00 | 0.00 | 5.00 | 0.00 | 0.35 | – | 0.35 | – | 1.0E-4 | – | 1.0E-4 | – | 1.0E-3 | 3.0E-4 | 1.0E-3 | 3.0E-4 |
| T106 | L19 | 3.00 | 0.00 | 3.00 | 0.00 | 0.25 | – | 0.25 | – | 2.5E-4 | – | 2.5E-4 | – | 1.0E-3 | 3.0E-4 | 1.0E-3 | 3.0E-4 |
| | L31 | 5.00 | 0.00 | 5.00 | 0.00 | 0.35 | – | 0.35 | – | 1.0E-4 | – | 1.0E-4 | – | 1.0E-3 | 3.0E-4 | 1.0E-3 | 3.0E-4 |
| | L41 | – | – | 5.00 | 0.00 | – | – | – | – | – | – | – | – | 1.0E-3 | 3.0E-4 | 1.0E-3 | 3.0E-4 |
| | L60 | 5.00 | 0.00 | 5.00 | 0.00 | 0.35 | – | 0.35 | – | 1.0E-4 | – | 1.0E-4 | – | 1.0E-3 | 3.0E-4 | 1.0E-3 | 3.0E-4 |
| | L39MA | 3.00 | 0.00 | 3.00 | 0.00 | 0.25 | – | 0.25 | – | 2.0E-4 | – | 2.0E-4 | – | 1.0E-3 | 3.0E-4 | 1.0E-3 | 3.0E-4 |
| | L47MA | 5.00 | 0.00 | 5.00 | 0.00 | 0.35 | – | 0.35 | – | 1.0E-4 | – | 1.0E-4 | – | 1.0E-3 | 3.0E-4 | 1.0E-3 | 3.0E-4 |
| | L49MA | 5.00 | 0.00 | 5.00 | 0.00 | 0.35 | – | 0.35 | – | 1.0E-4 | – | 1.0E-4 | – | 1.0E-3 | 3.0E-4 | 1.0E-3 | 3.0E-4 |
| | L87MA | 5.00 | 0.00 | 5.00 | 0.00 | 0.35 | – | 0.35 | – | 1.0E-4 | – | 1.0E-4 | – | 1.0E-3 | 3.0E-4 | 1.0E-3 | 3.0E-4 |
| | L90MA | 5.00 | 0.00 | 5.00 | 0.00 | 0.35 | – | 0.35 | – | 1.0E-4 | – | 1.0E-4 | – | 1.0E-3 | 3.0E-4 | 1.0E-3 | 3.0E-4 |
| | L95MA | 5.00 | 0.00 | 5.00 | 0.00 | 0.35 | – | 0.35 | – | 1.0E-4 | – | 1.0E-4 | – | 1.0E-3 | 3.0E-4 | 1.0E-3 | 3.0E-4 |
| | L191MA | 5.00 | 0.00 | 5.00 | 0.00 | 0.35 | – | 0.35 | – | 1.0E-4 | – | 1.0E-4 | – | 1.0E-3 | 3.0E-4 | 1.0E-3 | 3.0E-4 |

**Table D.2:** continued.

| | | cauloc | | | | cmfctop | | | | cprcon | | | | entrscv | | | |
|---|---|---|---|---|---|---|---|---|---|---|---|---|---|---|---|---|---|
| | | ECHAM5 | | EMAC | | ECHAM5 | | EMAC | | ECHAM5 | | EMAC | | ECHAM5 | | EMAC | |
| | | | coupled | | coupled | | coupled | | coupled | | coupled | | coupled | | coupled | | coupled |
| T159 | L19 | 3.00 | 0.00 | 3.00 | 0.00 | 0.25 | – | 0.25 | – | 2.5E-4 | – | 2.5E-4 | – | 1.0E-3 | 3.0E-4 | 1.0E-3 | 3.0E-4 |
| | L31 | 5.00 | 0.00 | 5.00 | 0.00 | 0.35 | – | 0.35 | – | 1.0E-4 | – | 1.0E-4 | – | 1.0E-3 | 3.0E-4 | 1.0E-3 | 3.0E-4 |
| | L41 | – | – | 5.00 | 0.00 | – | – | – | – | – | – | – | – | 1.0E-3 | 3.0E-4 | 1.0E-3 | 3.0E-4 |
| | L60 | 5.00 | 0.00 | 5.00 | 0.00 | 0.35 | – | 0.35 | – | 1.0E-4 | – | 1.0E-4 | – | 1.0E-3 | 3.0E-4 | 1.0E-3 | 3.0E-4 |
| | L39MA | 3.00 | 0.00 | 3.00 | 0.00 | 0.25 | – | 0.25 | – | 2.0E-4 | – | 2.0E-4 | – | 1.0E-3 | 3.0E-4 | 1.0E-3 | 3.0E-4 |
| | L47MA | 5.00 | 0.00 | 5.00 | 0.00 | 0.35 | – | 0.35 | – | 1.0E-4 | – | 1.0E-4 | – | 1.0E-3 | 3.0E-4 | 1.0E-3 | 3.0E-4 |
| | L49MA | 5.00 | 0.00 | 5.00 | 0.00 | 0.35 | – | 0.35 | – | 1.0E-4 | – | 1.0E-4 | – | 1.0E-3 | 3.0E-4 | 1.0E-3 | 3.0E-4 |
| | L87MA | 5.00 | 0.00 | 5.00 | 0.00 | 0.35 | – | 0.35 | – | 1.0E-4 | – | 1.0E-4 | – | 1.0E-3 | 3.0E-4 | 1.0E-3 | 3.0E-4 |
| | L90MA | 5.00 | 0.00 | 5.00 | 0.00 | 0.35 | – | 0.35 | – | 1.0E-4 | – | 1.0E-4 | – | 1.0E-3 | 3.0E-4 | 1.0E-3 | 3.0E-4 |
| | L95MA | 5.00 | 0.00 | 5.00 | 0.00 | 0.35 | – | 0.35 | – | 1.0E-4 | – | 1.0E-4 | – | 1.0E-3 | 3.0E-4 | 1.0E-3 | 3.0E-4 |
| | L191MA | 5.00 | 0.00 | 5.00 | 0.00 | 0.35 | – | 0.35 | – | 1.0E-4 | – | 1.0E-4 | – | 1.0E-3 | 3.0E-4 | 1.0E-3 | 3.0E-4 |
| T255 | L31 | 5.00 | 0.00 | 5.00 | 0.00 | 0.35 | – | 0.35 | – | 1.0E-4 | – | 1.0E-4 | – | 1.0E-3 | 3.0E-4 | 1.0E-3 | 3.0E-4 |
| | L41 | – | – | 5.00 | 0.00 | – | – | – | – | – | – | – | – | 1.0E-3 | 3.0E-4 | 1.0E-3 | 3.0E-4 |
| | L60 | 5.00 | 0.00 | 5.00 | 0.00 | 0.35 | – | 0.35 | – | 1.0E-4 | – | 1.0E-4 | – | 1.0E-3 | 3.0E-4 | 1.0E-3 | 3.0E-4 |
| | L39MA | 3.00 | 0.00 | 3.00 | 0.00 | 0.25 | – | 0.25 | – | 2.0E-4 | – | 2.0E-4 | – | 1.0E-3 | 3.0E-4 | 1.0E-3 | 3.0E-4 |
| | L47MA | 5.00 | 0.00 | 5.00 | 0.00 | 0.35 | – | 0.35 | – | 1.0E-4 | – | 1.0E-4 | – | 1.0E-3 | 3.0E-4 | 1.0E-3 | 3.0E-4 |
| | L49MA | 5.00 | 0.00 | 5.00 | 0.00 | 0.35 | – | 0.35 | – | 1.0E-4 | – | 1.0E-4 | – | 1.0E-3 | 3.0E-4 | 1.0E-3 | 3.0E-4 |
| | L87MA | 5.00 | 0.00 | 5.00 | 0.00 | 0.35 | – | 0.35 | – | 1.0E-4 | – | 1.0E-4 | – | 1.0E-3 | 3.0E-4 | 1.0E-3 | 3.0E-4 |
| | L90MA | 5.00 | 0.00 | 5.00 | 0.00 | 0.35 | – | 0.35 | – | 1.0E-4 | – | 1.0E-4 | – | 1.0E-3 | 3.0E-4 | 1.0E-3 | 3.0E-4 |
| | L95MA | 5.00 | 0.00 | 5.00 | 0.00 | 0.35 | – | 0.35 | – | 1.0E-4 | – | 1.0E-4 | – | 1.0E-3 | 3.0E-4 | 1.0E-3 | 3.0E-4 |

**Table D.2:** continued.

| | | cauloc | | | | cmfctop | | | | cprcon | | | | entrscv | | | |
|---|---|---|---|---|---|---|---|---|---|---|---|---|---|---|---|---|---|
| | | ECHAM5 coupled | | EMAC coupled | | ECHAM5 coupled | | EMAC coupled | | ECHAM5 coupled | | EMAC coupled | | ECHAM5 coupled | | EMAC coupled | |
| T255 | L191MA | 5.00 | 0.00 | 5.00 | 0.00 | 0.35 | – | 0.35 | – | 1.0E-4 | – | 1.0E-4 | – | 1.0E-3 | 3.0E-4 | 1.0E-3 | 3.0E-4 |
| T319 | L31 | 5.00 | 0.00 | 5.00 | 0.00 | 0.35 | – | 0.35 | – | 1.0E-4 | – | 1.0E-4 | – | 1.0E-3 | 3.0E-4 | 1.0E-3 | 3.0E-4 |
| | L60 | 5.00 | 0.00 | 5.00 | 0.00 | 0.35 | – | 0.35 | – | 1.0E-4 | – | 1.0E-4 | – | 1.0E-3 | 3.0E-4 | 1.0E-3 | 3.0E-4 |
| | L39MA | 3.00 | 0.00 | 3.00 | 0.00 | 0.25 | – | 0.25 | – | 2.0E-4 | – | 2.0E-4 | – | 1.0E-3 | 3.0E-4 | 1.0E-3 | 3.0E-4 |
| | L47MA | 5.00 | 0.00 | 5.00 | 0.00 | 0.35 | – | 0.35 | – | 1.0E-4 | – | 1.0E-4 | – | 1.0E-3 | 3.0E-4 | 1.0E-3 | 3.0E-4 |
| | L49MA | 5.00 | 0.00 | 5.00 | 0.00 | 0.35 | – | 0.35 | – | 1.0E-4 | – | 1.0E-4 | – | 1.0E-3 | 3.0E-4 | 1.0E-3 | 3.0E-4 |
| | L87MA | 5.00 | 0.00 | 5.00 | 0.00 | 0.35 | – | 0.35 | – | 1.0E-4 | – | 1.0E-4 | – | 1.0E-3 | 3.0E-4 | 1.0E-3 | 3.0E-4 |
| | L90MA | 5.00 | 0.00 | 5.00 | 0.00 | 0.35 | – | 0.35 | – | 1.0E-4 | – | 1.0E-4 | – | 1.0E-3 | 3.0E-4 | 1.0E-3 | 3.0E-4 |
| | L95MA | 5.00 | 0.00 | 5.00 | 0.00 | 0.35 | – | 0.35 | – | 1.0E-4 | – | 1.0E-4 | – | 1.0E-3 | 3.0E-4 | 1.0E-3 | 3.0E-4 |
| | L191MA | 5.00 | 0.00 | 5.00 | 0.00 | 0.35 | – | 0.35 | – | 1.0E-4 | – | 1.0E-4 | – | 1.0E-3 | 3.0E-4 | 1.0E-3 | 3.0E-4 |

**Table D.2:** continued.

# Glossary

| Term | Description | Page(s) |
|---|---|---|
| A-GCM | atmosphere general circulation model | 13, 39, 40 |
| A2O | Atmosphere2Ocean submodel, exchange of gridded fields between atmosphere and ocean | 43, 44, 55, 63, 64 |
| AIRSEA | AIRSEA submodel, calculating air-sea gas exchange | 36, 44, 45, 49, 56, 58–60, 64–66, 71, 73–76, 177 |
| AMIP | Atmospheric Model Intercomparison Project | 78 |
| AO-CCM | atmosphere-ocean chemistry climate model | 16, 39, 70, 71, 74 |
| AO-GCM | atmosphere-ocean general circulation model | 13, 14, 16, 39, 40, 42, 55, 66, 70, 78 |
| AOU | apparent oxygen utilisation | 91 |
| BDC | Brewer-Dobson Circulation | 13 |
| Br | bromine | 27, 30, 195 |
| BrO | bromine monoxide | 27, 30, 195 |
| $BrO_x$ | $BrO_x$ chemical family = Br + BrO | 30 |
| C | carbon | 25, 30, 31, 51, 53, 54, 170, 171 |

| Term | Description | Page(s) |
|---|---|---|
| $C_5H_8$ | isoprene (2-methyl-1,3-butadiene) | 6, 9, 10, 25, 26, 52, 53, 59, 71, 73, 74, 89–91, 93, 101–103, 109, 110, 116–118, 120, 124–126, 129–132, 138, 140–143, 164–166, 208, A |
| $CaCO_3$ | calcium carbonate | 33, 48 |
| CAM | Community Atmosphere Model | 79 |
| CbPM | Carbon-based Productivity Model | 76, 77, 82, 83 |
| CCM | chemistry climate model | 5, 6, 13–15, 39, 42, 64 |
| CCMVal | Chemistry-Climate Model Validation | 13 |
| CCN | cloud condensation nucleus (mostly plural: cloud condensation nuclei) | 4, 6, 9, 10, 196 |
| CDOM | coloured dissolved organic matter | 53, 54, 207, 208 |
| CFC | chlorofluorocarbon | 21 |
| CFC-11 | $CCl_3F$, trichlorofluoromethane | 46, 71 |
| CFC-12 | $CCl_2F_2$, dichlorodifluoromethane | 46, 71 |
| $CH_2Cl$ | chloromethyl radical | 25 |
| $CH_3OH$ | methanol | 6, 11, 59, 71, 73, 93, 107, 108, 117, 118, 120, 164 |
| $CH_4$ | methane | 21, 46, 71 |
| CHANNEL | CHANNEL submodel, memory and meta-data management and data output | 42, 61, 62, 67, 181 |
| Cl | chlorine | 25, 27, 30, 197 |

| Term | Description | Page(s) |
|---|---|---|
| CLAW hypothesis | hypothesis, that phytoplankton is regulating local climate by emission of DMS which acts as CCN; named after the authors' surnames of the study | 9 |
| ClO | chlorine monoxide | 27, 30, 197 |
| CLOUD | CLOUD submodel, ECHAM5 cloud scheme | 44, 46 |
| $ClO_x$ | $ClO_x$ chemical family = Cl + ClO | 30 |
| CMBA | chloromethylbutenal | 25 |
| CMBO | 1-chloro-3-methyl-3-buten-2-one | 25 |
| CMIP5 | Coupled Model Intercomparison Project | 83 |
| CO | carbon monoxide | 6, 10, 11, 23, 26, 52–54, 59, 71, 73, 74, 91–93, 104, 106, 107, 109, 110, 117, 118, 120, 124–126, 130, 131, 133, 138, 140–143, 164, 166, 207–211, A |
| $CO_2$ | carbon dioxide | 7, 8, 20, 21, 31, 33–35, 46, 48, 49, 52, 59, 60, 71, 73, 74, 88, 89, 93, 100, 101, 109, 110, 126, 129, 131, 132, 138, 140–143, 164–166, 207, 209, 210, A |
| CONTROL | CONTROL submodel, providing entry points to call submodels | 42, 55 |

| Term | Description | Page(s) |
|---|---|---|
| CONVECT | CONVECTion submodel, convection parameterisations | 44 |
| CVTRANS | ConVective tracer TRANSport submodel, calculating convective tracer transport | 44 |
| DDEP | Dry DEPosition submodel, calculating dry deposition of trace gases and aerosol | 44–46, 60, 62–64, 75 |
| DIC | dissolved inorganic carbon | 33 |
| DMS | dimethyl sulphide ($(CH_3)_2S$) | 6, 8, 9, 15, 26–28, 34, 48, 52, 59, 71, 73, 74, 86, 88, 92–99, 109–116, 124–126, 128, 129, 131, 132, 138, 140–143, 164–166, 172, 196, A |
| DMSO | dimethyl sulphoxide ($CH_3SOCH_3$) | 27, 28 |
| $DMSO_2$ | dimethyl sulphone ($CH_3SO_2CH_3$) | 27, 28 |
| DOC | dissolved organic carbon | 52, 54, 172, 207 |
| DOM | dissolved organic matter | 31, 32, 48, 130, 167, 171, 207 |
| E4CHEM | E4CHEM submodel, computationally efficient calculation of atmospheric chemistry based on MAECHAM4-CHEM | 145 |
| ECHAM | European Centre HAMburg general circulation model | 15, 36, 39, 42, 45, 46, 66, 70, 78, 145, 146, 150, 155, 159, 161, 163, 184, 189, 198, 203 |

| Term | Description | Page(s) |
|---|---|---|
| EMAC | ECHAM/MESSy Atmospheric Chemistry | 15, 16, 36, 39, 42, 45, 47, 49, 55, 64–66, 70, 75, 78, 145, 163, 184, 189 |
| EP | export production | 83, 84, 142, 165 |
| ESM | earth system model | 13, 14, 16, 39–42 |
| Fe | iron | 15, 30, 38, 48, 51, 61, 73, 74, 126–128, 133, 135–139, 143, 166–168, 170, A |
| GCM | general circulation model | 13, 147, 150 |
| GEIA | Global Emissions InitiAtive | 71 |
| GHG | greenhouse gas | 1, 4, 8, 13, 14, 20 |
| GRIDTRAFO | GRIDTRAnsFOrmation submodel, grid transformations | 42, 55 |
| GWAVE | Gravity WAVE submodel, gravity wave parameterisation | 44 |
| H | hydrogen | 26, 30, 31, 200 |
| H2O | H2O submodel, stratospheric water vapour and feedback | 42, 44, 46 |
| $H_2O$ | water | 7, 20–22, 25, 34, 42, 43, 46, 47, 201 |
| $H_2O_2$ | hydrogen peroxide | 24 |
| $H_2SO_4$ | sulphuric acid | 27, 112–116 |
| HadGEM2 | Hadley Centre Global Environmental Model version 2 | 14, 15 |

| Term | Description | Page(s) |
|---|---|---|
| HAMOCC | HAMburg Ocean Carbon Cycle model | 15, 31, 32, 43, 44, 47–50, 52–54, 61–64, 66, 70, 72, 74–76, 81, 83, 85, 88, 93, 95, 109, 128, 137, 138, 163, 169, 170 |
| HCHO | formaldehyde (methanal, HCHO) | 10, 11, 25–27, 117, 118, 120 |
| HCO | formyl radical | 26 |
| HD | Hydrological Discharge submodel, calculating river discharge to the ocean | 44, 47, 48, 66, 74, 161 |
| HNLC | high nutrient low chlorophyll (also: high nitrate low chlorophyll) | 3, 38 |
| $HNO_3$ | nitric acid | 24, 43, 46, 71, 120, 122, 124, 200, 201 |
| $HNO_{3nat}$ | $HNO_3$ in NAT phase | 46 |
| $HNO_4$ | hydroxy nitrate | 120, 122, 124 |
| $HO_2$ | hydroperoxyl radical | 24–26, 30, 200 |
| HONO | nitrous acid | 120, 122, 124 |
| $HO_x$ | $HO_x$ chemical family = H + OH + $HO_2$ | 24, 30, 118 |
| I | iodine | 28 |
| IMPORT | IMPORT submodel, data import | 42 |
| JVAL | J-VALues submodel, calculation of photolysis rate coefficients | 44 |
| KCl | potassium chloride | 80 |
| LNOX | Lightning $NO_x$ submodel, calculation of lightning induced NOx production | 44 |
| M7 | aerosol model using seven aerosol classes | 44, 45, 62, 63, 75 |
| MACR | methacrolein (2-Methylprop-2-enal, $C_4H_6O$) | 10, 25 |
| MBL | marine boundary layer | 9, 10, 27, 28 |

| Term | Description | Page(s) |
|---|---|---|
| MECCA | Module Efficiently Calculating the Chemistry of the Atmosphere | 44–46, 74 |
| MESSy | Modular Earth Submodel System | 15–17, 36, 39, 41–49, 55, 56, 60–64, 66, 67, 70, 71, 76, 145, 163, 169, 170, 181, 198, 203 |
| MICOM | Miami Isopycnic Coordinate Model | 79 |
| MPAN | peroxymethacryloylnitrate ($CH_2C(CH_3)C(O)OONO_2$) | 10 |
| MPI-ESM | Max Planck Institute Earth System Model | 83, 85, 155 |
| MPIOM | Max Planck Institute Ocean Model | 15, 16, 39, 43, 44, 47, 48, 55, 64, 66, 70, 78, 146, 163 |
| MSA | methanesulphonic acid ($CH_3S(O)_2OH$) | 9, 27, 28 |
| MSBM | MSBM submodel, multi-phase stratospheric box model | 42–44, 46, 71, 72 |
| MSIA | methanesulphinic acid ($CH_3S(O)OH$) | 28 |
| MSPN | methanesulphonylperoxynitrate ($CH_3S(O)_2OONO_2$) | 28 |
| MVK | methane vinyl ketone (butenone, $C_4H_6O$) | 10, 25 |
| N | nitrogen | 30, 31, 51, 143, 168, 170 |
| $N_2$ | nitrogen | 22, 32, 49, 52, 59, 73, 74, 126, 170, 209 |
| $N_2O$ | nitrous oxide | 7, 8, 21, 29, 34, 46, 52, 59, 71, 73, 74, 91, 93, 103–105, 109, 110, 130–133, 138, 140–142, 164–166, A |

| Term | Description | Page(s) |
|---|---|---|
| $N_2O_5$ | dinitrogen pentaoxide | 120, 121, 123 |
| NAT | nitric acid trihydrate, $HNO_3 \cdot 3\,H_2O$ | 46, 71, 200 |
| NCEP | National Centers for Environmental Prediction | 79 |
| NCREGRID | NetCdf-REGRIDding submodel, rediscretisation on different grids | 42 |
| $NH_3$ | ammonia | 121, 123 |
| NO | nitric oxide | 10, 22–25, 27, 30, 74, 120, 121, 123, 202 |
| $NO_2$ | nitrogen dioxide | 22, 24, 27, 30, 120, 121, 123, 202 |
| $NO_3$ | nitrate radical | 24–26, 38, 112, 120, 121, 123, 209 |
| $NO_3^-$ | nitrate in aqueous phase | 32, 48, 128, 139, 143, 167, 168, A |
| NorESM | Norwegian Earth System Model | 85 |
| $NO_x$ | nitrogen oxides, $NO_x$ chemical family = NO + $NO_2$ | 8, 10, 22–24, 27, 29, 30, 44, 120, 121, 123, 166, 200 |
| NPP | net primary production | 76, 77, 82–85, 88, 89, 91, 96, 101, 104, 127, 128, 130, 136–139, 142, 143, 165, 167, 168, A |
| NPZD-type | NPZD-type biogeochemistry models consist of the functional groups nutrients, phytoplankton, zooplankton, and detritus | 31, 32, 48, 50 |
| O | oxygen | 23, 29–31 |

| Term | Description | Page(s) |
|---|---|---|
| O-GCM | ocean general circulation model | 13, 15, 39, 40, 47, 48 |
| $O(^1D)$ | electronically excited oxygen atom | 8, 23, 29, 74 |
| $O_2$ | oxygen | 20, 22, 23, 25, 26, 28, 31, 34, 49, 51, 52, 59, 73, 74, 170 |
| $O_3$ | ozone | 7, 8, 10, 13, 20–25, 27–29, 34, 46, 71, 117, 118, 120 |
| OASIS | Ocean Atmosphere Sea Ice Soil | 62 |
| OCS | carbonyl sulphide | 27 |
| OFFEMIS | OFFline tracer EMISsions submodel, calculating tracer tendencies from offline provided emission fluxes | 44 |
| OH | hydroxyl radical | 9–11, 23–26, 28, 30, 112, 113, 117, 118, 120, 200 |
| ONEMIS | ONline tracer EMISsions submodel, calculating gas-phase tracer emissions and updating tracer tendencies | 44, 45, 75 |
| OTPHYSC | Ocean Tracer PHYsiCs submodel, calculating advection, convection, diffusion and dilution of oceanic tracers | 43, 44, 48, 60, 61, 66, 167, 177 |
| P | phosphorous | 30, 31, 51, 54, 61, 170 |
| PAN | peroxyacetylnitrate ($CH_3C(O)OONO_2$) | 10, 120, 122, 124 |
| PAR | photosynthetically available radiation | 2, 4, 6, 30, 31, 81 |
| pH | scale describing acidity | 7, 8 |

| Term | Description | Page(s) |
|---|---|---|
| $PO_4^{3-}$ | orthophosphate | 48, 76, 77, 83, 84, 128, 139, 165, 171, 208, 209 |
| POC | particulate organic carbon | 2, 52, 83 |
| PSC | polar stratospheric cloud | 43, 46, 71, 72 |
| QCTM | Quasi Chemistry-Transport Model | 41, 46, 47, 70–74, 76, 101 |
| RAD4ALL | ECHAM5 radiation scheme implemented as MESSy submodel | 42, 44, 46, 71, 72 |
| SCALC | Simple CALCulations submodel, performing simple calculations on channel objects | 44, 46, 63, 64, 67, 75, 134, 181, 182 |
| SCAV | SCAVenging submodel, calculating scavenging and wet deposition of trace gases and aerosol | 44–46, 62–64, 75, 177 |
| SCRIP | Spherical Coordinate Remapping and Interpolation Package | 55 |
| SeaWiFS | Sea-viewing Wide Field-of-view Sensor | 77, 82, 83 |
| SEDI | SEDImentation submodel, calculating sedimentation of aerosol particles | 44–46, 62–64, 75 |
| Si | silicon | 37, 49, 60, 62, 73, 74, 126, 128, 133, 136, 137, 143, 209 |
| $SiO_2$ | silica, silicon dioxide | 15, 49, 62, 167, 209, A |
| $Si(OH)_4$ | silicic acid | 33, 48, 76, 77, 85, 127, 128, 135–138, 143, 165–167, 171, A |
| SMIL | submodel interface layer | 55 |
| $SO_2$ | sulphur dioxide | 9, 27, 28, 34, 112–114, 116 |

| Term | Description | Page(s) |
|---|---|---|
| SOA | secondary organic aerosol | 6, 10 |
| SOLAS | Surface Ocean – Lower Atmosphere Study | 14 |
| SSS | sea surface salinity | 76, 77, 80, 81, 142, 164, 165 |
| SST | sea surface temperature | 14, 76–80, 142, 164 |
| SWITCH | SWITCH submodel, turning on/off submodels at runtime | 42 |
| TIMER | TIMER submodel, model system time control | 42 |
| TNUDGE | Tracer NUDG(E)ing submodel, nudging tracers with user-defined fields | 44, 74, 104, 132 |
| TOA | top of the atmosphere | 147, 148, 152, 155, 156, 159, 160 |
| TRACER | TRACER submodel, data management for chemical constituents | 42, 48 |
| TROPOP | TROPOPause submodel, providing tropopause and other diagnostics | 44 |
| UTLS | upper troposphere lower stratosphere | 13, 14 |
| VOC | volatile organic compound | 9, 10 |
| WOA | World Ocean Atlas | 76–80, 84, 85, 90, 164 |

# Symbols

| Symbol | Description | Units |
|---|---|---|
| $a_{320}$ | absorption coefficient at light wavelength $\lambda = 320\,\mathrm{nm}$ | 1 |
| $a_f$ | attenuation coefficient for taking into account absorption at ocean surface, $a_f = 0.4$ | 1 |
| $a_g$ | absorption coefficient of CDOM | 1 |
| $c$ | speed of light in vacuum, $c = 299\,792\,458\,\mathrm{m\,s^{-1}}$ [a] | $\mathrm{m\,s^{-1}}$ |
| $c_a$ | molar concentration in aqueous phase | $\mathrm{mol\,m^{-3}}$ |
| *cauloc* | parameter influencing accretion of cloud droplets by precipitation | 1 |
| $C_d$ | drag coefficient | 1 |
| $c_g$ | molar concentration in the gas phase | $\mathrm{mol\,m^{-3}}$ |
| [Chl] | mass concentration of chlorophyll | $\mathrm{mg\,l^{-1}}$ |
| *cmfctop* | fraction of convective mass flux above the level of non buoyancy | 1 |
| [CO] | molar concentration of CO | $\mathrm{kmol(C)\,m^{-3}}$ |
| [$CO_2$] | molar concentration of $CO_2$ | $\mathrm{kmol(C)\,m^{-3}}$ |
| *cprcon* | conversion rate from cloud water to rain in convective clouds | $\mathrm{s^{-1}}$ |
| $c_s$ | molar concentration of salt | $\mathrm{mol\,l^{-1}}$ |
| $c_w$ | molar seawater tracer concentration | $\mathrm{mol\,m^{-3}}$ |
| $\mathfrak{D}$ | dark production rate of CO | $\mathrm{\mu mol\,m^{-3}\,s^{-1}}$ |
| $\mathcal{D}$ | discharge | $\mathrm{m^3\,s^{-1}}$ |
| $D_{\mathrm{CO_2}}$ | molecular diffusivity of $CO_2$ | $\mathrm{m^2\,s^{-1}}$ |
| [DOC] | molar concentration of DOC | $\mathrm{kmol(C)\,m^{-3}}$ |
| [DOM] | molar concentration of DOM | $\mathrm{kmol(C)\,m^{-3}}$ |

| Symbol | Description | Units |
|---|---|---|
| $D_{\mathrm{X}}$ | molecular diffusivity of tracer X | $\mathrm{m^2\,s^{-1}}$ |
| $E_d$ | downwelling irradiance | $\mathrm{W\,m^{-2}}$ |
| *entrscv* | entrainment rate for shallow convection | $\mathrm{m^{-1}}$ |
| $F$ | bulk flux across the atmosphere ocean interface | $\mathrm{mol\,(m^2\,s)^{-1}}$ |
| $F_{Dust}$ | dust deposition flux | $\mathrm{kg\,(m^2\,a)^{-1}}$ |
| [Fe] | molar concentration of iron | $\mathrm{kmol(Fe)\,m^{-3}}$ |
| $f_g(\lambda)$ | fraction of energy absorbed by CDOM to total absorbed energy | 1 |
| $h$ | Planck's constant, $h = (6.626\,069\,57 \pm 0.000\,000\,29) \times 10^{-34}\,\mathrm{J\,s}$ [a] | $\mathrm{J\,s}$ |
| $I$ | solar irradiance | $\mathrm{W\,m^{-2}}$ |
| $I_0$ | solar irradiance at ocean's surface | $\mathrm{W\,m^{-2}}$ |
| [Isop] | molar concentration of isoprene | $\mathrm{kmol(Isop)\,m^{-3}}$ |
| $J$ | photochemical production rate of CO | $\mathrm{\mu mol\,m^{-3}\,s^{-1}}$ |
| $J(I)$ | light limited growth rate of phytoplankton | $\mathrm{d^{-1}}$ |
| $J_{tot}(I,\vartheta)$ | light and temperature limited growth rate of phytoplankton | $\mathrm{d^{-1}}$ |
| $K$ | transfer velocity | $\mathrm{m\,s^{-1}}$ |
| $K_{660}$ | transfer velocity for a Schmidt number of 660 | $\mathrm{m\,s^{-1}}$ |
| $k_c$ | specific light extinction coefficient of chlorophyll | $\mathrm{m^{-1}\,(kg(Chl)\,m^{-3})^{-1}}$ |
| $K_g$ | gas phase side exchange velocity | $\mathrm{m\,s^{-1}}$ |
| $k_H$ | Henry's Law coefficient | $\mathrm{mol\,(m^3\,Pa)^{-1}}$ |
| $k_H^0$ | Henry's Law coefficient in pure water | $\mathrm{mol\,(m^3\,Pa)^{-1}}$ |
| $k_H^{\ominus}$ | Henry's Law coefficient at standard temperature $T^{\ominus} = 298.15\,\mathrm{K}$ | $\mathrm{mol\,(m^3\,Pa)^{-1}}$ |
| $K_{Phy}^{\mathrm{PO_4}}$ | half-saturation constant for $\mathrm{PO_4}$ | $\mathrm{kmol(P)\,m^{-3}}$ |
| $k_s$ | Setschenow constant | $\mathrm{l\,mol^{-1}}$ |
| $K_{tot}$ | transfer velocity (piston velocity) | $\mathrm{m\,s^{-1}}$ |
| $K_w$ | liquid side exchange velocity | $\mathrm{m\,s^{-1}}$ |
| $k_w$ | extinction coefficient of seawater | $\mathrm{m^{-1}}$ |
| $\hat{K}_w$ | liquid side exchange velocity, normalised to $Sc_{liq} = 660$ | $\mathrm{cm\,h^{-1}}$ |
| $L$ | length scale | m |

| Symbol | Description | Units |
|---|---|---|
| $\mathfrak{M}$ | microbial consumption of CO | $\mu\text{mol}\,\text{m}^{-3}\,\text{s}^{-1}$ |
| $M$ | molar mass | $\text{g}\,\text{mol}^{-1}$ |
| $M_{\text{C}}$ | molar mass of carbon, $M_{\text{C}} = 12\,\text{g}\,\text{mol}^{-1}$ | $\text{g}\,\text{mol}^{-1}$ |
| $M_{\text{Fe}}$ | molar mass of iron, $M_{\text{Fe}} = 55.85\,\text{g}\,\text{mol}^{-1}$ | $\text{g}\,\text{mol}^{-1}$ |
| $M_{\text{P}}$ | molar mass of phosphorous, $M_{\text{P}} = 30\,\text{g}\,\text{mol}^{-1}$ | $\text{g}\,\text{mol}^{-1}$ |
| $M_{\text{SiO}_2}$ | molar mass of silica, $M_{\text{SiO}_2} = 60\,\text{g}\,\text{mol}^{-1}$ | $\text{g}\,\text{mol}^{-1}$ |
| $[\text{N}_2]$ | molar concentration of $\text{N}_2$ | $\text{kmol(N)}\,\text{m}^{-3}$ |
| $N_A$ | Avogadro's constant, $N_A =$ $(6.022\,141\,29 \pm 0.000\,000\,27) \times 10^{23}\,\text{mol}^{-1}$ [a] | $\text{m}\,\text{s}^{-1}$ |
| $[\text{NO}_3]$ | molar concentration of $\text{NO}_3$ | $\text{kmol(N)}\,\text{m}^{-3}$ |
| $p_g$ | partial pressure | Pa |
| [Phy] | molar concentration of phytoplankton | $\text{kmol(P)}\,\text{m}^{-3}$ |
| $[\text{PO}_4]$ | molar concentration of $\text{PO}_4$ | $\text{kmol(P)}\,\text{m}^{-3}$ |
| $Q$ | velocity scale | $\text{m}\,\text{s}^{-1}$ |
| $R$ | gas constant, $R = (8.314\,462\,1 \pm 0.000\,007\,5)\,\text{J}\,(\text{mol}\,\text{K})^{-1}$ [a] | $\text{J}\,(\text{mol}\,\text{K})^{-1}$ |
| $R_a$ | aerodynamic resistance | $\text{s}\,\text{m}^{-1}$ |
| $R_{\text{C:Chl}}$ | carbon to chlorophyll ratio | $\text{g(C)}\,\text{g(Chl)}^{-1}$ |
| $R_{\text{C:P}}$ | carbon to phosphorous ratio | $\text{mol(C)}\,\text{mol(P)}^{-1}$ |
| $R_{\text{Fe:P}}$ | iron to phosphorous ratio | $\text{mol(Fe)}\,\text{mol(P)}^{-1}$ |
| $R_g$ | gas phase side resistance for gas exchange | $\text{s}\,\text{m}^{-1}$ |
| $R_{\text{N:P}}$ | nitrogen to phosphorous ratio | $\text{mol(N)}\,\text{mol(P)}^{-1}$ |
| $R_{qbr}$ | quasi laminar boundary layer resistance | $\text{s}\,\text{m}^{-1}$ |
| $\mathfrak{R}_S[\chi]$ | flux of $\chi$ | $\mu\text{mol}\,\text{m}^{-3}\,\text{s}^{-1}$ |
| $R_w$ | liquid phase side resistance for gas exchange | $\text{s}\,\text{m}^{-1}$ |
| $Sc_{\text{CO}_2}$ | liquid phase Schmidt number for $\text{CO}_2$ | 1 |
| $Sc_{liq}$ | liquid phase Schmidt number | 1 |
| $S_{\text{Fe}}$ | iron solubility, $S_{\text{Fe}} = 0.01$ | 1 |
| [Si] | molar concentration of Si | $\text{kmol(Si)}\,\text{m}^{-3}$ |
| $[\text{SiO}_2]$ | molar concentration of $\text{SiO}_2$ | $\text{kmol(Si)}\,\text{m}^{-3}$ |
| $S_{\text{SiO}_2}$ | silica solubility, $S_{\text{SiO}_2} = 0.075$ | 1 |
| $T$ | temperature | K |
| $t$ | time | s |
| $T^{\ominus}$ | standard temperature, $T^{\ominus} = 298.15\,\text{K}$ | K |
| $U$ | wind velocity | $\text{m}\,\text{s}^{-1}$ |

| Symbol | Description | Units |
|---|---|---|
| $U_{10}$ | 10-metre wind velocity | $\mathrm{m\,s^{-1}}$ |
| $V$ | volume | $\mathrm{m^3}$ |
| $V_{\mathrm{CO_2}}$ | molar volume at boiling point of $CO_2$ | $\mathrm{cm^3\,mol^{-1}}$ |
| $V_{\mathrm{X}}$ | molar volume at boiling point | $\mathrm{cm^3\,mol^{-1}}$ |
| $x$ | grid coordinate index in x-direction, longitude | 1, ° |
| [X] | molar concentration of X | $\mathrm{kmol(P)\,m^{-3}}$ |
| $y$ | grid coordinate index in y-direction, latitude | 1, ° |
| $z$ | height/depth | m |
| *zasic* | correction for asymmetry factor of ice clouds | 1 |
| *zinhomi* | inhomogeneity factor for ice clouds | 1 |
| *zinhoml* | inhomogeneity factor for liquid phase clouds | 1 |
| *zinpar* | parameter for calculation of the inhomogeneity factor for liquid clouds | 1 |
| $\alpha$ | fractional increase in exchange constant due to chemical reactivity | 1 |
| $\alpha_{PI}$ | initial slope of the P-I-curve | $\mathrm{d^{-1}(W\,m^{-2})^{-1}}$ |
| $\beta_{Sc}$ | scaling factor, to convert from units $\mathrm{cm\,h^{-1}}$ to units $\mathrm{m\,s^{-1}}$, $\beta_{Sc} = 2.8 \times 10^{-6}\,(\mathrm{m\,s^{-1}})/(\mathrm{cm\,h^{-1}})$ | $(\mathrm{m\,s^{-1}})/(\mathrm{cm\,h^{-1}})$ |
| $\gamma_i$ | asymmetry factor for ice clouds | 1 |
| $\Delta c_{wg}$ | difference of molar concentrations in water and in gas phase | $\mathrm{mol\,m^{-3}}$ |
| $\Delta_{soln}H$ | enthalpy per mole of solution | $\mathrm{J\,mol^{-1}}$ |
| $\Delta t$ | time step | s |
| $\Delta z$ | layer thickness | m |
| $\epsilon_{\mathrm{Fe}}$ | weight fraction of iron in dust, $\epsilon_{\mathrm{Fe}} = 0.035$ | 1 |
| $\epsilon_{\mathrm{SiO_2}}$ | weight fraction of silica in dust, $\epsilon_{\mathrm{SiO_2}} = 0.308$ | 1 |
| $\lambda$ | wavelength | nm |
| $\lambda_0$ | wavelength | nm |
| $\lambda_{\mathrm{Fe}}$ | relaxation time constant for iron relaxation | $\mathrm{d^{-1}}$ |
| $\mu_\vartheta$ | temperature limitation for phytoplankton growth | $\mathrm{d^{-1}}$ |
| $\nu$ | kinematic viscosity | $\mathrm{m^2\,s^{-1}}$ |
| $\Phi(\lambda)$ | apparent quantum yield of CO formation | 1 |
| $\rho_{air}$ | air density density | $\mathrm{kg\,m^{-3}}$ |

| Symbol | Description | Units |
|---|---|---|
| $\rho_p$ | total phytoplankton production by photosynthesis | $\mathrm{kmol(P)\,m^{-3}\,d^{-1}}$ |
| $\tau$ | wind stress | Pa |
| $\vartheta$ | temperature | °C |
| $\chi(z,t)$ | molar concentration of CO at depth $z$ and time $t$ | $\mathrm{\mu mol\,m^{-3}}$ |

[a] Mohr et al. (2012)

# List of Figures

# List of Tables

# Bibliography


Andreae, M. O. and P. J. Crutzen. Atmospheric Aerosols: Biogeochemical Sources and Role in Atmospheric Chemistry. *Science*, 276(5315):1052–1058, **1997**. doi: 10.1126/science.276.5315.1052.

Andreae, M. O. and H. Raemdonck. Dimethyl sulfide in the surface ocean and the marine atmosphere: a global view. *Science*, 221(4612):744–747, **1983**. doi: 10.1126/science.221.4612.744.

Antonov, J. I., D. Seidov, T. P. Boyer, R. A. Locarnini, A. V. Mishonov, H. E. Garcia, O. K. Baranova, M. M. Zweng, and D. R. Johnson. *World Ocean Atlas 2009, Volume 2: Salinity*. Levitus, S. (Ed.), NOAA Atlas NESDIS 69, U.S. Government Printing Office, Washington, D.C., USA, 184 pp., **2010**.

Arakawa, A. and V. R. Lamb. Computational Design of the Basic Dynamical Processes of the UCLA General Circulation Model. In: Chang, J., B. Alder, and S. Fernbach (Eds.), *Methods in Computational Physics, Volume 17: General Circulation Models of the Atmosphere*, 173–265. Academic Press, New York, NY, USA, **1977**. ISBN 978-0-12-460817-7. doi: 10.1016/B978-0-12-460817-7.50009-4.

Arnold, S. R., D. V. Spracklen, J. Williams, N. Yassaa, J. Sciare, B. Bonsang, V. Gros, I. Peeken, A. C. Lewis, S. Alvain, and C. Moulin. Evaluation of the global oceanic isoprene source and its impacts on marine organic carbon aerosol. *Atmospheric Chemistry and Physics*, 9(4):1253–1262, **2009**. doi: 10.5194/acp-9-1253-2009.

Assmann, K. M., M. Bentsen, J. Segschneider, and C. Heinze. An isopycnic ocean carbon cycle model. *Geoscientific Model Development*, 3(1):143–167, **2010**. doi: 10.5194/gmd-3-143-2010.

Atkinson, R. Gas-Phase Tropospheric Chemistry of Volatile Organic Compounds: 1. Alkanes and Alkenes. *Journal of Physical and Chemical Reference Data*, 26(2): 215–290, **1997**. doi: 10.1063/1.556012.

Atkinson, R. Atmospheric chemistry of VOCs and NOx. *Atmospheric Environment*, 34(12-14):2063–2101, **2000**. doi: 10.1016/S1352-2310(99)00460-4.

Atkinson, R. and J. Arey. Gas-phase tropospheric chemistry of biogenic volatile organic compounds: a review. *Atmospheric Environment*, 37(2):197–219, **2003**. doi: 10.1016/S1352-2310(03)00391-1.

Ayers, G. P. and J. M. Cainey. The CLAW hypothesis: a review of the major developments. *Environmental Chemistry*, 4(6):366–374, **2007**. doi: 10.1071/EN07080.

Ayers, G. P., S. T. Bentley, J. P. Ivey, and B. W. Forgan. Dimethylsulfide in marine air at Cape Grim, 41°S. *Journal of Geophysical Research*, 100(D10):21013–21021, **1995**. doi: 10.1029/95JD02144.

Barnes, I., J. Hjorth, and N. Mihalopoulos. Dimethyl sulfide and dimethyl sulfoxide and their oxidation in the atmosphere. *Chemical Reviews*, 106(3):940–75, **2006**. doi: 10.1021/cr020529+.

Baumgaertner, A. J. G., P. Jöckel, B. Steil, H. Tost, and R. Sander. A fast stratospheric chemistry solver: the E4CHEM submodel for the atmospheric chemistry global circulation model EMAC. *Geoscientific Model Development*, 3(1):321–328, **2010**. doi: 10.5194/gmd-3-321-2010.

Behrenfeld, M. J., E. Boss, D. A. Siegel, and D. M. Shea. Carbon-based ocean productivity and phytoplankton physiology from space. *Global Biogeochemical Cycles*, 19(1):GB1006, **2005**. doi: 10.1029/2004GB002299.

Behrenfeld, M. J., R. T. O'Malley, D. A. Siegel, C. R. McClain, J. L. Sarmiento, G. C. Feldman, A. J. Milligan, P. G. Falkowski, R. M. Letelier, and E. S. Boss. Climate-driven trends in contemporary ocean productivity. *Nature*, 444(7120): 752–755, **2006**. doi: 10.1038/nature05317.

Bergamaschi, P., R. Hein, M. Heimann, and P. J. Crutzen. Inverse modeling of the global CO cycle 1. Inversion of CO mixing ratios. *Journal of Geophysical Research*, 105(D2):1909–1927, **2000**. doi: 10.1029/1999JD900818.

Bernard, C. Y., G. G. Laruelle, C. P. Slomp, and C. Heinze. Impact of changes in river fluxes of silica on the global marine silicon cycle: a model comparison. *Biogeosciences*, 7(2):441–453, **2010**. doi: 10.5194/bg-7-441-2010.

Bernard, C. Y., H. H. Dürr, C. Heinze, J. Segschneider, and E. Maier-Reimer. Contribution of riverine nutrients to the silicon biogeochemistry of the global ocean – a model study. *Biogeosciences*, 8(3):551–564, **2011**. doi: 10.5194/bg-8-551-2011.

Bigg, G. R., T. D. Jickells, P. S. Liss, and T. J. Osborn. The role of the oceans in climate. *International Journal of Climatology*, 23(10):1127–1159, **2003**. doi: 10.1002/joc.926.

Bleck, R. and L. T. Smith. A wind-driven isopycnic coordinate model of the north and equatorial Atlantic Ocean: 1. Model development and supporting experiments. *Journal of Geophysical Research*, 95(C3):3273–3285, **1990**. doi: 10.1029/JC095iC03p03273.

Bleck, R., C. Rooth, D. Hu, and L. T. Smith. Salinity-driven Thermocline Transients in a Wind- and Thermohaline-forced Isopycnic Coordinate Model of the North Atlantic. *Journal of Physical Oceanography*, 22(12):1486–1505, **1992**. doi: 10.1175/1520-0485(1992)022<1486:SDTTIA>2.0.CO;2.

Bodas-Salcedo, A., M. J. Webb, S. Bony, H. Chepfer, J.-L. Dufresne, S. A. Klein, Y. Zhang, R. Marchand, J. M. Haynes, R. Pincus, and V. O. John. COSP: Satellite simulation software for model assessment. *Bulletin of the American Meteorological Society*, 92(8):1023–1043, **2011**. doi: 10.1175/2011BAMS2856.1.

Bonsang, B., C. Polle, and G. Lambert. Evidence for marine production of isoprene. *Geophysical Research Letters*, 19(11):1129–1132, **1992**. doi: 10.1029/92GL00083.

Boyd, P. W., T. Jickells, C. S. Law, S. Blain, E. a. Boyle, K. O. Buesseler, K. H. Coale, J. J. Cullen, H. J. W. de Baar, M. Follows, M. Harvey, C. Lancelot, M. Levasseur, N. P. J. Owens, R. Pollard, R. B. Rivkin, J. Sarmiento, V. Schoemann, V. Smetacek, S. Takeda, A. Tsuda, S. Turner, and a. J. Watson. Mesoscale iron enrichment experiments 1993-2005: synthesis and future directions. *Science*, 315(5812):612–617, **2007**. doi: 10.1126/science.1131669.

Broadgate, W. J., P. S. Liss, and S. A. Penkett. Seasonal emissions of isoprene and other reactive hydrocarbon gases from the ocean. *Geophysical Research Letters*, 24(21):2675–2678, **1997**. doi: 10.1029/97GL02736.

Carr, M.-E., M. A. Friedrichs, M. Schmeltz, M. Noguchi Aita, D. Antoine, K. R. Arrigo, I. Asanuma, O. Aumont, R. Barber, M. Behrenfeld, R. Bidigare, E. T. Buitenhuis, J. Campbell, A. Ciotti, H. Dierssen, M. Dowell, J. Dunne, W. Esaias, B. Gentili, W. Gregg, S. Groom, N. Hoepffner, J. Ishizaka, T. Kameda, C. Le Quéré, S. Lohrenz, J. Marra, F. Mélin, K. Moore, A. Morel, T. E. Reddy, J. Ryan, M. Scardi, T. Smyth, K. Turpie, G. Tilstone, K. Waters, and Y. Yamanaka. A comparison of global estimates of marine primary production from ocean color. *Deep Sea Research Part II*, 53(5-7):741–770, **2006**. doi: 10.1016/j.dsr2.2006.01.028.

Carslaw, K. S., O. Boucher, D. V. Spracklen, G. W. Mann, J. G. L. Rae, S. Woodward, and M. Kulmala. A review of natural aerosol interactions and feedbacks within the Earth system. *Atmospheric Chemistry and Physics*, 10(4):1701–1737, **2010**. doi: 10.5194/acp-10-1701-2010.

Chapman, S. A Theory of Upper Atmospheric Ozone. *Memoirs of the Royal Meteorological Society*, 3(26):103–125, **1930**. `http://www.rmets.org/sites/default/files/chapman-memoirs.pdf`.

Charette, M. and W. Smith. The Volume of Earth's Ocean. *Oceanography*, 23(2): 112–114, **2010**. doi: 10.5670/oceanog.2010.51.

Charlson, R. J., J. E. Lovelock, M. O. Andreae, and S. G. Warren. Oceanic phytoplankton, atmospheric sulphur, cloud albedo and climate. *Nature*, 326(6114): 655–661, **1987**. doi: 10.1038/326655a0.

Chipperfield, M. P. Multiannual simulations with a three-dimensional chemical transport model. *Journal of Geophysical Research*, 104(D1):1781–1805, **1999**. doi: 10.1029/98JD02597.

Chu, S., S. Elliott, and D. Erickson. Basin-Scale Carbon Monoxide Distributions in the Parallel Ocean Program. *Earth Interactions*, 11(22):1–30, **2007**. doi: 10.1175/EI211.1.

Collins, N., G. Theurich, C. DeLuca, M. Suarez, A. Trayanov, V. Balaji, P. Li, W. Yang, C. Hill, and A. da Silva. Design and Implementation of Components in the Earth System Modeling Framework. *International Journal of High Performance Computing Applications*, 19(3):341–350, **2005**. doi: 10.1177/1094342005056120.

Collins, W. D., C. M. Bitz, M. L. Blackmon, G. B. Bonan, C. S. Bretherton, J. A. Carton, P. Chang, S. C. Doney, J. J. Hack, T. B. Henderson, J. T. Kiehl, W. G. Large, D. S. McKenna, B. D. Santer, and R. D. Smith. The Community Climate System Model Version 3 (CCSM3). *Journal of Climate*, 19(11):2122–2143, **2006**. doi: 10.1175/JCLI3761.1.

Collins, W. J., N. Bellouin, M. Doutriaux-Boucher, N. Gedney, P. Halloran, T. Hinton, J. Hughes, C. D. Jones, M. Joshi, S. Liddicoat, G. Martin, F. O'Connor, J. Rae, C. Senior, S. Sitch, I. Totterdell, A. Wiltshire, and S. Woodward. Development and evaluation of an Earth-System model – HadGEM2. *Geoscientific Model Development*, 4(4):1051–1075, **2011**. doi: 10.5194/gmd-4-1051-2011.

Conkright, M. E., T. D. O'Brien, C. Stephens, R. A. Locarnini, H. E. Garcia, T. P. Boyer, and J. I. Antonov. *World Ocean Atlas 2001, Volume 6: Chlorophyll*. Levitus, S. (Ed.), NOAA Atlas NESDIS 54, U.S. Government Printing Office, Washington, D.C., USA, 46 pp., **2002**.

Cotrim da Cunha, L., E. T. Buitenhuis, C. Le Quéré, X. Giraud, and W. Ludwig. Potential impact of changes in river nutrient supply on global ocean biogeochemistry. *Global Biogeochemical Cycles*, 21(4):GB4007, **2007**. doi: 10.1029/2006GB002718.

Crutzen, P. J. The influence of nitrogen oxides on the atmospheric ozone content. *Quarterly Journal of the Royal Meteorological Society*, 96(408):320–325, **1970**. doi: 10.1002/qj.49709640815.

Dauphinée, T. M., E. L. Lewis, J. Ancsin, M. Phillips, F. Culkin, N. Smith, A. Poisson, A. L. Bradshaw, K. Schleicher, R. Perkin, and H. Klein. Background papers and supporting data on the practical salinity scale 1978. Technical papers in marine science, 37, UNESCO, Paris, France, 144 pp., **1981**. `http://www.unesco.org/ulis/cgi-bin/ulis.pl?catno=47932`.

Deckert, R., P. Jöckel, V. Grewe, K.-D. Gottschaldt, and P. Hoor. A quasi chemistry-transport model mode for EMAC. *Geoscientific Model Development*, 4(1):195–206, **2011**. doi: 10.5194/gmd-4-195-2011.

Denman, K. L., G. Brasseur, A. Chidthaisong, P. Ciais, P. M. Cox, R. E. Dickinson, D. Hauglustaine, C. Heinze, E. Holland, D. Jacob, U. Lohmann, S. Ramachandran, P. L. da Silva Dias, S. C. Wofsy, and X. Zhang. Couplings Between Changes in the Climate System and Biogeochemistry. In: Solomon,

S., D. Qin, M. Manning, Z. Chen, M. Marquis, K. Averyt, M.Tignor, and H. Miller (Eds.), *Climate Change 2007: The Physical Science Basis. Contribution of Working Group I to the Fourth Assessment Report of the Intergovernmental Panel on Climate Change*, Chapter 7, 499–587. Cambridge University Press, Cambridge, United Kingdom and New York, NY, USA, **2007**. `http://www.ipcc.ch/publications_and_data/publications_ipcc_fourth_assessment_report_wg1_report_the_physical_science_basis.htm`.

Dixon, J. L., R. Beale, and P. D. Nightingale. Microbial methanol uptake in northeast Atlantic waters. *The ISME Journal*, 5(4):704–16, **2011**. doi: 10.1038/ismej.2010.169.

Doney, S. C., K. Lindsay, K. Caldeira, J.-M. Campin, H. Drange, J. C. Dutay, M. Follows, Y. Gao, A. Gnanadesikan, N. Gruber, A. Ishida, F. Joos, G. Madec, E. Maier-Reimer, J. C. Marshall, R. J. Matear, P. Monfray, A. Mouchet, R. Najjar, J. C. Orr, G. K. Plattner, J. Sarmiento, R. Schlitzer, R. Slater, I. J. Totterdell, M. F. Weirig, Y. Yamanaka, and A. Yool. Evaluating global ocean carbon models: The importance of realistic physics. *Global Biogeochemical Cycles*, 18(3):GB3017, **2004**. doi: 10.1029/2003GB002150.

Doney, S. C., I. Lima, R. A. Feely, D. M. Glover, K. Lindsay, N. Mahowald, J. K. Moore, and R. Wanninkhof. Mechanisms governing interannual variability in upper-ocean inorganic carbon system and air-sea $CO_2$ fluxes: Physical climate and atmospheric dust. *Deep-Sea Research II*, 56(8-10):640–655, **2009**. doi: 10.1016/j.dsr2.2008.12.006.

Duce, R. A., P. S. Liss, J. T. Merrill, E. L. Atlas, P. Buat-Menard, B. B. Hicks, J. M. Miller, J. M. Prospero, R. Arimoto, T. M. Church, W. Ellis, J. N. Galloway, L. Hansen, T. D. Jickells, A. H. Knap, K. H. Reinhardt, B. Schneider, A. Soudine, J. J. Tokos, S. Tsunogai, R. Wollast, and M. Zhou. The atmospheric input of trace species to the world ocean. *Global Biogeochemical Cycles*, 5(3):193–259, **1991**. doi: 10.1029/91GB01778.

Duncan, B. N., J. a. Logan, I. Bey, I. a. Megretskaia, R. M. Yantosca, P. C. Novelli, N. B. Jones, and C. P. Rinsland. Global budget of CO, 1988–1997: Source estimates and validation with a global model. *Journal of Geophysical Research*, 112:D22301, **2007**. doi: 10.1029/2007JD008459.

Dürr, H. H., M. Meybeck, J. Hartmann, G. G. Laruelle, and V. Roubeix. Global spatial distribution of natural riverine silica inputs to the coastal zone. *Biogeosciences*, 8(3):597–620, **2011**. doi: 10.5194/bg-8-597-2011.

Ehhalt, D., M. Prather, F. Dentener, R. Derwent, E. Dlugokencky, E. Holland, I. Isaksen, J. Katima, V. Kirchhoff, P. Matson, P. Midgley, M. Wang, T. Berntsen, I. Bey, G. Brasseur, L. Buja, W. J. Collins, J. Daniel, W. B. Demore, N. Derek, R. Dickerson, D. Etheridge, J. Feichter, P. Fraser, R. Friedl, J. Fuglestvedt, M. Gauss, L. Grenfell, A. Grübler, N. Harris, D. Hauglustaine, L. Horowitz, C. Jackman, D. Jacob, L. Jaeglé, A. Jain, M. Kanakidou, S. Karlsdottir, M. Ko, M. Kurylo, M. Lawrence, J. A. Logan, M. Manning, D. Mauzerall, J. Mcconnell, L. Mickley, S. Montzka, J. F. Müller, J. Olivier, K. Pickering, G. Pitari, G. J. Roelofs, H. Rogers, B. Rognerud, S. Smith, S. Solomon, J. Staehelin, P. Steele, D. Stevenson, J. Sundet, A. Thompson, M. van Weele, R. von Kuhlmann, Y. Wang, D. Weisenstein, T. Wigley, O. Wild, D. Wuebbles, and R. Yantosca. Atmospheric Chemistry and Greenhouse Gases. In: Houghton, J., Y. Ding, D. Griggs, M. Noguer, P. van der Linden, X. Dai, K. Maskell, and C. Johnson (Eds.), *Climate Change 2001: The Scientific Basis. Contribution of Working Group I to the Third Assessment Report of the Intergovernmental Panel on Climate Change*, Chapter 8, 239–287. Cambridge University Press, New York, NY, USA, **2001**. `http://www.grida.no/publications/other/ipcc_tar/`.

Eppley, R. W. Temperature and phytoplankton growth in the sea. *Fishery Bulletin*, 70(4):1063–1085, **1972**. `http://fishbull.noaa.gov/70-4/eppley.pdf`.

Fabricius, K. E., C. Langdon, S. Uthicke, C. Humphrey, S. Noonan, G. De'ath, R. Okazaki, N. Muehllehner, M. S. Glas, and J. M. Lough. Losers and winners in coral reefs acclimatized to elevated carbon dioxide concentrations. *Nature Climate Change*, 1(3):165–169, **2011**. doi: 10.1038/nclimate1122.

Fan, J. and R. Zhang. Atmospheric Oxidation Mechanism of Isoprene. *Environmental Chemistry*, 1(3):140–149, **2004**. doi: 10.1071/EN04045.

Feely, R. A., C. L. Sabine, K. Lee, W. Berelson, J. Kleypas, V. J. Fabry, and F. J. Millero. Impact of anthropogenic $CO_2$ on the $CaCO_3$ system in the oceans. *Science*, 305(5682):362–366, **2004**. doi: 10.1126/science.1097329.

Flato, G. M. Earth system models: an overview. *Wiley Interdisciplinary Reviews: Climate Change*, 2(6):783–800, **2011**. doi: 10.1002/wcc.148.

Fleagle, R. G. and J. A. Businger. *An Introduction to Atmospheric Physics*. Academic Press, New York, NY, USA, second edition, 346 pp., **1980**. ISBN 0122603559.

Forster, P., V. Ramaswamy, P. Artaxo, T. Berntsen, R. Betts, D. Fahey, J. Haywood, J. Lean, D. Lowe, G. Myhre, J. Nganga, R. Prinn, G. Raga, M. Schulz, and R. van Dorland. Changes in Atmospheric Constituents and in Radiative Forcing. In: Solomon, S., D. Qin, M. Manning, Z. Chen, M. Marquis, K. Averyt, M.Tignor, and H. Miller (Eds.), *Climate Change 2007: The Physical Science Basis. Contribution of Working Group I to the Fourth Assessment Report of the Intergovernmental Panel on Climate Change*, Chapter 2, 129–234. Cambridge University Press, Cambridge, United Kingdom and New York, NY, USA, **2007**. `http://www.ipcc.ch/publications_and_data/publications_ipcc_fourth_assessment_report_wg1_report_the_physical_science_basis.htm`.

Francis, P. N., A. Jones, R. W. Saunders, K. P. Shine, A. Slingo, and Z. Sun. An observational and theoretical study of the radiative properties of cirrus: Some results from ICE'89. *Quarterly Journal of the Royal Meteorological Society*, 120 (518):809–848, **1994**. doi: 10.1002/qj.49712051804.

Freing, A., D. W. R. Wallace, and H. W. Bange. Global oceanic production of nitrous oxide. *Philosophical transactions of the Royal Society of London. Series B, Biological sciences*, 367(1593):1245–1255, **2012**. doi: 10.1098/rstb.2011.0360.

Fung, I. Y., S. K. Meyn, I. Tegen, S. C. Doney, J. G. John, and J. K. B. Bishop. Iron supply and demand in the upper ocean. *Global Biogeochemical Cycles*, 14(1): 281–295, **2000**. doi: 10.1029/1999GB900059.

Galbally, I. E. and W. Kirstine. The Production of Methanol by Flowering Plants and the Global Cycle of Methanol. *Journal of Atmospheric Chemistry*, 43(3): 195–229, **2002**. doi: 10.1023/A:1020684815474.

Garcia, H. E., R. A. Locarnini, T. P. Boyer, J. I. Antonov, O. K. Baranova, M. M. Zweng, and D. R. Johnson. *World Ocean Atlas 2009, Volume 4: Nutrients (phosphate, nitrate, silicate)*. Levitus, S. (Ed.), NOAA Atlas NESDIS 71, U.S. Government Printing Office, Washington, D.C., USA, 398 pp., **2010**.

Gent, P. R., J. Willebrand, T. J. McDougall, and J. C. McWilliams. Parameterizing Eddy-Induced Tracer Transports in Ocean Circulation Models. *Journal of Physical Oceanography*, 25(4):463–474, **1995**. doi: 10.1175/1520-0485(1995)025<0463:PEITTI>2.0.CO;2.

Gent, P. R., G. Danabasoglu, L. J. Donner, M. M. Holland, E. C. Hunke, S. R. Jayne, D. M. Lawrence, R. B. Neale, P. J. Rasch, M. Vertenstein, P. H. Worley, Z.-L. Yang, and M. Zhang. The Community Climate System Model Version 4. *Journal of Climate*, 24(19):4973–4991, **2011**. doi: 10.1175/2011JCLI4083.1.

GESAMP. Land/sea boundary flux of contaminants: Contribution from rivers. Reports and Studies No. 32, UNESCO, 172 pp., **1987**. `http://www.gesamp.org/publications/publicationdisplaypages/rs32`.

Gläser, G., A. Kerkweg, and H. Wernli. The Mineral Dust Cycle in EMAC 2.40: sensitivity to the spectral resolution and the dust emission scheme. *Atmospheric Chemistry and Physics*, 12(3):1611–1627, **2012**. doi: 10.5194/acp-12-1611-2012.

Goody, R. M. and G. D. Robinson. Radiation in the troposphere and lower stratosphere. *Quarterly Journal of the Royal Meteorological Society*, 77(332):151–187, **1951**. doi: 10.1002/qj.49707733203.

Grewe, V., D. Brunner, M. Dameris, J. Grenfell, R. Hein, D. Shindell, and J. Staehelin. Origin and variability of upper tropospheric nitrogen oxides and ozone at northern mid-latitudes. *Atmospheric Environment*, 35(20):3421–3433, **2001**. doi: 10.1016/S1352-2310(01)00134-0.

Griffies, S. M. The Gent–McWilliams Skew Flux. *Journal of Physical Oceanography*, 28(5):831–841, **1998**. doi: 10.1175/1520-0485(1998)028<0831:TGMSF>2.0.CO;2.

Guenther, A., C. N. Hewitt, D. Erickson, R. Fall, C. Geron, T. Graedel, P. Harley, L. Klinger, M. Lerdau, W. A. Mckay, T. Pierce, B. Scholes, R. Steinbrecher, R. Tallamraju, J. Taylor, and P. Zimmerman. A global model of natural volatile organic compound emissions. *Journal of Geophysical Research*, 100(D5):8873–8892, **1995**. doi: 10.1029/94JD02950.

Hagemann, S. and L. Dümenil. A parametrization of the lateral waterflow for the global scale. *Climate Dynamics*, 14(1):17–31, **1998**. doi: 10.1007/s003820050205.

Hayduk, W. and H. Laudie. Prediction of diffusion coefficients for nonelectrolytes in dilute aqueous solutions. *AIChE Journal*, 20(3):611–615, **1974**. doi: 10.1002/aic.690200329.

Heikes, B. G., W. Chang, M. E. Q. Pilson, E. Swift, H. B. Singh, A. Guenther, D. J. Jacob, B. D. Field, R. Fall, D. Riemer, and L. Brand. Atmospheric methanol budget and ocean implication. *Global Biogeochemical Cycles*, 16(4):1133, **2002**. doi: 10.1029/2002GB001895.

Heinze, C. and E. Maier-Reimer. The Hamburg Oceanic Carbon Cycle Circulation Model Version "HAMOCC2s" for long time integrations. DKRZ Report No. 20, DKRZ, Hamburg, Germany, 72 pp., **1999**. doi: 10.2312/WDCC/DKRZ_Report_No20.

Henson, B. Acidification and more. *UCAR Magazine*, (Winter 2011):7–11, **2011**. `http://www2.ucar.edu/magazine/features/acidification-and-more`.

Hines, C. O. Doppler-spread parameterization of gravity-wave momentum deposition in the middle atmosphere. Part 1: Basic formulation. *Journal of Atmospheric and Solar-Terrestrial Physics*, 59(4):371–386, **1997a**. doi: 10.1016/S1364-6826(96)00079-X.

Hines, C. O. Doppler-spread parameterization of gravity-wave momentum deposition in the middle atmosphere. Part 2: Broad and quasi monochromatic spectra, and implementation. *Journal of Atmospheric and Solar-Terrestrial Physics*, 59(4): 387–400, **1997b**. doi: 10.1016/S1364-6826(96)00080-6.

Huneeus, N., M. Schulz, Y. Balkanski, J. Griesfeller, J. Prospero, S. Kinne, S. Bauer, O. Boucher, M. Chin, F. Dentener, T. Diehl, R. Easter, D. Fillmore, S. Ghan, P. Ginoux, A. Grini, L. Horowitz, D. Koch, M. C. Krol, W. Landing, X. Liu, N. Mahowald, R. Miller, J.-J. Morcrette, G. Myhre, J. Penner, J. Perlwitz, P. Stier, T. Takemura, and C. S. Zender. Global dust model intercomparison in AeroCom phase I. *Atmospheric Chemistry and Physics*, 11(15):7781–7816, **2011**. doi: 10.5194/acp-11-7781-2011.

Hurrell, J. W., J. J. Hack, D. Shea, J. M. Caron, and J. Rosinski. A New Sea Surface Temperature and Sea Ice Boundary Dataset for the Community Atmosphere Model. *Journal of Climate*, 21(19):5145–5153, **2008**. doi: 10.1175/2008JCLI2292.1.

Ilyina, T., K. D. Six, J. Segschneider, E. Maier-Reimer, H. Li, and I. Núñez Riboni. The global ocean biogeochemistry model HAMOCC: Model architecture and performance as component of the MPI-earth system model in different CMIP5 experimental realizations. *Journal of Advances in Modeling Earth Systems*, 5, **2013**. doi: 10.1029/2012MS000178.

Jacob, D. J., B. D. Field, Q. Li, D. R. Blake, J. de Gouw, C. Warneke, A. Hansel, A. Wisthaler, H. B. Singh, and A. Guenther. Global budget of methanol: Constraints from atmospheric observations. *Journal of Geophysical Research*, 110: D08303, **2005**. doi: 10.1029/2004JD005172.

Janenko, N. N. *Die Zwischenschrittmethode zur Lösung mehrdimensionaler Probleme der mathematischen Physik*, volume 91 of *Lecture Notes in Mathematics*. Springer, Berlin Heidelberg, Germany, 194 pp., **1969**. ISBN 978-3-540-04610-3. doi: 10.1007/BFb0098290.

Jickells, T. D. Nutrient Biogeochemistry of the Coastal Zone. *Science*, 281(5374): 217–222, **1998**. doi: 10.1126/science.281.5374.217.

Jickells, T. D., Z. S. An, K. K. Andersen, A. R. Baker, G. Bergametti, N. Brooks, J. J. Cao, P. W. Boyd, R. A. Duce, K. A. Hunter, H. Kawahata, N. Kubilay, J. LaRoche, P. S. Liss, N. Mahowald, J. M. Prospero, A. J. Ridgwell, I. Tegen, and R. Torres. Global iron connections between desert dust, ocean biogeochemistry, and climate. *Science*, 308(5718):67–71, **2005**. doi: 10.1126/science.1105959.

Jöckel, P. Technical note: Recursive rediscretation of geo-scientific data in the Modular Earth Submodel System (MESSy). *Atmos. Chem. Phys.*, 6:3557–3562, **2006**. doi: 10.5194/acp-6-3557-2006.

Jöckel, P. Earth System Modeling. In: Schumann, U. (Ed.), *Atmospheric Physics*, Chapter 35, 577–590. Springer, Berlin Heidelberg, Germany, **2012**. ISBN 978-3-642-30183-4. doi: 10.1007/978-3-642-30183-4_35.

Jöckel, P., R. Sander, A. Kerkweg, H. Tost, and J. Lelieveld. Technical Note: The Modular Earth Submodel System (MESSy) - a new approach towards Earth System Modeling. *Atmos. Chem. Phys.*, 5:433–444, **2005**. doi: 10.5194/acp-5-433-2005.

Jöckel, P., H. Tost, A. Pozzer, C. Brühl, J. Buchholz, L. Ganzeveld, P. Hoor, A. Kerkweg, M. G. Lawrence, R. Sander, B. Steil, G. Stiller, M. Tanarhte, D. Taraborrelli, J. van Aardenne, and J. Lelieveld. The atmospheric chemistry general circulation model ECHAM5/MESSy1: consistent simulation of ozone from the surface to the mesosphere. *Atmospheric Chemistry and Physics*, 6(12):5067–5104, **2006**. doi: 10.5194/acp-6-5067-2006.

Jöckel, P., A. Kerkweg, J. Buchholz-Dietsch, H. Tost, R. Sander, and A. Pozzer. Technical Note: Coupling of chemical processes with the Modular Earth Submodel System (MESSy) submodel TRACER. *Atmos. Chem. Phys.*, 8:1677–1687, **2008**. doi: 10.5194/acp-8-1677-2008.

Jöckel, P., A. Kerkweg, A. Pozzer, R. Sander, H. Tost, H. Riede, A. J. G. Baumgaertner, S. Gromov, and B. Kern. Development cycle 2 of the Modular Earth Submodel System (MESSy2). *Geoscientific Model Development*, 3(2):717–752, **2010**. doi: 10.5194/gmd-3-717-2010.

Jones, P. W. First- and Second-Order Conservative Remapping Schemes for Grids in Spherical Coordinates. *Monthly Weather Review*, 127(9):2204–2210, **1999**. doi: 10.1175/1520-0493(1999)127<2204:FASOCR>2.0.CO;2.

Jungclaus, J. H., M. Botzet, H. Haak, J. Marotzke, U. Mikolajewicz, E. Roeckner, N. Keenlyside, M. Latif, and J.-J. Luo. Ocean Circulation and Tropical Variability in the Coupled Model ECHAM5/MPI-OM. *J. Climate*, 19:3952–3972, **2006**. doi: 10.1175/JCLI3827.1.

Kalnay, E., M. Kanamitsu, R. Kistler, W. Collins, D. Deaven, L. Gandin, M. Iredell, S. Saha, G. White, J. Woollen, Y. Zhu, A. Leetmaa, R. Reynolds, M. Chelliah, W. Ebisuzaki, W. Higgins, J. Janowiak, K. C. Mo, C. Ropelewski, J. Wang, R. Jenne, and D. Joseph. The NCEP/NCAR 40-Year Reanalysis Project. *Bulletin of the American Meteorological Society*, 77(3):437–471, **1996**. doi: 10.1175/1520-0477(1996)077<0437:TNYRP>2.0.CO;2.

Kerkweg, A. and P. Jöckel. The 1-way on-line coupled atmospheric chemistry model system MECO(n) – Part 2: On-line coupling with the Multi-Model-Driver (MMD). *Geoscientific Model Development*, 5(1):111–128, **2012**. doi: 10.5194/gmd-5-111-2012.

Kerkweg, A., J. Buchholz, L. Ganzeveld, A. Pozzer, H. Tost, and P. Jöckel. Technical Note: An implementation of the dry removal processes DRY DEPosition and SEDImentation in the Modular Earth Submodel System (MESSy). *Atmospheric Chemistry and Physics*, 6(12):4617–4632, **2006a**. doi: 10.5194/acp-6-4617-2006.

Kerkweg, A., R. Sander, H. Tost, and P. Jöckel. Technical note: Implementation of prescribed (OFFLEM), calculated (ONLEM), and pseudo-emissions (TNUDGE) of chemical species in the Modular Earth Submodel System (MESSy). *Atmospheric Chemistry and Physics*, (11):3603–3609, **2006b**. doi: 10.5194/acp-6-3603-2006.

Kerkweg, A., P. Jöckel, A. Pozzer, H. Tost, R. Sander, M. Schulz, P. Stier, E. Vignati, J. Wilson, and J. Lelieveld. Consistent simulation of bromine chemistry from the marine boundary layer to the stratosphere – Part 1: Model description, sea salt aerosols and pH. *Atmospheric Chemistry and Physics*, 8(19):5899–5917, **2008**. doi: 10.5194/acp-8-5899-2008.

Kettle, A. Diurnal cycling of carbon monoxide (CO) in the upper ocean near Bermuda. *Ocean Modelling*, 8(4):337–367, **2005a**. doi: 10.1016/j.ocemod.2004.01.003.

Kettle, A. Comparison of the nonlocal transport characteristics of a series of one-dimensional oceanic boundary layer models. *Ocean Modelling*, 8(4):301–336, **2005b**. doi: 10.1016/j.ocemod.2004.01.002.

Kettle, A. J. and M. O. Andreae. Flux of dimethylsulfide from the oceans: A comparison of updated data sets and flux models. *Journal of Geophysical Research*, 105(D22):26793–26808, **2000**. doi: 10.1029/2000JD900252.

Kettle, A. J., M. O. Andreae, D. Amouroux, T. W. Andreae, T. S. Bates, H. Berresheim, H. Bingemer, R. Boniforti, M. A. J. Curran, G. R. DiTullio, G. Helas, G. B. Jones, M. D. Keller, R. P. Kiene, C. Leck, M. Levasseur, G. Malin, M. Maspero, P. Matrai, A. R. McTaggart, N. Mihalopoulos, B. C. Nguyen, A. Novo, J. P. Putaud, S. Rapsomanikis, G. Roberts, G. Schebeske, S. Sharma, R. Simó, R. Staubes, S. Turner, and G. Uher. A global database of sea surface dimethylsulfide (DMS) measurements and a procedure to predict sea surface DMS as a function of latitude, longitude, and month. *Global Biogeochemical Cycles*, 13 (2):399–444, **1999**. doi: 10.1029/1999GB900004.

Kirkevåg, A., T. Iversen, Ø. Seland, C. Hoose, J. E. Kristjánsson, H. Struthers, a. M. L. Ekman, S. Ghan, J. Griesfeller, E. D. Nilsson, and M. Schulz. Aerosol–climate interactions in the Norwegian Earth System Model – NorESM1-M. *Geoscientific Model Development*, 6(1):207–244, **2013**. doi: 10.5194/gmd-6-207-2013.

Kleypas, J. A., R. W. Buddemeier, D. Archer, J.-P. Gattuso, C. Langdon, and B. N. Opdyke. Geochemical Consequences of Increased Atmospheric Carbon Dioxide on Coral Reefs. *Science*, 284(5411):118–120, **1999**. doi: 10.1126/science.284.5411.118.

Kloster, S., J. Feichter, E. M. Reimer, K. D. Six, P. Stier, and P. Wetzel. DMS cycle in the marine ocean-atmosphere system - a global model study. *Biogeosciences*, 3 (1):29–51, **2006**. doi: 10.5194/bg-3-29-2006.

Kriest, I. Different parameterizations of marine snow in a 1D-model and their influence on representation of marine snow, nitrogen budget and sedimentation. *Deep Sea Research Part I: Oceanographic Research Papers*, 49(12):2133–2162, **2002**. doi: 10.1016/S0967-0637(02)00127-9.

Kriest, I. and G. T. Evans. A vertically resolved model for phytoplankton aggregation. *Journal of Earth System Science*, 109(4):453–469, **2000**. doi: 10.1007/BF02708333.

Lacis, A. A., D. J. Wuebbles, and J. A. Logan. Radiative Forcing of Climate by Changes in the Vertical Distribution of Ozone. *Journal of Geophysical Research*, 95(D7):9971–9981, **1990**. doi: 10.1029/JD095iD07p09971.

Lam, P. J., S. C. Doney, and J. K. B. Bishop. The dynamic ocean biological pump: Insights from a global compilation of particulate organic carbon, $CaCO_3$, and opal concentration profiles from the mesopelagic. *Global Biogeochemical Cycles*, 25(3): 1–14, **2011**. doi: 10.1029/2010GB003868.

Lana, A., T. G. Bell, R. Simó, S. M. Vallina, J. Ballabrera-Poy, A. J. Kettle, J. Dachs, L. Bopp, E. S. Saltzman, J. Stefels, J. E. Johnson, and P. S. Liss. An updated climatology of surface dimethlysulfide concentrations and emission fluxes in the global ocean. *Global Biogeochemical Cycles*, 25:GB1004, **2011**. doi: 10.1029/2010GB003850.

Landgraf, J. and P. J. Crutzen. An Efficient Method for Online Calculations of Photolysis and Heating Rates. *Journal of the Atmospheric Sciences*, 55(5):863–878, **1998**. doi: 10.1175/1520-0469(1998)055<0863:AEMFOC>2.0.CO;2.

Laws, E. A., P. G. Falkowski, W. O. Smith, H. Ducklow, and J. J. McCarthy. Temperature effects on export production in the open ocean. *Global Biogeochemical Cycles*, 14(4):1231–1246, **2000**. doi: 10.1029/1999GB001229.

Lelieveld, J., W. Peters, F. J. Dentener, and M. C. Krol. Stability of tropospheric hydroxyl chemistry. *Journal of Geophysical Research*, 107(D23):4715, **2002**. doi: 10.1029/2002JD002272.

Lelieveld, J., C. Brühl, P. Jöckel, B. Steil, P. J. Crutzen, H. Fischer, M. A. Giorgetta, P. Hoor, M. G. Lawrence, R. Sausen, and H. Tost. Stratospheric dryness: model simulations and satellite observations. *Atmospheric Chemistry and Physics*, 7(5): 1313–1332, **2007**. doi: 10.5194/acp-7-1313-2007.

Lelieveld, J., T. M. Butler, J. N. Crowley, T. J. Dillon, H. Fischer, L. Ganzeveld, H. Harder, M. G. Lawrence, M. Martinez, D. Taraborrelli, and J. Williams. Atmospheric oxidation capacity sustained by a tropical forest. *Nature*, 452(7188): 737–740, **2008**. doi: 10.1038/nature06870.

Levy, H. Normal atmosphere: large radical and formaldehyde concentrations predicted. *Science*, 173(3992):141–143, **1971**. doi: 10.1126/science.173.3992.141.

Li, F., J. Austin, and J. Wilson. The Strength of the Brewer–Dobson Circulation in a Changing Climate: Coupled Chemistry–Climate Model Simulations. *Journal of Climate*, 21(1):40–57, **2008**. doi: 10.1175/2007JCLI1663.1.

Liss, P. S. and P. G. Slater. Flux of Gases across the Air-Sea Interface. *Nature*, 247 (5438):181–184, **1974**. doi: 10.1038/247181a0.

Locarnini, R. A., A. V. Mishonov, J. I. Antonov, T. P. Boyer, H. E. Garcia, O. K. Baranova, M. M. Zweng, and D. R. Johnson. *World Ocean Atlas 2009, Volume 1: Temperature*. Levitus, S. (Ed.), NOAA Atlas NESDIS 68, U.S. Government Printing Office, Washington, D.C., USA, 184 pp., **2010**.

Longhurst, A. R. Role of the Marine Biosphere In the Global Carbon-cycle. *Limnology and Oceanography*, 36(8):1507–1526, **1991**. `http://www.aslo.org/lo/toc/vol_36/issue_8/1507.pdf`.

Lovelock, J. E., R. J. Maggs, and R. A. Rasmussen. Atmospheric Dimethyl Sulphide and the Natural Sulphur Cycle. *Nature*, 237(5356):452–453, **1972**. doi: 10.1038/237452a0.

Mahowald, N. M., A. R. Baker, G. Bergametti, N. Brooks, R. A. Duce, T. D. Jickells, N. Kubilay, J. M. Prospero, and I. Tegen. Atmospheric global dust cycle and iron inputs to the ocean. *Global Biogeochemical Cycles*, 19:GB4025, **2005**. doi: 10.1029/2004GB002402.

Maier-Reimer, E. Geochemical cycles in an ocean general circulation model. Preindustrial tracer distributions. *Global Biogeochemical Cycles*, 7(3):645–677, **1993**. doi: 10.1029/93GB01355.

Maier-Reimer, E. and K. Hasselmann. Transport and storage of $CO_2$ in the ocean—an inorganic ocean-circulation carbon cycle model. *Climate Dynamics*, 2(2):63–90, **1987**. doi: 10.1007/BF01054491.

Maier-Reimer, E., U. Mikolajewicz, and A. Winguth. Future ocean uptake of $CO_2$: interaction between ocean circulation and biology. *Climate Dynamics*, 12(10): 711–722, **1996**. doi: 10.1007/s003820050138.

Maier-Reimer, E., I. Kriest, J. Segschneider, and P. Wetzel. The HAMburg Ocean Carbon Cycle Model HAMOCC 5.1 - Technical Description Release 1.1. Berichte zur Erdsystemforschung No. 14, Max Planck Institute for Meteorology, Hamburg, Germany, 57 pp., **2005**. ISSN 1614-1199. `http://www.mpimet.mpg.de/fileadmin/publikationen/erdsystem_14.pdf`.

Manzini, E. and N. a. McFarlane. The effect of varying the source spectrum of a gravity wave parameterization in a middle atmosphere general circulation model. *Journal of Geophysical Research*, 103(D24):31523–31539, **1998**. doi: 10.1029/98JD02274.

Marchuk, G. I. On the Theory of the Splitting-Up Method. In: Hubbard, B. (Ed.), *Numerical Solution of Partial Differential Equations-II*, SYNSPADE 1970, 469–500. Academic Press, New York, NY, USA, **1971**. ISBN 0-12-358502-3.

Marsland, S. J., H. Haak, J. H. Jungclaus, M. Latif, and F. Röske. The Max-Planck-Institute global ocean/sea ice model with orthogonal curvilinnear coordinates. *Ocean Model.*, 5(2):91–127, **2003**. doi: 10.1016/S1463-5003(02)00015-X.

Martin, J. H., R. M. Gordon, and S. E. Fitzwater. The case for iron. *Limnology and Oceanography*, 36(8):1793–1802, **1991**. `http://www.aslo.org/lo/toc/vol_36/issue_8/1793.pdf`.

Martin, J. M. and M. Meybeck. Elemental mass-balance of material carried by major world rivers. *Marine Chemistry*, 7(3):173–206, **1979**. doi: 10.1016/0304-4203(79)90039-2.

Martin, S. T., M. O. Andreae, D. Althausen, P. Artaxo, H. Baars, S. Borrmann, Q. Chen, D. K. Farmer, A. Guenther, S. S. Gunthe, J. L. Jimenez, T. Karl, K. Longo, A. Manzi, T. Müller, T. Pauliquevis, M. D. Petters, a. J. Prenni, U. Pöschl, L. V. Rizzo, J. Schneider, J. N. Smith, E. Swietlicki, J. Tota, J. Wang, A. Wiedensohler, and S. R. Zorn. An overview of the Amazonian Aerosol Characterization Experiment 2008 (AMAZE-08). *Atmospheric Chemistry and Physics*, 10(23):11415–11438, **2010**. doi: 10.5194/acp-10-11415-2010.

Mauritsen, T., B. Stevens, E. Roeckner, T. Crueger, M. Esch, M. Giorgetta, H. Haak, J. Jungclaus, D. Klocke, D. Matei, U. Mikolajewicz, D. Notz, R. Pincus, H. Schmidt, and L. Tomassini. Tuning the climate of a global model. *Journal of Advances in Modeling Earth Systems*, 4:M00A01, **2012**. doi: 10.1029/2012MS000154.

Mayorga, E., S. P. Seitzinger, J. A. Harrison, E. Dumont, A. H. W. Beusen, A. F. Bouwman, B. M. Fekete, C. Kroeze, and G. van Drecht. Global Nutrient Export from WaterSheds 2 (NEWS 2): Model development and implementation. *Environmental Modelling & Software*, 25(7):837–853, **2010**. doi: 10.1016/j.envsoft.2010.01.007.

McGuffie, K. and A. Henderson-Sellers. *A climate modelling primer*. John Wiley & Sons Ltd, Chichester, England, 3rd edition, 296 pp., **2005**. ISBN 978-0-470-85751-9.

Meybeck, M. Carbon, nitrogen, and phosphorus transport by world rivers. *American Journal of Science*, 282:401–450, **1982**. doi: 10.2475/ajs.282.4.401.

Meybeck, M. The IGBP Water Group: a response to a growing global concern. *IGBP Newsletter*, (36):8–12, **1998**. `http://www.sisyphe.upmc.fr/~meybeck/MM/pdf/98B.pdf`.

Meybeck, M., H. H. Dürr, and C. J. Vörösmarty. Global coastal segmentation and its river catchment contributors: A new look at land-ocean linkage. *Global Biogeochemical Cycles*, 20(1):GB1S90, **2006**. doi: 10.1029/2005GB002540.

Millet, D. B., D. J. Jacob, T. G. Custer, J. a. de Gouw, a. H. Goldstein, T. Karl, H. B. Singh, B. C. Sive, R. W. Talbot, C. Warneke, and J. Williams. New constraints on terrestrial and oceanic sources of atmospheric methanol. *Atmospheric Chemistry and Physics*, 8(23):6887–6905, **2008**. doi: 10.5194/acp-8-6887-2008.

Mills, M. M., C. Ridame, M. Davey, J. La Roche, and R. J. Geider. Iron and phosphorus co-limit nitrogen fixation in the eastern tropical North Atlantic. *Nature*, 429(6989):292–294, **2004**. doi: 10.1038/nature02550.

Moberg, F. and C. Folke. Ecological goods and services of coral reef ecosystems. *Ecological Economics*, 29(2):215–233, **1999**. doi: 10.1016/S0921-8009(99)00009-9.

Mohr, P. J., B. N. Taylor, and D. B. Newell. CODATA recommended values of the fundamental physical constants: 2010. Preprint, 15 March 2012, National Institute of Standards and Technology, Gaithersburg, MD, USA, **2012**. `http://physics.nist.gov/cuu/`.

Molina, M. J. and F. S. Rowland. Stratospheric sink for chlorofluoromethanes: chlorine atom-catalysed destruction of ozone. *Nature*, 249(5460):810–812, **1974**. doi: 10.1038/249810a0.

Montzka, S. A., E. J. Dlugokencky, and J. H. Butler. Non-$CO_2$ greenhouse gases and climate change. *Nature*, 476(7358):43–50, **2011**. doi: 10.1038/nature10322.

Moore, C. M., M. M. Mills, E. P. Achterberg, R. J. Geider, J. LaRoche, M. I. Lucas, E. L. McDonagh, X. Pan, A. J. Poulton, M. J. a. Rijkenberg, D. J. Suggett, S. J. Ussher, and E. M. S. Woodward. Large-scale distribution of Atlantic nitrogen fixation controlled by iron availability. *Nature Geoscience*, 2(12):867–871, **2009**. doi: 10.1038/ngeo667.

Moore, J., S. C. Doney, J. A. Kleypas, D. M. Glover, and I. Y. Fung. An intermediate complexity marine ecosystem model for the global domain. *Deep Sea Research Part II*, 49(1-3):403–462, **2001**. doi: 10.1016/S0967-0645(01)00108-4.

Neale, R. B., J. Richter, S. Park, P. H. Lauritzen, S. J. Vavrus, P. J. Rasch, and M. Zhang. The Mean Climate of the Community Atmosphere Model (CAM4) in Forced SST and Fully Coupled Experiments. *Journal of Climate*, 26(14):5150–5168, **2013**. doi: 10.1175/JCLI-D-12-00236.1.

Nevison, C. D., R. F. Weiss, and D. J. Erickson. Global oceanic emissions of nitrous oxide. *Journal of Geophysical Research*, 100(C8):15809–15820, **1995**. doi: 10.1029/95JC00684.

Nguyen, B. C., A. Gaudry, B. Bonsang, and G. Lambert. Reevaluation of the role of dimethyl sulphide in the sulphur budget. *Nature*, 275(5681):637–639, **1978**. doi: 10.1038/275637a0.

NIST. *NIST Chemistry WebBook, NIST Standard Reference Database Number 69*. National Institute of Standards and Technology, Gaithersburg, MD, USA, Linstrom, P. and W. Mallard (Eds.), **2011**. `http://webbook.nist.gov/`. Retrieved 1 February 2013.

Nordeng, T. E. Extended versions of the convective parametrization scheme at ECMWF and their impact on the mean and transient activity of the model in the tropics. European Centre for Medium-Range Weather Forecasts, 41 pp., **1994**. http://www.ecmwf.int/publications/library/do/references/list/14.

O'Reilly, J. E., S. Maritorena, B. G. Mitchell, D. A. Siegel, K. L. Carder, S. A. Garver, M. Kahru, and C. McClain. Ocean color chlorophyll algorithms for SeaWiFS. *Journal of Geophysical Research*, 103(C11):24937–24953, **1998**. http://www.agu.org/journals/jc/v103/iC11/98JC02160/.

Orr, J. C., V. J. Fabry, O. Aumont, L. Bopp, S. C. Doney, R. A. Feely, A. Gnanadesikan, N. Gruber, A. Ishida, F. Joos, R. M. Key, K. Lindsay, E. Maier-Reimer, R. Matear, P. Monfray, A. Mouchet, R. G. Najjar, G.-K. Plattner, K. B. Rodgers, C. L. Sabine, J. L. Sarmiento, R. Schlitzer, R. D. Slater, I. J. Totterdell, M.-F. Weirig, Y. Yamanaka, and A. Yool. Anthropogenic ocean acidification over the twenty-first century and its impact on calcifying organisms. *Nature*, 437(7059): 681–686, **2005**. doi: 10.1038/nature04095.

Pacanowski, R. C. and S. G. H. Philander. Parameterization of vertical mixing in numerical models of tropical oceans. *Journal of Physical Oceanography*, 11: 1443–1451, **1981**. doi: 10.1175/1520-0485(1981)011<1443:POVMIN>2.0.CO;2.

Paerl, H. W. Coastal eutrophication and harmful algal blooms : Importance of atmospheric deposition and groundwater as " new " nitrogen and other nutrient sources. *Limnology and Oceanography*, 42(5/2):1154–1165, **1997**. http://www.aslo.org/lo/toc/vol_42/issue_5_part_2/1154.pdf.

Palmer, P. I. and S. L. Shaw. Quantifying global marine isoprene fluxes using MODIS chlorophyll observations. *Geophysical Research Letters*, 32:L09805, **2005**. doi: 10.1029/2005GL022592.

Pannell, D. J. Sensitivity analysis of normative economic models: theoretical framework and practical strategies. *Agricultural Economics*, 16(22):139–152, **1997**. doi: 10.1016/S0169-5150(96)01217-0.

Paulson, S. E., R. C. Flagan, and J. H. Seinfeld. Atmospheric photooxidation of isoprene part I: The hydroxyl radical and ground state atomic oxygen reactions. *International Journal of Chemical Kinetics*, 24(1):79–101, **1992a**. doi: 10.1002/kin.550240109.

Paulson, S. E., R. C. Flagan, and J. H. Seinfeld. Atmospheric photooxidation of isoprene part II: The ozone-isoprene reaction. *International Journal of Chemical Kinetics*, 24(1):103–125, **1992b**. doi: 10.1002/kin.550240110.

Poling, B. E., J. M. Prausnitz, and J. O' Connell. *The Properties of Gases and Liquids*. McGraw-Hill Professional, New York, NY, USA, fifth edition, 768 pp., **2001**. ISBN 0071499997. doi: 10.1036/0070116822.

Pozzer, A. *Simulating short lived carbonaceous compounds with an atmospheric chemistry general circulation model*. Diss., Johannes Gutenberg Universität, Mainz, **2007**. `http://ubm.opus.hbz-nrw.de/volltexte/2007/1315/`.

Pozzer, A., P. Jöckel, R. Sander, J. Williams, L. Ganzeveld, and J. Lelieveld. Technical Note: The MESSy-submodel AIRSEA calculating the air-sea exchange of chemical species. *Atmospheric Chemistry and Physics*, 6(12):5435–5444, **2006**. doi: 10.5194/acp-6-5435-2006.

Pozzer, A., P. Jöckel, B. Kern, and H. Haak. The Atmosphere-Ocean General Circulation Model EMAC-MPIOM. *Geoscientific Model Development*, 4(3):771–784, **2011**. doi: 10.5194/gmd-4-771-2011.

Press, W. H., S. A. Teukolsky, W. T. Vetterling, and B. P. Flannery. *Numerical Recipes: The Art of Scientific Computing, Third Edition*. Cambridge University Press, Cambridge, United Kingdom, 1256 pp., **2007**. ISBN 978-0521880688. `http://www.nr.com/`.

Redfield, A. C., B. H. Ketchum, and F. A. Richards. The Influence of Organisms on the Composition of Sea-Water. In: Hill, M. N. (Ed.), *The Sea - Ideas and Observations on Progress in the Study of the Seas, Volume 2: The Composition of Sea-Water - Comparative and Descriptive Oceanography*, Chapter 2, 26–77. John Wiley & Sons, Inc., New York, NY, USA, **1963**.

Redi, M. H. Oceanic Isopycnal Mixing by Coordinate Rotation. *Journal of Physical Oceanography*, 12(10):1154–1158, **1982**. doi: 10.1175/1520-0485(1982)012<1154:OIMBCR>2.0.CO;2.

Retamal, L., W. F. Vincent, C. Martineau, and C. L. Osburn. Comparison of the optical properties of dissolved organic matter in two river-influenced coastal regions of the Canadian Arctic. *Estuarine, Coastal and Shelf Science*, 72(1-2):261–272, **2007**. doi: 10.1016/j.ecss.2006.10.022.

Rhee, T. S., a. J. Kettle, and M. O. Andreae. Methane and nitrous oxide emissions from the ocean: A reassessment using basin-wide observations in the Atlantic. *Journal of Geophysical Research*, 114:D12304, **2009**. doi: 10.1029/2008JD011662.

Riemann, B., P. Simonsen, and L. Stensgaard. The carbon and chlorophyll content of phytoplankton from various nutrient regimes. *Journal of Plankton Research*, 11 (5):1037–1045, **1989**. doi: 10.1093/plankt/11.5.1037.

Riemer, D. D. and E. C. Apel. Confirming the Presence and Extent of Oxidation by Cl in the Houston Texas Urban Area Using Specific Isoprene Oxidation Products as Tracers. Texas Natural Resource Conservation Commission, Final Report, University of Miami, Rosenstiel School of Marine and Atmospheric Science, Miami, Florida, USA, 15 pp., **2001**. `http://www.tceq.texas.gov/assets/public/implementation/air/am/contracts/reports/oth/ConfirmingPresenceandExtentOfOxidationByCI.pdf`.

Rodolfo-Metalpa, R., F. Houlbrèque, E. Tambutté, F. Boisson, C. Baggini, F. P. Patti, R. Jeffree, M. Fine, A. Foggo, J.-P. Gattuso, and J. M. Hall-Spencer. Coral and mollusc resistance to ocean acidification adversely affected by warming. *Nature Climate Change*, 1(9):308–312, **2011**. doi: 10.1038/nclimate1200.

Roeckner, E., K. Arpe, L. Bengtsson, M. Christoph, M. Claussen, L. Dümenil, M. Esch, M. Giorgetta, U. Schlese, and U. Schulzweida. The atmospheric general circulation model ECHAM-4: Model description and simulation of present-day climate, Report No. 218. Report No. 218, Max Planck Institute for Meteorology, Hamburg, Germany, 94 pp., **1996**. `http://www.mpimet.mpg.de/fileadmin/publikationen/Reports/MPI-Report_218.pdf`.

Roeckner, E., G. Bäuml, L. Bonaventura, R. Brokopf, M. Esch, M. Giorgetta, S. Hagemann, I. Kirchner, L. Kornblueh, E. Manzini, A. Rhodin, U. Schlese, U. Schulzweida, and A. Tompkins. The atmospheric general circulation model ECHAM5: Part I - Model description. Report No. 349, Max Planck Institute for Meteorology, Hamburg, Germany, 140 pp., **2003**. ISSN 0937-1060. `http://www.mpimet.mpg.de/fileadmin/publikationen/Reports/max_scirep_349.pdf`.

Roeckner, E., R. Brokopf, M. Esch, M. Giorgetta, S. Hagemann, L. Kornblueh, E. Manzini, U. Schlese, and U. Schulzweida. Sensitivity of Simulated Climate to Horizontal and Vertical Resolution in the ECHAM5 Atmosphere Model. *Journal of Climate*, 19(16):3771–3791, **2006**. doi: 10.1175/JCLI3824.1.

Roelofs, G.-J. and J. Lelieveld. Model study of the influence of cross-tropopause $O_3$ transports on tropospheric $O_3$ levels. *Tellus B*, 49(1):38–55, **1997**. doi: 10.1034/j.1600-0889.49.issue1.3.x.

Sabine, C. L., R. A. Feely, N. Gruber, R. M. Key, K. Lee, J. L. Bullister, R. Wanninkhof, C. S. Wong, D. W. R. Wallace, B. Tilbrook, F. J. Millero, T.-H. Peng, A. Kozyr, T. Ono, and A. F. Rios. The oceanic sink for anthropogenic $CO_2$. *Science*, 305(5682):367–371, **2004**. doi: 10.1126/science.1097403.

Sander, R. *Compilation of Henry's Law Constants for Inorganic and Organic Species of Potential Importance in Environmental Chemistry*. Mainz, Germany, 107 pp., **1999a**. `http://www.henrys-law.org/`. Retrieved 1 February 2013.

Sander, R. Modeling Atmospheric Chemistry: Interactions between Gas-Phase Species and Liquid Cloud/Aerosol Particles. *Surveys in Geophysics*, 20(1):1–31, **1999b**. doi: 10.1023/A:1006501706704.

Sander, R., A. Kerkweg, P. Jöckel, and J. Lelieveld. Technical note: The new comprehensive atmospheric chemistry module MECCA. *Atmospheric Chemistry and Physics*, 5(2):445–450, **2005**. doi: 10.5194/acp-5-445-2005.

Sander, R., A. Baumgaertner, S. Gromov, H. Harder, P. Jöckel, A. Kerkweg, D. Kubistin, E. Regelin, H. Riede, A. Sandu, D. Taraborrelli, H. Tost, and Z.-Q. Xie. The atmospheric chemistry box model CAABA/MECCA-3.0. *Geoscientific Model Development*, 4(2):373–380, **2011**. doi: 10.5194/gmd-4-373-2011.

Sarmiento, J. L. and N. Gruber. *Ocean Biogeochemical Dynamics*. Princeton University Press, Princeton, New Jersey, USA, 526 pp., **2006**. ISBN 978-0-691-01707-5.

Schellnhuber, H. J. 'Earth system' analysis and the second Copernican revolution. *Nature*, 402(December):C19–C23, **1999**. doi: 10.1038/35011515.

Schirber, S., D. Klocke, R. Pincus, J. Quaas, and J. L. Anderson. Parameter estimation using data assimilation in an atmospheric general circulation model: From a perfect toward the real world. *Journal of Advances in Modeling Earth Systems*, 5(1):58–70, **2013**. doi: 10.1029/2012MS000167.

Schlitzer, R. Carbon export fluxes in the Southern Ocean: results from inverse modeling and comparison with satellite-based estimates. *Deep Sea Research Part II*, 49(9-10):1623–1644, **2002**. doi: 10.1016/S0967-0645(02)00004-8.

Schneider, B., M. Latif, and A. Schmittner. Evaluation of Different Methods to Assess Model Projections of the Future Evolution of the Atlantic Meridional Overturning Circulation. *Journal of Climate*, 20(10):2121–2132, **2007**. doi: 10.1175/JCLI4128.1.

Schneider, B., L. Bopp, M. Gehlen, J. Segschneider, T. L. Frölicher, P. Cadule, P. Friedlingstein, S. C. Doney, M. J. Behrenfeld, and F. Joos. Climate-induced interannual variability of marine primary and export production in three global coupled climate carbon cycle models. *Biogeosciences*, 5(2):597–614, **2008**. doi: 10.5194/bg-5-597-2008.

Sciare, J., N. Mihalopoulos, and F. J. Dentener. Interannual variability of atmospheric dimethylsulfide in the southern Indian Ocean. *Journal of Geophysical Research*, 105(D21):26369–26377, **2000**. doi: 10.1029/2000JD900236.

Seinfeld, J. H. and S. N. Pandis. *Atmospheric Chemistry and Physics - From Air Pollution to Climate Change*. John Wiley & Sons, Inc., New York, NY, USA, 1326 pp., **1998**. ISBN 0-471-17816-0.

Seitzinger, S. P., J. A. Harrison, E. Dumont, A. H. W. Beusen, and A. F. Bouwman. Sources and delivery of carbon, nitrogen, and phosphorus to the coastal zone: An overview of Global Nutrient Export from Watersheds (NEWS) models and their application. *Global Biogeochemical Cycles*, 19(4):GB4S01, **2005**. doi: 10.1029/2005GB002606.

Seitzinger, S. P., E. Mayorga, A. F. Bouwman, C. Kroeze, A. H. W. Beusen, G. Billen, G. Van Drecht, E. Dumont, B. M. Fekete, J. Garnier, and J. A. Harrison. Global river nutrient export: A scenario analysis of past and future trends. *Global Biogeochem. Cycles*, 24:GB0A08, **2010**. doi: 10.1029/2009GB003587.

Serreze, M. C., A. P. Barrett, A. G. Slater, R. A. Woodgate, K. Aagaard, R. B. Lammers, M. Steele, R. Moritz, M. Meredith, and C. M. Lee. The large-scale freshwater cycle of the Arctic. *Journal of Geophysical Research*, 111:C11010, **2006**. doi: 10.1029/2005JC003424.

Shallcross, D. E. and P. S. Monks. New Directions: A role for isoprene in biosphere-climate-chemistry feedbacks. *Atmospheric Environment*, 34(10):1659–1660, **2000**. doi: 10.1016/S1352-2310(99)00483-5.

Sharkey, T. D. and E. L. Singsaas. Why plants emit isoprene. *Nature*, 374(6525): 769–769, **1995**. doi: 10.1038/374769a0.

Sharkey, T. D., A. E. Wiberley, and A. R. Donohue. Isoprene emission from plants: why and how. *Annals of Botany*, 101(1):5–18, **2008**. doi: 10.1093/aob/mcm240.

Shaw, S. L. *The Production of Non-Methane Hydrocarbons by Marine Plankton*. PhD thesis, MIT, Cambridge, MA, USA, **2001**. `http://hdl.handle.net/1721.1/8255`.

Shaw, S. L., S. W. Chisholm, and R. G. Prinn. Isoprene production by Prochlorococcus, a marine cyanobacterium, and other phytoplankton. *Marine Chemistry*, 80(4):227–245, **2003**. doi: 10.1016/S0304-4203(02)00101-9.

Shi, Z., M. D. Krom, S. Bonneville, A. R. Baker, C. Bristow, N. Drake, G. Mann, K. Carslaw, J. B. McQuaid, T. Jickells, and L. G. Benning. Influence of chemical weathering and aging of iron oxides on the potential iron solubility of Saharan dust during simulated atmospheric processing. *Global Biogeochemical Cycles*, 25: GB2010, **2011**. doi: 10.1029/2010GB003837.

Simó, R. Production of atmospheric sulfur by oceanic plankton: biogeochemical, ecological and evolutionary links. *Trends in Ecology & Evolution*, 16(6):287–294, **2001**. doi: 10.1016/S0169-5347(01)02152-8.

Singh, H. B., A. Tabazadeh, M. J. Evans, B. D. Field, D. J. Jacob, G. Sachse, J. H. Crawford, R. Shetter, and W. H. Brune. Oxygenated volatile organic chemicals in the oceans: Inferences and implications based on atmospheric observations and air-sea exchange models. *Geophysical Research Letters*, 30(16):1862, **2003**. doi: 10.1029/2003GL017933.

Six, K. D. and E. Maier-Reimer. Effects of plankton dynamics on seasonal carbon fluxes in an ocean general circulation model. *Global Biogeochemical Cycles*, 10(4): 559–583, **1996**. doi: 10.1029/96GB02561.

SOLAS. The Surface Ocean – Lower Atmosphere Study Science Plan and Implementation Strategy. IGBP report No. 50, 94 pp., **2004**. `http://solas-int.org/resources/books.html?file=files/solas-int/content/downloads/pdf/SPIS/spis.pdf`.

Solomon, S. Stratospheric ozone depletion: A review of concepts and history. *Reviews of Geophysics*, 37(3):275, **1999**. doi: 10.1029/1999RG900008.

SPARC CCMVal. SPARC CCMVal Report on the Evaluation of Chemistry-Climate Models. SPARC report No. 5, WCRP-132, WMO/TD-No. 1526, Eyring, V., T. G. Shepherd, and D. W. Waugh (Eds.), 426 pp., **2010**. `http://www.sparc-climate.org/publications/sparc-reports/sparc-report-no5/`.

Spokes, L. J., S. G. Yeatman, S. E. Cornell, and T. D. Jickells. Nitrogen deposition to the eastern Atlantic Ocean. The importance of south-easterly flow. *Tellus B*, 52(1):37–49, **2000**. doi: 10.1034/j.1600-0889.2000.00062.x.

Spurgeon, J. P. The economic valuation of coral reefs. *Marine Pollution Bulletin*, 24 (11):529–536, **1992**. doi: 10.1016/0025-326X(92)90704-A.

Stephens, G. L., S.-C. Tsay, P. W. Stackhouse, and P. J. Flatau. The Relevance of the Microphysical and Radiative Properties of Cirrus Clouds to Climate and Climatic Feedback. *Journal of the Atmospheric Sciences*, 47(14):1742–1754, **1990**. doi: 10.1175/1520-0469(1990)047<1742:TROTMA>2.0.CO;2.

Stevens, B., M. Giorgetta, M. Esch, T. Mauritsen, T. Crueger, S. Rast, M. Salzmann, H. Schmidt, J. Bader, K. Block, R. Brokopf, I. Fast, S. Kinne, L. Kornblueh, U. Lohmann, R. Pincus, T. Reichler, and E. Roeckner. The atmospheric component of the MPI-M earth system model: ECHAM6. *Journal of Advances in Modeling Earth Systems*, 5:1–27, **2013**. doi: 10.1002/jame.20015.

Stier, P., J. Feichter, S. Kinne, S. Kloster, E. Vignati, J. Wilson, L. Ganzeveld, I. Tegen, M. Werner, Y. Balkanski, M. Schulz, O. Boucher, A. Minikin, and A. Petzold. The aerosol-climate model ECHAM5-HAM. *Atmospheric Chemistry and Physics*, 5(4):1125–1156, **2005**. doi: 10.5194/acp-5-1125-2005.

Stubbins, A., G. Uher, V. Kitidis, C. S. Law, R. C. Upstill-Goddard, and E. M. S. Woodward. The open-ocean source of atmospheric carbon monoxide. *Deep Sea Research Part II: Topical Studies in Oceanography*, 53(14-16):1685–1694, **2006**. doi: 10.1016/j.dsr2.2006.05.010.

Swinnerton, J. W., V. J. Linnenbom, and R. A. Lamontagne. The Ocean: A Natural Source of Carbon Monoxide. *Science*, 167(3920):984–986, **1970**. doi: 10.1126/science.167.3920.984.

Takahashi, T., W. S. Broecker, and S. Langer. Redfield Ratio Based on Chemical Data from Isopycnal Surfaces. *Journal of Geophysical Research*, 90(C4):6907–6924, **1985**. doi: 10.1029/JC090iC04p06907.

Takahashi, T., S. C. Sutherland, R. Wanninkhof, C. Sweeney, R. A. Feely, D. W. Chipman, B. Hales, G. Friederich, F. Chavez, C. Sabine, A. Watson, D. C. E. Bakker, U. Schuster, N. Metzl, H. Yoshikawa-Inoue, M. Ishii, T. Midorikawa, Y. Nojiri, A. Kortzinger, T. Steinhoff, M. Hoppema, J. Olafsson, T. S. Arnarson, B. Tilbrook, T. Johannessen, A. Olsen, R. Bellerby, C. S. Wong, B. Delille, N. R. Bates, and H. J. W. de Baar. Climatological mean and decadal change in surface ocean pCO(2), and net sea-air $CO_2$ flux over the global oceans. *Deep-Sea Research II*, 56 (8-10):554–577, **2009**. doi: 10.1016/j.dsr2.2008.12.009 10.1016/j.dsr.2009.07.007.

Tanre, D., J.-F. Geleyn, and J. M. Slingo. First results of the introduction of an advanced aerosol-radiation interaction in the ECMWF low resolution global model. In: Gerber, H. and A. Deepak (Eds.), *Aerosols and their climatic effects*, 133–177. A. Deepak, Hamton, VA, **1984**.

Taraborrelli, D., M. G. Lawrence, J. N. Crowley, T. J. Dillon, S. Gromov, C. B. M. Groß, L. Vereecken, and J. Lelieveld. Hydroxyl radical buffered by isoprene oxidation over tropical forests. *Nature Geoscience*, 5(3):190–193, **2012**. doi: 10.1038/ngeo1405.

Taylor, K. E. Summarizing multiple aspects of model performance in a single diagram. *Journal of Geophysical Research*, 106(D7):7183–7192, **2001**. doi: 10.1029/2000JD900719.

Taylor, K. E., D. Williamson, and F. Zwiers. PCMDI Report. No. 60, University of California, Lawrence Livermore National Laboratory, Livermore, CA, USA, 28 pp., **2000**. `http://www-pcmdi.llnl.gov/publications/ab60.html`.

Tegen, I., S. P. Harrison, K. Kohfeld, I. C. Prentice, M. Coe, and M. Heimann. Impact of vegetation and preferential source areas on global dust aerosol: Results from a model study. *Journal of Geophysical Research*, 107(D21):4576, **2002**. doi: 10.1029/2001JD000963.

Terry, G., N. Stokes, C. Hewitt, and T. Mansfield. Exposure to isoprene promotes flowering in plants. *Journal of Experimental Botany*, 46(10):1629–1631, **1995**. doi: 10.1093/jxb/46.10.1629.

Tiedtke, M. A Comprehensive Mass Flux Scheme for Cumulus Parameterization in Large-Scale Models. *Monthly Weather Review*, 117(8):1779–1800, **1989**. doi: 10.1175/1520-0493(1989)117<1779:ACMFSF>2.0.CO;2.

Timmreck, C. and M. Schulz. Significant dust simulation differences in nudged and climatological operation mode of the AGCM ECHAM. *Journal of Geophysical Research*, 109:D13202, **2004**. doi: 10.1029/2003JD004381.

Tjiputra, J. F., C. Roelandt, M. Bentsen, D. M. Lawrence, T. Lorentzen, J. Schwinger, Ø. Seland, and C. Heinze. Evaluation of the carbon cycle components in the Norwegian Earth System Model (NorESM). *Geoscientific Model Development*, 6 (2):301–325, **2013**. doi: 10.5194/gmd-6-301-2013.

Tost, H. *Global Modelling of Cloud, Convection and Precipitation Influences on Trace Gases and Aerosols*. Diss., Rheinische Friedrich-Wilhelms-Universität Bonn, Germany, **2006**. `http://hss.ulb.uni-bonn.de/2006/0731/0731-engl.htm`.

Tost, H., P. Jöckel, A. Kerkweg, R. Sander, and J. Lelieveld. Technical note: A new comprehensive SCAVenging submodel for global atmospheric chemistry modelling. *Atmospheric Chemistry and Physics*, 6(3):565–574, **2006a**. doi: 10.5194/acp-6-565-2006.

Tost, H., P. Jöckel, and J. Lelieveld. Influence of different convection parameterisations in a GCM. *Atmospheric Chemistry and Physics*, 6(12):5475–5493, **2006b**. doi: 10.5194/acp-6-5475-2006.

Tost, H., P. Jöckel, A. Kerkweg, A. Pozzer, R. Sander, and J. Lelieveld. Global cloud and precipitation chemistry and wet deposition: tropospheric model simulations with ECHAM5/MESSy1. *Atmospheric Chemistry and Physics*, 7(10):2733–2757, **2007a**. doi: 10.5194/acp-7-2733-2007.

Tost, H., P. Jöckel, and J. Lelieveld. Lightning and convection parameterisations – uncertainties in global modelling. *Atmospheric Chemistry and Physics*, 7(17): 4553–4568, **2007b**. doi: 10.5194/acp-7-4553-2007.

Trenberth, K. E., J. T. Fasullo, and J. Kiehl. Earth's Global Energy Budget. *Bulletin of the American Meteorological Society*, 90(3):311–323, **2009**. doi: 10.1175/2008BAMS2634.1.

Turing, A. M. Computing Machinery and Intelligence. *Mind*, LIX(236):433–460, **1950**. doi: 10.1093/mind/LIX.236.433.

Valcke, S., V. Balaji, A. Craig, C. DeLuca, R. Dunlap, R. W. Ford, R. Jacob, J. Larson, R. O'Kuinghttons, G. D. Riley, and M. Vertenstein. Coupling technologies for Earth System Modelling. *Geoscientific Model Development*, 5(6):1589–1596, **2012**. doi: 10.5194/gmd-5-1589-2012.

Valley, S. L. (Ed.). Handbook of Geophysics and Space Environments. Scientific Interim Report, Air Force Cambridge Research Laboratories, Hanscom Air Force Base, MA, USA, 702 pp., **1965**. `http://oai.dtic.mil/oai/oai?verb=getRecord&metadataPrefix=html&identifier=ADA056800`.

Ver, L. M. B., F. T. Mackenzie, and A. Lerman. Carbon cycle in the coastal zone: effects of global perturbations and change in the past three centuries. *Chemical Geology*, 159(1-4):283–304, **1999**. doi: 10.1016/S0009-2541(99)00042-X.

Vignati, E., J. Wilson, and P. Stier. M7: An efficient size-resolved aerosol microphysics module for large-scale aerosol transport models. *Journal of Geophysical Research*, 109:D22202, **2004**. doi: 10.1029/2003JD004485.

von Glasow, R. and P. J. Crutzen. Model study of multiphase DMS oxidation with a focus on halogens. *Atmospheric Chemistry and Physics*, 4(3):589–608, **2004**. doi: 10.5194/acp-4-589-2004.

von Kuhlmann, R., M. G. Lawrence, P. J. Crutzen, and P. J. Rasch. A model for studies of tropospheric ozone and nonmethane hydrocarbons: Model description and ozone results. *Journal of Geophysical Research*, 108(D9):4294, **2003**. doi: 10.1029/2002JD002893.

Wanninkhof, R. Relationship Between Wind Speed and Gas Exchange Over the Ocean. *Journal of Geophysical Research*, 97(C5):7373–7382, **1992**. doi: 10.1029/92JC00188.

Wanninkhof, R., W. E. Asher, D. T. Ho, C. Sweeney, and W. R. McGillis. Advances in Quantifying Air-Sea Gas Exchange and Environmental Forcing. *Annual Review of Marine Science*, 1:213–244, **2009**. doi: 10.1146/annurev.marine.010908.163742.

Warneck, P. and J. Williams. *The Atmospheric Chemist's Companion*. Springer, Dordrecht, Netherlands, 437 pp., **2012**. ISBN 978-94-007-2274-3. doi: 10.1007/978-94-007-2275-0.

Westberry, T., M. J. Behrenfeld, D. A. Siegel, and E. Boss. Carbon-based primary productivity modeling with vertically resolved photoacclimation. *Global Biogeochemical Cycles*, 22(2):GB2024, **2008**. doi: 10.1029/2007GB003078.

Wetzel, P., A. Winguth, and E. Maier-Reimer. Sea-to-air $CO_2$ flux from 1948 to 2003: A model study. *Global Biogeochemical Cycles*, 19(2):GB2005, **2005**. doi: 10.1029/2004GB002339.

Wetzel, P., E. Maier-Reimer, M. Botzet, J. Jungclaus, N. Keenlyside, and M. Latif. Effects of Ocean Biology on the Penetrative Radiation in a Coupled Climate Model. *J. Climate*, 16:3973–3987, **2006**. doi: 10.1175/JCLI3828.1.

Wilke, C. R. and P. Chang. Correlation of diffusion coefficients in dilute solutions. *AIChE Journal*, 1(2):264–270, **1955**. doi: 10.1002/aic.690010222.

Williams, J., R. Holzinger, V. Gros, X. Xu, E. Atlas, and D. W. R. Wallace. Measurements of organic species in air and seawater from the tropical Atlantic. *Geophysical Research Letters*, 31:L23S06, **2004**. doi: 10.1029/2004GL020012.

Xie, W.-H., W.-Y. Shiu, and D. Mackay. A review of the effect of salts on the solubility of organic compounds in seawater. *Marine Environmental Research*, 44 (4):429–444, **1997**. doi: 10.1016/S0141-1136(97)00017-2.

Yamada, T. and R. D. Gunn. Saturated liquid molar volumes. Rackett equation. *Journal of Chemical & Engineering Data*, 18(2):234–236, **1973**. doi: 10.1021/je60057a006.

Yassaa, N., I. Peeken, E. Zöllner, K. Bluhm, S. Arnold, D. Spracklen, and J. Williams. Evidence for marine production of monoterpenes. *Environmental Chemistry*, 5(6): 391–401, **2008**. doi: 10.1071/EN08047.

Zhang, Y., H. Xie, C. G. Fichot, and G. Chen. Dark production of carbon monoxide (CO) from dissolved organic matter in the St. Lawrence estuarine system: Implication for the global coastal and blue water CO budgets. *Journal of Geophysical Research*, 113:C12020, **2008**. doi: 10.1029/2008JC004811.